Tampere University

STEFANUS ARINNO WIRDATMADJA

Wireless Optogenetics Nanonetworking Device (WiOptND)

Opto-acoustic brain machine interface

STEFANUS ARINNO WIRDATMADJA

Wireless Optogenetics Nanonetworking Device (WiOptND)

Opto-acoustic brain machine interface

ACADEMIC DISSERTATION
To be presented, with the permission of
the Faculty of Information Technology and Communication Sciences
of Tampere University,
for public discussion at Tampere University
on 5 November 2020, at 12 o'clock.

ACADEMIC DISSERTATION
Tampere University, Faculty of Information Technology and Communication Sciences
Finland

Responsible supervisor and Custos	Professor Yevgeni Koucheryavy Tampere University Finland	
Supervisor	Dr Sasitharan Balasubramaniam Tampere University Finland	
Pre-examiners	Professor Özgur B. Akan Koç University Turkey	Professor Nicola Marchetti Trinity College Dublin Ireland
Opponent	Professor Wolfgang H. Gerstacker Friedrich-Alexander-Universität Germany	

Cover design: Roihu Inc.

In loving memory of:

Gabriel Wiroatmadja
and
Linda Rusli

PREFACE/ACKNOWLEDGEMENTS

ABSTRACT

More than 50 million people worldwide suffer from epilepsy and around 6.3 million have Parkinson's disease (PD). These are two examples of the many neurological disorders. Depending on the severity, one available solution is deep brain stimulation (DBS). DBS is a method to send electrical impulses to the desired region of the brain by using an electrode implant to regulate abnormal impulses. Another stimulation method, known as optogenetics, uses optical stimulation. This method is already popular in experiments on mice and non-human primates, but not in humans. Considering the recent research and development in optogenetics, its implementation in humans could be another solution for neurological treatment.

The objective of this thesis was to develop a wireless fully implantable brain machine interface (BMI) which can be applied to both animals and humans. In this thesis, we propose the concept of the Wireless Nanonetworking Device (WiOptND), which is batteryless and small in size. We found that this device is feasible to be implemented with existing technology by considering optogenetic specifications and light intensity requirements. Furthermore, we propose a system charging protocol that can be integrated into this device. We found that by employing a suitable charging protocol, the efficiency and the effectiveness of the device can be maximised. Moreover, it can support spatially distributed stimulation, where multiple devices can support synchronous neuronal stimulation. In addition to that, we investigated light propagation behaviour in neuronal tissue. Interestingly, the light exhibited focusing effect for spherical and pyramidal-shaped neurons.

In summary, all the results of this thesis contribute to the development of wireless BMI. This development opens up more opportunities for both laboratory observations, such as freely moving experimental subjects, and clinical implementations, such as daily neurological treatments.

CONTENTS

List of Figures

List of Tables

LIST OF ALGORITHMS

ABBREVIATIONS

AVV	adeno-associated virus
BMI	brain machine interface
CNS	central nervous system
CSF	cerebrospinal fluid
CW	continuous wave
dB	decibel
DBS	deep brain stimulation
DPF	differential path length factor
ECoG	electrocorticography
EEG	electrocorticography
EPSP	excitatory postsynaptic potential
EPSP	inhibitory postsynaptic potential
FES	functional electrical stimulation
IoBNT	Internet of Bio Nano Things
IoT	Internet of Things
IR	infra red
LED	light emitting diode
LGN	lateral geniculate nucleus
LoS	line of sight
MATLAB	matrix laboratory
MC	molecular communication

mIoT	Internet of Medical Things
NPC	neural progenitor cell
PD	Parkinson's disease
PDE	partial differential equation
PDP	power delay profile
PNS	peripheral nervous system
RF	radio frequency
RP	retinitis pigmentosa
VNS	vagus nerve stimulation
VOX	voice operated switch

ORIGINAL PUBLICATIONS

Publication I   S. A. Wirdatmadja, S. Balasubramaniam, Y. Koucheryavy and
J. M. Jornet. Wireless optogenetic neural dust for deep brain
stimulation. *2016 IEEE 18th International Conference on e-Health
Networks, Applications and Services (Healthcom)*. IEEE. 2016,
1–6. DOI: `10.1109/HealthCom.2016.7749532`.

Publication II   S. A. Wirdatmadja, M. T. Barros, Y. Koucheryavy, J. M. Jornet
and S. Balasubramaniam. Wireless optogenetic nanonetworks for
brain stimulation: Device model and charging protocols. *IEEE
Transactions on Nanobioscience* 16.8 (2017), 859–872. DOI: `10.
1109/TNB.2017.2781150`.

Publication III S. Balasubramaniam, S. A. Wirdatmadja, M. T. Barros, Y. Kouch-
eryavy, M. Stachowiak and J. M. Jornet. Wireless communica-
tions for optogenetics-based brain stimulation: Present technol-
ogy and future challenges. *IEEE Communications Magazine* 56.7
(2018), 218–224. DOI: `10.1109/MCOM.2018.1700917`.

Publication IV   S. Wirdatmadja, P. Johari, S. Balasubramaniam, Y. Bae, M. K.
Stachowiak and J. M. Jornet. Light propagation analysis in ner-
vous tissue for wireless optogenetic nanonetworks. *Optogenetics
and Optical Manipulation 2018*. Vol. 10482. International Society
for Optics and Photonics. 2018, 104820R. DOI: `10.1117/12.
2288786`.

Publication V   S. Wirdatmadja, P. Johari, A. Desai, Y. Bae, E. K. Stachowiak,
M. K. Stachowiak, J. M. Jornet and S. Balasubramaniam. Analysis
of Light Propagation on Physiological Properties of Neurons for
Nanoscale Optogenetics. *IEEE Transactions on Neural Systems and*

Rehabilitation Engineering 27.2 (2019), 108–117. DOI: `10.1109/ TNSRE.2019.2891271`.

Publication VI   S. Wirdatmadja, J. M. Jornet, Y. Koucheryavy and S. Balasubramaniam. Channel Impulse Analysis of Light Propagation for Point-to-point Nano Communications through Cortical Neurons. *IEEE Transactions on Communications* (2019). Accepted for publication. DOI: `10.1109/TCOMM.2020.3012477`.

Author's contribution

Stefanus Wirdatmadja is the author of all publications in this thesis. The entire process leading to each publication has been supervised by Prof. Yevgeni Koucheryavy and Dr Sasitharan Balasubramaniam by means of regular discussions to develop ideas and give feedback on the documentation process. Additionally, Prof. Josep Miquel Jornet contributed by suggesting and developing methods for all publications. All the work mentioned in this thesis was done at the Laboratory of Electronics and Communications Engineering, Tampere University, Finland.

Publication I   The author was responsible for designing the concept, conducting the simulations, and analysing the numerical performance.

Publication II   The author developed the protocols and simulated their implementation. Dr Michael Taynnan Barros contributed in analysing the connection probability.

Publication III   The author provided the state-of-the-art and analysis of the devices. Dr Michael Taynnan Barros improved the figures.

Publication IV   The author was responsible for the analytical analysis and simulations. Dr Pedram Johari contributed to the multiphysics simulation. Asst Prof. Yongho Bae and Prof. Michal K. Stachowiak were responsible for the laboratory experiment.

Publication V   The author analysed the model geometrically and numerically and conducted the simulations. Dr Pedram Johari contributed to improving the analysis. Dr Aesha Desai, Asst Prof. Yongho

Bae, Prof. Ewa K. Stachowiak, and Prof. Michal K. Stachowiak were responsible for the laboratory experiment.

Publication VI   The author was responsible for the analytical analysis, algorithm design and implementation, and simulation.

1 INTRODUCTION

The continuous development of wireless communication technology focuses on performance, scalability, reachability, accessibility, interoperability, and security. Performance — including data rate, stability, and latency — sets the upper bound of the application implementation feasibility [61] [80] [88]. Scalability anticipates the growing number of network elements during the implementation [27] [13] [106]. Reachability and accessibility are closely related to the network coverage, which measures the availability of connections with other network entities [91] [64]. Interoperability ensures the seamless communication compatibility among all communication system technologies [94] [74]. Security guarantees the separation between private and public domains [77] [22] [3]. In the broader scope of the wireless communication system, the concept of the Internet of Things (IoT) attempts to maximise scalability, reachability, accessibility, and interoperability. Its network entities are not limited to devices that only require human interaction, as in the existing conventional communication system, but are also capable of interaction among themselves. The IoT introduces autonomous communication, such as device-to-device (D2D) and vehicle-to-everything (V2X) communication [5] [37]. Furthermore, the concept inspires other concept categories, such as the Internet of Medical Things (mIoT) [23] [38], Internet of Nano Things (IoNT), and Internet of Bio Nano Things (IoBNT) [2] [7] [58] [25].

The concept of IoBNT or molecular communication (MC) emphasises the role of the (synthetic) biological entities in a novel communication and networking system [2] [69]. This extends the communication and network engineering from the conventional communication system that concentrates solely on radio frequency (RF) waves to a larger scope, including mechanical waves, electromagnetic waves, chemical signals, and biological signals. Calcium signalling [18] [70], neuronal communication [59], the microfluidic system [19], and pheromone communication [33] are some examples of MC. In this case, MC is considered a bio-inspired communica-

tion, since the technique either utilises natural/living things or mimics their natural behaviour. Therefore, there are two major components for a system to be considered an MC: information exchange and chemical/biological entities. In this case, the entities should play a major role during the communication process in the form of nanomachines and/or molecular carriers.

1.1 Brain Machine Interface (BMI)

A *brain machine interface* (BMI) is a device or system that has a direct connection to the brain and enables humans to monitor and/or manipulate neuronal activity. In order to do so, a BMI should be able to encode and decode human readable information into neuronal activity. BMIs are divided into two major categories based on the physical connection methods between the device and the brain: invasive and non-invasive [60]. A BMI is invasive when the device has direct contact with the brain tissue, while a non-invasive BMI has direct contact only with the scalp. Regarding neuronal activity monitoring and manipulation, an invasive BMI provides better accuracy in spatiotemporal resolution and a stronger received signal. However, an invasive BMI requires surgical procedures in order to implant the intracranial electrodes, which is one of the significant factors to consider in implementation in humans.

Concerns about device miniaturisation are more relevant in an invasive BMI compared to a non-invasive BMI. This is due to the nature of the former, which needs to be implanted inside the skull. The invasive device comprises three major components, namely the internal, external, and the connection between them. In most cases, the bigger components — such as the power supplies and controllers — are located in the external part.

The amount of electrodes has a proportional correlation with the spatiotemporal resolution. This translates into the accuracy of the information about the neuronal activity. In order to have a higher resolution, a BMI should accommodate a dense neuron population monitoring/manipulation in a certain coverage area. This is the reason why an optimal design is required to determine the size and the number of electrodes in the internal part.

Patients tend to choose a non-invasive rather than an invasive BMI. Earlier, for epilepsy treatments, patients underwent a surgical procedure called *electrocorticogra-*

phy (ECoG) to map a certain brain section in order to identify the damage caused by the seizure. In this treatment, part of the skull was removed in order to place the electrodes in direct contact with the brain tissue. Consequently, the patient was prone to infection during the ECoG procedure. By introducing the *electroencephalogram* (EEG), epilepsy patients have a less/non-invasive option. For example, a subdermal EEG requires only skin (dermis) removal, but not the skull. Therefore, a subdermal EEG is considered the less invasive option. Furthermore, a scalp EEG is clearly categorised as non-invasive [71] [1].

1.2 Objective of the Thesis

In this thesis, we focus on the future implementation of optogenetics on human brain. We emphasise neuron stimulation based on the human *neocortex/cerebral cortex*, which is the outer part of the *cerebrum*. Therefore, the main objective of this thesis is to design an implantable wireless BMI for optogenetic stimulation that supports spatially distributed stimulation. This device, which is called a *Wireless Optogenetics Nanonetworking Device* (WiOptND), communicates using both acoustic and optical signals rather than an RF signal. Therefore, in addition to the hardware components of the WiOptND, we also elaborate on these communication signals in order to design an efficient and effective small-scale BMI. Additionally, we propose a charging protocol that enables synchronous spatially distributed stimulation by a network of several WiOptNDs. In order to support this feature, a WiOptND also requires electrical circuit alteration to incorporate the time delays into its stimulation timing.

Furthermore, we analyse light propagation in the brain tissue and characterise its interaction with the neurons based on their morphology. This is important considering there are different types of neuron geometry and the possibility of direction deviation in light propagation. Additionally, we study light propagation behaviour through multiple neurons in order to observe its effect on the received light signal.

1.3 Methodology

The research reported in this thesis utilises a mainly quantitative approach based on theoretical formula derivations, computer simulations, and the existing experimen-

tal data from the corresponding research literature. All supporting data and theories were obtained by literature study, and the laboratory experiment was conducted by our collaborator at the University at Buffalo, New York, who has the authorisation for this experiment.

The data on the neuron and brain morphology, physiology, and activity were obtained from a literature study of the existing research on mammals including mice, non-human primates, and humans [76] [95]. In particular, we referred to the study on *macaque monkeys* for brain activity during specific tasks and the observation of mice regarding BMI implementation.

The aim of the literature review was to determine the most effective and suitable component in designing the WiOptND, whereas the theoretical and numerical analyses and computer simulations were to validate the WiOptND design and to assess its implementation feasibility. The simulation software used in this research was MATLAB, COMSOL Multiphysics, and Python. The data was preprocessed using Python and fed into MATLAB for further processing and final analysis, whereas COMSOL Multiphysics was used mainly for the investigation of light propagation behaviour [93] [73].

For the theoretical analysis, we applied well established theories, such as the Modified Beer-Lambert law and Mie scattering to investigate light propagation in scattering media. The difference between the traditional and modified Beer-Lambert law is that the latter approximates the mean path length instead of absolute values [6]. Furthermore, the Mie scattering analysis is based on the fact that the size of the organelles is comparable to the wavelength, and the size parameter lies in the range where it should be analysed by Mie scattering theory. Additionally, in COMSOL Multiphysics, we simulated photon diffusion based on the Helmholtz equation, which enables the simplification of *partial differential equations* (PDEs). Helmholtz omits the time dependency of PDEs, leaving only the space domain in the equations.

1.4 Main Results of the Thesis

The main results and the contributions of our publications included in this thesis are listed as follows.

Publication 1: Wireless Optogenetic Neural Dust for Deep Brain Stimulation

In publication [I], the concept of WiOptND is proposed to facilitate the wireless optogenetics stimulation. The proposal includes the system and hardware device architectures. The implementation concentrates on a fully implantable and batteryless BMI. This solution is feasible by incorporating micro-scale electrical components complemented by a piezoelectric-based energy harvester.

Publication 2: Wireless Optogenetic Nanonetworks for Brain Stimulation: Device Model and Charging Protocols

In publication [II], the improvement of WiOptND implementation in terms of synchronised multi-device operation control is elaborated upon. It includes the additional component of a voice–operated switch (VOX), which enables the charging control of multiple devices. Additionally, the time delay relay component is also introduced to elevate the functionality of the device in terms of stimulation timing management. The combination of these two additional components introduces charging protocols resulting in different behaviours in optogenetic stimulation.

Publication 3: Wireless Communications for Optogenetics-based Brain Stimulation: Present Technology and Future Challenges

In publication [III], the development of BMI is studied and compared to the proposed WiOptND. The comparison concentrates on the hardware implementation, energy management, and communication technology. Moreover, the future challenges, especially in communication perspective, are profoundly elaborated upon.

Publication 4: Light Propagation Analysis in Nervous Tissue for Wireless Optogenetic Nanonetworks

In publication [IV], the light propagation in nervous tissue is investigated. The analytical analysis based on cell geometry and propagation phenomena is elaborated upon. Phenomena such as the neuron focusing effect are introduced. This effect occurs due to blocking neurons along the path of the target neuron. Furthermore, the analysis is validated using COMSOL simulation. Regarding the multipath propagation, based on the optical properties of the neuron, it is observed that the reflected path has an insignificant effect on the received light intensity.

Publication 5: Analysis of Light Propagation on Physiological Properties of Neurons for Nanoscale Optogenetics

In publication [V], the light propagation analysis is extended by incorporating the cell geometry and the effect of organelles. The analysis is performed by considering Mie scattering and three different neuron shapes, namely spherical, pyramidal, and fusiform. The results from this publication can further support the axonal biophoton communication hypothesis.

Publication 6: Channel Impulse Analysis of Light Propagation for Point-to-point Nano Communications through Cortical Neurons

In publication [VI], the light channel impulse response from the source to the receiver is analysed. The analytical analysis is based on light propagation incorporating multiple neuron obstructions along the path. The study employs the ray tracing method and numerical analysis using MATLAB.

1.5 Potential Applications

It is envisioned that the WiOptND will be able to facilitate both laboratory experiments and human clinical implementations. For example, in laboratory experiments where mice are observed, the device would allow the mice move freely. As a result, the researchers could expand the experimental area or give freedom to the mice to explore tiny holes while controlling them wirelessly.

Particularly in human clinical implementations, this device focuses on the case where neuron stimulation is required, such as in epilepsy and tremor reduction in *Parkinson's disease* (PD). In epilepsy, this device can give *vagus nerve stimulation* (VNS) used to prevent or lessen seizures by sending a regular stimulus though the vagus nerve. Similar to epilepsy patients, PD patients can benefit from this device by its minimising the motor symptoms of stiffness, slowness, and tremor. This can be done by stimulating certain areas of the brain, such as the *subthalamic nucleus* or the *globus pallidus interna*. Thus, the WiOptND can be an alternative to the existing neuron stimulator.

1.6 Outline and Structure of the Thesis

The organisation of the remainder of this thesis is as follows.

The background and the fundamental theories of neuron morphology, optogenetics, wireless BMI, and light propagation in biological tissues are presented in Chapter 2. Furthermore, the problem formulation and challenges of the BMI are also elaborated on in this chapter.

In Chapter 3, the architecture and the circuit design of WiOptND concept are proposed. The elaboration of each hardware component, including theory and implementation, is presented in this chapter.

A detailed explanation of the phenomena occurring when a light wave interacts with the brain tissue/neurons is presented in Chapter 4. This includes an analysis of the neuron geometry that affects light propagation.

The end-to-end channel impulse responses for three neuron geometries are discussed in Chapter 5. The analysis incorporates light propagation though multiple neurons in a one-dimensional array arrangement.

Regarding the multiple device implementation, two charging protocols are elaborated on in Chapter 6. Each protocol translates into different implementation possibilities and limitations. Additionally, the analysis of each protocol is presented.

Finally, the conclusion of this thesis and the further discussion — on wireless BMIs in general and WiOptND in particular — are provided in Chapter 7.

2   BACKGROUND

2.1 Morphology of the Brain and Neurons

Nervous tissue is one of the four biological tissue types, along with the epithelium and the connective and muscle tissues [89]. In humans and bilateral animals, this tissue forms two major nervous systems, namely the central nervous system (CNS) and the peripheral nervous system (PNS). The brain and spinal cord are categorised under the CNS, and they act as the main controllers of the body organs. The PNS comprises the nerves and ganglia, which connect the CNS to all the limbs and organs of the body.

2.1.1 Brain

Anatomically, the brain is divided into three main parts, namely the cerebrum, cerebellum, and brainstem. The first is the largest, comprising the left and right hemispheres. It is responsible for the senses, such as sight, touch, and hearing, as well as memory, speech, and emotional response. The cerebellum (the little brain) is the smaller part of the brain, which is located under the cerebrum. This part is important for muscle coordination and motor control. The brainstem functions as a relay connection between the aforementioned parts of the brain and the spinal cord (the rest of the body). It plays an important role in basic bodily functions, such as breathing, the sleep cycle, digestion, and many other automatic bodily functions.

Based on its structure, the brain is divided into white and grey matter. Both contain blood vessels and glial cells, but they have different amounts of proteins and lipids, in the form of myelin, in their corresponding structure. White matter mostly consists of myelinated nerve fibres that are responsible for effective nerve signal conduction and axon protection, while the grey matter comprises the somata, axons,
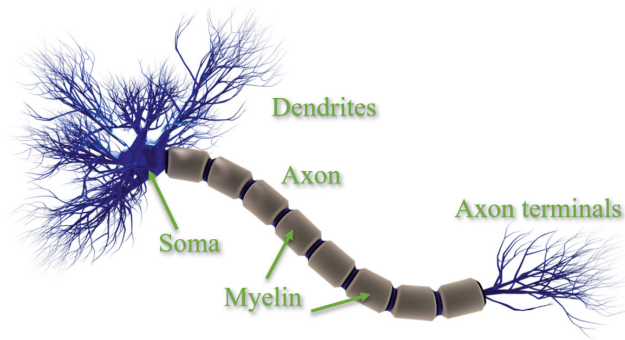
Figure 2.1   Illustration of the main components of a neuron

dendrites, and synapses. The thick and dense irregular membrane of the connective tissue on the outer layer of the brain and spinal cord is called the *dura mater*. This layer is inflexible in order to protect the CNS. It consists of two layers, namely the *pia mater* and *arachnoid mater*. In between the *dura mater* sublayers, the *subarachnoid space* is filled with the clear, colourless *cerebrospinal fluid* (CSF).

2.1.2   Neuron

A neuron is a structural and functional basic unit that forms the nervous system. It is a cell that carries and transfers electrical impulses. A neuron consists of the cell body (soma) and nerve fibres (dendrites and axon). The soma comprises the cell nucleus and other organelles, namely ribosomes, mitochondria, the endoplasmic reticulum, lysosomes, and the Golgi complex, which float in a fluidic medium called the cytoplasm. Both the dendrites and axon are cytoplasmic projections from the soma. However, the dendrites can be perceived as the signal receiver from the other neuron(s), while the axon is the signal transmitter. The axon is thicker and longer compared to the dendrites. Unlike the dendrites, which branch throughout its length, the axon branches only at its distal end. Figure 2.1 depicts a neuron with its main components [63].

Neurons use both chemical and electrical signals to build their communication network. An action potential is a form of electrical signal caused by a rapid change in the membrane potential of a neuron. This is used by the neuron to transfer signals from the dendrites to axon terminals, which can be further transmitted to adjacent

neurons. This process is dubbed intraneuron communication since it occurs within a single neuron. The next process of transferring information from one neuron to another is called interneuron communication. The structure that enables signal transmission between two neurons is the synapse. A synapse can either be electrical or chemical. A chemical synapse is triggered by the action potential of a presynaptic neuron and it stimulates the release of the neurotransmitters that are able to bind to the receptors of the postsynaptic neuron. Furthermore, the electrical synapse occurs via a special channel called the gap junction, which is capable of conducting action potential from presynaptic to postsynaptic neurons [52] [66].

2.1.3   Cerebral Cortex Neurons

The outer layer of the cerebrum is called the cerebral hemisphere, and it consists of a complex grey matter layer. The cerebral cortex is the outermost neural tissue layer in humans and mammals. Its thickness is approximately 2–4 mm and it is significantly populated by neural cell bodies and glial cells. Most of the neurons in the cerebral cortex have vertical arrangements forming unique cortical columns. This column exhibits information transmission among its layers. Neurons from different layers in each cortical column perform a specific function. In total, the six layers of cerebral cortex are

1. *Layer I (molecular layer)*

2. *Layer II (external granule layer)*

3. *Layer III (external pyramidal cell layer)*

4. *Layer IV (internal granule layer)*

5. *Layer V (ganglionic or internal pyramidal cell layer)*

6. *Layer VI (multiform layer)*

Morphologically, the neuron soma of the neocortex can be categorised into three main groups: pyramidal cells, granule cells, and fusiform/spindle-shaped cells.

1. *Pyramidal cells* are the major population of layers III and V of the neocortex. These cells have four size categories (height × width), namely *small (Schankleit)* (12 μm × 10 μm), *medium* (25 μm × 15 μm), *large* (45 μm × 15–20 μm), and *giant* (50-100 μm × 25–60 μm) [90].

2. *Granule cells* are mostly located in layers III and IV of the neocortex, and they vary geometrically. Their shapes are spherical, polygonal, or oval. In terms of size, these cells are approximately 15–30 μm × 10–15 μm [90].

3. *Fusiform/spindle-shaped cells* are located in layer VI of the neocortex. They are considered to be long, as their apical dendrites extend up to layer I and their basal dendrites spread into layer VI. The size range of these cells is approximately 15–30 μm × 10–15 μm [90].

2.2 Optogenetics

Artificial neuron stimulation might be needed in research or therapy. For this purpose, the most common methods are electrical and optical stimulation. Electrodes are required for electrical stimulation, while a genetically engineered neuron and a light source are the minimum requirements for optical stimulation. The technique for controlling neurons in–vivo using optical stimulation is called optogenetics [20] [105] [30].

Optogenetics outperforms electrical stimulation in many aspects, including precision, cell stress level during stimulation, and interference. As mentioned earlier, an electrical signal is basically the natural communication signal among the neurons; therefore, using the same means of stimulation causes disadvantages compared to optical stimulation.

Optogenetics utilises a certain wavelength to stimulate the neurons. Depending on the protein utilised to genetically engineer the neuron, optogenetic constructs can exhibit either excitatory or inhibitory characteristics. These effects can be observed based on the behaviour of the postsynaptic neurons. *Excitatory postsynaptic potential* (EPSP) occurs when the cell membrane depolarises — causing the sodium and calcium ion membrane channels open — and generates action potential. Conversely, *inhibitory postsynaptic potential* (IPSP) occurs when the cell membrane hyperpolarises, causing the chloride or potassium ion membrane channels to open, blocking the generation of action potential.

The *channelrhodopsin-2* (ChR2) optogenetic construct utilises the opsins from the green algae *chlamydomonas reinhardtii*, and it exhibits excitatory behaviour. The action potential generation is triggered by blue light (wavelength 430–520 nm) illumination. On the other hand, the *halorhodopsin* (NpHR) construct, which utilises the
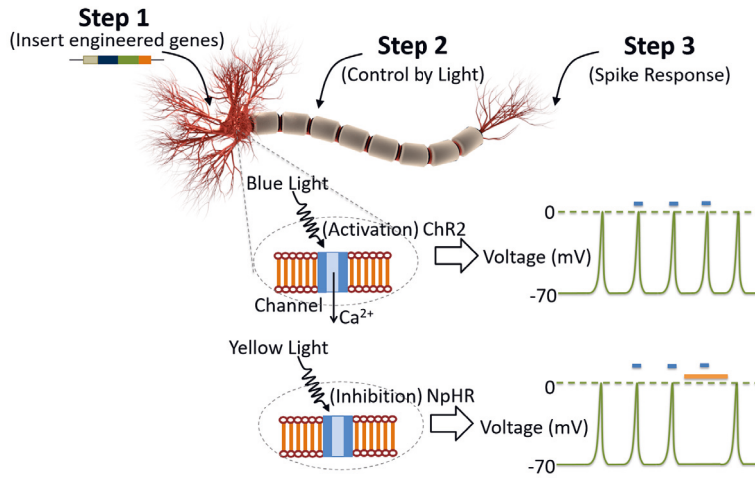
Figure 2.2 Steps towards developing an optogenetic construct and its stimulation process. The figure also illustrates the depolarisation process where ion pumps are activated. [II]

opsins from *archaen natronomonas pharaonis*, exhibits inhibitory behaviour. When it is illuminated by green, yellow, or red light (wavelength 500–600 nm), the chloride ion channels open, suppressing the action potential. Alternatively, the utilisation of proton pumps can also generate an inhibitory effect. The optogenetic constructs that activate proton pumps instead of chloride channels are *archaerhodopsin-3* (Arch) from *Halorubrum sodomense*, *mac* from the fungus *leptosphaeria maculans*, and *eBR* from *Halobacterium salinarum*. Figure 2.2 shows the optogenetic construct development and stimulation, as well as, the excitatory and inhibitory behaviour during the ion channel activations [39] [68] [40] [17].

2.3 Optogenetics in Humans

Optogenetic experiments and studies on mice and non-human primates have been conducted many times, and recently optogenetics has been considered ready for implementation in humans. In March 2016, RetroSense Therapeutics (Ann Arbor, Mich., USA) pioneered the first optogenetic clinical trial on humans using an optogenetics-based gene therapy, RST-001 for restoring vision in patients with *retinitis pigmentosa* (RP). The therapy is performed by injecting ChR2 into the patient's retinal ganglion cells. Later, in January 2018, GenSight Biologics (Paris, France) began the PIO-

NEER Phase I/II study of GS030 for patients with the same disorder. Instead of using ChR2, they used ChrimsonR in an adeno-associated virus (AAV) injection, resulting in sensitivity to orange/red light (wavelength of 590 and 630 nm).[1] If these clinical trials are successful, they will open up wider opportunities for optogenetics in treating other disorders such as cochlear cell loss [14] [32] [11].

2.4 Wireless Brain Machine Interface

In addition to the stimulation method, a BMI can be categorised further based on the communication method between two components. Those components are the attached device that interacts with the neuron and the device that interacts with humans and controls or monitors neuron activity. They can be connected by either a direct physical (wired) or wireless connection. An example of a wired BMI is the functional electrical stimulation (FES) device that helps patients to restore hand function and bladder control [65] [34] [51]. The wireless BMI offers a solution to a drawback that arises from wired implementation, which is wire tangle. During the experiment, an observed experimental subject might experience a movement limitation. An unexpected movement by the subject might cause the dislocation or detachment of the cable, resulting in disturbance in the experimental process.

The wireless BMI can either be head mounted or fully implantable. This is dictated by the size, the wireless technology/frequency, and the power supply method. A fully implantable device must be sufficiently small in size in order to minimise intrusion in the brain tissue. In many BMIs, the battery as a power supply component occupies a considerable amount of space. Additionally, the risk of battery leakage during the operational period should also be taken into consideration during design. Furthermore, some wireless technologies, such as infrared (IR), require an unobstructed path between the transmitter and the receiver. Table 2.1 shows the advantages and disadvantages of four wireless technologies that are commonly utilised for device communications. Figure 2.3 illustrates both head mounted and fully implantable solutions for optogenetic BMIs.

- *Wireless Optofluidic Systems* functions as the optogenetic stimulator and the drug deliverer (Figure 2.3a). This head-mounted BMI with the dimensions of

---

[1] It is claimed that for human eyes, red light is less harsh than blue light.

Table 2.1 Comparison of different wireless technology solutions. [III]

Wireless Technology (Frequency)	Pros
	Cons
Infrared (IR) (300 GHz – 430 THz) [45] [41]	Low power consumption; Multi-band transmissions.
	LoS between base station and implanted unit; Requires a battery unit for the head unit.
High Frequency (HF) (3 – 30 MHz) [86]	Medium propagation loss in biological tissue; Cheap and easy to manufacture; Supports energy harvesting circuitry.
	Coil dimension of approx. 1 cm; Requires surface mounted chip (NFC).
Ultra High Frequency (UHF) (300 MHz – 3 GHz) [31] [67] [75]	Smaller coil diameter than HF circuitry; Cheap and easy to manufacture; Supports energy harvesting circuitry.
	High propagation loss in biological tissue.
Ultrasound ($\geq$ 20 kHz) [85]	Low propagation loss in biological tissue; Size of hundreds of μm; Supports energy harvesting circuitry; Safe utilisation in human tissue.
	Complex circuit manufacturing; Difficulty in ultrasound frequency addressing.

$3 \times 9 \times 10$ mm^3 has two rechargeable lithium ion battery as its power supply. The communication between controller and the BMI uses IR technology [45].

- *Programmable Wireless LED Stimulator for Optogenetics* employs multiband-band IR and multicode signals to avoid interference for simultaneous multiple IR channel transmission (Figure 2.3b). The head-mounted receiver is supported by a lithium polymer battery to stimulate the ChR2 construct [41].

- *Flexible Near-Field Wireless Optoelectronics* combines power transmission and optogenetic stimulation by using a copper coil and micro-sized chip (Figure 2.3c). Since this fully implantable BMI adopts the near field communication (NFC)

concept, it operates on the frequency of 13.56 MHz. Furthermore, to ensure the biocompatibility and stability of the device, it is encapsulated by *Parylene* and *Polydimethylsiloxane* [86].

- *Combined Optogenetics and Electrophysiological Recording Wireless Headstage* supports both optogenetic stimulation and activity recording (Figure 2.3d). The head mount is powered by a lithium-ion battery which can support the device for 70–105 minutes depending on the stimulation activity. The communication between the controller and the BMI uses a frequency of 2.4 GHz [31].

- *Wireless Powered, Fully Internal Optogenetics* employs RF technology and a coil for both powering the device and sending the signal to trigger the optogenetics (Figure 2.3e). This fully implantable solution weighs approximately 20–50 mg with the dimensions of 10–25 mm^3. The operating frequency is 1.5 GHz, which is radiated by a large resonant cavity [67].

- *Soft, Stretchable, Wireless Optogenetics System* combines the stretchable filaments and a flexible polymer encapsulation to create a device that can comfortably be embedded into the spinal cord and peripheral nervous system (Figure 2.3f). It utilises RF technology for both energy harvesting and stimulation triggering. The antenna occupies a surface area of 3×3 mm^2 and it operates on a frequency of 2.3 GHz with a bandwidth of 200 MHz. The deformation of the device causes operating frequency shifting and coupling efficiency decrease [75].

2.5 Light Interaction Theory

When a light wave propagates in biological tissue, both its intensity and propagation direction can change. These changes are caused by several light-medium interactions, namely reflection, refraction, absorption, and scattering [48]. An illustration of these phenomena is depicted in Figure 2.4.

- *Reflection and Refraction*. As light propagates from one medium to another with different refractive indices, the light can be partially reflected and partially transmitted. Furthermore, the transmitted light experiences refraction
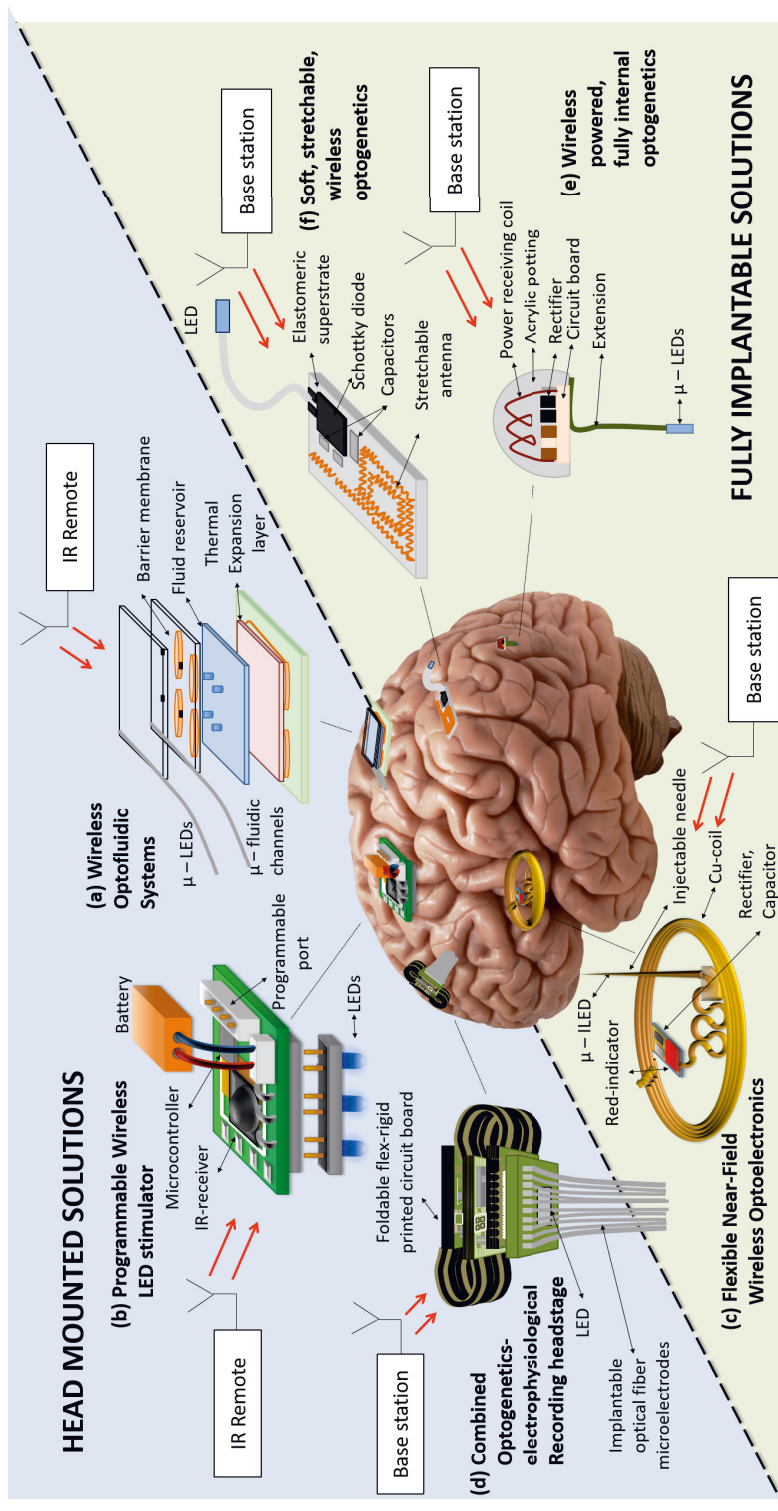
Figure 2.3 Various solutions for wireless optogenetics illustrating the different scale of the devices, as well as their locations in the brain. [III]
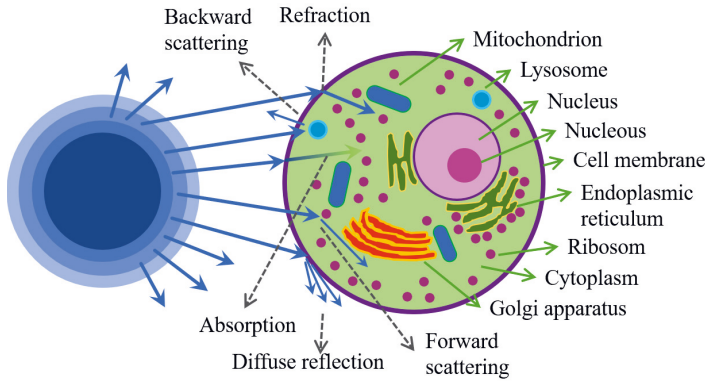
Figure 2.4 Illustration of refraction, reflection, absorption, and scattering of light on a soma. [IV]

(a change in the angle of propagation) due to the different refractive indices of the media. Since a biological component, such as a neuron, has a low reflectance index of 0.5%, the reflection is negligible [29].[2] The refracted part of the light undergoes changes in propagation direction as it traverses two different media. The effect of the refractive index difference on the propagation direction deviation is explained by *Snell's law*. Both reflection and refraction phenomena, which follow *Fresnel's equation* and *Snell's law* respectively, are dictated by the refractive indices.

- *Absorption*. The light energy decreases as it is absorbed and converted to heat due to the vibration of atoms and molecules in the biological tissues. The absorption behaviour of the tissue relies heavily on the light wavelength. Most of the visible light utilised in optogenetic applications is less than 625 nm, in which the absorption coefficients range from 0.5 to 5/cm [54].

- *Scattering*. The heterogeneous biological medium causes the deflection of light waves to one or more paths deviated from the straight trajectory. This situation occurs when waves pass through two different media with different optical properties. The *Henyey-Greenstein* phase function defines this phenomenon by the *anisotropy factor*, g [54]. The scattered light waves can be in either a forward or backward direction indicated by the value of g. A positive value indicates that forward scattering is more dominant, which is common

---

[2]The surface of the neuron can also be considered a *Lambertian surface*, resulting in the phenomenon of *Lambertian reflectance* or *diffuse reflection* [101]. As part of the light is reflected and the rest is transmitted, this kind of reflection can also be dubbed *Fresnel reflection*.

in biological tissues whose range is 0.5–0.95 [54]. A reduced scattering parameter, μ'_s, incorporates this factor so that a more accurate light propagation model can be implemented. It is defined as $\mu'_s = (1 - g)\mu_s$, where μ_s itself denotes the scattering coefficient. According to the size of the tissue components and the light wavelength, the scattering property may follow either the *Rayleigh* or the *Mie* regime.

2.6 Problem Formulation

Since a wired BMI with an electrode stimulator provides more reliability and freedom for direct human brain stimulation (intrusively), it is still the only option for medical treatment. However, it might not be the most comfortable option in terms of long-term treatment/usage. The same issue exists during observed laboratory experiments, such as the possibility of a tangled or detached wire due to certain movements. In addition, periodic battery replacement is needed to ensure the device continues to operate. The usage of batteries might introduce an additional issue due to the possibility of chemical leakage. As mentioned in Section 2.2, the electrode stimulator inherits some disadvantages, namely interference and cell stress. Additionally, when single-neuron stimulation is targeted, spatial temporal precision becomes an additional issue for this method. Thus, a novel approach is required for better and more comfortable BMI implementation.

The goal of wireless optogenetics nanonetworking devices (WiOptNDs) is to provide applicable interconnected miniature brain implants that are capable of synchronous spatial distributed neuron-level optogenetic stimulation. This device employs state-of-the-art components and technologies based on current studies and research. It focuses on the BMI component that is directly attached to the brain tissue. It is designed to be fully implantable, wireless, and biocompatible. Additionally, the device is supported by a compatible charging protocol that is suitable for handling the various neuron spike (action potential) patterns of a group of neurons. Moreover, since the light source of the device has a size that is comparable to a neuron, the light propagation behaviour in the brain tissue and single/multiple cell(s) needs to be investigated.

2.7 Challenges

There are many electrical components and wireless technologies that can be utilised for optogenetic BMI design. However, the chosen components and technology should fulfil both micro-scale design and optogenetic construct specification requirements. Also required are thorough investigations of the implementation feasibility through analytical analysis, modelling, and simulation.

Since a fully implantable BMI is the target of this research, the size of the device should be sufficiently small and biocompatible so that it does not trigger a severe foreign body reaction (FBR), which causes tissue-encapsulation of the implant. Furthermore, neuron size sets the limit for the light source size (hundreds of microns) and requirements, since single-neuron stimulation is the aim. Besides that, the dense population of the neurons should also be considered in the stimulation process, since undesired neurons can introduce an obstacle along the light propagation path. Finally, the biological components introduce various propagation phenomena, such as attenuation, that affect the propagation analysis.

3 WIRELESS OPTOGENETIC NANONETWORK SYSTEM ARCHITECTURE

In [I], the system architecture and the circuit design of WiOptND are proposed. The system architecture determines the placement and the operational environment of the device, which set the boundaries for the hardware and wireless technology requirements. Based on those requirements, the hardware components and electrical circuit of the device are specified. Furthermore, the energy and power compliance of the device are analysed numerically in both [I] and [II].

3.1 System Architecture

For the optogenetic stimulation system, several fundamental specifications of the BMI are concentrated in this thesis. First, the BMI is fully implantable, which means it is still intrusive but significantly small in size, and it is made from biocompatible material to avoid any severe disturbance to the brain tissue. Secondly, the device targets stimulation on the level of a single neuron, and lastly, the design proposal focuses on the implant, which has direct contact with brain tissue, not the human interface component, which controls the implant.

ChR2 is used in this this thesis. This construct is sensitive to blue light (wavelength approximately 470 nm) and exhibits exhibitory behaviour. Even though this device can stimulate any area of the brain, the neocortex is considered an ideal environment due to its layered structure, with its approximately uniform type of cell in each layer. The total thickness of the neocortex is approximately 2–4 mm.

Regarding wireless technology, there are several options that can be considered. One of them is RF, whose frequency ranges from 3 kHz to 300 GHz. However, considering the size requirement of a device at least in the mm level, the operating frequency should be in GHz. In this frequency range, the wave is significantly at-

tenuated by the brain tissue. On the other hand, when an acoustic wave (frequency more than 20 kHz) is utilised instead of RF, the attenuation caused by the tissue is significantly lower [43] [85].

The entire system architecture of the WiOptND is illustrated in Figure 3.1. A sub-dura transceiver interfaces between the external receiver, which is controlled by the human, and the WiOptNDs, which are directly attached to the brain tissue. They are located in the dura mater, under the skull. The sub-dura transceiver transmits the ultrasound signals to instruct the WiOptNDs to stimulate the neurons and at the same time providing (charging) the required energy for the stimulation.
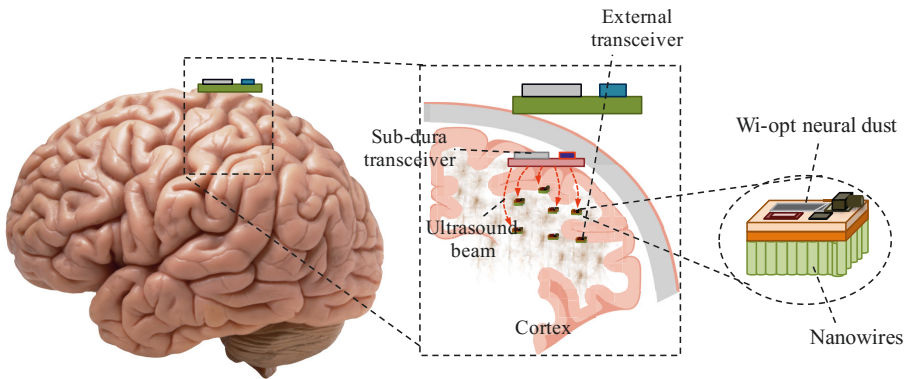
Figure 3.1 Illustration of the WiOptND system model where the sub-dura transceiver communicates with the external transceiver and transmits ultrasound signals to the WiOptNDs in the neocortex. [II]

One WiOptND is responsible for stimulating one optogenetic construct; therefore the light source should be located as close as possible to the target soma. Figure 3.2 illustrates the location of a WiOptND with respect to its corresponding optogenetic construct. This device uses a blue micro-light-emitting-diode (μ-LED) as a light source.

3.2 Circuit Diagram of the WiOptND

The WiOptND comprises three major components, namely an energy harvester, an energy storage component, and a light source. The energy harvester is required in order to omit a dedicated battery component as a power supply to the device. It avoids the need for periodic battery maintenance and omits potential chemical

Figure 3.2 Illustration of a WiOptND and its corresponding optogenetic construct in the brain tissue. [I]

leakage during implementation. Since the energy generated by the harvester cannot directly be used to power the device, the storage component acts as a temporary battery that stores the energy from the harvester for a very short period of time. Finally, when the stored energy is sufficient, it can power the light source to shine the optogenetic construct at a certain wavelength. Figure 3.3 shows the WiOptND circuit diagram in detail. In the following subsections, each component is elaborated on in detail.
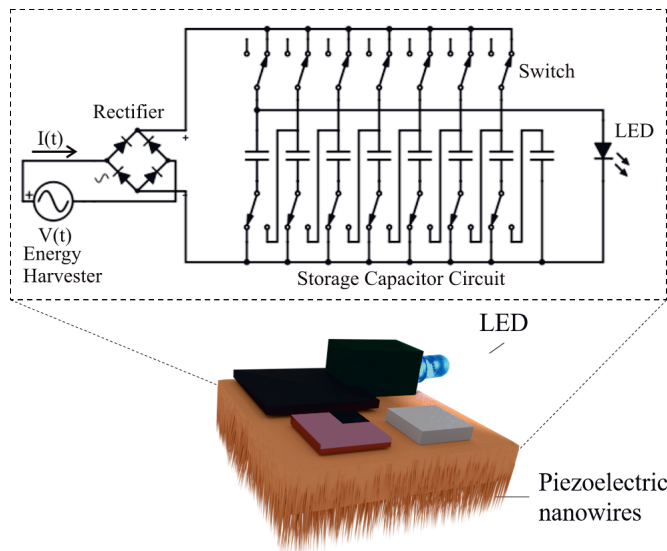
Figure 3.3 Circuit diagram of the WiOptND. [I]

3.2.1 Energy Harvester

A piezoelectric material is capable of generating electrical charges when a mechanical stress is applied to it, and this mechanism also works in the reverse direction. In this case, the WiOptND can benefit from this effect to convert mechanical energy from acoustic pressure sent by the sub-dura transceiver to the electrical charges. However, a piezoelectric transducer generates an alternating current (AC) that cannot be directly fed to the next stage (storage component). Therefore, a rectifier is needed to convert it into a direct current (DC). Regarding the ultrasound exposure, the Food and Drug Administration (FDA) regulates a safety limit of 720 mW/cm^2.

3.2.1.1 Material

There are variety of materials and geometries to choose from in terms of the piezo-electric transducer. For example, *lead zirconate titanate* (PZT), *aluminium nitride* (AlN), *barium titanate* (BaTiO$_3$), and *zinc oxide* (ZnO) in the form of either a crystal or nanowires can be used. The ZnO nanowire component is used for WiOptND since it generates sufficient energy to supply power for stimulation (determined by the electromechanical coupling coefficient). However, this material is not biocompatible, hence a biocompatible coating is needed. A thin layer ($<100\mu$m) of *poly-methyl methacrylate* is applied, since it does no harm to the brain tissue and introduces no performance degradation. Figure 3.4 illustrates the piezoelectric mechanism that is utilised by WiOptND. The vibration of the ultrasound bends the ZnO nanowires back and forth, generating AC electric charges. Besides the piezoelectric properties, the density of the nanowires also determines the amount of electricity charge generated [49].

3.2.1.2 Ultrasound Intensity

As the ultrasound wave traverses the brain tissue, its intensity degrades as a function of distance and frequency. The ultrasound attenuation in the brain tissue (α) is 0.435 dB/(cm·MHz). Furthermore, the received ultrasound power depends on the effective area of the energy harvester. During the vibration of the nanowires, the received power cannot be entirely converted from mechanical energy to electrical energy. The conversion rate (η) determines the amount of the converted electrical
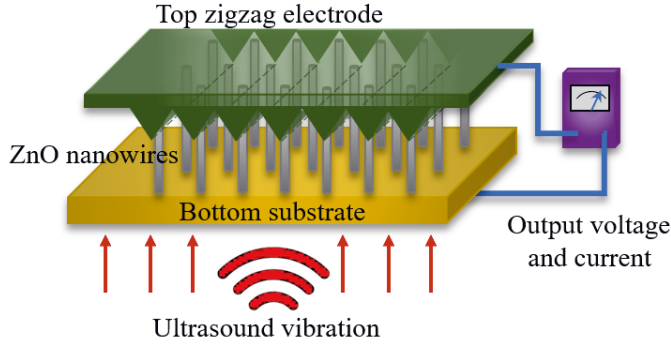
Figure 3.4 Piezoelectricity mechanism.

power with respect to the received mechanical power by the nanowires.

3.2.2 Electrical Storage Component

Before the converted electrical charges are stored in the storage component, namely the capacitors, the electrical current should be rectified, since the nanowires generate AC instead of DC. Therefore, a full-wave rectifier is connected between the energy harvester and the storage capacitors. The capacitors should comply with the size limitation; consequently, micro-supercapacitors based on interdigital electrodes of reduced graphene oxide and carbon nanotube composite are employed in the circuit [9]. They have a surface area of 100×100 μm^2 with a 280 μF capacitance. The storage component has two states, namely charging and discharging. In the charging state, the capacitors are connected in parallel, while in the discharging state, they are connected in a series to fulfil the voltage requirement of the light source in correspondence to the voltage generated by the energy harvester. The voltage level of the storage capacitors during the charging and discharging process can be obtained by

$$V_{cap}^{charge}(n_{cycle}) = V_g \left(1 - e^{-\frac{n_{cycle} \Delta Q}{V_g C_{cap}}} \right), \tag{3.1a}$$

$$V_{cap}^{discharge}(n_{cycle}) = V_g e^{-\frac{n_{cycle} \Delta Q}{V_g C_{cap}}}, \tag{3.1b}$$

where V_{cap} is the voltage level of the storage capacitor and the superscript charge/discharge indicates the corresponding process, n_{cycle} is the number of the cycle that is

49

related to the time duration, ΔQ represents the amount of electrical charge supplied and stored in the capacitors, and V_g is the generated voltage from the nanowires.

3.2.3 Light Source

There are two light source options to be used in optogenetic stimulation, namely lasers and LEDs. The latter has advantages in terms of price, size, and energy efficiency, but not directivity. Considering the size and the energy harvesting method of the WiOptND, the LED is the perfect candidate. The off-the-shelf InGaN Cree's Direct Attach DA2432 LED shines 450–470 nm blue light and requires only a minimum level of 5 mA of electrical current. Upon that operating condition, it can produce approximately 5 mW or more of optical power. This fulfils the operating requirement of the ChR2, which requires a light intensity of approximately 1 mW/mm^2. However, depending on the specification of the optogenetics, some have a lower sensitivity around of 8-12 mW/mm^2, and this factor is also taken into consideration in the analysis [53] [24] [82] [12].

3.3 Method and Evaluation

The analysis and justification of the hardware design is done by numerical analysis based on the data gathered and compiled from the various corresponding literature, books, and component specifications. Each incorporated hardware component is compatible according to either its technical specification or experimental data. Therefore, this methodology is limited for ideal cases and working environment. Energy and power numerical simulations are performed using MATLAB, while the simulation of light interaction with neurons is implemented using COMSOL Multiphysics, as discussed in Section 2.5. Table 3.1 shows the simulation parameters for the energy and power design validation.

Considering the power intensity requirement of the optogenetics and the distance between the light source and the neuron, the minimum light intensity from the LED can be obtained by considering the absorption coefficient of the brain tissue (depicted in Figure 3.5(a)). During the charging and discharging periods of the storage capacitors, depending on the required intensity, the stored energy level changes as a function of time (analysed in Figures 3.5(b) and 3.5(c)). It was also observed that a

Table 3.1 Simulation Parameters. [I][II] [104]

Parameter	Value [Unit]	Description
Neural Dust Density	0.024 to 1.2 $[/cm^3]$	Randomly scattered
Frequency	500 to 3M $[Hz]$	Ultrasound freq
Depth Radius	2 to 4 $[mm]$	Into the brain
Interfiring period	6 $[ms]$	Mean (exponential dist)
Data sample	10,000	Randomly generated
Nanowire surface area	10^4 to 2×10^4 $[\mu m^2]$	Energy harvester
LED diameter	100 $[\mu m]$	Light source
Neuron diameter	100 $[\mu m]$	Spherical soma

higher light intensity requirement causes faster charging and discharging behaviours. The same case but with doubled energy harvester surface area was also considered. For both (charging and discharging) scenarios, the time and the amount of stored energy are proportional to the surface area (shown in Figures 3.5(d) and 3.5(e)). Finally, Figure 3.5(f) shows no significant difference when the operating ultrasound frequency is varied.

The results confirm that the circuit design for the WiOptND is feasible for implementation. It complies with the size limitation (hundreds of microns), biocompatibility — by using proven material coating — and the implementation (light intensity) requirements for optogenetics.
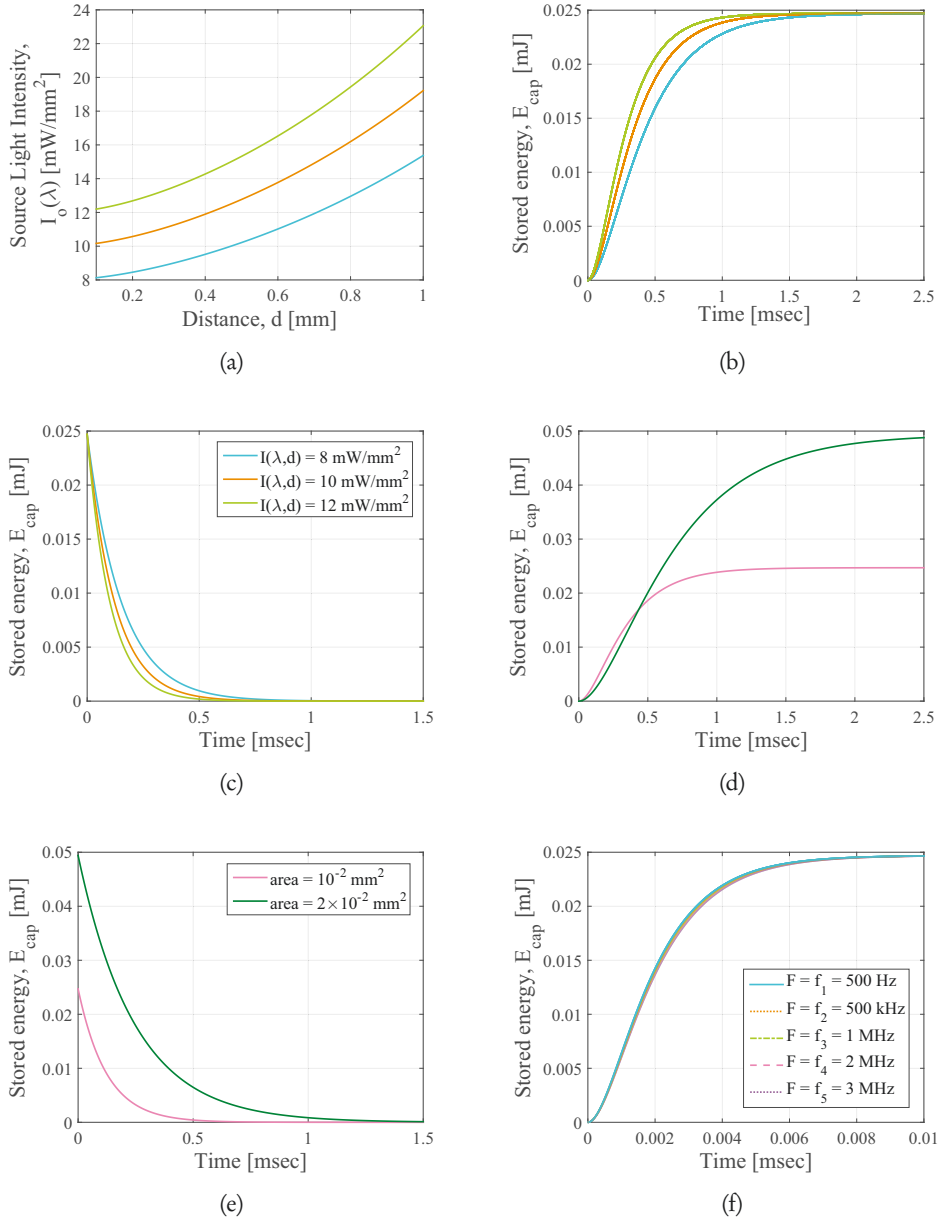
Figure 3.5 (a) The light source intensity as a function of distance for three different intensity requirements. (b) The capacitor energy during the charging period (ultrasound frequency of 500 Hz; 500 μm distance from the μ-LED). (c) The capacitor energy during the discharging period (frequency of 500 Hz; 500 μm distance). (d) The capacitor energy during the charging period for two different energy harvester surface areas (intensity $I(\lambda,d)$ of 10 mW/mm^2; frequency of 500 Hz; 500 μm distance). (e) The capacitor energy during the discharging period for two different energy harvester surface areas (Intensity $I(\lambda,d)$ of 10 mW/mm^2; frequency of 500 Hz; 500 μm distance). (f) The capacitor energy during the charging process with ultrasound frequency variations. [II]

4   LIGHT INTERACTION WITH NEURONS

The behaviour of light propagation in brain tissue and neurons are the focus of [IV], [V], and [VI]. This investigation is important considering the neuron density in the neocortex. A denser neuron population results in a greater probability that one or more neurons block the target neuron with respect to the line of sight of the light source. In addition, the micro movement of neurons due to natural growth or a probe/interface effect results in unpredictable neuron positions [56] [78] [79]. These aforementioned factors can lead to one or more undesired stimulation when they are not well understood. In [IV], the reflection, absorption, and refraction phenomena of one and two blocking neurons are analysed. Furthermore, the analysis is extended in [V] by considering three different cell geometries (spherical, pyramidal, and fusiform) and the scattering behaviour of light propagation.

4.1   Modified Beer Lambert Law

The modified Beer Lambert law is an extension of the Beer Lambert law, which is used for continuous wave (CW) absorption measurement in scattering media [21]. According to this photon transport model, light wave absorption is proportional to the concentration of the major chromophores in the tissue, which is defined as a semi-infinite medium. Additionally, the wave is considered to experience constant scattering losses. Due to the chromophores in biological tissue, the photon does not propagate in a straight line from the source to the detector; it experiences changes in direction caused by random collision with the chromophores. This phenomenon is represented as the differential path length factor (DPF). DPF is the scaling factor of the euclidean distance between two points in the biological tissue since the propagation path is deviated from the straight line as the light interacts with the biological components, and it is studied analytically, experimentally, and numerically for different kinds of biological tissues [84] [26] [55] [42]. This parameter is obtained from

$$DPF(\lambda,d) = \frac{1}{2}\sqrt{\frac{3\mu_s'(\lambda)}{\mu_a(\lambda)}}\left[1 - \frac{1}{1 + d\sqrt{(3\mu_a(\lambda)\mu_s'(\lambda))}}\right], \tag{4.1}$$

where $DPF(\lambda,d)$ is the differential path length factor as a function of the wavelength λ and the distance d, and $\mu_a(\lambda)$ and $\mu_s'(\lambda)$ are the absorption and the reduced scattering coefficients of the propagation medium, respectively.

After obtaining the DPF, the medium transmittance can be calculated by

$$\frac{I(\lambda,d)}{I_o(\lambda)} \equiv T(d) = e^{-\mu_a(\lambda)\,d\,DPF(\lambda,d)+G(\lambda)}, \tag{4.2}$$

where $I_o(\lambda)$ is the light source intensity, $I(\lambda,d)$ is the light intensity at distance d from the source, and $G(\lambda)$ is a medium- and geometry-dependent constant and is largely unknown.

In this thesis, the modified Beer Lambert law is particularly used for numerical analysis to assess the energy and power requirement of the device and their changes with respect to distance.

4.2 Helmholtz Equation

The Helmholtz equation simplifies the optical wave partial differential equation (PDE) form in both space and time by omitting its dependence on time. COMSOL models the system with Helmholtz representation using a finite element method. The considered optical phenomena in the COMSOL simulation include scattering and absorption given the optical and geometry of the brain tissue and neurons. The purpose of this simulation is to obtain the fluence rate (light intensity) u or $\Phi(r,t)$, as the function of the diffusion coefficient c or $D(r,t)$, the absorption coefficient a or μ_a, and the source term f or $S(r,t)$ according to the following Helmholtz equation

$$-\nabla D(r,t)\nabla^2\Phi(r,t) + \mu_a\Phi(r,t) = S(r,t)$$
$$\nabla(-c\nabla u) + au = f. \tag{4.3}$$

In this thesis, COMSOL is mainly used to solve the Helmholtz equation of the system and to analyse of the light radiation behaviour in the brain tissue.

4.3 Mie scattering

As discussed briefly in Section 2.5, scattering is one of the phenomena when light propagates through a heterogeneous biological medium. This causes the light to be deflected from its straight trajectory to one or more deviated paths. When the light traverses into the soma of a neuron, it encounters many cell organelles floating in the cytoplasm. Among those organelles, the nucleus is the largest. Furthermore, the nucleus has a slightly different refractive index compared to the cytoplasm, which results in the light wave being scattered. Based on the size parameter χ, scattering can be categorised into either Rayleigh or Mie. This category determines the shape of the radiation pattern. The value of parameter χ can be obtained by

$$\chi = \frac{2\pi n_o r}{\lambda} = kr, \tag{4.4}$$

where n_o is the refractive index of the cytoplasm, r is the particle radius, and k is the wave vector by definition.

Mie scattering occurs when the size parameter is between the range of 0.2 and 2,000, which means the particle size is comparable to the radiation wavelength, while Rayleigh scattering occurs when it is between 0.002 and 0.2. Numerical scattering analysis is used to determine the scattering radiation pattern in this thesis.

4.4 Method and Evaluation

The analysis of the light interaction with brain tissue and neurons was done analytically, numerically, and experimentally. The equation derivation for analytical analysis is based on the neuron geometry, the modified Beer Lambert law, Snell's law, ray tracing, and other formulas. This includes the evaluation of the light behaviour based on the power, geometry-related properties (angle, coordinates, vectors), and channel impulse response of the propagation medium. Afterwards, the system was analysed numerically by combining the derived formulas and the experimental data. It included comparing the numerical and experimental results for theoretical justification. The numerical evaluation was done mostly using MATLAB. The simulation based on the Helmholtz equation was implemented using COMSOL Multiphysics. Finally, one particular light interaction related to the focusing effect by the nucleus

was validated by the collaborators in a laboratory in the Department of Pathology and Anatomical Sciences, University at Buffalo, New York, USA. Table 4.1 lists the values that were used for the simulation of light propagation.

Table 4.1 Simulation Parameters. [IV] [VI]

Parameter	Value [Unit]	Description
$\bar{\rho}$	0.5 [%]	Reflectance index of the neuron [29]
v_0	$3 \cdot 10^8$ [m/s]	Speed of light in vacuum
λ	456 [nm]	Wavelength of light
n_t	1.35	Refractive index of the brain tissue [62]
n_c	1.36	Refractive index of the neuron
$\mu_a^{(c)}$	0.9 [/mm]	Neuron absorption coefficient [104]
$\mu_s'^{(c)}$	3.43 [/mm]	Neuron reduced scattering coefficient [104]
$\mu_a^{(u)}$	20 [/mm]	Brain tissue absorption coefficient [10]
$\mu_s'^{(u)}$	1.34 [/mm]	Brain tissue reduced scattering coefficient [10]

4.4.1 Multipath Propagation (Reflection) Model

The main components in the multipath are the waves that are reflected from the surrounding neurons. The total path loss and the delay must be characterised to investigate the significance for the received power. For a light that has been reflected k^{th} times, the power degradation can be written as

$$\Gamma^{(k)} = P_0 \bar{\rho}_1 \bar{\rho}_2 ... \bar{\rho}_k = k \, \bar{\rho} \, P_0 = k \left[\frac{n_t - n_c}{n_t + n_c} \right]^2 P_0, \tag{4.5}$$

where n_t and n_c are the refractive index for the brain tissue and neuron, $\bar{\rho}$ is the reflectance index, and P_0 is the power from the light source.

The total power delay profile (PDP) can be formulated as

$$h(t) = \sum_{k=0}^{N_{adj}} h^k(t; \Phi_n), \tag{4.6}$$

where $h^k(t; \Phi_n)$ is the PDP from each reflected component as a function of time and

propagation delay and N_{adj} is the total number of neurons that reflect the wave to the receiver.

The illustration of this scenario is depicted in Figure 4.1(a) where the light source is represented as red circle on the upper left, shining the intermediate neuron on the upper right, and bottom circle is considered as the target neuron. The direct light rays from the light source to the target neuron are not considered to limit the analysis solely for the light reflection case. Additionally the delay profile is visualised in Figure 4.1(b) showing the arrival time and transmittance of the reflected light rays. Based on the calculation, the effect of multipath propagation is negligible, since its value is extremely small compared to the line of sight (LoS) and the refracted components. The main reason is that the reflectance index of the neuron is significantly low (0.5%), in addition to the light absorption along the path to the target neuron, resulting more than 80 dB path loss in total.

4.4.2   Blocking Neuron (Refraction) Model

In this subsection, the blocking neuron propagation model is detailed. This is the situation where the space between the light source and the target neuron is occupied by other (blocking) neurons. When the light rays traverse these blocking neurons, they experience direction deviation. This behaviour can be evaluated by tracing the rays from the source to the target/receiver. By employing the Helmholtz equation, COMSOL simulates this scenario where two blocking neurons are incorporated into the system. The simulation results (Figures 4.2 and 4.3) show the light radiation pattern and the energy-preserving behaviour measured in decibels (dB). They depict the light behavior for two scenarios, the brain tissue without any neuron along the light propagation path and with three neurons. Furthermore, the geometrical and ray tracing analysis are presented in Figure 4.4 to show different interactions based on the neuron morphology.

In general, the total path loss that is experienced by a light wave traversing N
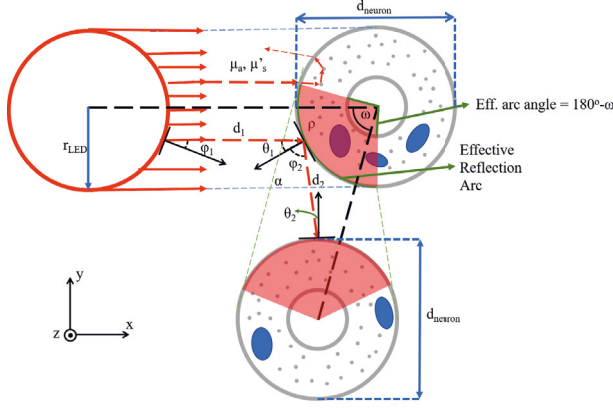
(a) The illustration of the reflected light rays by one neuron before hitting the target neuron.
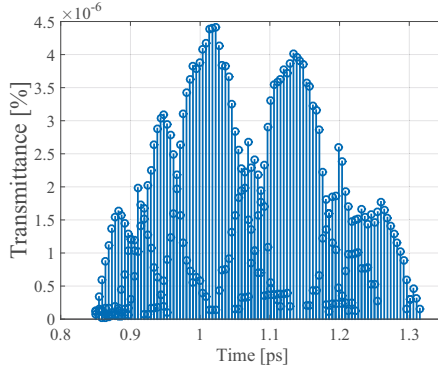
(b) Delayed components on the receiver.

Figure 4.1 Neuron reflection model. [IV]

number of any given shape of neurons is formulated as

$$
\begin{aligned}
PL_{total} =4.343\Big[& N\mu_a^{(c)}(\lambda)\overline{d_a}DPF(\lambda,\overline{d_a}) \\
&+(N-1)\mu_a^{(u)}(\lambda)\overline{d_e}DPF(\lambda,\overline{d_e}) \\
&+\mu_a^{(u)}(\lambda)(d_E+d_R)DPF(\lambda,(d_E+d_R))\Big],
\end{aligned}
\tag{4.7}
$$

where $\overline{d_a}$ and $\overline{d_e}$ indicate the average propagation distances inside a neuron and between two neurons, respectively, and d_E and d_R are the distances of the light source from the first neuron and the receiver from the last neuron, respectively. The superscript (c) or (u) indicate whether a parameter correlates with the neuron or brain

on=20000 1/m, musp_axon=1340 1/m, mua_myelin=20000 1/m, musp_myelin=134(axon=900 1/m, musp_axon=3430 1/m, mua_myelin=330 1/m, musp_myelin=1700
Slice: 10*log10(u)   Slice: 10*log10(u)

(a)   (b)
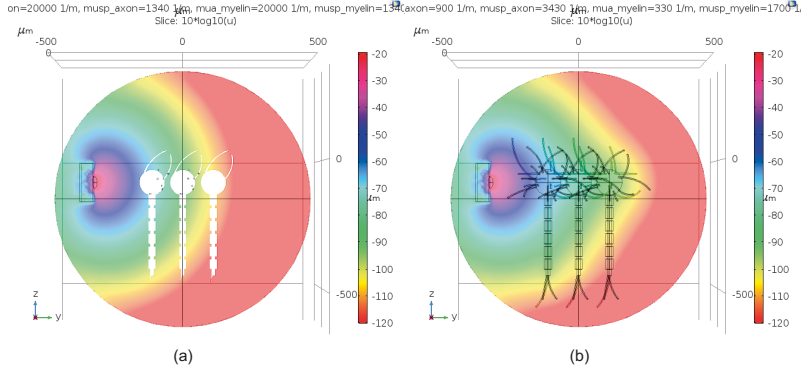
Figure 4.2 COMSOL simulations for light propagation in nervous tissue (a) without neurons and (b) with three neurons. [IV]
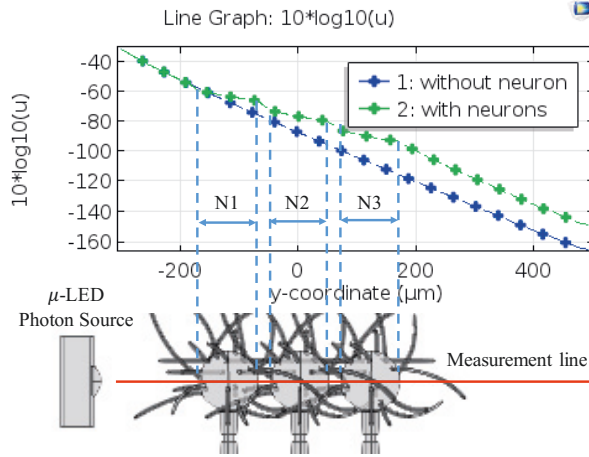
Figure 4.3 COMSOL numerical path loss simulations for light propagation in nervous tissues without neurons and with three neurons. [IV]

tissue, respectively.

By having knowledge of the light interaction on various neuron geometries, the optimum location and orientation of the WiOptND can be determined. The result can be combined with the hypothesis of biophoton communication proposed in [57] to direct the photon to the desired axon location, avoiding undesired stimulation.

59
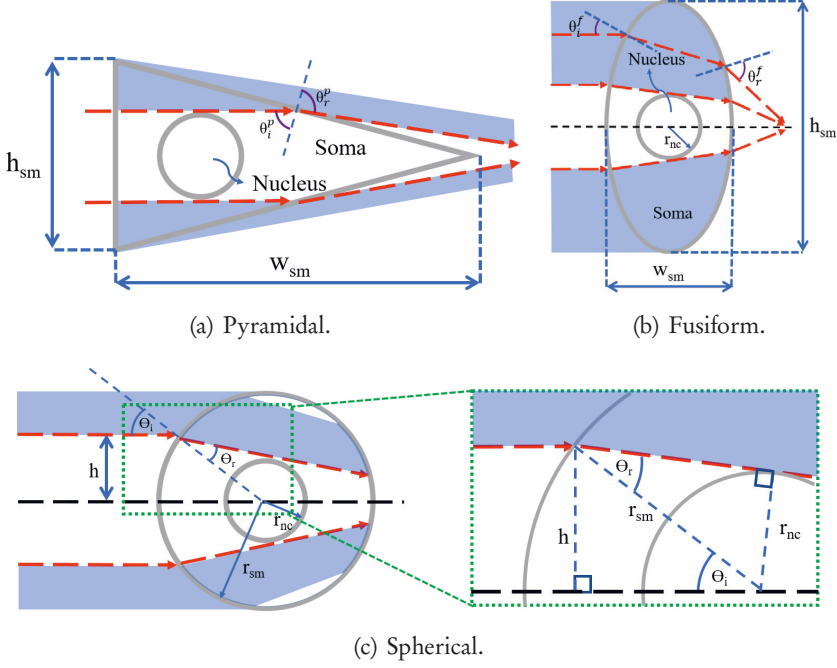
Figure 4.4 Ray tracing analysis for three different 2-D projected neuron geometries. [V]

4.4.3 Nucleus Scattering Model

As mentioned in Section 4.3, the size parameters should be calculated to determine the scattering category. Based on the system properties, such as using a 456-nm light, a nucleus with a diameter of 3–18 μm and the refractive index of the nucleus, n_{nuc}, of 1.39 [35], and the cytoplasm, n_{cyto}, of 1.36–1.39 [16], the size parameter is in the range of 28.32 to 169.89, which is obviously categorised as Mie scattering. In Mie scattering, the intensity in the forward direction is more dominant than in the backward direction; this is depicted in Figure 4.5. This shows that the neuron resembles a convex lens in behaviour [28].

4.4.4 Microscopy Experiment

The validation of the analytical and numerical analysis was performed in the microscopy laboratory of the Department of Pathology and Anatomical Sciences, University at Buffalo, New York, USA. It was done to observe the forward scattering
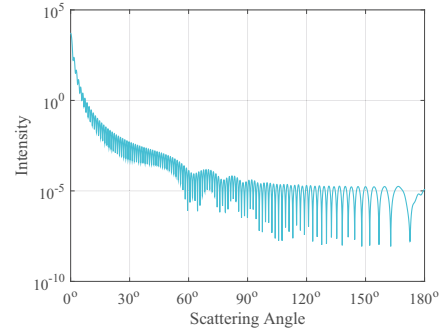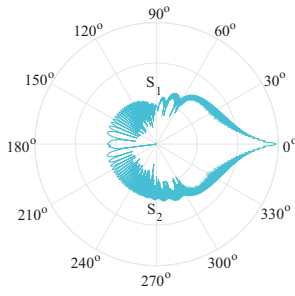
(a) The scattering amplitudes polar plot of S_1 on $0^o \leq 180^o$ and S_2 on $180^o \leq 360^o$.

(b) The logarithmic Cartesian plot of light intensity as a function of scattering angle.

Figure 4.5 The scattering intensity pattern when the light is scattered by the nucleus. [V]
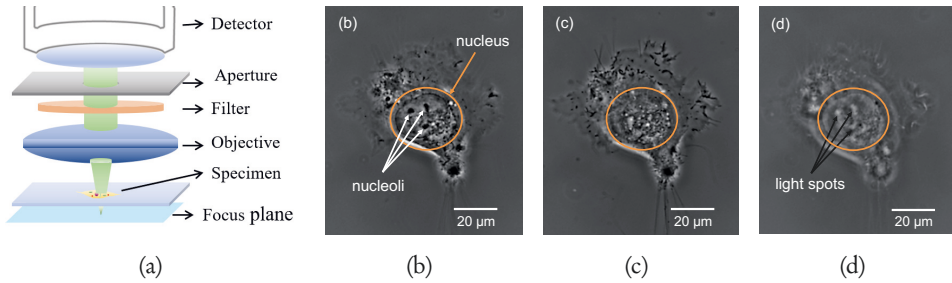
Figure 4.6 Neural progenitor cells (NPCs) differentiated from human embryonic stem cells were plated on a tissue culture dish. Phase contrast images of NPCs were acquired by changing the focal plane distance using a Zeiss AxioObserver inverted wide-field fluorescence microscope. The lateral view of the experiment is illustrated in (a). The focused light was observed at three distances; (b) on the cell surface, (c) and at 5 μm and (d) 10 μm below the cell surface. The orange circles in the figures show the region of interest (nucleus). The arrows indicate nucleoli in (b) and light spots of cumulated light in (d). [V]

and focusing effect of the incident light. The experimental setup is illustrated in Figure 4.6(a) by using fusiform-shaped neural progenitor cells (NPCs) as specimens. During the experiment, the focus plane was controlled to observe the focusing distance. Figures 4.6(b)–(d) show the imaging result difference among three focus plane distance variations. The light is focused at a distance of 10 μm below the specimen. This value is close to the lower bound of the focus area obtained from the numerical analysis, which is approximately 10.4 μm.

5   LIGHT PROPAGATION THROUGH NEURAL TISSUE

Depending on the path it takes, each light ray experiences a different level of interaction phenomena. In this case, the path is determined by the neuron morphology. The neuron shape variation causes a different delay profile of the light rays. When a light short pulse is transmitted, the received pulse form is altered as a result of the superposition of the delayed waves. In [VI], the end-to-end propagation is analysed by incorporating multiple neurons along the path. This analysis focuses on the channel impulse response using the time and frequency domain.

5.1   Ray Tracing Model

Light transmission though multiple neurons can be analysed using the ray tracing model. In this model, the geometry of the neurons is considered the main factor determining the propagation path of the rays. Therefore, with this method, all three neuron geometries — namely spherical, fusiform, and pyramidal — can be separately analysed. Figure 5.1 illustrates the difference in behaviour among the three aforementioned neuron shapes. In this illustration, it can be observed that some phenomena are unique to each geometry — for example, leaking rays in the spherical neuron where part of the transmitted rays are no longer transmitted to the next neuron, and consecutive refraction in the pyramidal neuron, which deviates the rays from the main propagation path. The common phenomena of geometrical gain or focusing effect can be found in the fusiform and spherical neuron model. Additionally, for all the shapes, the light experiences medium loss. The last two factors (geometrical gain and medium loss) affect the final received signal in terms of intensity level. For the ray tracing simulation using MATLAB incorporating multiple neurons, the pseudo code in Appendix A.1 is used.

Figure 5.1 Geometrical analysis of light propagation using ray tracing as it propagates through a one-dimensional array of neurons; this includes (a) fusiform, (b) spherical, (c) pyramidal neurons. [VI]
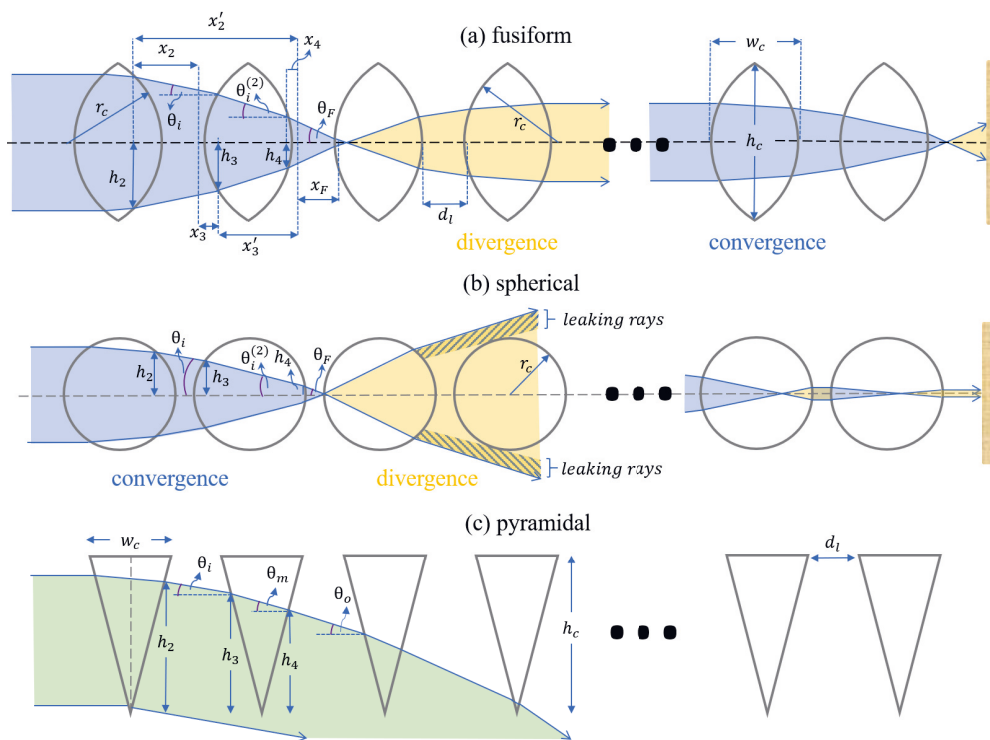
5.2 Channel Impulse Response

When understanding the channel impulse response of the propagation medium, it is important to characterise the transmission channel, since it alters the transmitted impulse form. The channel impulse response can be analysed in both the time and frequency domains. In the time domain, the impulse response of each channel component should be known [81]. Conversely, in the frequency domain, the received and the transmitted signals should be transformed and processed to obtain the channel impulse response. Equation 5.1 shows the analysis of the time domain based on the convolution of each channel component, while equation 5.2 is for the frequency

domain analysis.

$$h(t;d_{total},\lambda) = \underset{n=1}{\overset{N}{\circledast}} h_a^{(n)}(t;d,\lambda) \circledast \underset{n=1}{\overset{N+1}{\circledast}} h_e^{(n)}(t;d,\lambda), \tag{5.1}$$

where $h^{(k)}(t;d,\lambda)$ is the impulse response of the light ray corresponding to the nth neuron and subscript a or e indicates if it is intra- or inter-neuron propagation, λ is the wavelength, and t is the time.

$$h(t;d,\lambda) = \mathscr{F}^{-1}(H(f;d,\lambda) = \mathscr{F}^{-1}\left(\frac{\mathscr{F}(E_r(t;d_{total},\lambda))}{\mathscr{F}(E_t(t;d,\lambda))}\right), \tag{5.2}$$

where $\mathscr{F}(E_t)$ and $\mathscr{F}(E_r)$ are the Fourier transforms of the transmitted and the received signals, respectively.

5.3 Method and Evaluation

The channel impulse response characterisation was done analytically and numerically both in the time and frequency domains. The numerical simulation was implemented in MATLAB for three neuron geometries. The analysis incorporated the superposition of the received signals and the ray tracing to observe the delay profile of the system.

The impulse was implemented as a gaussian short pulse which has a full-width at half-maximum (FWHM) duration of 1 fs. The received signals are depicted in Figure 5.2 for three different shapes of neurons arranged in a one-dimensional array. The transmitted impulse propagates for several picoseconds and undergoes different signal form deviation depending on the shape of the neuron along the propagation path. Furthermore, Figure 5.3 shows the analysis of channel impulse responses and PDPs for the same neuron arrangement. It includes the intensity analysis representing the signal attenuation, frequency and channel impulse response analysis characterising the propagation medium, and power delay profile showing time difference between transmitted and arrival time of the impulse.

This analysis is important for characterising the neural tissue as the propagation medium for a light wave. It can generally be applied further for different transmitted light wave forms. In this simulation, the gaussian short pulse was used as the general light signal.
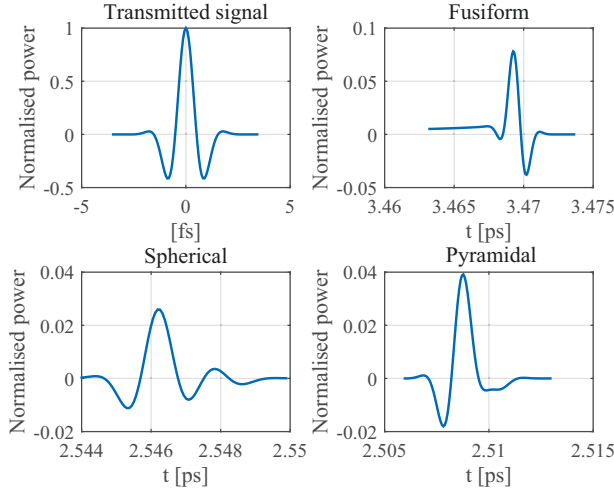
Figure 5.2 The pulse shapes of the transmitted and the received signals after 450 μm propagation through a one-dimensional array of neurons. [VI]
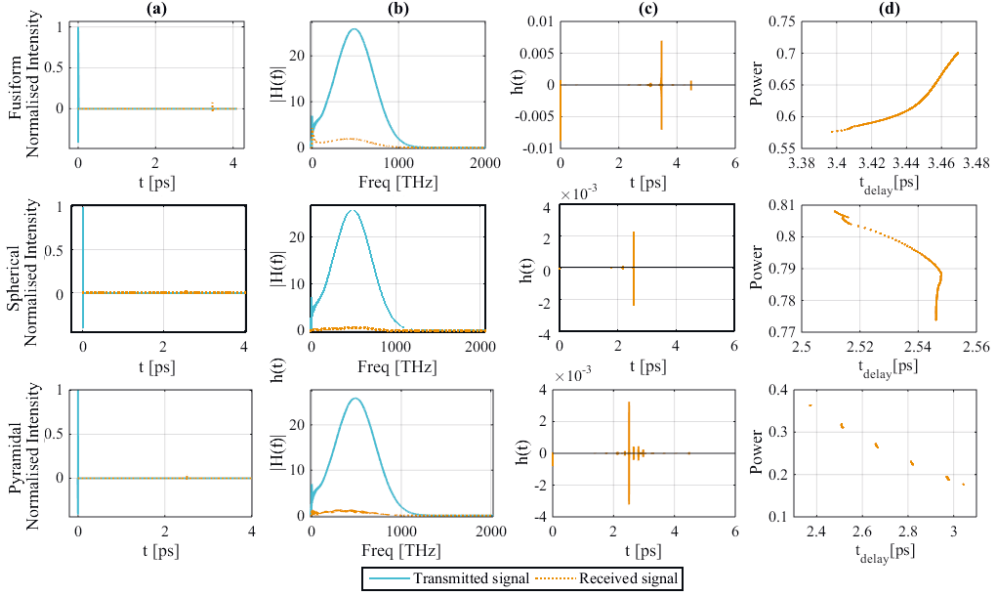
Figure 5.3 Time and frequency analysis of light propagation along fusiform, spherical, and pyramidal neurons. (a) The normalised intensity of the transmitted and the received signals in the time domain; (b) Absolute value of the transmitted and the received signal in the Fourier domain; (c) Channel impulse response; (d) Power delay profile. [VI]

6   SYSTEM CHARGING PROTOCOLS

In [II], the charging protocol to support the spatially distributed stimulation feature is elaborated upon. The purpose is to generate a certain stimulation pattern to stimulate the optogenetic constructs. For the protocols that require the integration of the time delay feature, an alteration of the device's electrical circuit is needed. There are two types of charging protocols introduced in [II]. The first protocol is the basic protocol that integrates the addressing capabilities into the system, and the second protocol is the improvement of the first one considering the requirement of the neurons' action potential firing pattern.

6.1   Spatial Distributed Nanonetworking

Even though the WiOptND is capable of working in any area of the brain, as mentioned in Chapter 3, the focus of the WiOptND is implementation in the neocortex. The neocortex's layered structure contains neurons that communicate with each other, especially within one cortical column. This connection is perceived as an opportunity for multiple WiOptND implementation, as it forms a particular pattern in neuron firings. By controlling synchronous device activation timing, the neuron firing pattern can be imitated. This is useful in the case of a failed neural communication due to a neuron connection problem, as illustrated in Figure 6.1. The solution given by WiOptND is to introduce the spatially distributed nanonetworking, which enables a synchronous cooperation among devices in terms of activation timing within a scattered but limited working environment. This requires the mechanism to at least activate a set of targeted devices (instead of all devices), which can be perceived as an addressing mechanism. This can be done by employing multiple ultrasound frequencies and assigning each device a unique frequency. Figure 6.2 illustrates the scattered devices in various layers of the neocortex.

   To describe the basic architecture of the system charging protocol, three element
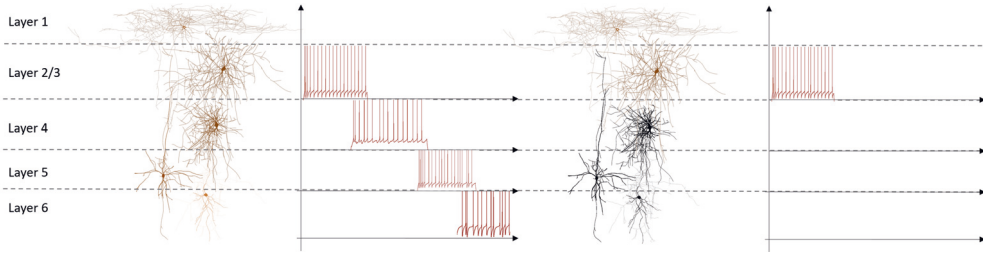
Figure 6.1 Illustration of the healthy (left) and the disconnected (right) cortical neural networks. Failing of action potential relays results in disconnected communication in the cortical column of the cerebral cortex. [II]
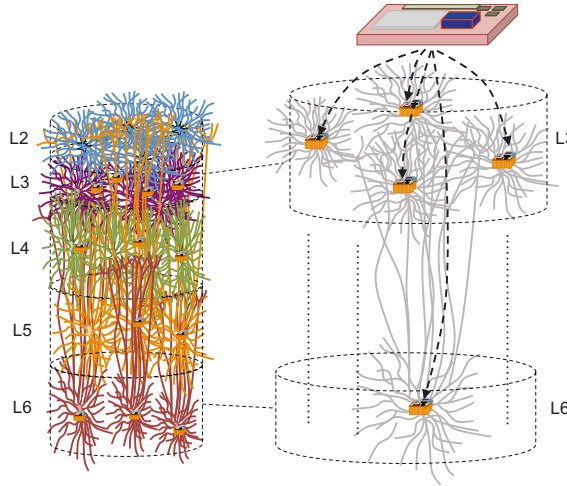
Figure 6.2 The WiOptND nanonetworks deployed in the cortical column, between L2/3 - L6. [II]

sets on both (neocortex) the environmental side and device side should be defined. They are the neocortex layer set, $L = \{2/3, 4, 5, 6\}$, ultrasound frequency set, $F = \{f_1, f_2, f_3, ..., f_n\}$, and device set, $ND = \{ND_1, ND_2, ND_3, ..., ND_m\}$, where $\{n, m\} \in \mathbb{N}^*_{\leq n}$. The system limitation from transmitter side is its capability to only transmit a single frequency ultrasound for each time instance to avoid interference and harmonic generation. However, the implementation of multiple frequency transmitter is still feasible by choosing sufficient spacing between operational frequencies. The frequency spacing will also determine the cutoff frequency for the band-pass filters.

6.2 Charge and Fire Protocol

In this protocol, one ultrasound frequency correlates to one device. In order to support its implementation, the sub-dura transceiver is required to have prior knowledge of the neuron firing sequence. Based on that, the corresponding frequency is transmitted to charge and activate the device. Regarding the data of neuron firing sequence, it can be obtained by prior observation on certain performed activity. However, this method can only accommodate limited number of simple activities due to its nature of direct observation. Since this protocol requires a mechanism to address the devices, a voice–operated switch (VOX) is integrated into the circuitry (Figure. 6.3). This component allows the device to be correlated to a certain ultrasound frequency for activation purposes. However, the frequencies allocated to this protocol increase linearly with the number of devices. Furthermore, a considerable distance between the frequencies used should be considered to avoid possible interference between them.
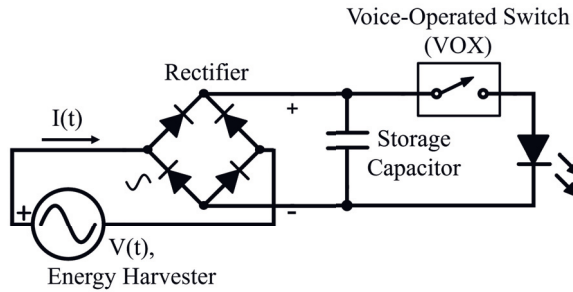
Figure 6.3 WiOptND circuit diagram with integrated VOX component for the Charge and Fire protocol. [II]

Figure 6.4 visualises the working principle of this protocol. The firing analysis is performed every time instance, and the corresponding WiOptND is activated to address it. The problem arises when more than one neural spike occurs in the same time instance. This leads to a misfiring event. Misfiring is a parameter to assess the effectiveness of the protocol. It indicates the unaddressed spikes of the sequence/-pattern.
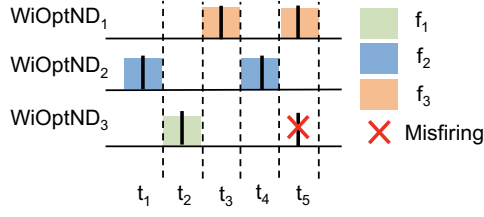
Figure 6.4 Charge and Fire protocol employs a one-to-one relation between frequency transmission from the sub-dura transceiver and the neural spike sequence. [II]

6.3 Predictive Sliding Detection Window Protocol

The second protocol is the improvement of the first protocol in terms of firing efficiency and prediction. This protocol enables the activation of several devices following a certain firing pattern. This can be done by incorporating a time delay relay component into the circuit. The fundamental idea is to activate several devices at different time instances to address the firing pattern requirement. However, this implementation increases the complexity of the device. The operation of this protocol is depicted in Figure 6.5. This protocol analyses and chooses the most similar required firing pattern and the pattern provided by the available frequencies. Algo-
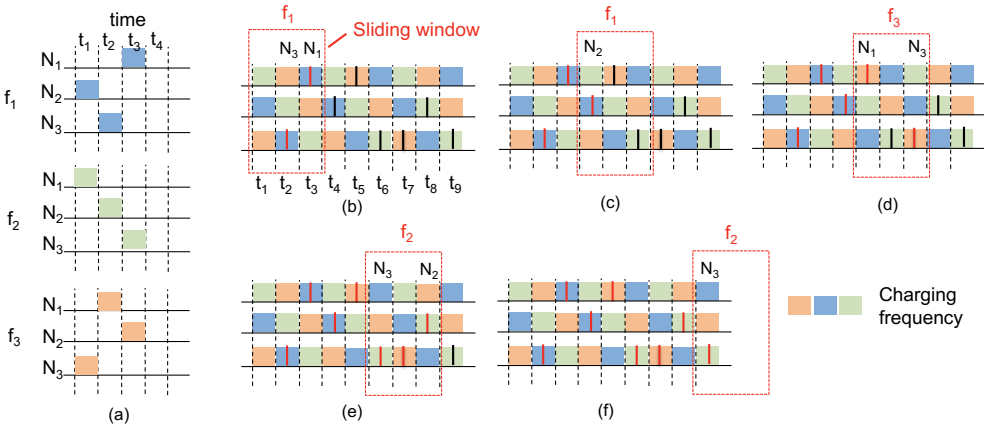
Figure 6.5 Illustration of the Predictive Sliding Detection Window mechanism with three ultrasound frequencies/patterns: (a) presents the predicted patterns for three frequencies for three WiOpt-NDs with respect to time, and (b) – (f) illustrates the sliding window with respect to time. The selected frequency is based on the highest number of the matched firing pattern. [II]

rithm 1 details the step-by-step mechanism of this protocol. The initial step of this

protocol is data provision regarding the frequencies and their corresponding firing pattern (P[1...n]). The firing pattern prediction M_{ij} is truncated into a smaller unit size based on the firing matrix size of one frequency M_{ii}. Afterwards, all the spikes from the first column are checked to see if they have been addressed. If not yet addressed, the pattern M_{ii} is compared with the available patterns (from all frequencies) and the most identical one is chosen. Based on that, the corresponding frequency is transmitted.

Algorithm 1 Predictive Sliding Detection Window

1: Initialize P[1...n]   ▷ where n is total number of available frequencies
2: $M_{ij} \leftarrow$ Pattern Prediction
3: **for** a $= 1$ to j **do**
4:       $M_{ii} \leftarrow M[:, a : a - 1 + \text{column}(P[b])]$
5:       **if** $M[:, 1] \neq 0$ & $M_{ii} \neq 0$ **then**
6:             **for** b $= 1$ to n **do**
7:                   simTest $\leftarrow$ compare $M_{ii} == P[b]$
8:             **end for**
9:             maxSim $\leftarrow$ max(simTest)
10:            tempFiringSlot $\leftarrow 2 \times P[maxSim] - M_{ii}$
11:            $M_{ii} \leftarrow$ tempFiringSlot
12:      **end if**
13: **end for**

6.3.1   Markov Chain-based Time-Delay Pattern

Determining the amount of frequencies and the individual firing pattern of each frequency should not be done randomly. As mentioned above, within a cortical column, neurons from different layers communicate to each other. Based on the connection probability and its connection flow, a certain pattern is more likely to occur than others. Thus, this method is an option to assign a certain pattern that corresponds to each ultrasound frequency. Figure. 6.6 shows the Markov Chain model for connection probability and flow direction in the cortical column. This model is derived based on the digital reconstruction of neocortical circuitry from the experimental data done as a part of the Blue Brain Project at École Polytechnique Fédérale de Lausanne, Switzerland. Furthermore, Table. 6.1 lists the connection pattern that is more likely to occur.
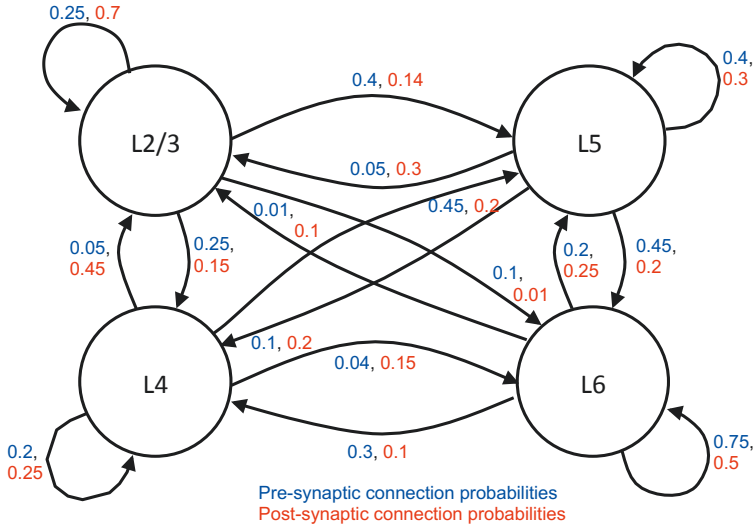
Figure 6.6 Markov Chain model of inter- and intra-layer connectivity for the cortical column. [II]

Table 6.1 Rank and Connection pattern. [II]

Rank	Connection Patterns
1	$L[5] \rightarrow L[6] \rightarrow L[4] \rightarrow L[2/3]$
2	$L[4] \rightarrow L[5] \rightarrow L[6] \rightarrow L[2/3]$
3	$L[2/3] \rightarrow L[6] \rightarrow L[5] \rightarrow L[4]$
4	$L[6] \rightarrow L[4] \rightarrow L[5] \rightarrow L[2/3]$
$\vdots$	
24	$L[6] \rightarrow L[2/3] \rightarrow L[4] \rightarrow L[5]$

6.3.2 Circuit Alteration for the Sliding Window Mechanism

The number of patterns solely depends on the amount of ultrasound frequencies used. Each frequency in the system corresponds to a VOX and a time delay relay component as depicted in Figure 6.7. VOX controls the switch in choosing which time delay relay is activated.
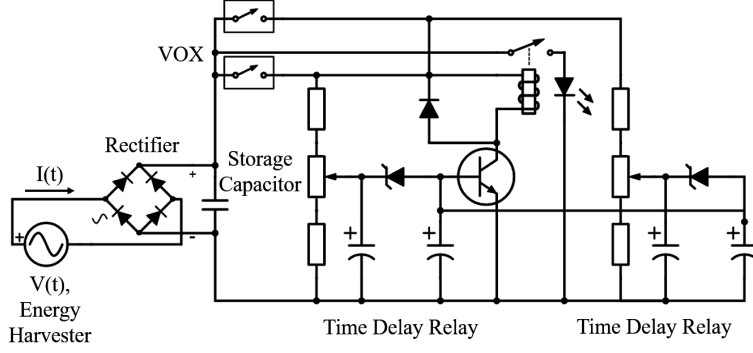
Figure 6.7 WiOptND circuit diagram with integrated time-delay relay for the Predictive Sliding Detection Window protocol. [II]

6.3.3 Firing Pattern Prediction Model

To automate the pattern prediction process, the mathematical model in [50] was adopted. Based on the stimulus, this model can decide if the firing is generated. It calculates the values of the threshold and the feedback in order to determine the response of the stimulus. The model is represented as

$$r(t) = \delta(h(t)) - \theta)\dot{h}(t)H(\dot{h}(t)), \tag{6.1}$$

where

$$h(t) = g(t) + a(t) + \int_{-\infty}^{t} r(\tau)(1 + b(\tau))P(t-\tau)d\tau, \tag{6.2}$$

$$g(t) = \int_{-\infty}^{t} s(\tau)F(t-\tau)d\tau, \tag{6.3}$$

$$H(x) = \begin{cases} 1, & \text{if } x > 0 \\ 0, & \text{otherwise,} \end{cases} \tag{6.4}$$

where $r(t)$ represents the sum of delta function spikes when $h(t)$ crosses the predetermined threshold θ with a positive gradient slope. The function $g(t)$ is the filtered stimulus $s(t)$ with filter $F(t)$ in the time domain. The parameters $a(t)$ and $b(t)$ are the Gaussian noises, while $P(t)$ is the feedback potential.

One scenario that can be implemented using this model is vision detection, as

depicted in Figure 6.8. The optical intensity captured in the eye can provide the input to the external receiver in cases where there is a connection problem with the connection from the eye to the *lateral geniculate nucleus* (LGN) cells. By employing the mathematical model in (6.1), the neural firing pattern can be predicted.
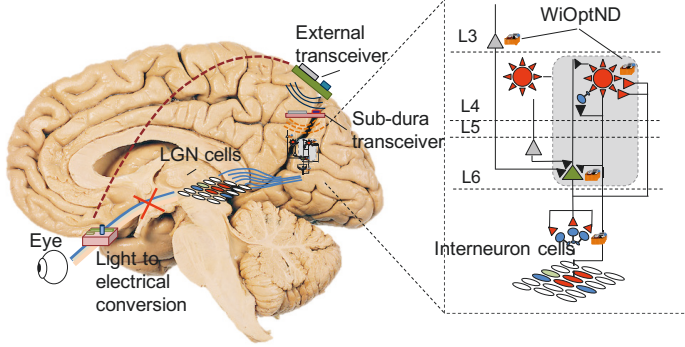
Figure 6.8 Example deployment of the WiOptND nanonetwork in the brain's visual cortex. The circuit connection to the V1 primary visual cortex is impaired, requiring the deployment of WiOpt-NDs, where the coordinated stimulation will compensate for the failed neurons. [II]

6.4 Method and Evaluation

The effectiveness of the protocol was analysed numerically based on the MATLAB simulation of the predefined firing pattern. The pattern was randomly generated using frequency data from a *middle temporal cortex* experiment on a *macaque monkey*. It uses dynamic a visual stimulus (Figure 6.10(a)) causing the variation of two distinctive lower and higher neural spike frequencies (Figure 6.10(b)) [102]. In order to assess the protocol performance, several measurement metrics were defined as follows

$$n_{mis} = \sum_{t=0}^{T}\sum_{y=0}^{|L|}\left[\sum_{k=0}^{|L|}[\min(s(L[y],t),s(L[k],t))\right]+H[L[y],t],\qquad(6.5)$$

where $s(L[\cdot], t)$ indicates the state of a layer at time t, while y and k represent a neocortex layer and a unit firing from a pattern of an ultrasound transmission, and

$$H[n, t] = \begin{cases} 0, & \text{if } E[n, t] < E_{max}, \\ 1, & \text{if } E[n, t] = E_{max}, \end{cases} \tag{6.6}$$

which represents whether the stored energy $E[n, t]$ is sufficient to turn on the LED at time t, by comparing it to the required energy E_{max}.

The three other metrics of the neural spike misfiring ratio ($\gamma_{mis}(L[y])$), stimulation efficiency ratio ($\eta_{stim}(L[y])$), and stimulation ratio ($\gamma_{stim}(L[y])$), which directly represent the effectiveness of the protocol are written as

$$\gamma_{mis}(L[y]) = \frac{n_{mis}}{\sum_{t=0}^{T} s[L[y], t]}, \tag{6.7}$$

$$\eta_{stim}(L[y]) = 100\% - \gamma_{mis}(L[y]), \tag{6.8}$$

$$\gamma_{stim}(L[y]) = \frac{\sum_{t=0}^{T} |Tx_{sub}[f_n, t]|}{\sum_{t=0}^{T} s[L[y], t]}, \tag{6.9}$$

where $\sum_{t=0}^{T} |Tx_{sub}[f_n, t]|$ is the total number of frequency transmission during the period of T.

Particularly for the predictive sliding detection window protocol, increasing the number of ultrasound frequencies, which corresponds to available firing patterns, does not show significant improvement in the stimulation ratio. However, it ensures that each stimulation is more efficient by precisely addressing the desired neuron firings. The results of the simulations are shown in Figure 6.9.

To compare both protocols, two neural firing frequencies were simulated. For both cases, the predictive sliding detection window outperformed the charge and fire protocol. In the charge and fire protocol, the sub-dura transceiver transmitted more charging signals, but it did not necessarily lower the misfiring amount. On the other hand, the predictive sliding detection window protocol showed a reasonable increment for both the misfiring ratio and charging signal transmission when the firing frequency increased due to certain activity. The simulation results are depicted in Figures 6.10(c) and 6.10(d).
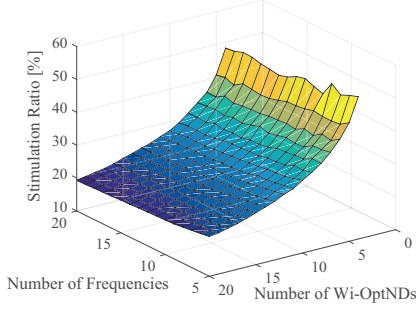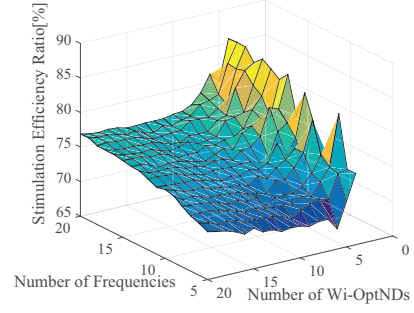
Figure 6.9 The stimulation ($\gamma_{stim}(L[y])$) and efficiency ($\eta_{stim}(L[y])$) ratios for Predictive Sliding De-
tection Window as a function of radiated ultrasound frequency quantity and the number of
WiOptNDs. [II]

Defining an optimum charging protocol was necessary to minimise the ultra-
sound transmission and to obtain certain precision in addressing the neural firing
pattern. Besides the WiOptND implementation, this charging protocol also offers
an energy efficiency solution for the operation of any BMI device.
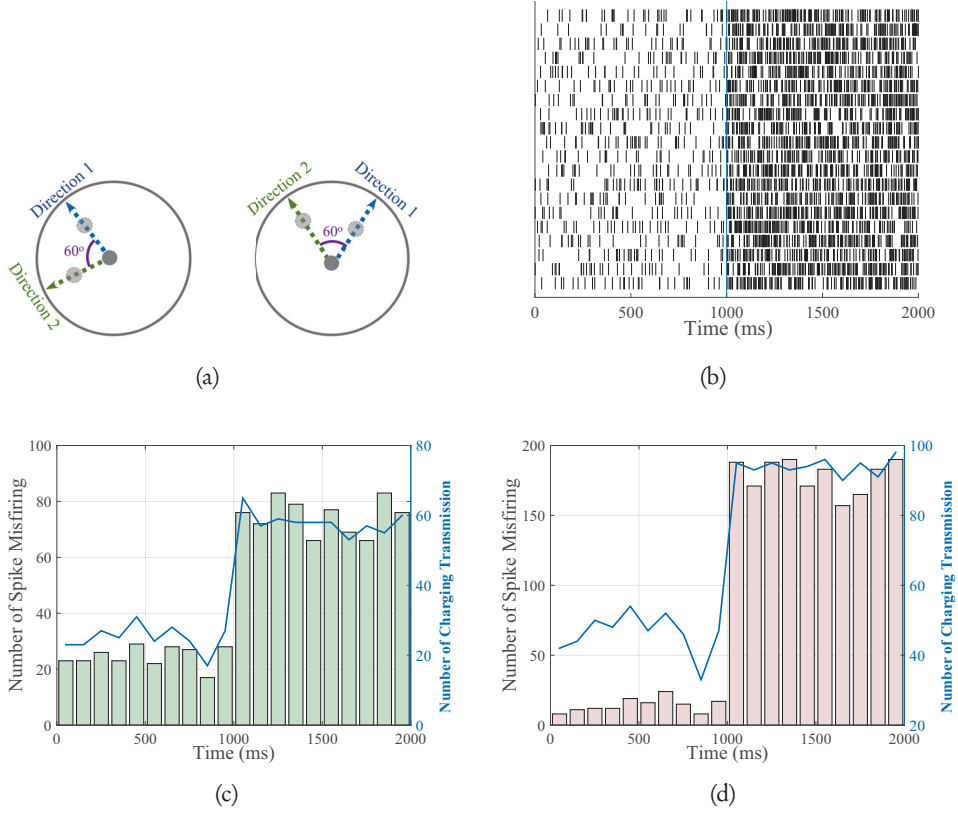
Figure 6.10 (a) The illustration of bi-directional stimuli separated by 60° for an achromatic random-dots pattern that is visually observed by a *macaque monkey*. (b) The raster plot simulation generated based on the experiment. As shown in the raster plot, both directions affect the neuron spike frequency response [102]. (c) and (d) present the simulation results from the number of misfirings before and after the frequency transition for both the Predictive Sliding Detection Window and the Charge and Fire protocols. [II]

7   CONCLUSIONS AND DISCUSSION

7.1 Conclusions

In this thesis, we focused on defining the system for wireless BMI that concentrates on optogenetic stimulation. As presented in [I], we showed that it is feasible to design a small fully implantable brain implant for a long-term period using existing technology. This implant, which is called the WiOptND, utilises a combination of optical (light) and acoustic (ultrasound) waves for stimulation and energy harvesting. The prominent features of this device are its miniaturised, wireless and batteryless solutions, which we compared to the device for a similar purpose reviewed in [III]. Each component of the device is elaborated on with technical details to some extent in [I]. In addition, we analysed how the acoustic and light propagations define the device requirements and limitations in [I] and [II]. According to the acoustic propagation numerical analysis, the FDA ultrasound safety limit of 720 mW/cm² provides sufficient energy of approximately 60 mW to power the device, which is 100×100 μm². In a further calculation, this amount of power can generate the light intensity required to stimulate ChR2. Furthermore, we investigated in depth the light interaction with neuron and brain tissue in [IV]–[VI]. The interesting phenomena of geometrical (focusing) gain and medium loss dictate the received signal power. From the numerical analysis of three different neuron shapes, the transmitted light wave is attenuated the least when it traverses an array of multiple spherical neurons (approximately 20% of the transmitted power). In [VI], we characterised the channel impulse response of the neural tissue and presented an algorithm for the recursive numerical ray tracing analysis for point-to-point light propagation. Finally, to integrate the spatially distributed stimulation feature, we proposed a system charging protocol that offers synchronous firing pattern stimulation. The implementation requires the integration of VOX and time delay relay components into the device circuitry. Furthermore, we employed a prediction algorithm for firing decision. Ac-

cording to this algorithm, the firing decision is based on a mathematical model by processing the stimuli intensity.

7.2 Discussion

Optogenetic treatment in humans is very promising, since an in vitro experiment for human-derived cells and a clinical trial have been performed [83] [4]. The technique that can be applied to humans involves gene therapies utilising the *adeno-associated virus* (AAV) vector. This has been successfully performed without exhibiting long-term toxicity in humans [72]. In [44] [46], treatment for heart failure is implemented using this particular technique. However, this treatment stimulates an immunological reaction against the injected virus, which reduces the efficiency of the treatment. Thus, the reaction should be suppressed to maximise the treatment effect. In the research field, the in vitro optogenetic application in human neuromuscular disease and retinitis pigmentosa (RP) shows promising results by utilising ChR2 and NpHR optogenetics [14] [87]. Thus, both the research and implementation of optogenetics will significantly advance in the near future.

Regarding the hardware improvement, the research on biocompatible and micro scale components is facilitating the implant miniaturisation even further, for example μ-LEDs [15] [103], micro-super capacitors [92] [36], and piezoelectric nanowires [47]. With this, a higher level of spatial resolution can be achieved by the BMI.

In this thesis, both the WiOptND concept and supporting scientific analysis contribute to the advancement of future BMI design. Future improvements can include considerations of both the advantages and disadvantages of the light propagation behaviour elaborated on in this thesis. The proposed concept still concentrates on implant internal network system communication, but in the future, this will be a part of the bigger network of IoBNT and IoT. At this point, the interoperability of this heterogenous network should be carefully considered, including integrated system security.

REFERENCES

[1] Z. Ahmed, J. Reddy, K. Deshpande, A. Krishnan, P. Venkatesh, S. Kelly, P. Grover and M. Chamanzar. Flexible Ultra-resolution Subdermal EEG Probes. *2018 IEEE Biomedical Circuits and Systems Conference (BioCAS)*. IEEE. 2018, 1–4.

[2] I. F. Akyildiz, M. Pierobon, S. Balasubramaniam and Y. Koucheryavy. The internet of bio-nano things. *IEEE Communications Magazine* 53.3 (2015), 32–40.

[3] M. Al Ameen, J. Liu and K. Kwak. Security and privacy issues in wireless sensor networks for healthcare applications. *Journal of Medical Systems* 36.1 (2012), 93–101.

[4] M. Andersson, N. Avaliani, A. Svensson, J. Wickham, L. H. Pinborg, B. Jespersen, S. H. Christiansen, J. Bengzon, D. P. Woldbye and M. Kokaia. Optogenetic control of human neurons in organotypic brain cultures. *Scientific Reports* 6 (2016), 24818.

[5] L. Atzori, A. Iera and G. Morabito. The internet of things: A survey. *Computer Networks* 54.15 (2010), 2787–2805.

[6] W. B. Baker, A. B. Parthasarathy, D. R. Busch, R. C. Mesquita, J. H. Greenberg and A. Yodh. Modified Beer-Lambert law for blood flow. *Biomedical Optics Express* 5.11 (2014), 4053–4075.

[7] S. Balasubramaniam and J. Kangasharju. Realizing the internet of nano things: challenges, solutions, and applications. *Computer* 46.2 (2012), 62–68.

[8] S. Balasubramaniam, S. A. Wirdatmadja, M. T. Barros, Y. Koucheryavy, M. Stachowiak and J. M. Jornet. Wireless communications for optogenetics-based brain stimulation: Present technology and future challenges. *IEEE Communications Magazine* 56.7 (2018), 218–224. DOI: 10.1109/MCOM.2018.1700917.

[9]   M. Beidaghi and C. Wang. Micro-supercapacitors based on interdigital electrodes of reduced graphene oxide and carbon nanotube composites with ultrahigh power handling performance. *Advanced Functional Materials* 22.21 (2012), 4501–4510.

[10]   N. Bosschaart, G. J. Edelman, M. C. Aalders, T. G. van Leeuwen and D. J. Faber. A literature review and novel theoretical approach on the optical properties of whole blood. *Lasers in Medical Science* 29.2 (2014), 453–479.

[11]   E. S. Boyden. Optogenetics and the future of neuroscience. *Nature Neuroscience* 18.9 (2015), 1200.

[12]   E. S. Boyden, F. Zhang, E. Bamberg, G. Nagel and K. Deisseroth. Millisecond-timescale, genetically targeted optical control of neural activity. *Nature Neuroscience* 8.9 (2005), 1263–1268.

[13]   N. Bulusu, D. Estrin, L. Girod and J. Heidemann. Scalable coordination for wireless sensor networks: self-configuring localization systems. *International Symposium on Communication Theory and Applications (ISCTA 2001), Ambleside, UK*. 2001.

[14]   V. Busskamp, S. Picaud, J.-A. Sahel and B. Roska. Optogenetic therapy for retinitis pigmentosa. *Gene Therapy* 19.2 (2012), 169.

[15]   J. Carreira, E. Xie, R. Bian, C. Chen, J. McKendry, B. Guilhabert, H. Haas, E. Gu and M. Dawson. On-chip GaN-based dual-color micro-LED arrays and their application in visible light communication. *Optics Express* 27.20 (2019), A1517–A1528.

[16]   W. Choi, C. Fang-Yen, K. Badizadegan, S. Oh, N. Lue, R. R. Dasari and M. S. Feld. Tomographic phase microscopy. *Nature Methods* 4.9 (2007), 717.

[17]   B. Y. Chow, X. Han, A. S. Dobry, X. Qian, A. S. Chuong, M. Li, M. A. Henninger, G. M. Belfort, Y. Lin, P. E. Monahan et al. High-performance genetically targetable optical neural silencing by light-driven proton pumps. *Nature* 463.7277 (2010), 98–102.

[18]   D. E. Clapham. Calcium signaling. *Cell* 131.6 (2007), 1047–1058.

[19]   E. De Leo, L. Donvito, L. Galluccio, A. Lombardo, G. Morabito and L. M. Zanoli. Communications and switching in microfluidic systems: Pure hydrodynamic control for networking labs-on-a-chip. *IEEE Transactions on Communications* 61.11 (2013), 4663–4677.

[20]   K. Deisseroth. Optogenetics. *Nature Methods* 8.1 (2011), 26.

[21]   D. T. Delpy, M. Cope, P. van der Zee, S. Arridge, S. Wray and J. Wyatt. Estimation of optical pathlength through tissue from direct time of flight measurement. *Physics in Medicine & Biology* 33.12 (1988), 1433.

[22]   H. Deng, W. Li and D. P. Agrawal. Routing security in wireless ad hoc networks. *IEEE Communications Magazine* 40.10 (2002), 70–75.

[23]   D. V. Dimitrov. Medical internet of things and big data in healthcare. *Healthcare Informatics Research* 22.3 (2016), 156–163.

[24]   *Direct Attach DA2432^{TM} LEDs*. CPR3FM. Rev A. Cree Inc. 2013.

[25]   F. Dressler and S. Fischer. Connecting in-body nano communication with body area networks: Challenges and opportunities of the Internet of Nano Things. *Nano Communication Networks* 6.2 (2015), 29–38.

[26]   A. Duncan, J. H. Meek, M. Clemence, C. E. Elwell, L. Tyszczuk, M. Cope and D. Delpy. Optical pathlength measurements on adult head, calf and forearm and the head of the newborn infant using phase resolved optical spectroscopy. *Physics in Medicine & Biology* 40.2 (1995), 295.

[27]   D. Estrin, L. Girod, G. Pottie and M. Srivastava. Instrumenting the world with wireless sensor networks. *icassp*. Vol. 1. Citeseer. 2001, 2033–2036.

[28]   X. Fan, W. Zheng and D. J. Singh. Light scattering and surface plasmons on small spherical particles. *Light: Science & Applications* 3.6 (2014), e179.

[29]   C. Fang-Yen and M. S. Feld. Intrinsic optical signals in neural tissues: Measurements, mechanisms, and applications. *ACS Sym. Ser* 963 (2007), 219–235.

[30]   L. Fenno, O. Yizhar and K. Deisseroth. The development and application of optogenetics. *Annual Review of Neuroscience* 34 (2011).

[31]   G. Gagnon-Turcotte, Y. LeChasseur, C. Bories, Y. Messaddeq, Y. De Koninck and B. Gosselin. A wireless headstage for combined optogenetics and multi-channel electrophysiological recording. *IEEE Transactions on Biomedical Circuits and Systems* (2016).

[32] F. Gilbert, A. R. Harris and R. M. Kapsa. Controlling brain cells with light: ethical considerations for optogenetic clinical trials. *AJOB Neuroscience* 5.3 (2014), 3–11.

[33] L. P. Giné and I. F. Akyildiz. Molecular communication options for long range nanonetworks. *Computer Networks* 53.16 (2009), 2753–2766.

[34] C. Godec, A. Cass and G. Ayala. Bladder inhibition with functional electrical stimulation. *Urology* 6.6 (1975), 663–666.

[35] P. M. Groves and G. V. Rebec. *Introduction to biological psychology*. McGraw-Hill Humanities, Social Sciences & World Languages, 1988.

[36] F. Guan, S. Chen, N. Sheng, Y. Chen, J. Yao, Q. Pei and H. Wang. Mechanically robust reduced graphene oxide/bacterial cellulose film obtained via biosynthesis for flexible supercapacitor. *Chemical Engineering Journal* 360 (2019), 829–837.

[37] J. Gubbi, R. Buyya, S. Marusic and M. Palaniswami. Internet of Things (IoT): A vision, architectural elements, and future directions. *Future Generation Computer Systems* 29.7 (2013), 1645–1660.

[38] M. Haghi, K. Thurow and R. Stoll. Wearable devices in medical internet of things: scientific research and commercially available devices. *Healthcare Informatics Research* 23.1 (2017), 4–15.

[39] X. Han. In vivo application of optogenetics for neural circuit analysis. *ACS Chemical Neuroscience* 3.8 (2012), 577–584.

[40] X. Han and E. S. Boyden. Multiple-color optical activation, silencing, and desynchronization of neural activity, with single-spike temporal resolution. *PloS One* 2.3 (2007), e299.

[41] M. Hashimoto, A. Hata, T. Miyata and H. Hirase. Programmable wireless light-emitting diode stimulator for chronic stimulation of optogenetic molecules in freely moving mice. *Neurophotonics* 1.1 (2014), 011002–011002.

[42] M. Hiraoka, M. Firbank, M. Essenpreis, M. Cope, S. Arridge, P. Van Der Zee and D. Delpy. A Monte Carlo investigation of optical pathlength in inhomogeneous tissue and its application to near-infrared spectroscopy. *Physics in Medicine & Biology* 38.12 (1993), 1859.

[43]   P. R. Hoskins, K. Martin and A. Thrush. *Diagnostic ultrasound: physics and equipment*. Cambridge University Press, 2010.

[44]   B. E. Jaski, M. L. Jessup, D. M. Mancini, T. P. Cappola, D. F. Pauly, B. Greenberg, K. Borow, H. Dittrich, K. M. Zsebo, R. J. Hajjar et al. Calcium upregulation by percutaneous administration of gene therapy in cardiac disease (CUPID Trial), a first-in-human phase 1/2 clinical trial. *Journal of Cardiac Failure* 15.3 (2009), 171–181.

[45]   J.-W. Jeong, J. G. McCall, G. Shin, Y. Zhang, R. Al-Hasani, M. Kim, S. Li, J. Y. Sim, K.-I. Jang, Y. Shi et al. Wireless optofluidic systems for programmable in vivo pharmacology and optogenetics. *Cell* 162.3 (2015), 662–674.

[46]   M. Jessup, B. Greenberg, D. Mancini, T. Cappola, D. F. Pauly, B. Jaski, A. Yaroshinsky, K. M. Zsebo, H. Dittrich and R. J. Hajjar. Calcium upregulation by percutaneous administration of gene therapy in cardiac disease (CUPID) a phase 2 trial of intracoronary gene therapy of sarcoplasmic reticulum Ca2+-ATPase in patients with advanced heart failure. *Circulation* 124.3 (2011), 304–313.

[47]   L. Jiang, Y. Yang, R. Chen, G. Lu, R. Li, D. Li, M. S. Humayun, K. K. Shung, J. Zhu, Y. Chen et al. Flexible piezoelectric ultrasonic energy harvester array for bio-implantable wireless generator. *Nano Energy* 56 (2019), 216–224.

[48]   P. Johari and J. M. Jornet. Nanoscale optical wireless channel model for intrabody communications: Geometrical, time, and frequency domain analyses. *IEEE Transactions on Communications* 66.4 (2017), 1579–1593.

[49]   J. M. Jornet and I. F. Akyildiz. Joint energy harvesting and communication analysis for perpetual wireless nanosensor networks in the terahertz band. *IEEE Transactions on Nanotechnology* 11.3 (2012), 570–580.

[50]   J. Keat, P. Reinagel, R. C. Reid and M. Meister. Predicting every spike: a model for the responses of visual neurons. *Neuron* 30.3 (2001), 803–817.

[51]   H. Kern, S. Boncompagni, K. Rossini, W. Mayr, G. Fanò, M. E. Zanin, M. Podhorska-Okolow, F. Protasi and U. Carraro. Long-term denervation in humans causes degeneration of both contractile and excitation-contraction coupling apparatus, which is reversible by functional electrical stimulation (FES): a role for myofiber regeneration?: *Journal of Neuropathology & Experimental Neurology* 63.9 (2004), 919–931.

[52]   T. Khan, B. A. Bilgin and O. B. Akan. Diffusion-based Model for Synaptic Molecular Communication Channel. *IEEE Transactions on NanoBioscience* (2017).

[53]   T.-i. Kim, J. G. McCall, Y. H. Jung, X. Huang, E. R. Siuda, Y. Li, J. Song, Y. M. Song, H. A. Pao, R.-H. Kim et al. Injectable, cellular-scale optoelectronics with applications for wireless optogenetics. *Science* 340.6129 (2013), 211–216.

[54]   A. D. Klose and E. W. Larsen. Light transport in biological tissue based on the simplified spherical harmonics equations. *Journal of Computational Physics* 220.1 (2006), 441–470.

[55]   M. Kohl, C. Nolte, H. R. Heekeren, S. Horst, U. Scholz, H. Obrig and A. Villringer. Determination of the wavelength dependence of the differential pathlength factor from near-infrared pulse signals. *Physics in Medicine & Biology* 43.6 (1998), 1771.

[56]   T. D. Kozai, A. S. Jaquins-Gerstl, A. L. Vazquez, A. C. Michael and X. T. Cui. Brain tissue responses to neural implants impact signal sensitivity and intervention strategies. *ACS Chemical Neuroscience* 6.1 (2015), 48–67.

[57]   S. Kumar, K. Boone, J. Tuszyński, P. Barclay and C. Simon. Possible existence of optical communication channels in the brain. *Scientific Reports* 6 (2016), 36508.

[58]   M. Kuscu and O. B. Akan. Maximum likelihood detection with ligand receptors for diffusion-based molecular communications in internet of bio-nano things. *IEEE Transactions on Nanobioscience* 17.1 (2018), 44–54.

[59]   S. B. Laughlin and T. J. Sejnowski. Communication in neuronal networks. *Science* 301.5641 (2003), 1870–1874.

[60]   M. A. Lebedev and M. A. Nicolelis. Brain–machine interfaces: past, present and future. *TRENDS in Neurosciences* 29.9 (2006), 536–546.

[61]   W. C. Lee. *Mobile communications engineering*. McGraw-Hill Professional, 1982.

[62]   A. Levinson and A. Serby. THE REFRACTOMETRIC AND VISCOSIMETRIC INDEXES OF CEREBROSPINAL FLUID. *Archives of Internal Medicine* 37.1 (1926), 144–150.

[63] I. B. Levitan and L. K. Kaczmarek. *The neuron: cell and molecular biology*. Oxford University Press, USA, 2015.

[64] Y.-D. Lin and Y.-C. Hsu. Multihop cellular: A new architecture for wireless communications. *Proceedings IEEE INFOCOM 2000. Conference on Computer Communications. Nineteenth Annual Joint Conference of the IEEE Computer and Communications Societies (Cat. No. 00CH37064)*. Vol. 3. IEEE. 2000, 1273–1282.

[65] C. L. Lynch and M. R. Popovic. Functional electrical stimulation. *IEEE Control Systems Magazine* 28.2 (2008), 40–50.

[66] D. Malak and O. B. Akan. A communication theoretical analysis of synaptic multiple-access channel in hippocampal-cortical neurons. *IEEE Transactions on Communications* 61.6 (2013), 2457–2467.

[67] K. L. Montgomery, A. J. Yeh, J. S. Ho, V. Tsao, S. M. Iyer, L. Grosenick, E. A. Ferenczi, Y. Tanabe, K. Deisseroth, S. L. Delp et al. Wirelessly powered, fully internal optogenetics for brain, spinal and peripheral circuits in mice. *Nature Methods* (2015).

[68] G. Nagel, T. Szellas, W. Huhn, S. Kateriya, N. Adeishvili, P. Berthold, D. Ollig, P. Hegemann and E. Bamberg. Channelrhodopsin-2, a directly light-gated cation-selective membrane channel. *Proceedings of the National Academy of Sciences* 100.24 (2003), 13940–13945.

[69] T. Nakano, A. W. Eckford and T. Haraguchi. *Molecular communication*. Cambridge University Press, 2013.

[70] T. Nakano, T. Suda, M. Moore, R. Egashira, A. Enomoto and K. Arima. Molecular communication for nanomachines using intercellular calcium signaling. *5th IEEE Conference on Nanotechnology, 2005*. IEEE. 2005, 478–481.

[71] N. Nakasato, M. F. Levesque, D. S. Barth, C. Baumgartner, R. L. Rogers and W. W. Sutherling. Comparisons of MEG, EEG, and ECoG source localization in neocortical partial epilepsy in humans. *Electroencephalography and Clinical Neurophysiology* 91.3 (1994), 171–178.

[72]   A. C. Nathwani, E. G. Tuddenham, S. Rangarajan, C. Rosales, J. McIntosh, D. C. Linch, P. Chowdary, A. Riddell, A. J. Pie, C. Harrington et al. Adenovirus-associated virus vector–mediated gene transfer in hemophilia B. *New England Journal of Medicine* 365.25 (2011), 2357–2365.

[73]   E. Oakley, B. Wrazen, D. A. Bellnier, Y. Syed, H. Arshad and G. Shafirstein. A new finite element approach for near real-time simulation of light propagation in locally advanced head and neck tumors. *Lasers in Surgery and Medicine* 47.1 (2015), 60–67.

[74]   P. P. Parikh, M. G. Kanabar and T. S. Sidhu. Opportunities and challenges of wireless communication technologies for smart grid applications. *IEEE PES General Meeting*. IEEE. 2010, 1–7.

[75]   S. I. Park, D. S. Brenner, G. Shin, C. D. Morgan, B. A. Copits, H. U. Chung, M. Y. Pullen, K. N. Noh, S. Davidson, S. J. Oh et al. Soft, stretchable, fully implantable miniaturized optoelectronic systems for wireless optogenetics. *Nature Biotechnology* 33.12 (2015), 1280–1286.

[76]   R. Passingham. How good is the macaque monkey model of the human brain?: *Current Opinion in Neurobiology* 19.1 (2009), 6–11.

[77]   A. Perrig, J. Stankovic and D. Wagner. Security in wireless sensor networks. (2004).

[78]   M. Polanco, H. Yoon and S. Bawab. Micromotion-induced dynamic effects from a neural probe and brain tissue interface. *Journal of Micro/Nanolithography, MEMS, and MOEMS* 13.2 (2014), 023009.

[79]   D. Prodanov and J. Delbeke. Mechanical and biological interactions of implants with the brain and their impact on implant design. *Frontiers in Neuroscience* 10 (2016), 11.

[80]   T. S. Rappaport et al. *Wireless communications: principles and practice*. Vol. 2. prentice hall PTR New Jersey, 1996.

[81]   S. P. Rodrıguez, R. P. Jiménez, B. R. Mendoza, F. J. L. Hernández and A. J. A. Alfonso. Simulation of impulse response for indoor visible light communications using 3D CAD models. *EURASIP Journal on Wireless Communications and Networking* 2013.1 (2013), 7.

[82]   M. A. Rossi, V. Go, T. Murphy, Q. Fu, J. Morizio and H. H. Yin. A wirelessly controlled implantable LED system for deep brain optogenetic stimulation. *Frontiers in Integrative Neuroscience* 9 (2015).

[83]   F. Schmieder, S. Klapper, N. Koukourakis, V. Busskamp and J. Czarske. Optogenetic Stimulation of Human Neural Networks Using Fast Ferroelectric Spatial Light Modulator—Based Holographic Illumination. *Applied Sciences* 8.7 (2018), 1180.

[84]   F. Scholkmann and M. Wolf. General equation for the differential pathlength factor of the frontal human head depending on wavelength and age. *Journal of Biomedical Optics* 18.10 (2013), 105004.

[85]   D. Seo, J. M. Carmena, J. M. Rabaey, E. Alon and M. M. Maharbiz. Neural dust: An ultrasonic, low power solution for chronic brain-machine interfaces. *arXiv preprint arXiv:1307.2196* (2013).

[86]   G. Shin, A. M. Gomez, R. Al-Hasani, Y. R. Jeong, J. Kim, Z. Xie, A. Banks, S. M. Lee, S. Y. Han, C. J. Yoo et al. Flexible Near-Field Wireless Optoelectronics as Subdermal Implants for Broad Applications in Optogenetics. *Neuron* 93.3 (2017), 509–521.

[87]   E. E. Steinberg, R. Keiflin, J. R. Boivin, I. B. Witten, K. Deisseroth and P. H. Janak. A causal link between prediction errors, dopamine neurons and learning. *Nature Neuroscience* 16.7 (2013), 966.

[88]   V. Tarokh, N. Seshadri and A. R. Calderbank. Space-time codes for high data rate wireless communication: Performance criterion and code construction. *IEEE Transactions on Information Theory* 44.2 (1998), 744–765.

[89]   V. V. Tuchin. Tissue optics and photonics: biological tissue structures. *Journal of Biomedical Photonics & Engineering* 1.1 (2015).

[90]   C. Von Economo. *Cellular structure of the human cerebral cortex*. Karger Medical and Scientific Publishers, 2009.

[91]   H. J. Wang, R. H. Katz and J. Giese. Policy-enabled handoffs across heterogeneous wireless networks. *Proceedings WMCSA'99. Second IEEE Workshop on Mobile Computing Systems and Applications*. IEEE. 1999, 51–60.

[92]   S. Wang, Z.-S. Wu, F. Zhou, X. Shi, S. Zheng, J. Qin, H. Xiao, C. Sun and X. Bao. All-solid-state high-energy planar hybrid micro-supercapacitors based on 2D VN nanosheets and $Co(OH)_2$ nanoflowers. *npj 2D Materials and Applications* 2.1 (2018), 7.

[93]   Z. Wang, S. Ha and K. Kim. Evaluation of finite-element-based simulation model of photoacoustics in biological tissues. *Medical Imaging 2012: Ultrasonic Imaging, Tomography, and Therapy*. Vol. 8320. International Society for Optics and Photonics. 2012, 83201L.

[94]   S. Warren, J. Lebak, J. Yao, J. Creekmore, A. Milenkovic and E. Jovanov. Interoperability and security in wireless body area network infrastructures. *2005 IEEE Engineering in Medicine and Biology 27th Annual Conference*. IEEE. 2006, 3837–3840.

[95]   K. K. Watson and M. L. Platt. Of mice and monkeys: using non-human primate models to bridge mouse-and human-based investigations of autism spectrum disorders. *Journal of Neurodevelopmental Disorders* 4.1 (2012), 21.

[96]   S. A. Wirdatmadja, S. Balasubramaniam, Y. Koucheryavy and J. M. Jornet. Wireless optogenetic neural dust for deep brain stimulation. *2016 IEEE 18th International Conference on e-Health Networking, Applications and Services (Healthcom)*. IEEE. 2016, 1–6. DOI: `10.1109/HealthCom.2016.7749532`.

[97]   S. A. Wirdatmadja, M. T. Barros, Y. Koucheryavy, J. M. Jornet and S. Balasubramaniam. Wireless optogenetic nanonetworks for brain stimulation: Device model and charging protocols. *IEEE Transactions on Nanobioscience* 16.8 (2017), 859–872. DOI: `10.1109/TNB.2017.2781150`.

[98]   S. Wirdatmadja, P. Johari, S. Balasubramaniam, Y. Bae, M. K. Stachowiak and J. M. Jornet. Light propagation analysis in nervous tissue for wireless optogenetic nanonetworks. *Optogenetics and Optical Manipulation 2018*. Vol. 10482. International Society for Optics and Photonics. 2018, 104820R. DOI: `10.1117/12.2288786`.

[99]   S. Wirdatmadja, P. Johari, A. Desai, Y. Bae, E. K. Stachowiak, M. K. Stachowiak, J. M. Jornet and S. Balasubramaniam. Analysis of Light Propagation on Physiological Properties of Neurons for Nanoscale Optogenetics. *IEEE Transactions on Neural Systems and Rehabilitation Engineering* 27.2 (2019), 108–117. DOI: `10.1109/TNSRE.2019.2891271`.

[100] S. Wirdatmadja, J. M. Jornet, Y. Koucheryavy and S. Balasubramaniam. Channel Impulse Analysis of Light Propagation for Point-to-point Nano Communications through Cortical Neurons. *IEEE Transactions on Communications* (2019). Accepted for publication. DOI: 10.1109/TCOMM.2020.3012477.

[101] J. Xia and G. Yao. Angular distribution of diffuse reflectance in biological tissue. *Applied Optics* 46.26 (2007), 6552–6560.

[102] J. Xiao and X. Huang. Distributed and dynamic neural encoding of multiple motion directions of transparently moving stimuli in cortical area MT. *Journal of Neuroscience* 35.49 (2015), 16180–16198.

[103] H. Xu, L. Yin, C. Liu, X. Sheng and N. Zhao. Recent advances in biointegrated optoelectronic devices. *Advanced Materials* 30.33 (2018), 1800156.

[104] A. Yaroslavsky, P. Schulze, I. Yaroslavsky, R. Schober, F. Ulrich and H. Schwarzmaier. Optical properties of selected native and coagulated human brain tissues in vitro in the visible and near infrared spectral range. *Physics in Medicine and Biology* 47.12 (2002), 2059.

[105] O. Yizhar, L. E. Fenno, T. J. Davidson, M. Mogri and K. Deisseroth. Optogenetics in neural systems. *Neuron* 71.1 (2011), 9–34.

[106] S. Zhou, M. Zhao, X. Xu, J. Wang and Y. Yao. Distributed wireless communication system: a new architecture for future public wireless access. *IEEE Communications Magazine* 41.3 (2003), 108–113.

A   APPENDIX

A.1 Ray tracing algorithm for fusiform neuron

This algorithm requires input data, namely the optical properties of the medium (n_c, n_t), physical properties of the neuron (r_c, d_c), and coordinates/direction of the incoming ray (x_2, h_2, θ_i). It calculates the angle and coordinates of the focus point $(foc(\theta_F, x_F))$ and the propagation direction and coordinates inside the neuron $(l_i(x'_3, h_3), l_o(x_4, h_4), \theta_i^{(2)})$. This algorithm is executed iteratively depending on the number of neurons along the path.

Algorithm 2 Ray tracing for fusiform cell

Require:
    n_c, n_t (refractive indices of neuron and tissue)
    r_c (the radius of the neuron)
    x_2 (the x ray coordinate of the previous cell)
    h_2 (the radius of incoming illumination)
    d_c (the distance between cells)
    θ_i (the angle of the incoming ray)

Ensure:
    $foc(\theta_F, x_F)$ (the distance and angle of focus point)
    $l_i(x'_3, h_3)$ (the coordinate of the incoming ray)
    $l_o(x_4, h_4)$ (the coordinate of the outgoing ray)
    $\theta_i^{(2)}$ (the ray propagation angle in the cell)

1: CALCULATE(x'_2)   ▷ $x'_2 = x_2$ measured from the 1st surface,

$$x'_2 = (d_c + 2r_c) - x_2$$

2: CALCULATE(x_3, h_3) ▷ $x_3, h_3 =$ the coordinate where the ray hits the 1st surface,

$$m_2 = tan(180^o - \theta_i)$$

$$h_3 = \begin{bmatrix} m_2^2 + 1 \\ 2m_2(h_2 + m_2 x_2') \\ (h_2 + m_2 x_2')^2 - r_c^2 \end{bmatrix}^T \begin{bmatrix} x_3^2 \\ x_3 \\ 1 \end{bmatrix}$$

3: CALCULATE$(\theta_i^{(1)})$ ▷ the incoming angle with respect to normal line of the 1nd surface

$$\theta_i'^{(1)} = arctan\left(\frac{h_3}{|x_3|}\right) - \theta_i^{(1)}$$

4: CALCULATE$(\theta_o^{(1)})$ ▷ the refracted angle due to 1st surface

$$\theta_o^{(1)} = arcsin\left(\frac{n_t sin(\theta_i'^{(1)})}{n_c}\right)$$

5: CALCULATE$(x_3, \theta_o^{(1)})$ ▷ with respect to 2nd surface

$$x_3' = 2r_c - (d_c + |x_3|)$$

$$\theta_i^{(2)} = \theta_i^{(1)} + (\theta_i''1) + \theta_o^{(1)})$$

6: CALCULATE(x_4, h_4) ▷ the coordinate where the ray hits the 2nd surface

$$m_3 = tan(-\theta_i^{(2)})$$

$$h_4 = \begin{bmatrix} m_3^2 + 1 \\ 2m_3(h_3 + m_3 x_3') \\ (h_3 + m_3 x_3')^2 - r_c^2 \end{bmatrix}^T \begin{bmatrix} x_4^2 \\ x_4 \\ 1 \end{bmatrix}$$

7: CALCULATE$(\theta_o^{(2)})$ ▷ the refracted angle due to 2nd surface

$$\theta_o^{(2)} = arcsin\left(\frac{n_c}{n_t} sin\left(arctan\left(\frac{h_4}{x_4}\right) + \theta_i^{(2)}\right)\right)$$

8: CALCULATE(x_F)   ▷ the focus distance

$$\theta_F = \theta_o^{(2)} - arctan\left(\frac{h_4}{x_4}\right)$$

$$m_4 = tan(\theta_F)$$

$$x_F = \frac{m_4 x_4 - h_4}{m_4}$$

PUBLICATIONS

PUBLICATION

I

Wireless optogenetic neural dust for deep brain stimulation

S. A. Wirdatmadja, S. Balasubramaniam, Y. Koucheryavy and J. M. Jornet

Wireless Optogenetic Neural Dust for Deep Brain Stimulation

Stefanus A. Wirdatmadja*, Sasitharan Balasubramaniam*, Yevgeni Koucheryavy*, Josep Miquel Jornet†

*Department of Electrical Engineering and Communications
Tampere University of Technology, Finland
Email: (stefanus.wirdatmadja, sasi.bala, yk)@tut.fi
†Department of Electrical Engineering
University at Buffalo, The State University of New York
Buffalo, NY, 14260
Email: jmjornet@buffalo.edu

Abstract—In recent years, numerous research efforts have been dedicated towards developing efficient implantable devices for Deep Brain Stimulation (DBS). However, there are limitations and challenges with the current technologies. Firstly, the stimulation of neurons currently is only possible through implantable electrodes which target a population of neurons. This results in challenges in the event that stimulation at the single neuron level is required. Secondly, a major hurdle still lies in developing miniature devices that can last for a lifetime in the patient's brain. Recently, the concept of neural dust has been introduced as a way to achieve single neuron monitoring and potentially actuation. In parallel to this, the field of optogenetics has emerged where the aim is to stimulate neurons using light, usually by means of optical fibers inserted through the skull. Obviously, this introduces many challenges in terms of user friendliness and biocompatibility. We address this shortcoming by proposing the wireless optogenetic neural dust (*wi-opt neural dust*). The wi-opt neural dust is equipped with a miniature LED that is able to stimulate the genetically engineered neurons, and at the same time harvest energy from ultrasonic vibrations. The simulation results presented in the paper investigates the behaviour of the light propagation in the brain tissue, as well as the performance of designed circuitry for the energy harvesting process. The results demonstrates the feasibility of utilizing wi-opt neural dust for long term implantation in the brain, and a new direction towards precise stimulation of neurons in the cortex.

I. INTRODUCTION

In recent years numerous neurological disorders have led researchers to seek new solutions to improve monitoring as well as treatment techniques. For example, solutions have been developed for electrodes to be placed into the brain and upon stimulation will lead to minimisation of trembling due to parkinson disease. In another work, known as *optogenetics*, optical light is used to stimulate genetically engineered neurons that are sensitive to light at a particular wavelength [1]. The use of optogenetics can lead to precise single neuron stimulation. However, a major drawback with the current techniques is the fact that the technologies require insertion of electrodes or optical cables into the skull. While it does solve the problems, and opens up innovation, the proposed techniques are not practical for everyday use by the patients.

In this paper, we propose the *wireless optogenetics neural dust*, which we refer to as *wi-opt neural dust*. The wi-opt

neural dust advances the neural dust proposed by [2], which is only limited to monitoring the neurons and reporting back to the *sub-dura transceiver* through back scattering. The benefits of integrating the wireless optogenetic component to the neural dust is to enable single neuron stimulation, while envisioning long term implantation of the device. However, there are a number of challenges in realising a fully operational wi-opt neural dust. Firstly, the devices will need to be powered, and this is a challenge given the miniature size of the entire unit. For practical use, the device must avoid the use of batteries, which could potentially lead to toxic leaks as well as requirements of surgery to change them. Secondly, since our objective is to stimulate the neurons, the energy harvesting component is required to absorb sufficient amount of energy that can be used for stimulation. The paper addresses each of these challenges by proposing a design of the device that is able to harvest energy from ultrasound waves, which is used to power a LED unit. The paper presents simulation work to demonstrate the feasibility of the wi-opt neural dust, by initially presenting the behaviour of the light propagation in the brain tissue based on the energy harvested, as well as the energy harvesting efficiency based on variations of the ultrasonic frequency, as well as size and components of the wi-opt neural dust circuitry.

This paper is organized as follows: Sec. II introduces the system model of the wi-opt neural dust. Sec. III presents the circuitry of the device, while the simulation of the wi-opt neural device is discussed in Sec. IV. Lastly, Sec. V presents the conclusion.

II. SYSTEM MODEL

The neural dust architecture, first introduced in [2] is illustrated in Fig. 1. It will be the same proposed in this paper. The architecture consist of wi-opt neural dust devices that are embedded in various parts of the cortex and interfaces to neurons.

Unlike the neural dust, the wi-opt neural dust contains a LED that interfaces to neurons and stimulates it using light, as illustrated in Fig. 2. The neurons in this case are engineered to be sensitive to light at a specific wavelength
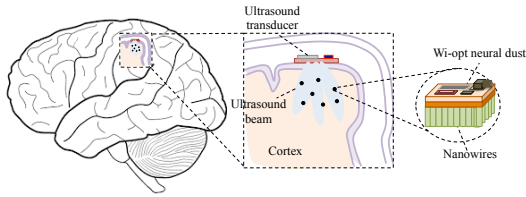
Fig. 1. Illustration of the ultrasound wi-opt neural dust network, which are scattered in the various layers of the cortex. The sub-dura transceiver is used to emit ultrasound signals to charge and trigger the wi-opt neural dust for deep brain stimulation.

Fig. 2. Illustration of an wi-opt neural dust that interfaces to an engineered neuron that is sensitive to light at a specific wavelength.

(in our case, this will be at 470nm). Above the cortex is the *sub-dura transceiver* that communicates with the wi-opt neural dust using ultrasonic signals. The purpose of the ultrasound communication to the device is two fold: ultrasonic waves are both used to instruct the device to stimulate the neuron and to provide the required energy. The sub-dura transceiver acts as a middle-man device that in turn communicates with the external transceiver. Therefore, the entire architecture consists of three layers of communication. In this paper, we only limit the interaction between the sub-dura transceiver and the wi-opt neural dust devices.

The cortex is composed of gray matter where the neural cell bodies and glial cells are the major population. The neurons are grouped into six vertical stacked layers with different cell types, such as: *pyramidal cells*, *spiny stellate cells*, *basket cells*, *chandelier cells*, and *smooth stellate cells* [3]. The total thickness of the cortex is approximately 2-6 mm, and it is within this region that the wi-opt neural dusts will be scattered. In addition to vertical scattering, the wi-opt neural dust can also be horizontally scattered, where each layer will have the devices scattered at different densities. The average human brain length and width is approximately 167 mm and 140 mm. Therefore, the wi-opt neural dusts should have certain coverage to operate properly considering the attenuation due to brain tissue absorption of the ultrasound, as well as the number of damaged neurons that are required to be stimulated.

III. WIRELESS OPTOGENETIC NEURAL DUST

Fig. 3 illustrates the circuit diagram of the wi-opt neural dust. The energy harvester of the wi-opt neural dust contains
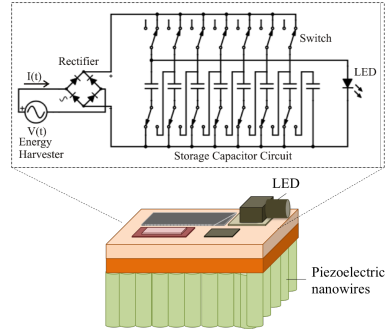
Fig. 3. Device architecture of the wi-opt neural dust, including the internal circuit diagram.

piezoelectric nanowires that that vibrate because of the ultrasounds, and through a transducer converts the mechanical energy to electrical energy. The power intensity of the ultrasound wave source is regulated by the Food and Drug Administration (FDA), where the safety level limit is $720 mW/cm^2$. Since the current generated from the piezoelectric nanowire is in AC, the conversion to DC is achieved through a rectifier. The DC current is then be charged through a series of capacitors which stores the required energy for powering the LED. The circuit also contains a switch that passes the current to the LED, and this is also sensitive to specific frequency of the ultrasound waves (this is the inherent addressing mechanism of each of the devices)

A. Energy Harvester

There are a wide range of available piezoelectric materials, and these include *lead zirconate titanate* (*PZT*), *aluminum nitride* (*AlN*), *barium titanate* (*BaTiO3*), and *zinc oxide* (*ZnO*) in the form of crystal or nanowires [4] [2] [5]. The energy harvester used in this paper is based on the ZnO nanowires with thin coating to eliminate any negative effect on the brain tissue. An example coating that could be used is based on the works of [4] that used a thin layer (<100 *μm*) of acrylic *Polymethyl methacrylate*) coating. Experiments have also shown that the coating did not exhibit any significant performance degradation on the energy harvesting process. One important component required in energy harvesting applications is the electromechanical coupling coefficient. This parameter defines the conversion efficiency between mechanical and electrical energy. It is affected by the geometry structure of the material [6].

The generated ultrasound wave traverses through the brain tissue whose attenuation coefficient α is 0.435 dB/(cm·MHz) [7]. As a result, the power intensity level received by the wi-opt neural dust is less due to the attenuation according to the following equation:

$$P_{nd} = P_s \exp^{-(\alpha f d/10)}, \qquad (1)$$

where P_{nd} and P_s are the power intensity level at the surface of the device and the acoustic wave source, respectively, α is the attenuation coefficient of the brain tissue, f is the acoustic wave frequency, and d is the distance between the wi-opt neural dust and the sub-dura transceiver. Due to this factor, 720 mW/cm^2 acoustic wave radiation is attenuated to $\approx 60mW$ on a $100 \times 100\mu m^2$ wi-opt neural dust mote implanted at 2 mm brain tissue of the cortex. Moreover, not all the acoustic wave power received by the neural dust mote is converted to electrical power, and this depends on the conversion rate of the corresponding energy harvester. Suppose that the conversion rate (η) is 0.5, the electrical power generated by it is 30 mW. The conversion process is represented as

$$P_{nd} = i_{nd}A_{EH}, \qquad (2)$$

$$P_e = P_{nd}\eta, \qquad (3)$$

where P_{nd} and P_e are the power received to vibrate the nanowire energy harvester and the electrical power after the conversion from mechanical to electrical energy; A_{EH} is the effective surface area of the energy harvester.

B. Storage Capacitors

As the nanowires generates AC current, full-wave rectification is required before the generated signal is fed to the capacitors. Since the generated voltage from nanowires (V_g) is 0.42 V [8], several capacitors are required to fulfill the energy requirement of the LED. For this purpose, micro-supercapacitors based on interdigital electrodes of reduced graphene oxide and carbon nanotube composite can be used [9]. Based on the electrical power and voltage supplied by energy harvester, the flowing current (I_g) can be represented as:

$$I_g = \frac{P_e}{V_g}. \qquad (4)$$

A single micro-supercapacitor with the surface area of 100 x 100 μm^2 has a capacitance value of 280 μF. Due to the limited voltage source and power requirements of the LED, different capacitor circuits are required during the charging and discharging cycles. A parallel capacitor circuit is used during the charging process, while a series connection is used for the discharging process. For a single supercapacitor C_{cap}, the number of different capacitance value n for the series $C_{cap_{ser}}$ and parallel $C_{cap_{par}}$ connections can be represented as:

$$C_{cap_{par}} = nC_{cap}, \qquad (5a)$$

$$C_{cap_{ser}} = \frac{C_{cap}}{n}. \qquad (5b)$$

Therefore, the total voltage fed to the LED is the sum of the voltage of the n capacitors. Depending on the vibration frequency of the nanowires, the electrical charging rate can be formulated as [8]:

$$\Delta Q = I_g t_{cycle} = \frac{I_g}{freq}, \qquad (6)$$

where ΔQ is the electrical charge per cycle, I_g is the current from the energy harvester, and $t_{cycle} = \frac{1}{freq}$ is the cycle period for the emitted ultrasound waves.

C. Light Source and Optogenetics

In optogenetics, the neurons are genetically engineered so that the ion channels are sensitive to light at a specific wavelength. Upon illumination of light, the neuron generates Action Potential (AP) which in turn triggers an electro-chemical signal along the axon of the cell. One approach of engineering the cell is to use *Channelrhodopsin-2 (ChR2)* which is a protein extracted from green alga *Chlamydomonas reinhardtii* that modifies the cells to have light-gated cation-selective membrane channels [10].

In order to model the circuit to excite the optogenetic process, the light intensity level should be at an optimum level. The excitation needs to be low enough to utilize the limited electrical energy and sufficiently high to satisfy the power requirements of the LED. The optogenetic construct *ChR2* gets activated by $\approx$ 470 nm light with an intensity of $\approx$ 1 mW/mm^2 [11]. For the LED unit, the InGaN Cree's Direct Attach DA2432 LED [12] can be used in this application. This LED can operate with an electrical current level starting from 5 mA with wave length of 465 nm that generates $\approx$ 5 mW of optical power [13].

Inside the brain tissue, light wave experiences scattering, absorption, and conical (geometrical) spreading. This effect can be formulated by the *Kubelka-Munk* model which gives the theoretical calculation for light propagation through scattering and absorptive media [14].

$$\frac{I(z)}{I(z=0)} = \frac{\rho^2}{(Sz+1)(z+\rho)^2}, \qquad (7)$$

$$\rho = r\sqrt{\left(\frac{n}{NA}\right)^2 + 1}, \qquad (8)$$

where r is the radius of the light source, NA is the numerical aperture, n is the refractive index of the tissue (1.36 for gray matter), and S is the scatter coefficient per unit thickness (z).

The calculation of time required by the storage capacitors to be able to have enough energy to illuminate the LED with respect to the number of cycles (of ultrasound frequency) is formulated as [8]:

$$n_{cycle_{charge}} = \left\lceil -\frac{V_{g_{par}}C_{cap_{par}}}{\Delta Q_{par}} \ln\left(1 - \sqrt{\frac{2E_{max_{par}}}{C_{cap}V_{g_{par}}^2}}\right)\right\rceil. \qquad (9)$$

Meanwhile for illuminating the LED which is related to storage capacitor discharging, the required time with respect to the number of cycle is calculated using the series circuitry, and is represented as follows:

$$n_{cycle_{discharge}} = \left\lceil -\frac{V_{g_{ser}}C_{cap_{ser}}}{\Delta Q_{ser}} \ln\left(\sqrt{\frac{2E_{max_{ser}}}{C_{cap}V_{g_{ser}}^2}}\right)\right\rceil, \qquad (10)$$

where E_{max} is the maximum electrical energy that can be stored in the storage circuit.

Furthermore, the voltage value during the charging and discharging process can be calculated based on the approach in [8], and is represented as follows:

$$V_{cap_{charge}}(n_{cycle}) = V_{g_{par}}\left(1 - e^{-\frac{n_{cycle_{par}}\Delta Q_{par}}{V_{g_{par}}C_{cap_{par}}}}\right), \quad (11)$$

$$V_{cap_{discharge}}(n_{cycle}) = V_{g_{ser}}e^{-\frac{n_{cycle_{ser}}\Delta Q_{ser}}{V_{g_{ser}}C_{cap_{ser}}}}. \quad (12)$$

In Eq. (11) and (12), subscript *par* and *ser* indicate the parallel and series connection of the storage capacitors, respectively.

Lastly, since we want to be able to invoke specific wi-opt neural dust to stimulate certain neurons, an addressing mechanism is required. In order to enable frequency selective lighting of the LEDs, a frequency filter switch can be incorporated into the circuit. The switch is a logical 'AND' gate that decides if the energy storage in the capacitor will lead to the discharging process of the LED. In this case, the concept of VOX (Voice Operated Switch) can be applicable.

IV. SIMULATIONS

TABLE I
SIMULATION PARAMETERS

Parameter	Value [Unit]	Description
Neural Dust Density	0.024 to 1.2 [/cm^3]	Randomly scattered
Frequency	500 to 3M [Hz]	Ultrasound freq
Depth Radius	2 to 60 [mm]	Into the brain
Interfiring period	6 [ms]	Mean (exponential dist)
Data sample	10,000	Random data
Nanowire surface area	10^4 to 2×10^4 [μm^2]	Energy harvester

The wi-opt neural dust are simulated to investigate its optical behaviour when interfaced to cells as well as the behaviors of the device with respect to its charging and discharging capabilities to light up the LED. The parameters used for the simulations are presented in Table I.

A. Optical Light Behavior in Brain Tissue

Since the light source is embedded in the brain tissue, the light intensity is attenuated as it propagates through the tissue according to the attenuation coefficient of the medium. The optical power produced by the LED depends on the applied current percentage [13]. As the optical power level lessened by distance, the placement of the wi-opt neural dust has to consider the optimal position with regard to the optogenetic construct.

Monte Carlo simulations [15] and the Kubelka-Munk model [16] are often used to analyse light propagation in optogenetics field. In this work, we simulate the light propagation in human brain tissue using COMSOL Multiphysics software with Helmholtz model representation. The light transport model with Finite Element Method in COMSOL simulation includes the geometry and optical properties of the materials such as scattering and absorption. The model solves the fluence rate (light intensity) u or $\Phi(r,t)$, given the diffusion coefficient c

or $D(r,t)$, absorption coefficient a or μ_a, and source term f or $S(r,t)$ according to the following Helmholtz equation:

$$-\nabla D(r,t)\nabla^2\Phi(r,t) + \mu_a\Phi(r,t) = S(r,t)$$
$$\nabla(-c\nabla u) + au = f. \quad (13)$$

In our scenario, the LED is modeled as an ellipsoid, whereas the neuron cells and propagation medium as spheres. The absorption coefficients of LED, neuron cells, and brain tissue are set to 0, 0.36/mm, and 0.014/mm, respectively [15]. The diameters of LED and brain tissue model are $\approx100\mu m$ and $500\mu m$, while we set $100\mu m$ diameter for single neuron cell and various diameters for more than one neuron cell model. The frequency domain study is chosen for wavelength of 470 nm which corresponds to blue light.

Fig.4(a) shows the light intensity generated by the light source radiated by half of the ellipsoid surface. Close to the source, the light intensity is high depicted by the red color. When we add the neuron cell model with the distance of $10\mu m$ from the light source, the intensity pattern changes due to different absorption coefficient of the materials. This phenomenon is shown in Fig.4(b). We also investigate the intensity pattern for the situation similar to the brain environment where there are more than one neuron cell close to each other. The distance range is between 10-20 μm by LED vicinity. Therefore, we add several neuron cells with the same optical properties but different sizes and distances from the light source. Fig.4(c) shows the light intensity pattern affected by multiple neuron cells.

From the simulation, it can be seen that distance and cells affect the attenuation of light propagation. As a result, the narrower pattern is formed as the number of surrounding neuron cells increases. This can be beneficial as one wi-opt neural dust might excite several optogenetic constructs if desired. On the other hand, it will create unwanted effects when excitation of undesired neuron occurs.
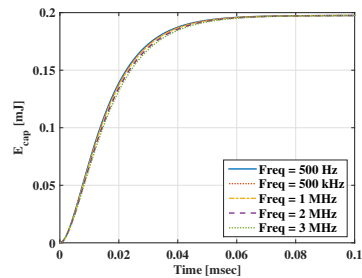
Fig. 5. Illustration of storage energy as a function of time with frequency variation where the neural dust mote is 2 mm deep into the brain during charging process.

B. Energy and Power Evaluation

In order to figure out the operational characteristics of a single wi-opt neural dust, it is important to evaluate the charging

(a) Wi-opt neural dust LED light emission model

(b) LED light emission on a single neuron cell.

(c) LED light propagation surrounded by several neuron cells.
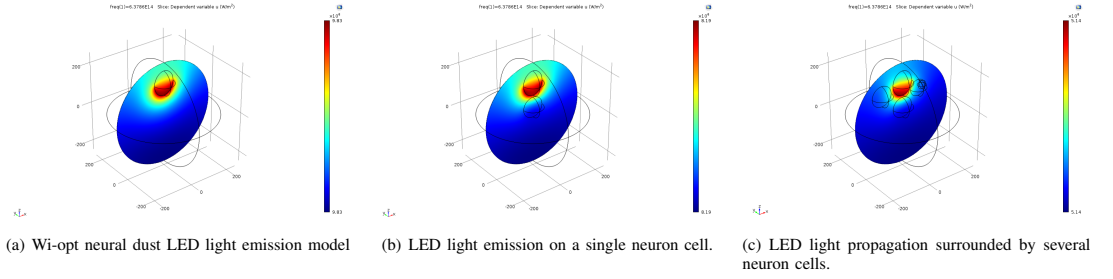
Fig. 4. COMSOL multiphysics simulation of the LED light propagation behaviour within the brain tissue.
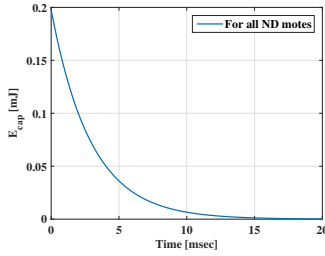
Fig. 6. Illustration of the storage energy as a function of time where the neural dust mote is 2 mm deep into the brain during discharging process.
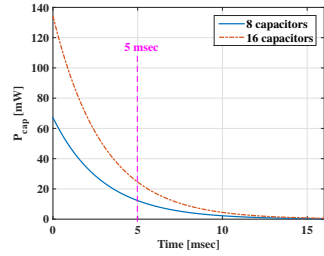
Fig. 8. Illustration of the capacitor power as a function of time where the neural dust mote is 2 mm deep into the brain during discharging process. The 5 msec limit is the minimum duration threshold required by the LED to emit light in order to successfully stimulate the neuron.
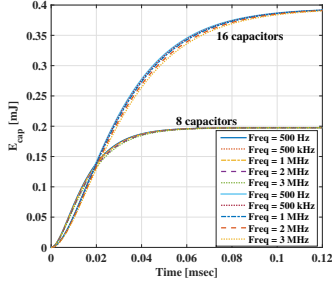
Fig. 7. Illustration of storage energy as a function of time with frequency variation where the neural dust mote is 2 mm deep into the brain during charging process.
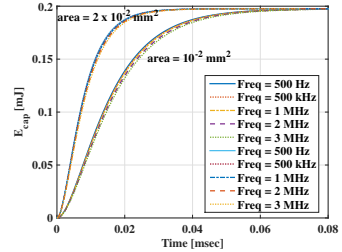
Fig. 9. Illustration of storage energy as a function of time for various frequencies and two different nanowire surface area.

and the discharging duration of the storage capacitors. These factors are affected mainly by the depth of the device planted into the brain and the frequency of the ultrasonic waves emitted from the sub-dura transceiver, while the constant intrinsic values of the storage capacitors are calculated based on the energy harvester and light source component. Considering the ontogenetic requirements for neuron stimulation, the circuit model explained in Sec.III has to be able to illuminate the LED for at least 5 msec duration [17]. In our simulations, each cycle utilizes 10 thousand random values for neuron sequence firing. The neuron inter-firing period is based on exponential

distribution as their sequences can be represented as a poisson process (Rate as a Spike Count and Fano Factor) [18]. Fig. 5 presents the amount of stored energy with respect to time. Although higher frequencies suffer from higher attenuation within the brain tissue, this difference is very small in terms of the amount of energy stored with respect to time, as shown in Fig. 5. This also means that using different frequencies for the addressing mechanism will not come at a cost of variations in the charging durations. This factor must also be included in design consideration, especially when selective frequency is required to invoke specific wi-opt neural devices as well as the design of the sub-dura transceiver. Fig. 6 shows the graph

of the energy discharging of the capacitor storage. As shown in the discharging plot, the period to release the energy goes beyond the minimum 5 msec duration, ensuring that sufficient light intensity is applied to the neurons. Comparing Fig. 5 and Fig. 6, there is significant gap in time. The reason behind this is because the parallel and series capacitor connections during charging and discharging process. This configuration affects the electrical properties of the storage circuit, such as the capacitance value and the voltage value.

Fig. 7 present the results when different quantity of capacitors are used for the devices. Intuitively, we can see that an increase in the number of capacitors will definitely increase the quantity of energy stored, but comes at a cost of longer charging durations. This also means that higher number of ultrasound frequency cycles are required. The benefit of this configuration is that the device can maintain a certain amount of energy to stimulate neuron with short inter-firing periods, provided that a pausing process can be incorporated into the circuit. Fig. 8 presents the amount of energy discharged and compares between the different number of capacitors. For both configurations we can see that the discharging process provides sufficient amount of power and within the 5msec limit needed to stimulate the neuron. Since the charging process is reliant on vibration of the piezoelectric nanowires, Fig. 9 presents the results for variations in the area of the nanowire. There is no difference in the amount of energy charged when there are variations in the ultrasonic frequency. However, we can observe that the quantity of energy produced is increased when the area is doubled.

V. Conclusions

The increased attention towards Deep Brain Stimulation has attracted researchers to search for innovative solutions that can enable long-term deployment as well as design of miniaturised devices that can self-generate power. The emergence of optogenetics has provided a new approach for precise stimulation at the single neuron level. In this paper, we propose the wi-opt neural dust that is constructed from nanoscale components and can be embedded into the cortex of the brain. A thorough description of the circuitry as well as the components are presented, including mechanisms of generating power through ultrasonic wave vibrations. The paper presented simulation results on the behaviour of optical light transmission and its effect on the brain tissue, as well as the energy performance of the device based on variations of ultrasonic frequencies and circuitry devices (e.g. capacitors and piezoelectric nanowire area). The positive results from our simulation study has demonstrated the feasibility of using the wi-opt neural dust for long term deployments in the brain in order to stimulate neurons and provide new approaches for treating neurological diseases so that this study motivates future work in this direction.

Acknowledgment

References

[1] X. Han. In vivo application of optogenetics for neural circuit analysis. *ACS chemical neuroscience*, 3(8):577–584, 2012.

[2] D. Seo, J. M. Carmena, J. M. Rabaey, E. Alon, and M. M. Maharbiz. Neural dust: An ultrasonic, low power solution for chronic brain-machine interfaces. *arXiv preprint arXiv:1307.2196*, 2013.

[3] V. B. Mountcastle. *Perceptual neuroscience: the cerebral cortex*. Harvard University Press, 1998.

[4] S. Song, A. Kim, and B. Ziaie. Omni-directional ultrasonic powering for millimeter-scale implantable devices. 2015.

[5] R. J. Przybyla, S. E. Shelton, A. Guedes, I. Izyumin, M. H. Kline, D. Horsley, B. E. Boser, et al. In-air rangefinding with an aln piezoelectric micromachined ultrasound transducer. *Sensors Journal, IEEE*, 11(11):2690–2697, 2011.

[6] M. Kim, J. Kim, and W. Cao. Electromechanical coupling coefficient of an ultrasonic array element. *Journal of applied physics*, 99(7):074102, 2006.

[7] P. R. Hoskins, K. Martin, and A. Thrush. *Diagnostic ultrasound: physics and equipment*. Cambridge University Press, 2010.

[8] J. M. Jornet and I. F. Akyildiz. Joint energy harvesting and communication analysis for perpetual wireless nanosensor networks in the terahertz band. *Nanotechnology, IEEE Transactions on*, 11(3):570–580, 2012.

[9] M. Beidaghi and C. Wang. Micro-supercapacitors based on interdigital electrodes of reduced graphene oxide and carbon nanotube composites with ultrahigh power handling performance. *Advanced Functional Materials*, 22(21):4501–4510, 2012.

[10] G. Nagel, T. Szellas, W. Huhn, S. Kateriya, N. Adeishvili, P. Berthold, D. Ollig, P. Hegemann, and E. Bamberg. Channelrhodopsin-2, a directly light-gated cation-selective membrane channel. *Proceedings of the National Academy of Sciences*, 100(24):13940–13945, 2003.

[11] T.-i. Kim, J. G. McCall, Y. H. Jung, X. Huang, E. R. Siuda, Y. Li, J. Song, Y. M. Song, H. A. Pao, R.-H. Kim, et al. Injectable, cellular-scale optoelectronics with applications for wireless optogenetics. *Science*, 340(6129):211–216, 2013.

[12] Cree Inc. *Direct Attach DA2432^{TM} LEDs*, 2013. Rev A.

[13] M. A. Rossi, V. Go, T. Murphy, Q. Fu, J. Morizio, and H. H. Yin. A wirelessly controlled implantable led system for deep brain optogenetic stimulation. *Frontiers in integrative neuroscience*, 9, 2015.

[14] A. M. Aravanis, L.-P. Wang, F. Zhang, L. A. Meltzer, M. Z. Mogri, M. B. Schneider, and K. Deisseroth. An optical neural interface: in vivo control of rodent motor cortex with integrated fiberoptic and optogenetic technology. *Journal of neural engineering*, 4(3):S143, 2007.

[15] Z. Wang, L. Wang, Y. Zhang, and X. Chen. Monte carlo simulation of light propagation in human tissue models. In *2009 3rd International Conference on Bioinformatics and Biomedical Engineering*, pages 1–4. IEEE, 2009.

[16] G. Yona, N. Meitav, I. Kahn, and S. Shoham. Realistic numerical and analytical modeling of light scattering in brain tissue for optogenetic applications. *eneuro*, pages ENEURO–0059, 2016.

[17] E. S. Boyden, F. Zhang, E. Bamberg, G. Nagel, and K. Deisseroth. Millisecond-timescale, genetically targeted optical control of neural activity. *Nature neuroscience*, 8(9):1263–1268, 2005.

[18] W. Gerstner, W. M. Kistler, R. Naud, and L. Paninski. *Neuronal dynamics: From single neurons to networks and models of cognition*. Cambridge University Press, 2014.

PUBLICATION

II

Wireless optogenetic nanonetworks for brain stimulation: Device model and charging protocols

S. A. Wirdatmadja, M. T. Barros, Y. Koucheryavy, J. M. Jornet and
S. Balasubramaniam

Wireless Optogenetic Nanonetworks for Brain Stimulation: Device Model and Charging Protocols

Stefanus A. Wirdatmadja, Michael T. Barros, Yevgeni Koucheryavy, Josep Miquel Jornet, Sasitharan Balasubramaniam

Abstract—In recent years, numerous research efforts have been dedicated towards developing efficient implantable devices for brain stimulation. However, there are limitations and challenges with the current technologies. They include neuron population stimulation instead of single neuron level, the size, the biocompatibility, and the device lifetime reliability in the patient's brain. We have recently proposed the concept of *wireless optogenetic nanonetworking devices (WiOptND)* that could address the problem of long term deployment, and at the same time target single neuron stimulation utilizing ultrasonic as a mode for energy harvesting. Additionally, a number of charging protocols are also proposed, in order to minimize the quantity of energy required for charging, while ensuring minimum number of neural spike misfirings. These protocols include the simple *Charge and Fire*, which requires the full knowledge of the raster plots of neuron firing patterns, and the *Predictive Sliding Detection Window*, and its variant *Markov-Chain based Time-Delay Patterns*, which minimizes the need for full knowledge of neural spiking patterns as well as number of ultrasound charging frequencies. Simulation results exhibit a drop for the stimulation ratio of ~25% and more stable trend in its efficiency ratio (standard deviation of ~0.5%) for the *Markov-Chain based Time-Delay Patterns* protocol compared to the baseline *Change and Fire*. The results show the feasibility of utilizing WiOptND for long-term implants in the brain, and a new direction towards precise stimulation of neurons in the cortical microcolumn of the brain cortex.

I. INTRODUCTION

Each year, the prevalence of neurodegenerative diseases, such as Alzheimer's disease, amyotrophic lateral sclerosis and Parkinson's disease, is increasing. According to the 2016 *World Health Organization* (*WHO*) data statistics, more than five million Americans are living with Alzheimer's and it is predicted that the number will increase to around 16 million by 2050 [1]. Parkison's affects 500,000 people in the US and it will double by 2030 [2]. It has an estimated cost of 20 billion dollars in the US [3] and 13 billion euros in Europe [4]. This situation demands scientists and researchers to not only develop prevention programs, but also solutions that might assist the patients to live a normal lifestyle. In certain cases, patients with Parkinson's disease may receive benefits from brain stimulation by placing *Implantable Pulse Generator (IPG)* [5] to the targeted areas of the brain to treat essential

S. A. Wirdatmadja, S. Balasubramaniam and Y. Koucheryavy are with Department of Electrical Engineering and Communications, Tampere University of Technology, Finland. Email: (stefanus.wirdatmadja, sasi.bala, yk)@tut.fi

M. T. Barros is with the Telecommunication Software & Systems Group (TSSG) at Waterford Institute of Technology (WIT), Ireland. e-mail: mbarros@tssg.org

J. Jornet is with the Department of Electrical Engineering, University at Buffalo, The State University of New York, US. Email: jmjornet@buffalo.edu

tremor and dystonia symptoms. In the field of neuroscience, *optogenetics* is gaining popularity as an alternative method for neural stimulation. In optogenetics, the neurons are engineered so that they are sensitive to light at specific wavelengths in order to have either excitatory or inhibitory effects [6]. Optogenetics provides an advantage over the use of electrodes due to its higher precision, less stress to the cells, and lower noises. These noises may disturb the neural activity recording process since the recorded signal does not merely come from the target neurons, but also from the stimulation electrodes [7]. However, further improvements are still required to the current solutions. They include the degree of intrusion through the skull and alternative power supply compared to the use of batteries. These shortcomings limit the degree of practicality for the patients in their daily life.

On neural networks, neurons communicate with each other through the process of action potentials and synapses. The neuron cell body (soma) connects to other cells using the dendrites and axons, which receives and transmits signals with neighbouring cells. The problem arises when this physical transportation network is impaired due to various problem such as aging, disease, or the death of cells, among others. Even a single neuron failure may result in communication impairments along the cortical circuit. This communication impairment due to single cell level failure will result in the discontinued transmission of action potential among cortical layers as depicted in Fig. 1. In this case, the implementation of a single neuron level stimulation implant can restore the neural circuit communication between the layers.

We have recently proposed the concepts of wireless optogenetics integrated using nanoscale components [8], which we term *wireless optogenetic nanonetworking devices* (*WiOptND*). Considering the size of the soma which varies between 4-$100\mu m$ in diameter, the WiOptND is required to be approximately several hundreds microns in size in order to deliver the required light intensity needed for the stimulation. Since our aim is to embed the device into the brain, this means that this miniaturization will require a light source that can emit sufficient light intensity, and is powered using energy harvesting [8] [9]. In this paper, we investigate the light propagation behaviour through the tissue to determine the effective distance required between the light source and the neurons, and the energy harvesting technique based on ultrasound vibrations of piezoelectric nanowires.

In addition, since we anticipate a network of WiOptNDs, a suitable charging protocol is required to maximize the energy efficiency and ensure that all devices are charged to minimize misfiring of the neurons. In particular, since these devices will
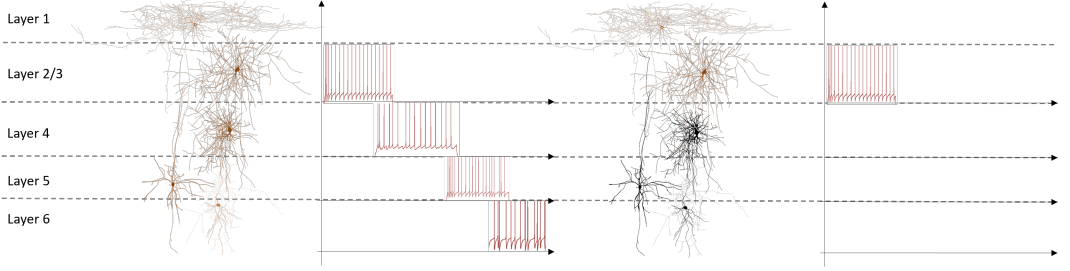
Fig. 1: Illustration of healthy and disconnected cortical neural networks. Failing of action potential relays will result in disconnected communication in the cortical column of the cerebral cortex.

be embedded into the cerebral cortex, the charging protocol should consider the characteristics of the neural circuit, and in particular, knowledge of the neural spike sequence. We propose three protocols, including the simple *Charge and Fire* protocol based on utilizing the full knowledge of the raster plot firing sequence to individually charge each device in the network, the *Predictive Sliding Detection Window* protocol which employs the combination of neural spike prediction and a more complex circuit for parallel charging in order to minimize usage of ultrasound frequencies, and its variant the *Markov-Chain based Time-Delay Patterns*, which utilizes knowledge of the neuron population and their connection probability between the cortical layers to predict the firing sequence to also minimize the required ultrasound frequencies.

The structure of the paper is as follows: background information on optogenetics and its biological features are provided in Sec. II. Going more into the WiOptND, the overall model and the components are discussed in Sec. III. Light propagation properties through the brain tissue is discussed in Sec. IV, while in Sec. V the power management of WiOptND is presented, particularly focusing on the energy charging and releasing performance to power the light source. The charging protocols of the WiOptND nanonetwork is discussed in Sec. VI. Finally, the paper is concluded in Sec. VII.

II. OPTOGENETICS

Naturally, the communication between neurons is done both electrically and chemically. In most cases, the electric signal is used in transferring the information in one single neuron, while chemical is used in inter-neuronal communications [10] [11]. The electrical stimulation, action potential, propagates from dendrites to the axons and stimulates the release of neurotransmitter for inter-neuronal synapse communications. The most common method in controlling the neural communications is using electrical and light stimulation (optogenetics). Comparing both methods, optogenetics gives higher precision in targeting specific neuron, minimizes the cell stress as compared to electrical stimulation, and creates less interference with the surrounding cells.

Optogenetics is a method of artificially manipulating neural communication using light at a specific wavelength. According to its characteristics, the optogenetic construct can have

either excitatory or inhibitory effects. *Excitatory postsynaptic potential (EPSP)* refers to the case when the cell membrane depolarizes as a result of the opening of sodium and calcium ion membrane channels, causing action potential to be generated. On the other hand, *inhibitory postsynaptic potential (IPSP)* is when the cell membrane hyperpolarizes caused by the opening of chloride or potassium ion membrane channels which results in blockage of action potential generation.

In optogenetics, *channelrhodopsin-2 (ChR2)* exhibits excitatory characteristics. This construct is obtained by genetically engineering neurons with the *opsins* from green algae *Chlamydomonas reinhardtii* (Step 1 in Fig. 2) [12]. The blue light illumination triggers the action potential generation (Step 2 and 3 in Fig. 2). For inhibitory effect, the hyperpolarization can be done in two ways, using either chloride or proton pumps. Chloride pump is realized by utilizing the *halorhodopsin (NpHR)* from archaeon *Natronomonas pharaonis* [13]. The improved version of NpHR is called eNpHR3.0 which can be activated by green, yellow, or red light (Step 2 and 3 in Fig. 2). During its activation, chloride ion channel gates open, bringing chloride ions into the cells. Proton pump is the alternative of chloride pump to perform the inhibitory effect. To create proton pumps, there are four types of optogenetics that can be used. They are archaerhodopsin-3 (Arch) from *Halorubrum sodomense*, Mac from the fungus *Leptosphaeria maculans*, archaerhodopsin (ArchT) from *Halorubrum strain TP009*, and eBR (an enhanced version of bacteriorhodopsin from *Halobacterium salinarum*) [14]. In a nutshell, Fig. 2 concludes how the implementation of ChR2 and NpHR affects the generation of action potentials upon the illumination of blue light (480 nm) and yellow light (570 nm).

Since the focus of this paper is to excite the neurons, the optogenetic construct that is used is the ChR2, which is activated by blue light whose wavelength is approximately 480 nm.

III. SYSTEM MODEL

This section will first describe the devices for each of the layers of the architecture, and this will be followed by the device design, including the different components of the circuitry.
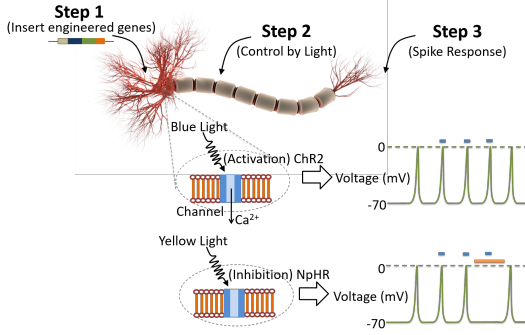
Fig. 2: Steps towards developing an optogenetic neuron and its stimulation process. The figure also illustrates the depolarization process where ion pumps are activated.

A. Wireless Optogenetic Nanonetworking Architecture

The entire network of the Wireless Optogenetic Nanonetworking architecture is composed of three layers, which is adopted from [15]. The lowest layer is the cerebral cortex where the WiOptNDs are distributed, each are interfaced to a neuron that requires stimulation as illustrated in Fig. 4. Cerebral cortex is the gray matter of the brain and is responsible for sensory, motor, and associated functions. Horizontally, the cerebral cortex is categorized based on their functional areas, while vertically, it comprises of six layers containing different type of neurons, which includes: *pyramidal cells*, *spiny stellate cells*, *basket cells*, *chandelier cells*, and *smooth stellate cells* [16], each of which can have a WiOptND interfaced to the cell. The next layer up is the *sub-dura transceiver*, which is located on the dura and below the skull, and communicates with the WiOptND. The role of the sub-dura transceiver is to emit ultrasound waves which are used to charge the WiOptND. The sub-dura transceiver contains the algorithm the determines both the charging and stimulation sequence of the WiOptND, and this in turn emits the sequence of ultrasound signals. Above the sub-dura transceiver is the *external transceiver*, which communicates with the sub-dura transceiver (please note that this paper does not focus on the interactions between the *external transceiver* and the *sub-dura transceiver*). However, for readers who are interested in design of ultrasonic external device, [17] makes the Internet of Medical Things (IoMT) ultrasonic patch and compares the performance between ultrasonic link and Bluetooth Low Energy (BLE). Ultrasonic link outperforms BLE mainly due to biological tissue propagation.

B. Wireless Optogenetic Nanonetworking Devices

The circuit diagram of the WiOptND is illustrated in Fig. 5. Acting as the energy harvester, the *piezoelectric* nanowires vibrate in response to the radiated ultrasound wave emitted from the sub-dura transceiver. As the nanowires oscillate, the AC voltage is generated. In this stage, the mechanical energy from the ultrasound pressure is converted into electrical
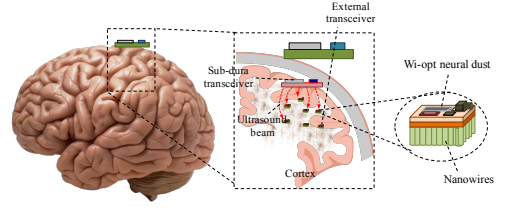
Fig. 3: Illustration of the overall architecture of the Wireless Optogenetic Nanonetwork. The WiOptND are scattered in the various layers of the cortex, and is charged by the ultrasound signals emitted from the *sub-dura transceiver*, which in turn is communicated from the *external transceiver*.

Fig. 4: Illustration of a WiOptND that interfaces to an engineered neuron that is sensitive to light at a specific wavelength.

energy in accordance to the piezoelectric material. However, the ultrasound intensity must abide with the Food and Drug Administration (FDA) safety regulation stating that the maximum permissible level is $720 \ mW/cm^2$. The generated AC voltage is converted to DC by using a *rectifier*. The converted electrical energy is then stored in the storage capacitor which is charged to power the light source component, and in our case is a *Light Emitting Diode* (*LED*). Since our aim is to be able to signal each individual WiOptND in order to charge and trigger the stimulation process, a unique addressing scheme is required for each device. One approach is through the utilization of a *Voice Operated Switch* (*VOX*) that responds to different ultrasound frequencies. By integrating the frequency filter switch, adopted from the VOX, enables the discharging selection of one particular device, and this is achieved by integrating a piezo element that is sensitive to specific resonant frequency.

IV. LIGHT PROPAGATION IN BRAIN TISSUE

As the light emitted from the LED traverses via the brain tissue, the irradiance or the intensity decreases. Absorption due to the tissue *chromophores* increases as the light is scattered along its propagation path. The main chromophores in biological tissue include water, lipids, melatonin, oxygenated and deoxygenated haemoglobin. Eighty percent of an average human brain contains water, however, its absorption coefficient is negligible especially for visible light. The same phenomenon occurs for lipids as well, since the lipid content is approximately 5% of the brain [18]. The large percentage of the brain comprises blood which delivers oxygen from the lungs

Fig. 5: Device architecture of the WiOptND, including the internal circuit diagram.

Fig. 6: Intensity ratio as a function of distance from the light source. The curve is greatly affected by the light absorption and scattering phenomenon in the brain tissue.

to the brain and vice versa. Haemoglobin of red blood cells contains the highest light absorbing chromophores.

For the light intensity requirement analysis for ChR2 activation, the *Modified Beer-Lambert Law* can be used for photon transport modelling. According to the differential form of this model, the absorption in the tissue is proportional to the major chromophores concentration. Furthermore, this model assumes constant scattering losses and homogeneous semi infinite medium (tissue) reflected on the absorption factor. The *Differential Pathlength Factor* (*DPF*) is dependent on the light wavelength λ, absorption coefficient μ_a, reduced scattering coefficient μ_s', and the distance from the source. This factor can be estimated by [19]:

$$DPF(\lambda, d) = \frac{1}{2}\sqrt{\frac{3\mu_s'(\lambda)}{\mu_a(\lambda)}}\left[1 - \frac{1}{1 + d\sqrt{(3\mu_a(\lambda)\mu_s'(\lambda))}}\right]. \quad (1)$$

After obtaining the *DPF* value, the intensity ratio measured from the light source can be formulated as:

$$\frac{I(\lambda, d)}{I_o(\lambda)} \equiv T(d) = e^{-\mu_a(\lambda)\, d\, DPF(\lambda,d) + G(\lambda)}, \quad (2)$$

where $I_o(\lambda)$ is the light source intensity, $I(\lambda, d)$ is the light intensity at distance d from the source, and $G(\lambda)$ is a medium and geometry dependent constant and largely unknown.

The required light power intensity for ChR2 signal triggering is 8-12 mW/mm^2 [20]. From [21], the absorption coefficient μ_a and the reduced scattering coefficient μ_s' for brain tissue are 0.07 mm^{-1} and 1.404 mm^{-1}, respectively. Based on these values, the light intensity ratio or transmittance follows the curve depicted in Fig. 6, which decr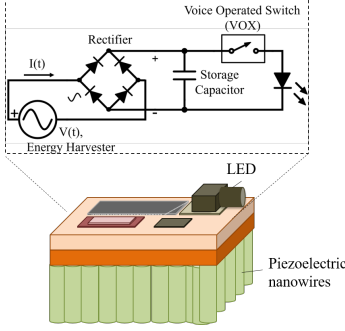eases exponentially as the distance from the light source increases. This phenomenon occurs due to the absorption and scattering factors which are represented as the DPF value.

V. ENERGY HARVESTING FOR WIOPTND

A. Piezoelectric Nanowires

The piezoelectric material has been widely used for harvesting energy due to its unique ability to produce electric charge with respect to the applied mechanical stress. The utilization
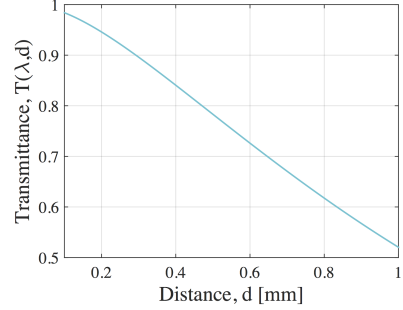
of certain piezoelectric material is based on the consideration of the type of application, power requirement, vibration frequency, and the geometry structure. Some well-known materials used are *lead zirconate titanate* (*PZT*), *aluminum nitride* (*AlN*), *barium titanate* (*BaTiO3*), and *zinc oxide* (*ZnO*) in the form of crystal or nanowires [22] [15] [23]. Taking into account the energy requirement, the WiOptND uses ZnO nanowires complemented by thin coating of (<100 μm) of acrylic *Polymethyl methacrylate*). The coating is important to avoid harmful effects on the brain tissue. Related to the power/energy conversion of the material, the electromechanical coupling coefficient is one important parameter to consider in deciding the appropriate material and geometry structure to be used in harvesting the energy [24].

The attenuation experienced by ultrasound wave depends on the frequency and the depth of the tissue. In this paper, the maximum frequency used is 3 MHz. For brain tissue, the attenuation coefficient, α, is 0.435 $dB/(cm \cdot MHz)$ [25]. The effect on the transmitted signal power intensity can be formulated as follows:

$$I_{nd} = I_s 10^{-(\alpha f d/10)}, \quad (3)$$

where I_{nd} and I_s are the power intensity levels at the surface of the energy harvester and the acoustic wave source, respectively, α is the attenuation coefficient of the brain tissue, f is the ultrasound wave frequency, and d is the distance between the WiOptND and the sub-dura transceiver.

According to (3), if the ultrasound source emits 720 mW/cm^2 wave intensity, the power for a $100 \times 100\mu m^2$ energy harvester is ~60 mW. This calculation is based on the 2-mm depth of the cerebral cortex since dense population of neuron bodies is within this depth (gray matter). While white matter of the brain is mostly populated by myelinated axons. The electromechanical conversion occurs in the energy harvesting element, therefore, its conversion rate needs to be taken into consideration. Assuming that the electromechanical conversion rate, η, is 50% [26] [27], the effective electrical energy generated is 30 mW. This result can be obtained from:

$$P_{nd} = I_{nd}A_{EH}, \quad (4)$$

$$P_e = P_{nd}\eta, \tag{5}$$

where P_{nd} and P_e are the power received to vibrate the nanowires of the energy harvester and the electrical power after the conversion from mechanical to electrical energy, respectively, and A_{EH} is the effective surface area of the energy harvester.

B. Storage Capacitor

The next stage after the energy is produced by the harvester and is rectified, is the storage of charge in the micro-supercapacitor based on the generated voltage V_g from the ZnO nanowires [28]. The micro-supercapacitor can be based on the interdigital electrodes of reduced graphene oxide and carbon nanotube composite [29]. This capacitor is considered the most efficient for the WiOptND due to its miniature size and large charge storage capacity. Using the power and voltage of the energy harvester, the electrical current, i_g, flowing in the circuit can be represented as:

$$i_g = \frac{P_e}{V_g}. \tag{6}$$

The amount of electrical charge, ΔQ, supplied and stored in the storage capacitor per charge cycle, t_{cycle}, can be estimated based on the nanowire vibration frequency, f, and the current, i_g, flowing from the energy harvester to the storage circuit. This value can be obtained from [28]:

$$\Delta Q = i_g t_{cycle} = \frac{i_g}{f}. \tag{7}$$

C. Charging Cycles

The energy from the capacitor is utilized to power the LED. For the LED, the minimum light intensity requirement should be fulfilled and at the same time having the low power demand in accordance to the power availability in the storage capacitor is important.

The time duration for charging and discharging period of the storage capacitor can be represented by the number of cycles, $n_{cycle_{charge}}$ and $n_{cycle_{discharge}}$, and this can be represented as follows [28]:

$$n_{cycle_{charge}} = \left\lceil -\frac{V_g C_{cap}}{\Delta Q} \ln\left(1 - \sqrt{\frac{2E_{max}}{C_{cap}V_g^2}}\right) \right\rceil, \tag{8a}$$

$$n_{cycle_{discharge}} = \left\lceil -\frac{V_g C_{cap}}{\Delta Q} \ln\left(\sqrt{\frac{2E_{max}}{C_{cap}V_g^2}}\right) \right\rceil, \tag{8b}$$

where E_{max} is the maximum electrical energy that can be stored in the capacitor, C_{cap}.

The voltage level in every cycle can also be determined for both the charging and discharge processes. The instantaneous voltage level in terms of cycle numbers is represented as:

$$V_{cap_{charge}}(n_{cycle}) = V_g\left(1 - e^{-\frac{n_{cycle}\Delta Q}{V_g C_{cap}}}\right), \tag{9a}$$

$$V_{cap_{discharge}}(n_{cycle}) = V_g e^{-\frac{n_{cycle}\Delta Q}{V_g C_{cap}}}. \tag{9b}$$

TABLE I: Simulation Parameters

Parameter	Value [Unit]	Description
WiOptND density	0.024 to 1.2 [$/cm^3$]	Randomly scattered
Ultrasound Frequency	500 to 3M [Hz]	-
Cortical Cortex Depth	2 to 4 [mm]	-
Neural spike period	$\lambda = 6$ [ms]	Exponential dist.
Data sample	10,000	Randomly generated
Nanowire surface area	10^4 to 2×10^4 [μm^2]	Energy harvester

D. WiOptND Energy and Power Evaluation

In this section, we numerically evaluate the energy and power storage circuitry of the WiOptND. The parameters used for the simulations are presented in Table I. Since the duration of the charging and discharging of storage capacitor is sufficiently fast regardless of the 2-mm thickness of the cerebral cortex layer and operating frequencies variants, the main concern lies in the electrical specifications of the light source component and energy harvester. This, in turn, affects the constant intrinsic values of the storage capacitor.

Our analysis is based on determining the radiated intensity from the LED in order to obtain desired light intensity on the target neuron. Fig. 7(a) shows the result of the required emitted light intensity of the LED to achieve the level inside the range of optogenetics stimulating intensity, which is 8-12 mW/mm^2 with respect to distance. Similar to the previous calculations, Fig. 7(b) and 7(c) illustrates the effect of the storage capacitor component to the required light intensity by the optogenetics. For both charging and discharging processes, higher light intensity exhibits faster periods related to larger ΔQ electrical charge. Fig. 7(d) and 7(e) presents the difference of energy storage phenomena when the effective area of the energy harvester is doubled. Larger effective surface area leads to higher electrical charge supply. However, when the frequency is varied, no significant change is noticeable in term of energy in the storage capacitor, which is depicted in Fig. 7(f).

The relation between the charging time duration and the piezoelectric nanowires surface area with varying ultrasound frequencies is analyzed in Fig. 8. From this simulation, it can be observed that the surface area of the energy harvester is linearly proportional to the generated energy resulting in faster charging process. As shown in the result, the differences in the frequencies have no effect on the quantity of stored energy.

VI. System Charging Protocols

While the previous sections discussed the functionalities as well as system performance of each device, this section will discuss its operation as a network. Fig. 9 illustrates the heterogeneous nature and density variation of neuronal networks in a cortical cortex. The deployment and topology of the WiOptNDs are highly correlated to the network structure and characteristics of the neuronal networks. To represent the basic system architecture, three element sets should be defined, i.e., $L = \{2/3, 4, 5, 6\}$ which represents the set of cortical layers, $F = \{f_1, f_2, f_3, ..., f_n\}$ which represents the list of transmitted frequencies, and ND = {ND$_1$, ND$_2$, ND$_3$, ... ND$_m$}, $\{n, m\} \in \mathbb{N}^*_{\leq n}$ is for the set of WiOptNDs signalled
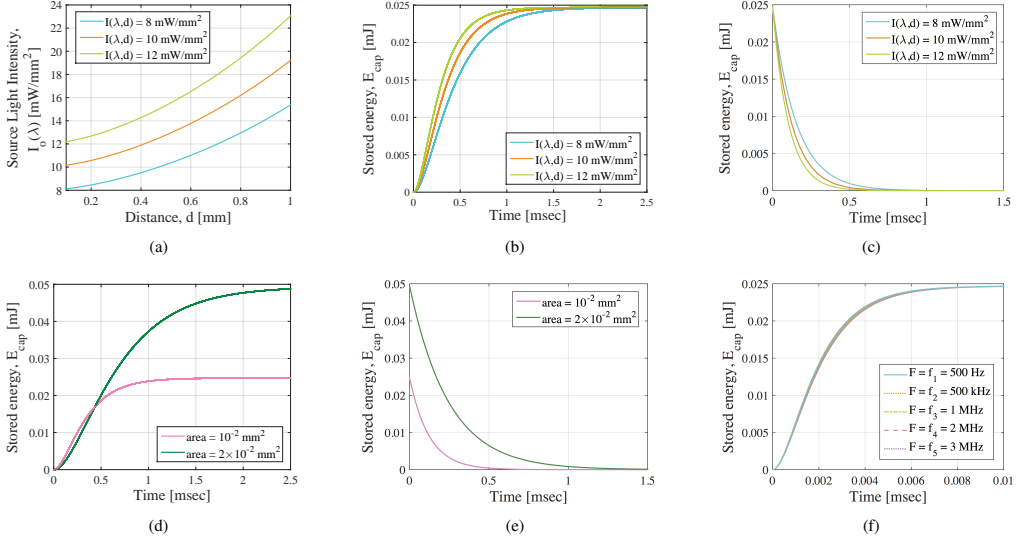
Fig. 7: (a) Intensity at the light source as a function of distance with variations in the required intensity for the optogenetics. (b) Illustration of storage energy during the charging period as a function of time with light intensity variations, and a constant frequency of 500 Hz at $500\mu m$ distance. (c) Illustration of storage energy during the discharging period as a function of time with light intensity variations, and a constant frequency of 500 Hz at $500\mu m$ distance. (d) Illustration of storage energy during the charging period as a function of time with energy harvester effective area variations, and $I(\lambda,d)$ of $10mW/mm^2$ with constant frequency of 500 Hz at $500\mu m$ distance. (e) Illustration of storage energy during the discharging period as a function of time with energy harvester nanowire area variations, and $I(\lambda,d)$ of $10mW/mm^2$ with constant frequency of 500 Hz at $500\mu m$ distance. (f) Illustration of storage energy charging process with ultrasound frequency variations.

by the sub-dura transceiver, Tx_{sub}. Additionally, $Tx_{sub}(F)$ represents the transmitting frequency F emitted by the sub-dura transceiver. Since multiple devices are concerned, and energy harvesting is required through the sub-dura transceiver, a charging protocol is required. The charging protocols that will be discussed in this section range from a simple *Charge and Fire*, to more complex protocols that will maximize energy efficiency, which include *Predictive Sliding Detection Window* and its variant the *Markov-Chain based Time-Delay Patterns* protocols.

A. Charge and Fire Protocol

For this protocol, the sub-dura transceiver transmits one frequency, $f_i \in F$, which corresponds to one specific WiOptND when stimulation of a neuron is required. Considering $s(L[n],t)$ is the firing state of a neuron of nth layer in time slot t, $s \in \{0,1\}$, the frequency transmission process could be translated as $s[L[y],t] = 1 \rightarrow Tx_{sub}(f_n)$. The protocol operating principle is as follows: The full neuron firing sequence raster plot knowledge is held inside the sub-dura transceiver. The sub-dura transceiver also has the knowledge of which WiOptND device is interfaced to a specific neuron. Based on a time-division access scheme, as the sub-dura transceiver scans through the raster plot and encounters a spike, it emits an ultrasound frequency f_i to charge the device.
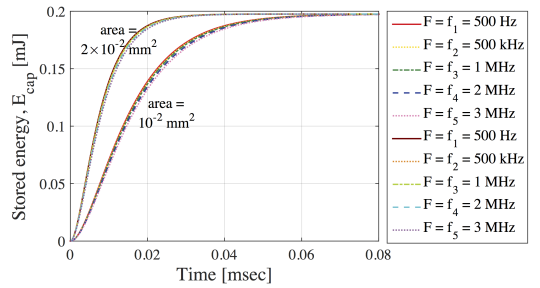
Fig. 8: Illustration of storage energy performance as a function of time with ultrasound frequency variations. The performance compares the storage energy performance for two different nanowires surface area.

The design of the circuitry is very simple, as soon as the ultrasound frequency is emitted, it immediately charges to the full capacity of the micro-supercapacitor, $E[n,t] \rightarrow E_{max}$, which in turn discharges and powers the LED. This leads to the illumination of the neuron. Based on our analysis in Fig. 7(b), the ultrasound wave emission will last approximately 1 ms in order to fully charge the micro-supercapacitor to maximum
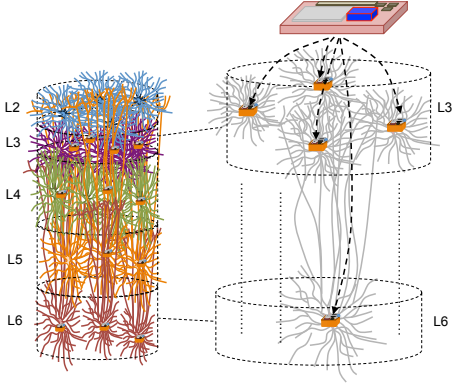
Fig. 9: WiOptNDs nanonetwork deployed in the cortical microcolumn, between $L2/3$ - $L6$.

capacity.

As an example, Fig. 10 illustrates how this protocol handles the firing pattern for three WiOptNDs. As shown in the figure, each of the WiOptND has a unique ultrasound frequency, which is based on the specific resonant frequency of the piezo element of the VOX. At approximately t_5, a misfiring occurs for WiOptND$_3$ and this is due to the clash in time-slot with the WiOptND$_1$ (in our proposed approach, the sub-dura transceiver can only emit ultrasound with a single frequency). While the protocol is very simple, and requires very basic circuitry, the major drawback is that the sub-dura transceiver is required to emit ultrasound signals at a unique frequency that corresponds to a device. This also becomes a major challenge, when we consider that the piezo element for addressing will also require different resonant frequencies that have considerable spacings to not lead to overlap with signaling other devices. However, by utilizing the photoacoustic effect of the intermediate material which has the property of rapid heating and thermoelastic expansion, the sub-dura transceiver can generate the desired ultrasound frequencies by adjusting the optical pulse duration and beam width [30]. Another limitation is that the sub-dura transceiver is required to have full knowledge of the raster plots for all the cortical micro-column functionalities.
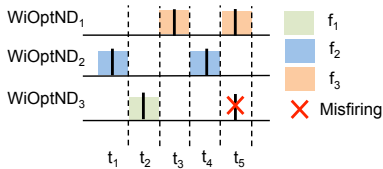
Fig. 10: *Charge and Fire* scans the neural spike sequence, and employs one-to-one relation between frequency transmission from the sub-dura transceiver, and the WiOptND that needs to be charged to stimulate a neuron. More than one neural spikes in a single time-slot leads to a misfiring event.

B. Predictive Sliding Detection Window

Since ultrasound signals will emanate to the entire region of the nanonetwork, this also means that all devices will automatically get charged each time a sub-dura transceiver emits an ultrasound signal. However, the fact that each device requires a unique resonant frequency addressing scheme, means that in the *Charge and Fire* protocol, the sub-dura transceiver will still need to signal each device. This results in excessive energy depletion of the sub-dura transceiver, and waste of repeated charging signals that are emitted to devices that have already been charged. At the same time, the diverse charging frequencies may be limited by the piezo element technologies that is used for the addressing scheme. Therefore, to address this issue, this section presents the *Predictive Sliding Detection Window*, which aims to, (1) lower the number of frequencies that are required to signal to all the WiOptNDs, and (2) minimize the emitted ultrasound frequencies from the sub-dura transceiver to lower the energy depletion, by exploiting a parallel charging scheme. In the case of (1), the different devices should respond to the same ultrasound frequency to charge multiple devices.

1) Parallel Charging: Fig. 11 illustrates an example of the *Predictive Sliding Detection Window* charging protocol. In this example, there are three different WiOptND devices and three ultrasound charging frequencies. As illustrated in Fig. 11 (a), each of the frequencies and the WiOptND devices forms a matrix M_{ii} that represents a random simulated pattern with respect to time. For example, ultrasound frequency f_1 signals WiOptND$_2$ in the first time-slot, $t = t_0$, followed by WiOptND$_3$ after one time-slot delay, $t = t_0 + 1$, and finally WiOptND$_1$ after another time-slot delay, $t = t_0 + 2$. This means that if ultrasound frequency f_1 is emitted at t_0, there needs to be a time delay for WiOptND$_3$ and WiOptND$_1$ before they can discharge to light the LED and stimulate the neuron. Frequencies f_2 and f_3 utilize similar three time-slot durations but implementing different pattern predictions as illustrated in Fig. 11 (a). The total frequencies and time-slots of one pattern can be dubbed as the size of the sliding detection window.

In Fig. 11 (b) - (f), the sliding detection window protocol is illustrated. The objective here is to slide the detection window and find the overlaps between the neuron firing sequence and time-slot of the pattern prediction for discharging the device. Starting at t_1 in Fig. 11 (b), the pattern prediction sequence for frequency f_1 perfectly matches to the sequence of spikes for WiOptND$_1$ and WiOptND$_3$. Compared to the other frequencies, the pattern of f_1 is able to accommodate parallel charging for most of the devices (2 out of 3). As the sliding window moves along, it continuously checks prediction matrix to decide which frequency pattern is the most compatible to be emitted. Fig. 11 (c) shows that for all the three frequencies, only one pattern matches to a device with a neural spike, which is WiOptND$_2$. Moving the sliding detection window along in Fig. 11 (d), the pattern of f_2 overlaps with two neural spikes of WiOptND$_1$ and WiOptND$_3$. The remaining process is illustrated for Fig. 11 (e) and (f).

Algorithm 1 explains in more detail the *Predictive Sliding Detection Window* protocol. Initialization of the number of
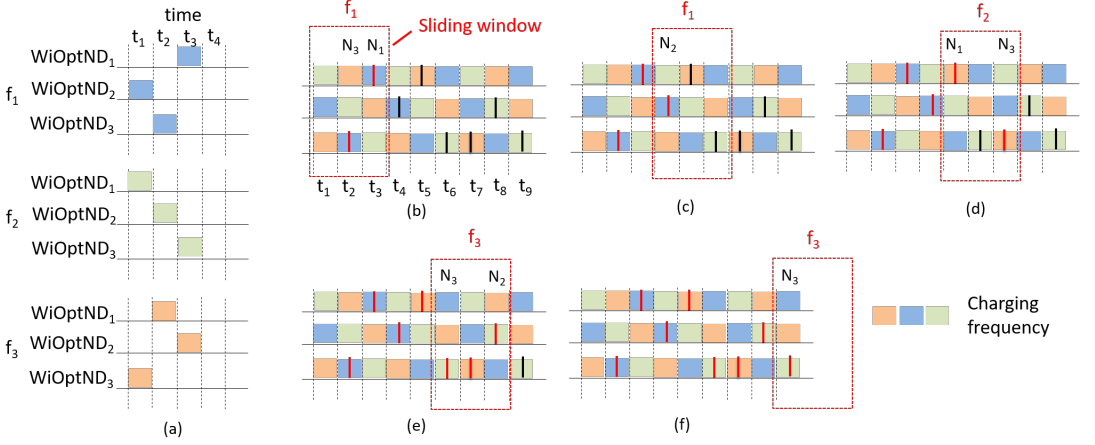
Fig. 11: Illustration of Sliding Detection Window mechanism utilizing three different frequencies/patterns. (a) presents the predicted patterns for 3 different frequencies for 3 WiOptNDs with respect to time. (b) - (f) illustrates the sliding window with respect to time, and the frequency used to charge the devices. The selected frequency is based on the highest number of parallel devices that can be charged in that window.

patterns and time-delays can be represented as the array matrix $P[1..n]$ where n is the total amount of neural spiking patterns. Based on the pattern prediction process, matrix M_{ij} is obtained which will be compared with the known neural spikes within each window. Before moving to the next phase, this protocol makes sure if the first time-slot of the detection window contains at least a spike. Afterwards, matrix M_{ij} will be truncated so that the size is matched with the matrix of the patterns. This truncated matrix M_{ii} is compared against all the patterns and the highest number of overlapping pattern is selected by emitting the corresponding frequency. Finally, when the selected frequency f_i has been radiated, corresponding spikes will be omitted and the protocol will analyze the next time-slot until it reaches the end of the pattern sequence.

Algorithm 1 Predictive Sliding Detection Window

1: Initialize P[1...n]   ▷ where n is total number of available frequencies
2: M_{ij} $PatternPrediction$
3: **for** a = 1 to j **do**
4:     $M_{ii} \leftarrow M[:, a : a - 1 + column(P[b])]$
5:     **if** $M[:, 1] \neq 0$ & $M_{ii} \neq 0$ **then**
6:         **for** b = 1 to n **do**
7:             $simTest \leftarrow$ compare $M_{ii} == P[b]]$
8:         **end for**
9:         $maxSim \leftarrow max(simTest)$
10:         $tempFiringSlot \leftarrow 2 \times P[maxSim] - M_{ii}$
11:         $M_{ii} \leftarrow tempFiringSlot$
12:     **end if**
13: **end for**

---

2) Circuitry: The challenge is that since each device is interfaced to different neurons that spike at different time-

slots, the charging process must consider the timing difference between the spikes when a single charging ultrasound frequency is emitted. This means that when an ultrasound frequency is emitted at t_{0+j}, a time-delay for a predicted overlap at $t > t_{0+j}$ is required for the circuit. This time delay will count down until the specific time-slot has arrived, at which point the charge will be released from the capacitor to light the LED. This could be achieved by adding a time-delay circuitry that extends over the original circuit presented in Fig. 5, and used in the *Charge and Fire* protocol. The circuit design of the WiOptND for the *Predictive Sliding Detection Window* is illustrated in Fig. 12. Depending on the detected frequency, the VOX switches on the desired time delay relay. As the switch closes, the capacitor C_1 is charged to forward bias the zener diode D_Z. This process activates the transistor T_1 whose collector is connected to the relay. To prevent the relay clicking, the capacitor T_2 is used to keep the base bias steady. The diode D_1 is to prevent counter-electromotive force (CEMF) as the transistor T_1 switched off. In this circuit, the value of C_1 determines the time delay period. In this circuit, the time-delay relay circuit is situated between the storage capacitor and the LED. The number of frequency-dependent switch and time-delay relay pairs corresponds to the number of operating frequencies used in the system. For instance, the set of frequencies $F = \{f_1, f_2, f_3, ..., f_i\}$, where the complete pattern that can be formed using i number of frequencies is $i!$ (factorial of i). However, the designated number of patterns are kept as an independent variable during the design process and currently it does not support real-time tuning.

3) Neural Spike Prediction: One limitation with the *Charge and Fire* protocol, is that the sub-dura transceiver is required to have the full knowledge of the raster plot neural spike sequence. This could be a major challenge, given that the
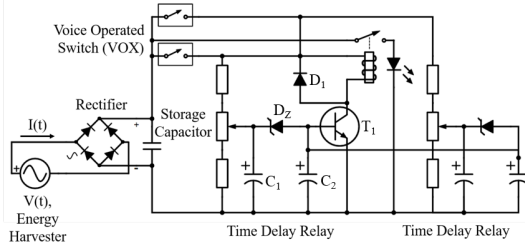
Fig. 12: WiOptND circuit diagram with integrated time-delay relay for the *Predictive Sliding Detection Window* protocol and its variant the *Markov-Chain based Time-Delay Patterns* protocol.

Fig. 13: Example deployment of the WiOptND nanonetwork in the Brain Visual Cortex. The neural circuit connection to the $V1$ primary visual cortex is impaired, requiring the deployment of WiOptNDs, where its coordinated stimulation will compensate for the failed neurons.

sequence changes for variations in activities (this will be illustrated later in Sec. VI-B4, when we demonstrate the changes in the raster plot of the *macaque monkey's* visual cortex). Since the *Predictive Sliding Detection Window* protocol is already predicting the neural spikes, one approach is to augment the protocol with existing neural spike prediction solutions. In particular, since the sliding window is required to scan future spikes, a prediction process can be integrated. Numerous research has investigated prediction processes for neural spikes, where in majority of the cases *in-vivo* neuronal system have been known to contain patterns that corresponds to a certain stimulus [31]. For example, when *retinal cells* receive visual information, this data is conveyed through the optic nerve and stimulates neurons firing in the *V1 primary visual cortex*. The pattern of the neural spikes is directly related to the light intensity, and determines four related parameters which includes the time of occurrence, number of spikes, jitter periods, and number of jitters [32]. In this paper, we employ this specific neural spike prediction process which is illustrated in Fig. 13. In this scenario, a light to electrical converter will wirelessly transmit signals to the external transceiver based on changes in the light intensity, which is then transmitted to the sub-dura transceiver, and this is used to guide the charging protocol.

Based on the mathematical model in [32], the pattern prediction maps of the firing rate and spiking sequence is formulated as follows:

$$r(t) = \delta(h(t)) - \theta)\dot{h}(t)H(\dot{h}(t)) \quad (10)$$

considering

$$h(t) = g(t) + a(t) + \int_{-\infty}^{t} r(\tau)(1+b(\tau))P(t-\tau)\,d\tau \quad (11)$$

$$g(t) = \int_{-\infty}^{t} s(\tau)F(t-\tau)\,d\tau \quad (12)$$

$$H(x) = \begin{cases} 1, & \text{if } x > 0 \\ 0, & \text{otherwise,} \end{cases} \quad (13)$$

where $r(t)$ is the sum of delta function spikes at one particular time instance when $h(t)$ crosses the threshold θ with a positive gradient slope. The function $g(t)$ defines the filtered time domain response for stimulus $s(t)$ and is obtained from the convolution operation with filter $F(t)$. The parameters $a(t)$ and $b(t)$ represent Gaussian noises, while $P(t)$ is a feedback potential. This particular model has proved to perform well when compared with real neural spiking patterns.

TABLE II: Simulation Parameters

Parameter	Value [Unit]	Description
Neural spike rate	100:5:130 [Hz]	Exponential dist.
Cortical column layers	4 [$layers$]	-
Number of predicted patterns	5, 10, 20	No. of Ultra. freq.
Raster plot period	10 [sec]	-
Number of data	10 [$cycles$]	Sim. cycles/freq.

4) Evaluation: In this section, we evaluate the performance of the *Predictive Sliding Detection Window* protocol, and compare this to the *Charge and Fire* protocol, using the light stimulated neural spike prediction model of [32] as a case study. We will first define the metrics that is used in our evaluation. The total neural spike misfiring number, n_{mis}, is represented as:

$$n_{mis} = \sum_{t=0}^{T} \sum_{y=0}^{|L|} \left[\sum_{k=0}^{|L|} [\min(s(L[y],t), s(L[k],t))] \right] + H[L[y],t] \quad (14)$$

where

$$H[n,t] = \begin{cases} 0, & \text{if } E[n,t] < E_{max}, \\ 1, & \text{if } E[n,t] = E_{max}. \end{cases} \quad (15)$$

which represents whether the stored energy $E[n,t]$ is sufficient to turn on the LED at time t, by comparing it to the required energy E_{max}.

The neural spike misfiring ratio, stimulation efficiency ratio, and stimulation ratio can be formulated as:

$$\gamma_{mis}(L[y]) = \frac{n_{mis}}{\sum_{t=0}^{T} s[L[y],t]} \quad (16)$$

$$\eta_{stim}(L[y]) = 100\% - \gamma_{mis}(L[y]) \qquad (17)$$

$$\gamma_{stim}(L[y]) = \frac{\sum_{t=0}^{T}|Tx_{sub}[f_n,t]|}{\sum_{t=0}^{T}s[L[y],t]} \qquad (18)$$

where $\sum_{t=0}^{T}|Tx_{sub}[f_n,t]|$ is the total number of frequency transmission during period of T.

As mentioned above, the time-delay patterns affect the matching probability to the predicted neural spike sequence and this is related to the number of ultrasound resonant frequencies. In order to evaluate the protocols, simulations were conducted in Matlab with the parameters presented in Table II. The results presented in Fig. 14(a) and 14(b), compare the performance of the *Charge and Fire* and *Predictive Sliding Detection Window* protocols with respect to variations in the spike frequencies.

Stimulation ratio (18) defines how many times the sub-dura transceiver transmits the frequencies in comparison to the total amount of neural spikes. However, in terms of stimulation efficiency ratio (17) which defines the total amount of spikes successfully targeted during the stimulation process compared to the total amount of spikes, the randomness in the results is observed, and this can be attributed to the randomly chosen pattern predictions used.

Fig. 15(a) and 15(b) presents the performance analysis when the number of ultrasound frequencies/patterns and number of devices are varied. The number of devices has significant effect on the stimulation ratio, while the number of frequencies/patterns does not make a significant impact. This is due to the increased possibility of targeting multiple neural spikes based on using a smaller number of frequency transmission.

(a) Stimulation ratio vs Spike frequency.

(b) Stimulation efficiency ratio vs Spike frequency.

Fig. 14: Comparison of the stimulation and efficiency ratio for the randomly chosen patterns of the *Predictive Sliding Detection Window* and *Charge and Fire* protocols. The simulation generates the average and standard deviation values for WiOptNDs deployed in four layers of the cortical column of the cerebral cortex.

The results show that improved performance results from higher neural firing rate as the stimulation ratio decreases.

(a)

(b)

Fig. 15: The effect of the radiated ultrasound frequency quantity and the number of WiOptNDs on stimulation and efficiency ratio for *Predictive Sliding Detection Window*. Utilizing higher number of ultrasound frequencies/patterns does not have significant effect on the stimulation ratio, but it results in each stimulation process to be more efficient by targeting the desired neurons.

Our evaluation also considers how the changes in the firing patterns can affect the misfiring ratio. In this evaluation, we utilized the raster plot of the *Middle Temporal Cortex* neurons

of a *macaque monkey* when the visual image is dynamically changed. Fig. 16(a) illustrates two disks with moving dots that were used in the experiments. The initial image is presented on the left, where dots from Direction 1 and 2 are slowly moving from the center to the circle perimeter. This movement is later shifted as shown in the disk on the right. As we can see from the raster plot in Fig. 16(b), this small change in the image can totally change the sequence of neural spike patterns. This raster plot is related to the visual stimulus $s(t)$, which based on the model in (10) will yield to the predicted sequence $r(t)$ [33]. Tuning curve represents the graphical presentation of the neurons as a result of changes in the stimuli. For example, the tuning curve can provide firing rate fluctuation information as the angle of stimulus is varied (Fig. 16(a)). As the spike frequency increases, both stimulation and misfiring events are more likely to occur. This is simulated in Fig. 16(c) and 16(d) for both the *Predictive Sliding Detection Window* and the *Charge and Fire* protocols. However, we can observe that for lower spike frequencies, the *Charge and Fire* protocol experiences less misfirings since it scans each time-slots one by one, unlike the *Predictive Sliding Detection Window*, which uses the time-slot pattern matching based on the size of the window. The lower stimulation number in the plots also indicates the smaller number of radiated ultrasound signals from the sub-dura transceiver.

C. Markov-Chain based Time-Delay Patterns

While the previous section demonstrated the benefits of the *Predictive Sliding Detection Window* protocol, one issue is the generation of the pattern prediction sequences, which was randomly generated. In order to improve the accuracy, knowledge of the connectivity in the cortical layers could be utilized to determine the firing order patterns between neurons of each layer. This could be used to minimize the inaccuracies between the pattern prediction and the target neural spikes, which in turn minimizes the energy expenditure from the sub-dura transceiver. This section will discuss how the connectivity knowledge of the different neurons in the cortical layers can be utilized to improve the time-delay patterns.

Cortical columns of the brain gray matter are characterized by highly sophisticated connections for both the intra and inter layers. This complexity is largely based on the large number of neurons with over 125 trillions of synapses in the cortex alone [34]. There is an immeasurable effort from the neuroscience community in modelling cortex connections, and one proposal is a *discrete-time* Markov chain with $|L|$ states, each representing one layer of the cortical column. The transition probability matrix Pr is characterized by $|L| \times |L|$ elements, and P should satisfy $\forall i, j, Pr_{i,j} \in [0,1]$, and, $\forall i, \sum_{j=1}^{|L|} Pr_{i,j} = 1$. The markov chain representing the connectivity between the six layers of the cortical column is represented in Fig. 17 [35].

Even though synapses can be stimulated from different layers of the cortical column containing the WiOptND nanonetworks, the misfiring of neural spikes may still occur. This scenario can result from the frequent number of optogenetic excitation that occurs in layers with high connection distribution, which will result in the WiOptNDs of that layer to be

(a)

(b)

(c)

(d)
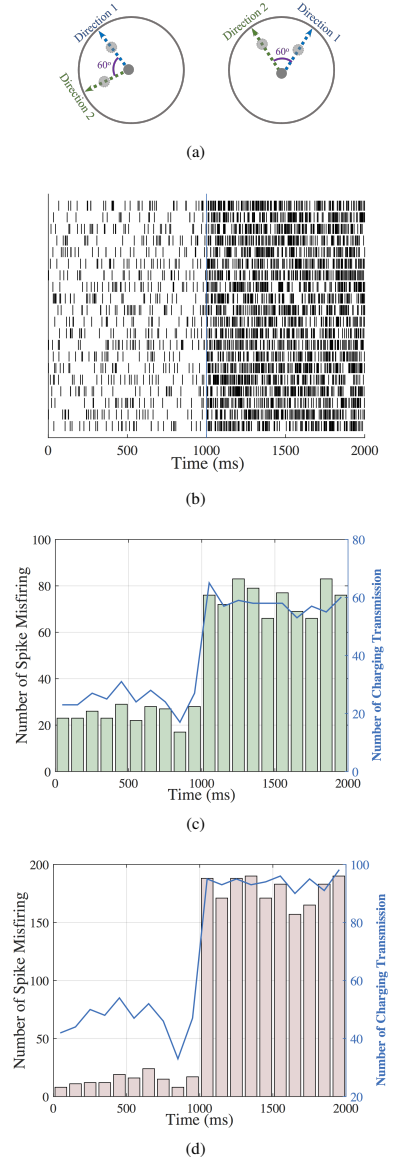
Fig. 16: (a) The illustration of bi-directional stimuli separated by 60° for achromatic random-dots pattern that is visually observed by a *macaque monkey*. (b) The raster plot simulation generated based on the experiment. As shown in the raster plot, both directions affect the neuron spike frequency response [33]. (c) and (d) presents the simulation results from the number of misfiring before and after the frequency transition for both the *Predictive Sliding Detection Window* and the *Charge and Fire* protocols.
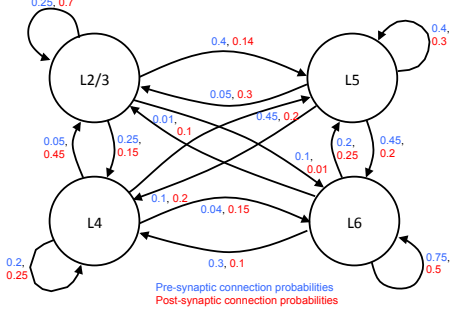
Fig. 17: Markov Chain model of inter and intra-layer connectivity for the cortical column.

TABLE III: Connection flow probability among cortical layers.

| | | Postsynaptic neuron | | | |
		II/III	IV	V	VI
Presynaptic	II/III		0.2	0.27	0.055
	IV	0.25		0.325	0.095
	V	0.175	0.15		0.325
	VI	0.055	0.2	0.225	

TABLE IV: Rank and Connection pattern.

Rank	Connection Patterns
1	$L[5] \to L[6] \to L[4] \to L[2/3]$
2	$L[4] \to L[5] \to L[6] \to L[2/3]$
3	$L[2/3] \to L[6] \to L[5] \to L[4]$
4	$L[6] \to L[4] \to L[5] \to L[2/3]$
⋮	
24	$L[6] \to L[2/3] \to L[4] \to L[5]$

(a) Stimulation ratio vs Spike frequency.

(b) Stimulation efficiency ratio vs Spike frequency.

Fig. 18: Comparison of the stimulation and efficiency ratio of predefined patterns for the *Markov-Chain Time Delay Patterns* and the *Charge and Fire* protocols. The simulation generates the average and standard deviation values of devices deployed in four layers of the cortical column of the cerebral cortex.

discharged more frequently. Therefore, the selection of these layers with high centrality for charging will highly depend on the probability of connectivity between the layers as illustrated in Fig. 17, and this particular property can be utilized to improve the *Predictive Sliding Detection Window* protocol.

We can calculate the distribution of a connection either entering to a layer (pre-synaptic synapse - Pr_{pre}) or leaving a layer (post-synaptic synapse - Pr_{post}). For the Markov chain depicted in Fig. 17, the difference between the two is in the transition probabilities. The probability of the connection distribution $L[y]$ for layer y can be represented as:

$$Pr(L[y]) = E[Pr_{pre}(L[y]) + Pr_{post}(L[y])], \quad (19)$$

where $E[.]$ is the expected value, $P_{pre}(.)$ is the probability of a pre-synaptic connection and $P_{post}(.)$ is the probability of a post-synaptic connection for a layer. These probabilities can be calculated in the same way, but ultimately the behaviour is different due to the transition probability values. Therefore,

$$Pr_{(.)}(L[y]) = \frac{\sum_{k=0}^{|L|} Pr(L[k]|L[y])}{\sum_{n=0}^{|L|} \sum_{m=0}^{|L|} Pr(L[n]|L[m])}. \quad (20)$$

Using the $Pr(L[y])$, the predefined time-delay patterns can be adjusted based on the $\max\{\forall Pr(L[y])\}$. According to the number of cortical layers, there are $|L|!$ possible patterns to be selected from. The connection probability is summarized in Table III. An example of a single connection comparison is between $Pr(L[5] \to L[6]) = 0.325$ and $Pr(L[5] \to L[4]) = 0.15$, which means that the connection flow from layer V to layer VI is more probable than to layer IV. For this reason, in the connection ranking process, a connection from Layer V to layer VI will be placed higher. Table IV presents a partial table of the ranks for all the feasible connection patterns of the four layers in the cortical column. The combination of connection chain probability is used for the ranking process. Based on the analysis, the pattern of $L[5] \to L[4] \to L[6] \to L[2/3]$ is ranked the highest, while the $L[6] \to L[2/3] \to L[4] \to L[5]$ is ranked the lowest. By listing all the $|L|! = 4! = 24$ possible connections (Table IV), each predicted sequence patterns can be assigned to the available frequencies. For a frequency set of $F = \{f_1, f_2, f_3, ..., f_i\}$, there are i individual frequencies which can be mapped to i ranked sequences in the list.

Based on the predefined connection ranking table that is used to define the pattern predictions for selected frequencies, simulations in MATLAB was conducted and the results are presented in Fig. 18. The stimulation ratio shows stable decreasing trend with respect to the neuronal spiking rate. However, lower stimulation ratio does not always translate to higher efficiency if it results in higher number of spike misfiring. This is reflected in the stimulation efficiency ratio result. The efficiency ratio of *Charge and Fire* protocol experiences steep decrement as the the firing rate increases, where we can see that when the firing rate reaches $130\ Hz$, the *Markov-Chain based Time Delay Patterns* with 5 patterns starts to outperform the *Charge and Fire* protocol. This is due to the nature of the sliding detection window protocol in targeting several firing sequences of the neurons based on low number of ultrasound frequency charging. Compared to the randomly chosen pattern simulation (Fig. 14), the stimulation efficiency is higher with smaller standard deviation showing consistent improvement.

VII. Conclusions

The increased attention towards brain stimulation has attracted researchers to search for innovative solutions that can enable long-term deployment as well as design of miniaturized devices that can self-generate power. At the same time, the emergence of optogenetics has provided a new approach for precise stimulation at the single neuron level. In this paper, we propose the WiOptND that is constructed from nanoscale components and can be embedded into the cortex of the brain to stimulate neurons using light. A thorough description of the circuitry, as well as the components, are presented, including mechanisms of generating power through ultrasonic wave vibrations. The paper presented simulation results on the behaviour of optical light transmission and its effect on the brain tissue, as well as the energy performance of the device based on variations of ultrasonic frequencies and circuitry devices (e.g. capacitors and piezoelectric nanowire area). A number of charging protocols have also been evaluated ranging from the simple *Charge and Fire* to the *Predictive Sliding Detection Window*, and its variant the *Markov-Chain Time Delay Patterns*. The *Predictive Sliding Detection Window* utilizes predicted patterns of ultrasound frequencies to match to the neural spike patterns. The difference between the protocols is to improve energy efficiency by lowering the number of ultrasound emissions from the sub-dura transceiver while ensuring that neural spike misfiring ratio is low. In particular, the *Markov-Chain Time Delay Patterns* extension protocol resulted in the best performance. However, when the efficiency ratio is considered, the protocol highly depends on the neural spike rate and number of applied predicted patterns. The results from our simulation study have demonstrated the feasibility of using the WiOptND nanonetworks for long term deployments in the brain in order to stimulate neurons and provide new approaches for treating neurological diseases.

Acknowledgment

References

[1] L. E. Hebert, J. Weuve, P. A. Scherr, and D. A. Evans. Alzheimer disease in the United States (2010–2050) estimated using the 2010 census. *Neurology*, 80(19):1778–1783, 2013.

[2] E. Dorsey, R. Constantinescu, J. Thompson, K. Biglan, R. Holloway, K. Kieburtz, F. Marshall, B. Ravina, G. Schifitto, A. Siderowf, et al. Projected number of people with parkinson disease in the most populous nations, 2005 through 2030. *Neurology*, 68(5):384–386, 2007.

[3] D. M. Huse, K. Schulman, L. Orsini, J. Castelli-Haley, S. Kennedy, and G. Lenhart. Burden of illness in parkinson's disease. *Movement Disorders*, 20(11):1449–1454, 2005.

[4] A. Gustavsson, M. Svensson, F. Jacobi, C. Allgulander, J. Alonso, E. Beghi, R. Dodel, M. Ekman, C. Faravelli, L. Fratiglioni, et al. Cost of disorders of the brain in Europe 2010. *European Neuropsychopharmacology*, 21(10):718–779, 2011.

[5] R. Strother, J. Mrva, and G. Thrope. Implantable pulse generator for providing functional and/or therapeutic stimulation of muscles and/or nerves and/or central nervous system tissue, Oct. 12 2010. US Patent 7,813,809.

[6] X. Han. In vivo application of optogenetics for neural circuit analysis. *ACS Chemical Neuroscience*, 3(8):577–584, 2012.

[7] K. J. Weegink, P. A. Bellette, J. J. Varghese, P. A. Silburn, P. A. Meehan, and A. P. Bradley. A parametric simulation of neuronal noise from microelectrode recordings. *IEEE Transactions on Neural Systems and Rehabilitation Engineering*, 25(1):4–13, 2017.

[8] S. A. Wirdatmadja, S. Balasubramaniam, Y. Koucheryavy, and J. M. Jornet. Wireless optogenetic neural dust for deep brain stimulation. In *e-Health Networking, Applications and Services (Healthcom), 2016 IEEE 18th International Conference on*, pages 1–6. IEEE, 2016.

[9] H. Guo, P. Johari, J. M. Jornet, and Z. Sun. Intra-body optical channel modeling for in vivo wireless nanosensor networks. *IEEE Transactions on NanoBioscience*, 15(1):41–52, 2016.

[10] T. Khan, B. A. Bilgin, and O. B. Akan. Diffusion-based model for synaptic molecular communication channel. *IEEE Transactions on NanoBioscience*, 2017.

[11] D. Malak and O. B. Akan. A communication theoretical analysis of synaptic multiple-access channel in hippocampal-cortical neurons. *IEEE Transactions on Communications*, 61(6):2457–2467, 2013.

[12] G. Nagel, T. Szellas, W. Huhn, S. Kateriya, N. Adeishvili, P. Berthold, D. Ollig, P. Hegemann, and E. Bamberg. Channelrhodopsin-2, a directly light-gated cation-selective membrane channel. *Proceedings of the National Academy of Sciences*, 100(24):13940–13945, 2003.

[13] X. Han and E. S. Boyden. Multiple-color optical activation, silencing, and desynchronization of neural activity, with single-spike temporal resolution. *PloS One*, 2(3):e299, 2007.

[14] B. Y. Chow, X. Han, A. S. Dobry, X. Qian, A. S. Chuong, M. Li, M. A. Henninger, G. M. Belfort, Y. Lin, P. E. Monahan, et al. High-performance genetically targetable optical neural silencing by light-driven proton pumps. *Nature*, 463(7277):98–102, 2010.

[15] D. Seo, J. M. Carmena, J. M. Rabaey, E. Alon, and M. M. Maharbiz. Neural dust: An ultrasonic, low power solution for chronic brain-machine interfaces. *arXiv preprint arXiv:1307.2196*, 2013.

[16] V. B. Mountcastle. *Perceptual neuroscience: the cerebral cortex*. Harvard University Press, 1998.

[17] G. E. Santagati and T. Melodia. An implantable low-power ultrasonic platform for the internet of medical things. In *INFOCOM 2017-IEEE Conference on Computer Communications, IEEE*, pages 1–9. IEEE, 2017.

[18] M. Cope. *The development of a near infrared spectroscopy system and its application for non invasive monitoring of cerebral blood and tissue oxygenation in the newborn infants*. PhD thesis, University of London, 1991.

[19] F. Scholkmann and M. Wolf. General equation for the differential pathlength factor of the frontal human head depending on wavelength and age. *Journal of Biomedical Optics*, 18(10):105004–105004, 2013.

[20] E. S. Boyden, F. Zhang, E. Bamberg, G. Nagel, and K. Deisseroth. Millisecond-timescale, genetically targeted optical control of neural activity. *Nature Neuroscience*, 8(9):1263–1268, 2005.

[21] A. Yaroslavsky, P. Schulze, I. Yaroslavsky, R. Schober, F. Ulrich, and H. Schwarzmaier. Optical properties of selected native and coagulated human brain tissues in vitro in the visible and near infrared spectral range. *Physics in Medicine and Biology*, 47(12):2059, 2002.

[22] S. H. Song, A. Kim, and B. Ziaie. Omnidirectional ultrasonic powering for millimeter-scale implantable devices. *IEEE Transactions on Biomedical Engineering*, 62(11):2717–2723, 2015.

[23] R. J. Przybyla, S. E. Shelton, A. Guedes, I. Izyumin, M. H. Kline, D. Horsley, B. E. Boser, et al. In-air rangefinding with an aln piezoelectric micromachined ultrasound transducer. *IEEE Sensors*, 11(11):2690–2697, 2011.

[24] M. Kim, J. Kim, and W. Cao. Electromechanical coupling coefficient of an ultrasonic array element. *Journal of Applied Physics*, 99(7):074102, 2006.

[25] P. R. Hoskins, K. Martin, and A. Thrush. *Diagnostic ultrasound: physics and equipment*. Cambridge University Press, 2010.

[26] K. Uchino. High electromechanical coupling piezoelectrics-how high energy conversion rate is possible. *MRS Online Proceedings Library Archive*, 459, 1996.

[27] M. Donohoe, S. Balasubramaniam, B. Jennings, and J. M. Jornet. Powering in-body nanosensors with ultrasounds. *IEEE Transactions on Nanotechnology*, 15(2):151–154, 2016.

[28] J. M. Jornet and I. F. Akyildiz. Joint energy harvesting and communication analysis for perpetual wireless nanosensor networks in the terahertz band. *IEEE Transactions on Nanotechnology*, 11(3):570–580, 2012.

[29] M. Beidaghi and C. Wang. Micro-supercapacitors based on interdigital electrodes of reduced graphene oxide and carbon nanotube composites with ultrahigh power handling performance. *Advanced Functional Materials*, 22(21):4501–4510, 2012.

[30] G. E. Santagati and T. Melodia. Opto-ultrasonic communications for wireless intra-body nanonetworks. *Nano Communication Networks*, 5(1):3–14, 2014.

[31] M. J. Schnitzer and M. Meister. Multineuronal firing patterns in the signal from eye to brain. *Neuron*, 37(3):499–511, 2003.

[32] J. Keat, P. Reinagel, R. C. Reid, and M. Meister. Predicting every spike: a model for the responses of visual neurons. *Neuron*, 30(3):803–817, 2001.

[33] J. Xiao and X. Huang. Distributed and dynamic neural encoding of multiple motion directions of transparently moving stimuli in cortical area mt. *Journal of Neuroscience*, 35(49):16180–16198, 2015.

[34] R. Marois and J. Ivanoff. Capacity limits of information processing in the brain. *Trends in Cognitive Sciences*, 9(6):296–305, 2005.

[35] B. B. Project. Digital reconstruction of neocortical microcircuitry (microcircuit fact sheet). https://bbp.epfl.ch/nmc-portal/microcircuit. Accessed: 17-03-2017.

PUBLICATION

III

Wireless communications for optogenetics-based brain stimulation: Present technology and future challenges

S. Balasubramaniam, S. A. Wirdatmadja, M. T. Barros, Y. Koucheryavy, M. Stachowiak and J. M. Jornet

Wireless Communications for Optogenetics-based Brain Stimulation: Present Technology and Future Challenges

Sasitharan Balasubramaniam, Stefanus A. Wirdatmadja, Michael Taynnan Barros, Yevgeni Koucheryavy, Michal Stachowiak, Josep Miquel Jornet

Abstract—The ability to decipher brain functions and understand the neuronal communication networking properties to develop innovative solutions to treat neurodegenerative diseases remains to be one of the biggest challenges in biomedicine. Since the early days, numerous solutions have been proposed for Brain Machine Interface (BMI), largely concentrating on the use of tethered electrodes that are inserted into the brain to either stimulate or suppress neural activities. In recent years, the field of optogenetics has provided a new alternative of utilising light to stimulate genetically engineered neurons. While the original approach has proposed the use of tethered optical cables inserted into the skull to transfer light into the brain for stimulation, numerous advances have been made to incorporate wireless technologies that will allow these devices to be attached to the skull or implanted into the brain. This article presents a review on the current technologies that have been proposed for different wireless optogenetics solutions, ranging from devices that are head mounted to miniature devices that can be embedded deep into the brain. We focus on a comparative analysis of the architecture and structure of the devices, the wireless technology used for signaling to the unit, as well as the energy consumption profile for each of the devices. Finally, the article presents future challenges to further miniaturize wireless optogenetic devices, concentrating specifically on the communication properties.

Index Terms—Wireless optogenetics, Brain Stimulations, Ultrasound, Nano and Molecular Communications.

❖

1 INTRODUCTION

Neurodegeneration, which is a systematic cause of neuron death, can lead to a number of diseases that includes Alzheimer's, Parkinson's, as well as Amyotrophic Lateral Sclerosis. The field of *Brain Machine Interface* (*BMI*) [1] aims to support patients who suffer from neurodegenerative diseases. The traditional BMI method is based on electrical simulation, which is also known as *focal brain stimulation*. This method requires implanting electrodes deep into the brain, and is widely used in neuroscience for providing therapeutic effects to patients with epilepsy and Parkinson's disease. A more recent approach is based on optogenetics, which aims to utilise light to stimulate genetically engineered neurons, providing a better option for controlling the cells compared to the conventional electrical stimulation [2]. First, it can excite the particular neuron with approximately 10% higher precision [2]. Second, for neural activity recording using light stimulation, activity recording can be easily conducted since there is no electromagnetic interference. Third, with light stimulation, the target cells can be restricted only to certain cells which are genetically engineered as opposed to the electric stimulation. This provides a very fine granular control of neural circuits, which to date has been a major challenge. Unlike electrical brain stimulation, optogenetics has not yet been clinically tested on human's brain. Recently, *Retina Foundation of the Southwest*, through the

Sasitharan Balasubramaniam, Stefanus A. Wirdatmadja, and Yevgeni Koucheryavy are with the Department of Electrical Engineering and Communications, Tampere University of Technology, Finland. Emails: {sasi.bala,stefanus.wirdatmadja}@tut.fi; yk@cs.tut.fi. Michael Taynnan Barros is with TSSG, Waterford Institue of Technology, Ireland. Email: mbarros@tssg.org. Michal K. Stachowiak is with the Department of Pathology and Anatomical Sciences, University at Buffalo, State University of New York. Email: mks4@buffalo.edu. Josep M. Jornet is with the Department of Electrical Engineering, University at Buffalo, State University of New York. Email: jmjornet@buffalo.edu.

sponsorship of *RetroSense Therapeutics*, plans to carry out the first clinical trial on human patients with *retinitis pigmentosa*.

The early solutions for optogenetics utilised optical fibers that are inserted into the skull to stimulate the neurons, which are impractical for daily use. However, in recent years, thanks to the wireless communications community, advancements have been made by incorporating wireless technologies for optogenetics to make them less invasive [2]. In this paper, we review a number of solutions for wireless optogenetics, where we investigate the use of wireless communication for head mountable devices to the more recent approaches of miniaturization that can be embedded into the cortex. Building on this, we provide a number of future challenges for further miniaturization of wireless optogenetics, touching in particular on the challenges for communications as well as other emerging applications.

The paper is organised as follows: Section II presents background on optogenetics. Section III presents a comprehensive review of current solutions for wireless optogenetics, while section IV presents the future challenges. Lastly, section V presents the conclusion.

2 BACKGROUND ON OPTOGENETICS

Before realizing the full operation of the optogenetic system, the first step is to genetically engineer the neurons by specific transmembrane proteins (*opsins*) (Fig. 1). These proteins include *Channelrhodopsin 2* (*ChR2*) for triggering action potential, *Halorhodopsin* (*Halo*) for neural activity inhibition, and *Archaerhodopsins* (*Arch*) which hyperpolarizes the neuron (action potential inhibition). The next step is light stimulation. The ChR2 is a light-gated ion channel, where upon illumination of blue light will result in the opening of cation channel depolarize the neuron.

On the other hand, NpHR (Halorhodopsin) is a light-controlled pump, which injects chloride ions into the neuron upon yellow light illumination, resulting in an inhibitory effect.

The current choice of optical neurostimulation components are limited to lasers or μ-LED (micro-Light Emitting Diode). Laser and laser diodes require high power consumption, slow warm-up time, high cost, and the use of tethered optical fibers to steer the light. However, they use narrow spectral bandwidth to produce high light intensity with low beam divergence. On the other hand, μ-LED has advantages in terms of wavelength range, low cost, power consumption, stable illumination, compact size, and fast response. The examples of the wavelength range with respect to the required power include, blue μ-LED (465 nm) that can deliver 25 mW, while yellow μ-LED (585 nm) can only deliver 3 mW from 200 μm diameter optical fiber. Sufficient power is also required for the μ-LEDs to trigger the optogenetic process. Therefore, a challenge for miniaturization and implantable wireless optogenetics is the ability to harvest the energy or wirelessly transfer the energy.

There are two methods of creating optogenetic construct in animals. First is the transgenic method where animals are bred specifically with optogenetic induced cells. The second is through virus injection for gene therapy to an existing neuron, which is more suitable as long as there is no rejection from the immune system. Another novel method is culturing and engineering in-vitro neurons that can be implanted into the human brains. Currently, the optogenetic applications for humans is being planned for clinical trials in the near future.
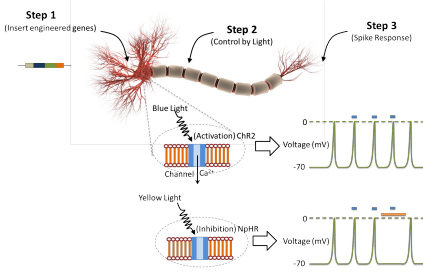

Fig. 1. Illustration of Wireless Optogenetic. Step 1 requires engineered genes to be placed in the neuron. Step 2 illustrates the wireless optogenetic process, where light is emitted onto the neurons that will either lead to stimulation or inhibition (step 3).

3 CURRENT DEVELOPMENTS

Fig. 2 illustrates a subset of solutions that we will discuss in this section, where we start with head mounted to fully implantable units embedded into the brain or the nervous systems. The wireless communication technologies used for these solutions include IR (Infrared), HF/NFC (High Frequency/Near Field Communication), and UHF (Ultra High Frequency). We evaluate each device which respect to their size, device construction, and wireless technology. The consideration for selecting the appropriate technology includes propagation characteristics in the medium, size of the device, and power sufficiency. Based on this, we provide a comparison in Table 1 between the different wireless optogenetic solutions, including ultrasound which is part of our proposed system in this article. In terms of signal propagation performance, ultrasound should be considered instead of IR, HF/NFC and UHF technologies. In parallel, the ultrasound energy has lower attenuation in biological tissues. According to FDA (Food and Drug Administration) regulation, the ultrasound exposure threshold level on the human body is 720 mW/cm^2, while RF is 10 mW/cm^2. The drawback of ultrasound technology is the manufacturing complexity. As the frequency goes up, the antenna size gets smaller, which makes the usage of both HF and UHF technologies more appealing for device miniaturization. In conclusion, BMI design has to consider specific types of communication for different types of application for a superior communication performance.

3.1 WIRELESS OPTOGENETICS BASED ON INFRARED (IR)

3.1.1 WIRELESS OPTOFLUIDIC SYSTEMS

Device Properties: The device presented in [3], and illustrated in Fig. 2 (a), combined drug delivery pharmacology and optogenetics stimulation. The drug delivery is through the microfluidic channel that also contains the microscale inorganic light emitting diodes (μ-ILEDs) based on Gallium Nitride (GaN) used for the opto-stimulation. The major novelty of this solution is that the conventional rigid metal cannulas and fiber optics are replaced by four miniature, soft, and flexible microfludic channels made of 50 μm thick and $\sim$450 μm width *elastomer polydimethylsiloxane* (*PDMS*) and μ-ILEDs. Each channel has cross-sectional area of $10 \times 10 \ \mu m^2$. The PDMS material used for the microfluidic channel is so transparent, that 95% of 400-700 nm wavelength is able to traverse through.

Energy Management: Two small rechargeable lithium ion batteries are used as the power source. The weight of the battery

TABLE 1
Comparison of different wireless optogenetic solutions.

| Wireless Technology	Frequency	Pros	Cons
Infrared (IR) [3] [4]	300 GHz - 430 THz	Low power consumption; Multi-band transmissions.	LoS between base station and implanted unit; Requires a battery unit for the head unit.
High Frequency (HF) [5]	3 - 30 MHz	Medium propagation loss in biological tissue; Cheap and easy to manufacture; Supports energy harvesting circuitry.	Coil dimension of approx. 1 cm; Requires surface mounted chip (NFC).
Ultra High Frequency (UHF) [6] [7] [8]	300 MHz - 3 GHz	Smaller coil diameter than HF circuitry; Cheap and easy to manufacture; Supports energy harvesting circuitry.	High propagation loss in biological tissue.
Ultrasound [9]	$\geq$ 20 kHz	Low propagation loss in biological tissue; Size of hundreds of μm; Supports energy harvesting circuitry; Safe utilisation in human tissue.	Complex circuit manufacturing; Difficulty in ultrasound frequency addressing.
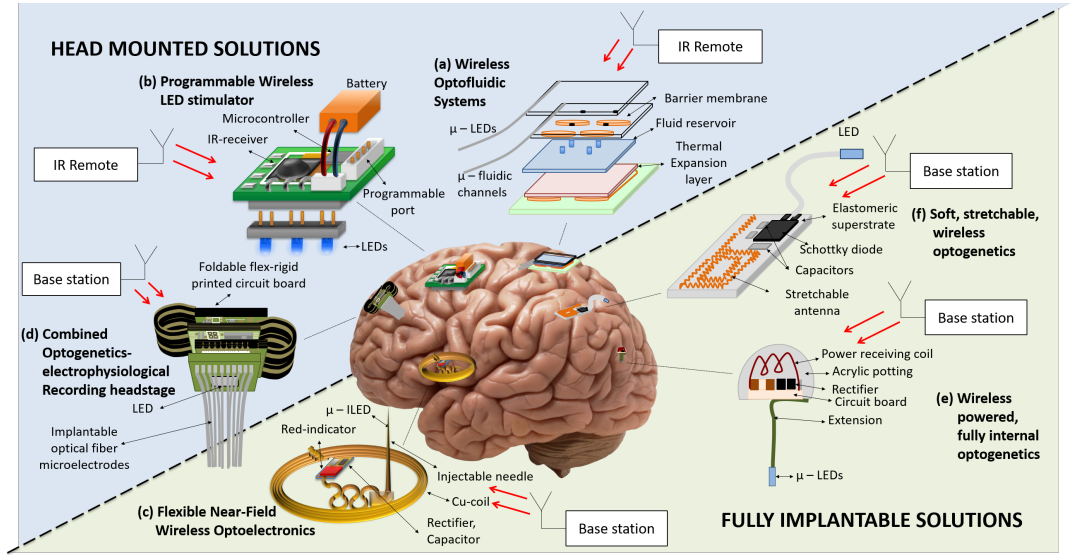
Fig. 2. Various solutions for wireless optogenetics illustrating the different scale of the devices, as well as their locations on the brain.

is approximately 330 mg and the dimension is $3 \times 9 \times 10$ mm^3 with an operating voltage of 3.6 V.

Communications: The signaling between a base station and a head-mounted receiver using IR is based on 10 ms pulse width with frequencies of 5, 10, 20, and 40 Hz. Since the receiver is programmed to distinguish different activation signal, the head-mounted receiver can have multiple functionalities for releasing certain drugs. While the IR signaling at multiple frequencies provides flexibility in controlling the device, the major disadvantage is the need for LoS (Line of Sight) communication which means there should be clear path between transmitter and receiver.

3.1.2 PROGRAMMABLE WIRELESS LED STIMULATOR FOR OPTO-GENETICS

Device Properties: A miniature wireless LED stimulator using multiband infrared and multicode signals was developed in [4] (Fig. 2 (b)). The system comprises three main components, i.e. IR transmitter for the operator to control the desired signals, LED stimulator mounted on the head and penetrating into the skull, and small LEDs to trigger the action potential on the optogenetic constructs.

Energy Management: The 12 V DC power to operate the IR transmitter is provided through an AC adapter. For the LED stimulator, the power is supplied using a lithium polymer battery whose output is 3.7 V at 10 mAh.

Communications: The IR transmitted signal comprises of three components, which includes the leader code, a 8-bit binary code, and a stop bit. These 8-bit binary codes consist of 256 unique identifications for each channel. These specific codes are used to identify multiple IR transmitter for crosstalk avoidance between the channels. Furthermore, the IR code can be modulated using amplitude shift keying to carrier frequencies of 30, 38, or 56 kHz, which features the multiband transmission.

As for the LED stimulator, 470 nm blue light LED is used to trigger the ChR2 proteins. Here, the received IR signals are decoded by an on board microcontroller which converts the 8 bit binary code in order to activate the LED. Using IR instead of RF transmission brings the advantage in term of weight, complexity in constructing the IR communication system, which also has benefits in terms of cost and power consumption. However, LoS transmission is still required for the IR communication.

3.2 WIRELESS OPTOGENETICS BASED ON HIGH FREQUENCY (HF)

3.2.1 FLEXIBLE NEAR-FIELD WIRELESS OPTOELECTRONICS

Device Properties: The device proposed in [5] incorporates a copper coil for power transmission with surface-mounted chip for control, a capacitor for impedance matching, a rectifier, and an μ-ILED for optogenetic excitation (Fig. 2 (c)). Since the copper coil is put on the surface of the brain, an injectable needle is required to precisely locate the target neurons. The bilayer encapsulation of *Parylene* and *Polydimethylsiloxane* applied on the device ensures the stability during the operation.

Energy Management: The energy transfer and control signaling is achieved through a combination of the copper coil and a micro-sized chip. The fundamental operation of the coil is based on the passive Near Field Communication (NFC) concept, which utilises electromagnetic induction. The total size of the coil is $9.8mm \times 60\mu m \times 18\mu m$. The optical output power of the device depends on the distance and orientation of the RF generator.

Communications: The NFC frequency of 13.56 MHz can accommodate transmission distance up to 30 cm between the RF generator and the receiver loop antenna. At the same time, multiple antenna operation can be supported using a multiplexer. Based on the voltage-current measurement, the power generated is sufficient enough to turn on the μ-ILEDs emitting different wavelengths (UV - 390 nm, blue - 470 nm, green - 540 nm, yellow - 580 nm, and red - 650 nm).

Using the NFC approach for both power transfer and optogenetic excitation introduces a cheap and relatively easy avenue towards manufacturing the device. From the propagation loss point of view, the HF band utilisation gives lower loss than UHF band. While this design is smaller than other similar design for BMI applications, the size of the coil (diameter of 9.8 mm) should still be considered for multiple device implementation.

3.3 WIRELESS OPTOGENETICS BASED ON ULTRA HIGH FREQUENCY (UHF)

3.3.1 COMBINED OPTOGENETICS AND ELECTROPHYSIOLOGICAL RECORDING WIRELESS HEADSTAGE

Device Properties: The combination of optogenetic stimulator and multichannel electrophysiologcal recording using wireless headstage is proposed in [6], and illustrated in Fig. 2 (d). This device facilitates both neural activity recording and optogenetics stimulation. The headstage is composed of two main components, i.e. foldable printed circuit board (PCB) and a detachable implanted module. A major issue with this solution is the large head mounted unit, which is impractical for daily use.

Energy Management: The power supply of the headstage unit is fairly bulky and supplied by a 3.7 V, 100 mAh Lithium-ion battery with a weight of 2.1 g, operating for 105 min. As far as stimulation efficiency is concerned, for a 150 mA stimulation current with 10% duty cycle at a firing rate of 45 spikes/s, it lasts approximately 70 mins.

Communications: The communication for transmitting control signals is from an external base station that operates on the 2.4 GHz frequency. The data rate is reasonably fast, reaching a maximum of 1.4 Mbps. For the light communication between the LED and the neuron used for the stimulation, this device uses a train of 10 ms pulse width with a current of 150 mA that is used to drive the 465 nm blue LEDs generating 70 mW/mm^2 light intensity.

3.3.2 WIRELESS POWERED, FULLY INTERNAL OPTOGENETICS

Device Properties: A fully implantable wireless optogenetic device for stimulating the brain, spinal cord, and peripheral circuits in mice is proposed in [7]. The radio-frequency transmitter is in the form of a relatively huge resonant cavity, allowing the animal to freely move. The entire light emitting implant, illustrated in Fig. 2 (e), weighs around 20-50 mg and has a size of 10-25 mm^3 which is claimed to be substantially smaller than the previous version of wireless optogenetic implants.

Energy Management: In terms of optogenetics stimulation, the μ-LED used in the system has an optimum efficiency (emitted light power/input power) of 19%. This power level is sufficient to emit the light power density required for optogenetics excitation, which is 1-20 mW/mm^2. Since the system utilises resonant cavity to transmit the energy by resonance inductive coupling, the mouse location interferes with the reception power. However, the center point of the resonant cavity has the highest measurement of light power density, which is approximately 27 mW/mm^2.

Communications: The wireless power transmission consists of a 1.6 mm diameter power receiving coil, while an aluminium resonant cavity (21 cm diameter, 15 cm height) was used as the transmitter. The wireless implant consists of the power receiving coil, rectifier, circuit board, and blue μ-LED. On the transmitter unit, the cavity radiates 1.5 GHz electromagnetic energy to wirelessly power the implant. Considering the propagation of the electromagnetic wave, the implanted device is placed around 3 cm above the resonant cavity, and this includes the floor surface structure in between. Since the system requires a large resonant cavity which radiates RF frequency to transmit power and control the implant, this is only suitable for a controlled lab environment not for daily use in patients.

3.3.3 SOFT, STRETCHABLE, WIRELESS OPTOGENETICS SYSTEM

Device Properties: The optoelectronic systems proposed in [8] utilised the combination of a stretchable filaments and a flexible polymer encapsulation, that was embedded into the spinal cord and peripheral nervous system (Fig. 2 (f)). The device comprises of four major components i.e. RF power-harvesting unit, rectifier, voltage multiplier, and a cellular-scale 470 nm LED. The durability of the entire unit has been tested by immersing into 37°C saline for two months, and for six days in 90°C supraphysiological temperature saline. Recently, authors in [10] developed this system including smaller and lighter implant, and multichannel antenna to control up to four reservoirs.

Energy Management: The unique design of the RF energy harvester uses a miniaturized stretchable antenna whose total surface area is 3×3 mm with an operational frequency of 2.3 GHz and a wide bandwidth of 200 MHz. This wider bandwidth, in comparison to conventional patch antenna that uses 50 MHz bandwidth, enables the device to harvest more energy. The transmitter antenna from the base station is located outside the body and transmits RF signals to power the device. The configuration of four transmitter antennas can distribute approximately 2 W which is sufficient for multiple devices activation within 20 cm range.

Communications: The same RF signal used for the energy harvester is also used for control signaling to activate the LED. The LED communicating to the neuron has an optical power density of 10 mW/mm^2, operating at a frequency of 20 Hz with 40% duty cycle, and pulse width of 20 ms. Even though the device has been improved by using flexible material compared to conventional rigid antenna, the size is still considered big for large scale deployments if they are to be embedded into different parts of the brain. In addition, they can be deformed due to movements and biological strains. This can shift the center frequency to lower values causing 12% coupling efficiency decrease for 30% strain in the worst case.

4 FUTURE CHALLENGES OF MINIATURIZATION

The previous section describes developments in miniaturization of wireless optogenetics devices, from head mounted units with implantable optical fiber cables, to fully wireless devices that can be embedded into the brain. However, the current solutions are still in the millimeter scale. In order to target long-term deployment into patients, to enable them to pursue a normal active life, further miniaturization is required. Fig. 3 (a) illustrates our proposed wireless optogenetic nanoscale device as well as the corresponding components. As illustrated in the figure, energy management will be a major issue, where a nano super-capacitor will be used to store energy that is coming from a harvesting source, such as piezoelectric nanowires [11]. Fig. 3 (b) illustrates how these devices can be embedded into the cortex of the brain, and using the architecture from [9], will receive power from a sub-dural transceiver, which in turn will receive power from an external transceiver. The size reduction of the device will minimize the irritation and other side effects on the tissue, such as excessive heating. However,
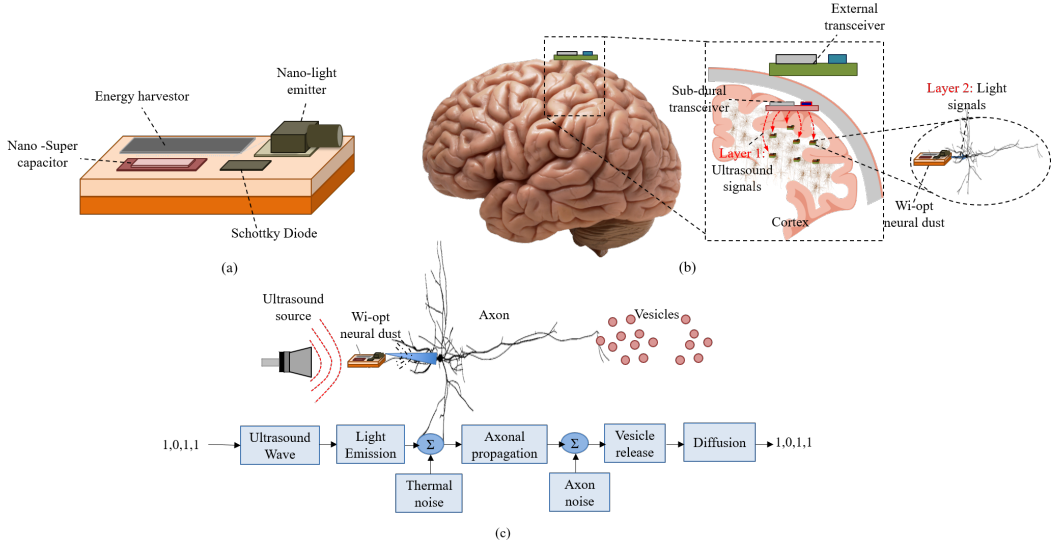
Fig. 3. Future miniaturization of wireless optogenetics unit: (a) proposed device architecture for a wireless optogenetic nanoscale device, (b) insertion of the wireless optogenetic nanoscale device in the cortex (the architecture includes a sub-dural transceiver that stimulates the device and provides the energy, where this in turn will receive signals from an external transceiver), (c) an interface of the wireless optogenetic nanoscale device to a neuron, illustrating the communication blocks from the light communication, to the vesicle release by the neuron.

this will result in a number of challenges, in particular from the constraints of the component size, and how this will affect the communication performance. The field of nano communications, which has emerged recently, can play a major role in directing the future evolvement towards miniaturisation. Fig. 3 (c) illustrates the communication representation of a miniature wireless optogenetic nanoscale device stimulating a neuron. In this section, we will present the challenges from the perspective of communications.

4.1 Communication Challenges

4.1.1 Data Link Layer

The challenge at the Data Link Layer lies mainly in the Layer 1 communication for *charging* as well as for *initiating* the device to stimulate light. This may require separate ultrasound beams for each of the two functionalities. The benefit of emitting ultrasound waves for charging is the fact that this could be performed in parallel due to the wide spread propagation of the signal that covers all the devices. The schedule for the initiation, however, will be dictated by the required firing patterns of the neuronal networks within the cortex (e.g., specific activities will require a certain pattern of neuron stimulation). Therefore, the scheduling of device initiation will vary and change depending on the user's activities, and this will be controlled by programming into the sub-dural transceiver. A challenge also lies in the optimal scheduling of emitting ultrasound waves for charging from the sub-dural transceiver to minimize energy depletion, since this device will be embedded under the skull and will also require energy harvesting capabilities on its own (e.g., heat or vibration).

4.1.2 Physical Layer

While miniaturization causes no significant impact on the Layer 1 communication, it will indeed have an impact on the Layer 2 light

emission propagation for optogenetics stimulation. Although the *Gallium Nitride (GaN)* μ-LEDs by McCall et al. [12] successfully decreased the thickness to only 6.5 μm, there are issues with temperature increase that limits the illumination duration. A major challenge also lies in the light propagation of light from a miniature source to ensure that maximum intensity is applied to the neuron's surface. This is also important due to the blockages that can occur from the soma, axons, and dendrites of neighbouring neurons. These components can block the light signal propagation and at the same time lead to excessive reflections, resulting from specular and diffusive scattered propagation. The light reflection from the cell material is also highly dependent on the contents of the cells (e.g., cytoplasm), and the coefficients of absorption and reflections are open research challenges. In [13], a nanoscale plasmonic antenna was proposed for emitting electromagnetic waves in the infrared spectrum. A similar approach can be developed for wireless optogenetics at the nanoscale, which may enable further miniaturization of the device.

4.1.3 Network Layer

One of the challenges in the network layer is addressing of the wireless optogenetic nanoscale devices for the Layer 1 ultrasound communication. Due to the minimal computational capabilities, utilising a bit sequence addressing scheme may not be a viable option, since a processor will be required for the device to process the signals. Integrating the processor, will in turn, also increase the size of the device. At the same time, a bit sequence of address for each device will also mean that the sub-dural transceiver will need to emit ultrasound signals for each bit (assuming a simple on-off keying modulation is used where the clocks of all the devices and the sub-dural transceiver are synchronised), leading to excessive energy depletion. Another option is to use separate

piezoelectric crystals that have different resonant frequencies, each corresponding to an address of a device. However, a question remains as to how scalable the network of the wireless optogenetic nanoscale devices will be, given the limited separation of the resonant frequencies between the different types of crystals.

4.1.4 Security Implications

A major issue is the security threats that wireless optogenetics nanonetworks can pose, and in particular if the operation of the devices can be controlled through the external signaling of Layer 1. This means that the external transceiver, and possibly the sub-dural transceiver will require security countermeasures from misbehaving malicious sources that would like to change the neural stimulation patterns. Since the wireless optogenetic units are below the skull, and will only operate in response to ultrasound signals, this prevents security threats from malicious ultrasound signals. However, a challenge lies in the signaling between the external transceiver and the sub-dural transceiver. Therefore, the challenge for the external transceiver as well as the sub-dural transceiver is to be able to recognize signals from malicious devices that aim to get access to stimulating the wireless optogenetic units. The security response must be performed instantly as soon as an attack is performed to minimize any harmful damage that can occur. Although the security threat is a challenge with our proposed miniaturization of wireless optogenetics, and its accompanying architecture, the threat also exists with the current implantable solutions. The communication security system on the higher layers (data link and network) is quite robust, since the units are implanted into the brain. The physical access to the unit itself are considerably difficult without surgical procedures to open the cranium. The security breach on this level can only be performed by inserting the intruder unit among the existing implanted units. This requires the opening of the cranium to implant the intruder unit.

4.2 Further Challenges

4.2.1 Interfacing to Molecular Communications

The field of molecular communications aims to develop artificial communication systems from biological components. In particular, the Internet of Bio-Nano Things (IoBNT) [14] will interface the artificial molecular communication systems to the Internet, through a Bio-Cyber Interface. The wireless optogenetic unit can represent a Bio-Cyber Interface that enters information into the brain as illustrated in Fig. 3 (c). In this form of communication, the bit transmission will be achieved through light stimulation of neuron that releases the vesicles to communicate to the post-synaptic neuron. The challenge is to engineer the neuron to respond to different light intensity, and at the same time having different synthetic circuits within the neuron that can produce varying concentration of vesicle release. The reconnection of the neurons (neuroplasticity) can further add noise into the network. This can affect how digital information is transmitted through the neurons as well as the scheduling sequence of light emission during stimulation.

4.2.2 Nanoscale Dual Stimulation and Recording

An ideal implantable device should incorporate monitoring and recording mechanisms. In [9], experimental validation have shown how the *neural dust mote*, which powers itself through vibrating piezoelectric crystal from an external ultrasound source, is able to monitor the nerve signaling based on back scattering. However, incorporating this onto the wireless optogenetic nanoscale devices will be challenging. The current device do not penetrate through the neuron, but rather emit light externally onto the cell, which implies the lack of a mechanism for sensing the electro-chemical signals propagated through the axon. Alternatively, the usage of electrodes (e.g., optrode, stereotrode and tetrode microdrives) can measure the signal along the axon. Another solution is to engineer the neurons to emit genetically encoded fluorescence-based indicator upon stimulation. Using this technique, each device can be incorporated with a molecular imaging module that will capture the stimulation process of the neuron. However, incorporating this may lead to an increase in the size and power requirements of the device.

4.2.3 Ethical Issues

Apart from technical and security challenges, ethical issues are another important issues for BMI, including the field of optogenetics. These ethical issues can be perceived from both personal and social points of view [15]. The patient's consent to access information on their brain functions will be mandatory and a major hurdle due to the fact that this can be categorized as mind reading, and potentially control a body subconsciously. This also includes the optogenetic implementation for humans, which will spark controversy on the use of genetic modification. From a social perspective, the integration between human and machine leads to liability issue if a misbehaved action is vaguely triggered by either human intention or machine error. Besides this, social interactions between BMI users and ordinary people in certain settings (e.g., competitions), may be questionable in terms of fairness in an individual's capabilities.

5 Conclusion

The emergence of optogenetic has proven to be an attractive solution for treating neurodegenerative diseases, and numerous advancements have been made in integrating wireless communication technologies to enable the devices to be implanted for long term applications. In this article we review a number of devices that have been proposed for wireless optogenetics, ranging from larger units that are head mounted with deep insertion into the cortex, all the way to miniature devices that can be implanted into the cortex. While enormous strides have been made in miniaturizing the wireless optogenetic devices, to the point that they can be embedded into the brain or the peripheral nervous systems, there still remains numerous challenges going forward into the future. The particular challenges are the ability to scale the devices down to the size of a typical neuron and having these devices interface directly one-to-one for specific types of neurons. Another emerging challenge is the ability to communicate and power these devices, while considering the side effects that can occur to the brain. In this article, we proposed the architecture that can realize wireless optogenetic nanoscale devices, where we also discuss the challenges from the perspective of communications. We specifically touched on the challenges at the physical, the data link, and the network layers, as well as discussions on the security implications, and how the new field of nano and molecular communication principles can be incorporated into the design consideration. Realizing the development of wireless optogenetic devices at the nanoscale can be a game changer for future Brain Machine Interface technologies, and at the same time address important challenges for treating neurodegenerative diseases.

REFERENCES

[1] C. T. Moritz, P. Ruther, S. Goering, A. Stett, T. Ball, W. Burgard, E. H. Chudler, and R. P. Rao, "New perspectives on neuroengineering and neurotechnologies: Nsf-dfg workshop report," *IEEE Transactions on Biomedical Engineering*, vol. 63, no. 7, pp. 1354–1367, 2016.

[2] S. Goncalves, J. Ribeiro, A. Silva, R. Costa, and J. Correia, "Design and manufacturing challenges of optogenetic neural interfaces: a review," *Journal of Neural Engineering*, vol. 14, no. 4, 2017.

[3] J.-W. Jeong, J. G. McCall, G. Shin, Y. Zhang, R. Al-Hasani, M. Kim, S. Li, J. Y. Sim, K.-I. Jang, Y. Shi *et al.*, "Wireless optofluidic systems for programmable in vivo pharmacology and optogenetics," *Cell*, vol. 162, no. 3, pp. 662–674, 2015.

[4] M. Hashimoto, A. Hata, T. Miyata, and H. Hirase, "Programmable wireless light-emitting diode stimulator for chronic stimulation of optogenetic molecules in freely moving mice," *Neurophotonics*, vol. 1, no. 1, pp. 011 002–011 002, 2014.

[5] G. Shin, A. M. Gomez, R. Al-Hasani, Y. R. Jeong, J. Kim, Z. Xie, A. Banks, S. M. Lee, S. Y. Han, C. J. Yoo *et al.*, "Flexible near-field wireless optoelectronics as subdermal implants for broad applications in optogenetics," *Neuron*, vol. 93, no. 3, pp. 509–521, 2017.

[6] G. Gagnon-Turcotte, Y. LeChasseur, C. Bories, Y. Messaddeq, Y. De Koninck, and B. Gosselin, "A wireless headstage for combined optogenetics and multichannel electrophysiological recording," *IEEE Transactions on Biomedical Circuits and Systems*, 2016.

[7] K. L. Montgomery, A. J. Yeh, J. S. Ho, V. Tsao, S. M. Iyer, L. Grosenick, E. A. Ferenczi, Y. Tanabe, K. Deisseroth, S. L. Delp *et al.*, "Wirelessly powered, fully internal optogenetics for brain, spinal and peripheral circuits in mice," *Nature Methods*, 2015.

[8] S. I. Park, D. S. Brenner, G. Shin, C. D. Morgan, B. A. Copits, H. U. Chung, M. Y. Pullen, K. N. Noh, S. Davidson, S. J. Oh *et al.*, "Soft, stretchable, fully implantable miniaturized optoelectronic systems for wireless optogenetics," *Nature Biotechnology*, vol. 33, no. 12, pp. 1280–1286, 2015.

[9] D. Seo, J. M. Carmena, J. M. Rabaey, E. Alon, and M. M. Maharbiz, "Neural dust: An ultrasonic, low power solution for chronic brain-machine interfaces," *arXiv preprint arXiv:1307.2196*, 2013.

[10] K. N. Noh, S. I. Park, R. Qazi, Z. Zou, A. D. Mickle, J. G. Grajales-Reyes, K.-I. Jang, R. W. Gereau, J. Xiao, J. A. Rogers *et al.*, "Miniaturized, battery-free optofluidic systems with potential for wireless pharmacology and optogenetics," *Small*, vol. 14, no. 4, 2018.

[11] M. Donohoe, S. Balasubramaniam, B. Jennings, and J. M. Jornet, "Powering in-body nanosensors with ultrasounds," *IEEE Transactions on Nanotechnology*, vol. 15, no. 2, pp. 151–154, 2016.

[12] J. G. McCall, T.-i. Kim, G. Shin, X. Huang, Y. H. Jung, R. Al-Hasani, F. G. Omenetto, M. R. Bruchas, and J. A. Rogers, "Fabrication and application of flexible, multimodal light-emitting devices for wireless optogenetics," *Nature Protocols*, vol. 8, no. 12, pp. 2413–2428, 2013.

[13] H. Guo, P. Johari, J. M. Jornet, and Z. Sun, "Intra-body optical channel modeling for in vivo wireless nanosensor networks," *IEEE Transactions on Nanobioscience*, vol. 15, no. 1, pp. 41–52, 2016.

[14] I. Akyildiz, M. Pierobon, S. Balasubramaniam, and Y. Koucheryavy, "The internet of bio-nano things," *IEEE Communications Magazine*, vol. 53, no. 3, pp. 32–40, 2015.

[15] K.-Y. Lee and D. Jang, "Ethical and social issues behind brain-computer interface," in *Brain-Computer Interface (BCI), 2013 International Winter Workshop on*. IEEE, 2013, pp. 72–75.

SASITHARAN BALASUBRAMANIAM (sasi.bala@tut.fi) received his bachelor (electrical and electronic engineering) and Ph.D. degrees from the University of Queensland in 1998 and 2005, respectively, and the masters (computer and communication engineering) degree in 1999 from Queensland University of Technology. He is currently an editor for IEEE Internet of Things and Elseviers Nano Communication Networks. His current research interests include Internet of Nano Things and molecular communication.

STEFANUS WIRDATMADJA (stefanus.wirdatmadja@tut.fi) received his B.Sc in electrical engineering from Universitas Indonesia, Depok, Indonesia, in 2005. He received his M.Sc in wireless communication circuits and system from Tampere University of Technology, Finland, in 2015. Currently, he is pursuing his Ph.D. degree with the Department of Electronics and Communications Engineering, Tampere University of Technology, Finland.

MICHAEL TAYNNAN BARROS (mbarros@tssg.org) received the B.Tech. degree in telematics from the Federal Institute of Education, Science and Technology of Paraiba, Brazil, in 2011, the M.Sc. degree in computer science from the Federal University of Campina Grande in 2012, and the Ph.D. degree in telecommunication software from Waterford Institute of Technology (WIT), Ireland, in 2016. He is currently an IRC Government of Ireland Postdoctoral Fellow associated with the Telecommunications Software and Systems Group, WIT.

YEVGENI KOUCHERYAVY (yk@tut.fi) is a full professor at the Laboratory of Electronics and Communications Engineering of Tampere University of Technology. He received his Ph.D. degree (2004) from Tampere University of Technology. He is the author of numerous publications in the field of advanced wired and wireless networking and communications. He is an Associate Technical Editor of IEEE Communications Magazine and an Editor of IEEE Communications Surveys & Tutorials.

MICHAL K. STACHOWIAK (mks4@buffalo.edu) has completed his Ph.D from the Gdansk Medical University, Poland, in 1980, and postdoctoral studies at the University of Pittsburgh. He is director of the Molecular and Structural Neurobiology and Gene Therapy Program and Western New York Stem Cell Engraftment and In Vivo Analysis Core. He has published more than 100 papers in reputed journals. His book: "Stem Cells - from Mechanisms to Technologies" (World Scientific Publishing) describes fundamental mechanisms in the biology of stem cells and their therapeutic utilization.

JOSEP MIQUEL JORNET [S'08–M'13] (jmjornet@buffalo.edu) is an Assistant Professor with the Department of Electrical Engineering, University at Buffalo, The State University of New York. From 2007 to 2008, he was a Visiting Researcher with the Massachusetts Institute of Technology (MIT), Cambridge, MA, USA. Since 2016, he has been the Editor-in-Chief of the Nano Communication Networks (Elsevier) Journal and serves in the Steering Committee of the ACM Nanoscale Computing and Communications Conference Series.

PUBLICATION

IV

Light propagation analysis in nervous tissue for wireless optogenetic nanonetworks

S. Wirdatmadja, P. Johari, S. Balasubramaniam, Y. Bae, M. K. Stachowiak and
J. M. Jornet

Publication reprinted with the permission of the copyright holders

Light Propagation Analysis in Nervous Tissue for Wireless Optogenetic Nanonetworks

Stefanus Wirdatmadja[a], Pedram Johari[b], Sasitharan Balasubramaniam[a], Yongho Bae[b], Michal K. Stachowiak[b], and Josep M. Jornet[b]

[a]Tampere University of Technology, Korkeakoulunkatu 10, Tampere, Finland
[b]University at Buffalo, The State University of New York, Buffalo, New York, USA

ABSTRACT

In recent years, numerous methods have been sought for developing novel solutions to counter neurodegenerative diseases. An objective that is being investigated by researchers is to develop cortical implants that are able to wirelessly stimulate neurons at the single cell level. This is a major development compared to current solutions that use electrodes, which are only able to target a population of neurons, or optogenetics, which requires optical fiber-leads to be embedded deep into the brain. In this direction, the concept of wireless optogenetic nanonetworks has been recently introduced. In such architecture, miniature devices are implanted in the cortex for neuronal stimulation through optogenetics. One of the aspects that will determine the topology and performance of wireless optogenetic nanonetworks is related to light propagation in genetically-engineered neurons. In this paper, a channel model that captures the peculiarities of light propagation in neurons is developed. First, the light propagation behavior using the modified Beer-Lambert law is analyzed based on the photon transport through the nervous tissue. This includes analyzing the scattering light diffraction and diffusive reflection that results from the absorption of neural cell chromophores, as well as validating the results by means of extensive multiphysics simulations. Then, analysis is conducted on the path loss through cells at different layers of the cortex by taking into account the multi-path phenomenon. Results show that there is a light focusing effect in the soma of neurons that can potentially help the to stimulate the target cells.

Keywords: Optogenetics, Single-neuron Stimulation, Light Propagation, Wireless Nanonetworks

1. INTRODUCTION

In recent years the field of Brain Machine Interfaces (BMI) has led to numerous research initiatives aimed at developing new solutions to interfacing to neural systems. These initiatives are discovering new solutions ranging from neuron stimulation for patients who suffer from neurodegenerative diseases, all the way to the most recent vision of interfacing the brain to computing systems to enhance their capabilities.

A traditional approach for stimulating the brain is through the use of electrodes. However, a major limitation is the large population of neurons that get targeted during stimulation. This has led the research community to develop new approaches to stimulate at single-cell level. The field of optogenetics enables single cells to be stimulated using light at a specific wavelength. This requires that neurons are first engineered with genes that will express proteins to make the neurons sensitive to light, where the emission of the lights can both activate or inhibit the neuron's action potential. Since the original proposed optogenetics architecture, which requires an insertion of optical cable into the skull, wireless device models have also been proposed to provide more autonomy in the subjects that require stimulation.[1][2][3] Most recently, we proposed integrating the concept of wireless optogenetic for devices constructed from nanoscale components, i.e., Wireless Optogenetic Nanonetworking Device (WiOptND), where these devices could form nanonetworks to coordinate stimulations.[4]

Further author information: (Send correspondence to Pedram Johari)
Stefanus Wirdatmadja: E-mail: stefanus.wirdatmadja@tut.fi
Pedram Johari: E-mail: pedramjo@buffalo.edu, Telephone: 1 (716) 907-3086
Sasitharan Balasubramaniam: E-mail: sasib@tssg.org
Yongho Bae: E-mail: yonghoba@buffalo.edu
Michal K. Stachowiak: E-mail: mks4@buffalo.edu
Josep M. Jornet: E-mail: jmjornet@buffalo.edu

An important element in the wireless optogenetics is the light stimulation process between the device and the target neurons. New constraints will need to be considered compared to previous approaches, and in particular due to the nanoscale components of the light source as well as energy produced by the device. Since the light component is miniaturized, this means that its location within the neuron population and distance from the target cell are important factors to understand the required intensity for stimulating the neuron. The location within the neural population, as well as its density and connectivity is an important factor, since the light reflection and scattering from the neighboring cells will affect the intensity at the target cell.[5,6] This also varies within the cell population, since certain regions will have sparse density of somas that are largely filled with axons and dendrites, while in other regions dense somas will be found. Each of these cases will affect the light intensity that arrives at the target cell. Indirectly, this will also be impacted by the distance between the light source to the target cell.

In this paper, we develop a channel model for wireless optogenetic nano communication. The nano spacing considered for the channel model is between the light source and the target neuron. We develop geometric analysis to consider the light propagation, reflection, refraction, as well as scattering from the neighboring cells and how this impacts on the intensity at the target cells. Our channel model also considers the variation that is due to the density of neighboring somas and dendrites, as well as the shapes and structures of the cells. In a nutshell, by understanding the behavior of light in the brain tissues, efficient design for BMI can be achieved and the implants are feasible for long term operation and wirelessly interact with neurons forming the reliable optogenetic nanonetworks.

The remainder of the paper is organized as follows. In Section 2 we will define a system model including architecture for wireless optogenetic nanonetworking and the fundamental of light propagation in biological tissues. Section 3 contains a complete light propagation channel model for a single cell as well as the numerical analysis and results.In Section 4, we consider the multipath scenario due to the heterogeneous neuron population. Finally, we conclude the paper in Section 5.

2. SYSTEM MODEL

2.1 Wireless Optogenetic Nanonetwork Architecture

The entire network of the Wireless Optogenetic Nanonetworking architecture is composed of three layers (Figure 1). The lowest layer is the cerebral cortex where WiOptNDs are deployed and interfaced to individual neurons that require stimulation (Figure 2). The cerebral cortex is the gray matter of the brain and is responsible for sensory, motor, and associated functions. Horizontally, the cerebral cortex is categorized based on its functional areas, namely, the molecular layer, the external granular layer, the external pyramidal layer, the internal granular layer, the internal pyramidal layer, and the multiform layer. Those layers contain various types of cells, including pyramidal cells, spiny stellate cells, basket cells, chandelier cells, and smooth stellate cells,[7] each of which can have an interfaced WiOptND. The next layer up is the sub-dura transceiver, which is located on the dura and below the skull, and communicates with the WiOptNDs. The role of the sub-dura transceiver is to emit ultrasound waves, which are used to charge the WiOptND. The sub-dura transceiver contains the algorithm that determines both the charging and stimulation sequence of the WiOptND, and this in turn emits the sequence of ultrasound signals. Above the sub-dura transceiver is the external transceiver, which communicates with the sub-dura transceiver. While the communication between the external transceiver and the sub dura transceiver is a very relevant aspect of the system, our focus is on the interfacing of the individual WiOptNDs with neurons through light.
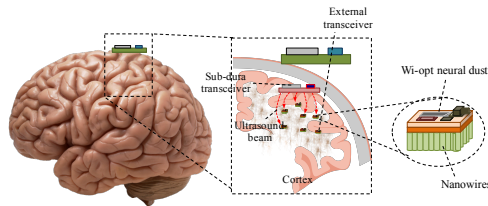

Figure 1: Illustration of the overall architecture of the Wireless Optogenetic Nanonetwork. The WiOptND are scattered in the various layers of the cortex, and is charged by the ultrasound signals emitted from the *sub-dura transceiver*, which in turn is communicated from the *external transceiver*.

Figure 2: Illustration of a WiOptND that interfaces to an engineered neuron that is sensitive to light at a specific wavelength.

2.2 Fundamentals of Light Propagation in Biological Tissues

When the light propagates in the biological tissue, there are four main phenomena that might occur (Figure 3).

- *Scattering*, which can be perceived as deflection of the ray of light from a straight path due to heterogeneous medium or the interface between two media. As the light experiences scattering, it might be transmitted or back scattered. Light scattering in biological tissues is well defined by the *Henyey-Greenstein* phase function introducing the coefficient *anisotropy factor, g.*[8] For biological tissues, typically this parameter is in the range of $0.5 \leq g \leq 0.95$, which indicates that forward scattering is dominant.[8] For a more accurate model of light propagation in biological tissues, the reduced scattering parameter, $\mu_s' = (1-g)\mu_s$, is used since the light undergoes multiple scattering effect.[8]

- *Absorption*, where the light energy is absorbed and converted to heat as the result of atoms and molecule vibration. The atoms and molecules have the selective natural behavior of certain light frequency absorption. For wavelength used in optogenetics, which is less than 625 nm, the absorption parameters are in the range of $0.5 - 5$ cm^{-1}.[8]
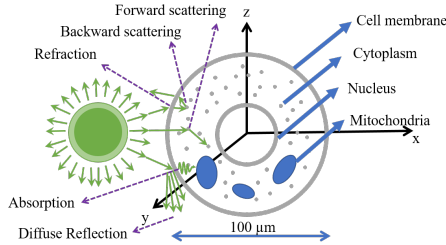
Figure 3: Model of refraction, reflection, absorption, and scattering of light on a neuron's soma.

- *Reflection* is the phenomenon where the the direction of the light propagation is reflected back to the same medium as it is originated. For biological tissues, diffuse reflection is most likely to occur. The common simplification for biological environment is by assuming that the surface is *Lambertian*.[9]

- *Refraction* occurs due to the light traversing via two media with different density. This causes the change in propagation direction. This phenomenon is described by *Snell's law* where ratio of the angle of incident θ_i and refraction θ_r is proportional to the phase velocities (v_1/v_2), or equivalently, inversely proportional to refraction indices of the two media (n_2/n_1):

$$\frac{sin\theta_i}{sin\theta_r} = \frac{v_i}{v_r} = \frac{n_r}{n_i}.$$ (1)

3. SINGLE CELL CHANNEL MODEL

3.1 Analytical Model

The light transportation through biological tissue can be modeled using the modified Beer-Lambert law as:

$$I(\lambda) = I_0(\lambda)e^{-\mu_a(\lambda)dDPF(\lambda)+G(\lambda)},$$ (2)

where $I(\lambda)$ is the measured λ wavelength light intensity on distance d, $I_o(\lambda)$ is the light intensity on the source, μ_a is the absorption coefficient of the biological tissue, $DPF(\lambda)$ is the differential path length, which indicates the mean light propagation distance in the tissue, and $G(\lambda)$ is a wavelength, medium, and geometry dependent constant. The value of the DPF depends on the medium characteristics including absorption (μ_a) and reduced scattering (μ'_s) as follows:[10]

$$DPF(\lambda) = \frac{1}{2}\left(\frac{3\mu'_s(\lambda)}{\mu_a(\lambda)}\right)^{1/2}\left[1 - \frac{1}{1 + d(3\mu_a(\lambda)\mu'_s(\lambda))^{1/2}}\right]. \tag{3}$$

The distance parameter d is less significant when $d > 2.5$ cm and $d\sqrt{3\mu_a\mu'_s} \gg 1$. Given the very small separation between the WiOptNDs and neurons, this parameter is crucial for DPF calculation.

As mentioned in Section 2.2, the traversing light rays undergo refraction phenomenon. Part of the rays, which are transmitted through the cells, experience the propagation through two different media with different refractive indices. This has been further analyzed in Johari et al.[11] that the transmitted light is focused to certain points on the other side of the illuminated part of the cell. Understanding this phenomenon is important in optogenetics considering the heterogeneous population of neurons in the cortex. The light might penetrate beyond neurons and excite a neuron in a dense neuron population. The most important aspects for optogenetics experiencing this situation is how far the light propagates after traversing through neuron and what is its intensity as illustrated on Figure 4.
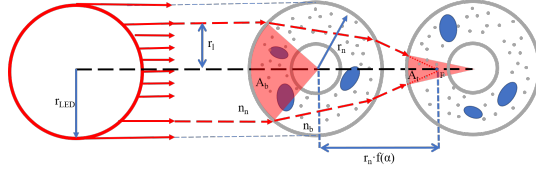

Figure 4: Illustration of light propagation with a light source, a blocking neuron, and a target neuron.

In this first model, for mathematical tractability, we model neurons as spherical cells due to its shape of roughly spherical.[12][13] The distance between the center of a spherical cell and focus point is $r_n f(\alpha)$, where α is the ratio of $\frac{r_L}{r_n}$. The lower and upper bounds, $f_l(\alpha \to 0)$ and $f_u(\alpha \to 1)$ of the focal points are dictated by the real part of refractive indices of the media that the light traverse through as:[11]

$$f_l(\alpha) = \frac{n_n^2}{2n_b\sqrt{n_n^2 - n_b^2}}, \quad \text{when } \alpha \to 0;$$
$$f_u(\alpha) = \frac{n_n}{2(n_n - n_b)}, \quad \text{when } \alpha \to 1, \tag{4}$$

where n_b and n_n are the refractive indices of brain tissue and neuron respectively. The distance of focus points from the center of the neuron is defined as $r f_{l/u}(\alpha)$.

The light propagation decreases the intensity due to scattering and absorption while the focusing effect of the cell aggregates the light rays, which increases the intensity. This focusing effect aggregates the light power with respect to the ratio of spherical caps of both blocking, A_b and target neurons, A_t. The values of A_b and A_t can be obtained by geometrically analyzing the solid angles, β_b and β_t, from the focus point angle ψ as shown in Figure 5. Assuming that the half surface of total spherical cell of blocking neuron is illuminated by the light source, the effective arc, $2\beta_b$, is π rad, while the effective arc of the target neuron depends on the focus point and it can be formulated as:

$$2\beta_t = 2\psi\frac{r_n f(\alpha) - d_{ss} - r_n}{r_n}. \tag{5}$$

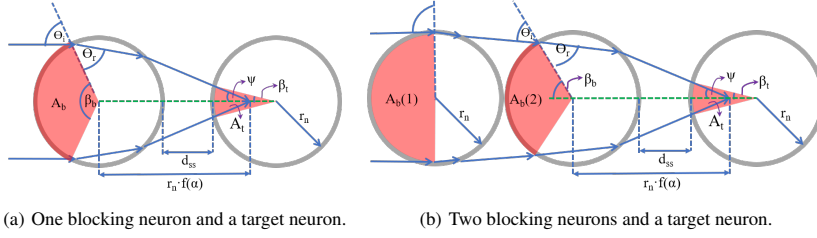(a) One blocking neuron and a target neuron.   (b) Two blocking neurons and a target neuron.

Figure 5: Refraction and focusing effect due to blocking neuron(s).

Note that the maximum value of the intensity is achieved when $rf_u(\alpha) = r_n + d_{ss}$, which means the light rays focus at a single point on the target neuron surface. The solid angles and spherical cap of both blocking and target neurons can be obtained by:

$$\omega_{b/t} = 2\pi(1 - cos\beta_{b/t}), \tag{6}$$

$$A_{b/t} = \omega_{b/t}r_n^2, \tag{7}$$

where subscript b/t indicates either blocking or target neuron.

The final intensity after the blocking neuron penetration depends on the light-exposed spherical cap area ratio γ between the blocking neuron A_b and the target neuron A_t. Thus, the final intensity can be formulated as:

$$
\begin{aligned}
I_t &= \frac{A_b}{A_t} I_o e^{-\mu_a^i(\lambda)d_i DPF_i + G(\lambda)} \\
&= \gamma\, I_o e^{-\mu_a^i(\lambda)d_i DPF_i + G(\lambda)}.
\end{aligned}
\tag{8}
$$

For multiple blocking neurons between light source and target neuron, the focus distance should be calculated based on the output of the previous blocking neuron. Therefore, the distance of focus point can be obtained by:[11]

$$r_n f(\alpha) = r_n \frac{sin(\pi - \theta_i)}{sin(\theta_i - \theta_r)}. \tag{9}$$

3.2 Numerical Results

Table. 1 lists the parameters used in the MATLAB simulation. Figure 6 shows the output intensity, path loss, and time delay characteristics comparison among three difference cases. For the output intensity, *no-blocking* case shows no significant changes, while cases with blocking neuron, intensity tends to rise and followed by decrements due to focusing effect of the light rays. Maximum intensity reaches when the rays focus to approximately infinitesimal point. This effect can be explained theoretically by ratio γ in (8) with the target neuron spherical area A_t as the denominator. Not only γ, the focus point $rf(\alpha)$ determines at which distance the maximum intensity occurs. Without blocking neuron(s), the propagation path loss tends to decrease faster since the energy propagate to all directions, unlike in the presence of blocking neurons where the light energy aggregates due to the effect of the blocking cell. Regarding the light ray arrival to the target neuron, the blocking neurons causes more propagation delay. This mainly depends on the light speed on the medium, which depends on refractive index. In this simulation, the speed of light propagating via neuron is 2.05×10^8 m/s, while via brain tissue, the speed is 2.15×10^8 m/s. Therefore, the more blocking neurons between light source and target neuron, the delay increases. However, the delay is considered small and the whole transmission process is only within pico second unit (one blocking neuron introduces additional delay of approximately 0.02 pico seconds).

To further validate the light focusing effect in the neurons, we have run extensive simulations by using COMSOL Multiphysics.[18] Photon diffusion by solving *Helmholtz Equations* has been considered to simulate the light propagation through the soma of neurons as shown in Figure 7. This figure shows the propagation of light through the nervous tissues when (a) there is no neuron and (b) there are three neurons in a row. The pattern intensity depicted on Figure. 7 shows the

Table 1: Simulation Parameters

Parameter	Value [Unit]	Description
r_n	50 [μm]	Spherical radius of neuron
$\bar{\rho}$	0.5 [%]	Reflectance index of neuron[14]
v_{vacuum}	3×10^8 [m/s]	Speed of light in vacuum
λ	456 [nm]	Wavelength of light
n_b	1.35	Refractive index of brain tissue[15]
n_n	1.36	Refractive index of neuron
$\phi_{1/2}$	$\frac{55}{180}$ [rad]	Half power point angle
$\mu_{a_{neuron}}$	0.9 [/mm]	Absorption coefficient of neuron[16]
$\mu'_{s_{neuron}}$	3.43 [/mm]	Reduced scattering coefficient of neuron[16]
$\mu_{a_{tissue}}$	20 [/mm]	Absorption coefficient of brain tissue[17]
$\mu'_{s_{tissue}}$	1.34 [/mm]	Reduced scattering coefficient of brain tissue[17]
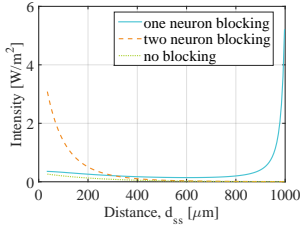
(a) Light intensity.
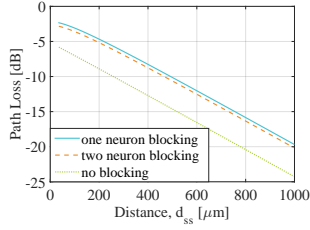
(b) Path Loss.

(c) Time Delay of rays of light arriving the surface of target neuron after two blocking neurons.
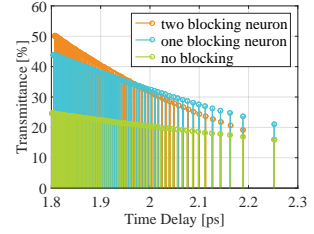
Figure 6: Light measurements on the surface of the target neurons. The distance between blocking and target neuron (d_{ss}) is varied for (a) and (b), while it is kept constant on (c).

possibility of farther extension where neurons are positioned along the propagation path. The color map indicates the soma has positive effect in increasing the light propagation distance due to focusing effect phenomenon. Therefore, the blocking neuron scenario can be exploited in the dense neuron population environment.

Figure 8 shows the photon counts in a logarithmic scale to compare the *with-* and *without-neuron* scenarios. Measuring the perpendicular path from the source, the *with-neuron* scenario is able to maintain the light intensity longer. At around the distance of 400μm from the light source, the intensity difference between two scenarios is approximately 18 dB. Each neuron along the propagation path contributes in maintaining the higher intensity longer with respect to distance. Considering the neuron diameter of 100μm, the intensity is approximately 6 dB higher after the light traverses the neuron.

4. MULTIPATH PROPAGATION MODEL

Considering the heterogeneous neuron population in the brain tissue, the light propagation in the tissue might include three components, namely, a line of sight (LoS) component, time delayed components, and reflected components.

4.1 Analytical Model

In this case, the power delay profile (PDP) can be used to analyze the light intensity with regards to multipath channel as a function of time delay. The PDP for LoS component is given by:[19]

$$h^{(0)}(t; \Phi_0) = L_0 P_0 \delta \left(t - \frac{d_0}{c} \right), \tag{10}$$

where

$$L_0 = e^{-\mu_a(\lambda)d_0 DPF(\lambda) + G(\lambda)}. \tag{11}$$
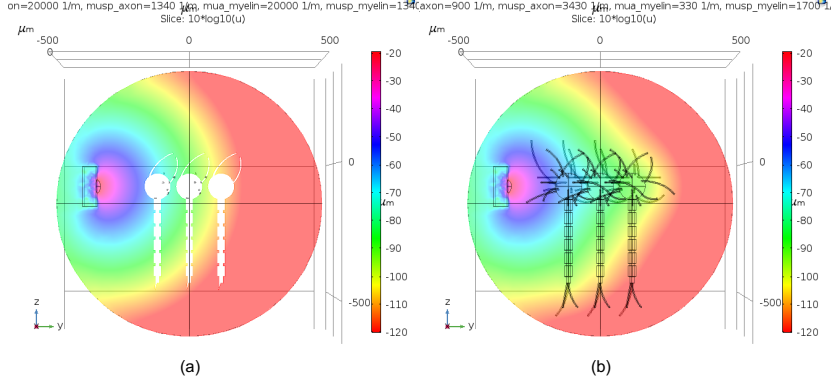
Figure 7: COMSOL simulations for light propagation in nervous tissue a) without neurons b) with three neurons.
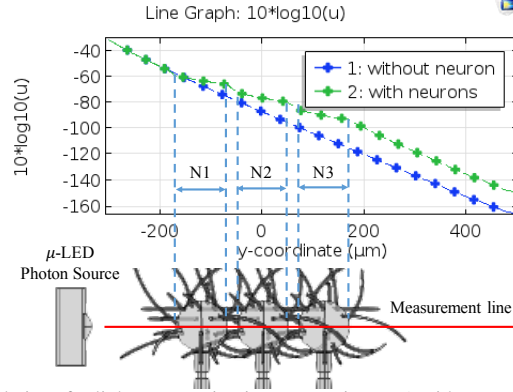
Figure 8: COMSOL simulations for light propagation in nervous tissues a) without neurons b) with three neurons.

For the reflected component (after k bounces), the PDP is given by:

$$h^k(t; \Phi) = \int_S \left[L_1 L_2 ... L_{k+1} \Gamma^{(k)} \times \delta \left(t - \frac{d_1 + d_2 + ... d_{k+1}}{c} \right) \right] dA_{ref}, k \geq 1, \tag{12}$$

where each path-loss term for each paths is represented by:

$$L_1 = \frac{A_{ref}^1}{2\pi d_1^2} e^{-\mu_a(\lambda)d_1 DPF(\lambda) + G(\lambda)} \iint (m+1) cos^m \phi_1 \, cos\theta_1 \, d\phi_1 \, d\theta_1,$$

$$L_2 = \frac{A_{ref}^2}{2\pi d_2^2} e^{-\mu_a(\lambda)d_2 DPF(\lambda) + G(\lambda)} \iint cos\phi_2 \, cos\theta_2 \, d\phi_2 \, d\theta_2, ...,$$

$$L_{(k+1)} = \frac{A_{eff}^{target}}{2\pi d_{(k+1)}^2} e^{-\mu_a(\lambda)d_{(k+1)}^2 DPF(\lambda) + G(\lambda)} \iint cos\phi_{(k+1)} \, cos\theta_{(k+1)} \, d\phi_{(k+1)} \, d\theta_{(k+1)}.$$

The PDP is integrated with respect to all neighboring neuron S and A_{ref} is the effective area on which the light is reflected. The directivity of the light source can be represented as $m = -1/log_2(cos\phi_{1/2})$, where $2\phi_{1/2}$ indicates the angle

(a) One blocking neuron and a target neuron.
(b) Two blocking neurons and a target neuron.

Figure 9: One hop reflection model.

of the light half power point. The angles of irradiance and incidence are represented by ϕ_k and θ_k respectively. The speed of light in the brain tissue is represented by c. The parameter d_k is the distance between light source and target neuron.
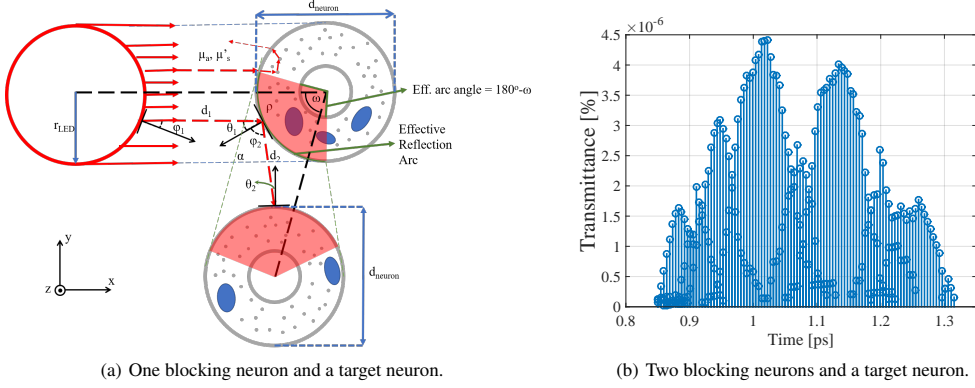
The reflected power after k bounces is represented by:

$$\Gamma^{(k)} = P_0 \bar{\rho}_1 \bar{\rho}_2 ... \bar{\rho}_k = k \, \bar{\rho} \, P_0 = k \left[\frac{n_b - n_n}{n_b + n_n} \right]^2 P_0,$$ (13)

where $\bar{\rho}$ is the reflectance index.

Finally the total PDP can be obtained by:

$$h(t) = \sum_{k=0}^{N_{adj}} h^k(t; \Phi_n).$$ (14)

Figure 9(a) illustrates two dimensional projection of one hop light reflection. The LoS component is not illustrated and the light rays are propagated on the x-axis and polarized on the y-axis. The A_{ref} is obtained by intersecting the projected area of the LED and the target neuron to the reflecting neuron. When $\angle\omega$ represents the angle connecting the center of the LED, reflecting neuron, and target neuron, the effective reflection arc angle is $\angle(180^o - \omega) = (\pi - \omega)$ rad. Let the azimuthal and polar angle of the cone formed between the center and the surface of the neuron be ω' and β respectively, the solid angle Ω can be calculated by:

$$\Omega = \iint_S \sin\omega' \, d\alpha' \, d\beta = \int_0^{2\pi} \int_0^{\frac{1}{2}(\pi-\omega)} \sin\omega' \, d\omega' \, d\beta = 2\pi(1 - \sin\frac{1}{2}\omega).$$ (15)

Thus, the spherical cap of the cone, which represents the reflecting area A_{ref}, can be obtained by:

$$A_{ref} = \Omega r_{neuron}^2.$$ (16)

4.2 Numerical Results

The time delay caused by the path of the light propagation hitting the *Lambertian* surface is shown in Figure 9(b). The power transmittance of reflection components is very low since the reflectance index of neuron cell is very low ($\approx 0.5\%$[14]) and the multipath time is approximately 0.5 pico seconds for one reflecting neuron.

The in-vivo neuron population structure is randomly scattered, therefore, the reflection interference might occur due to this reason. Figure 10(a) depicts one case where *Light source 2* unintentionally illuminates cell *Target 1* with the light reflected by cell *Target 2*. The simulation is conducted by varying both the angle ω and the distance d_{ss}. The output shows that the pathloss is so high (more than 80 dB) that the light interference does not cause any significant effect to the undesired target (Figure 10(b)).
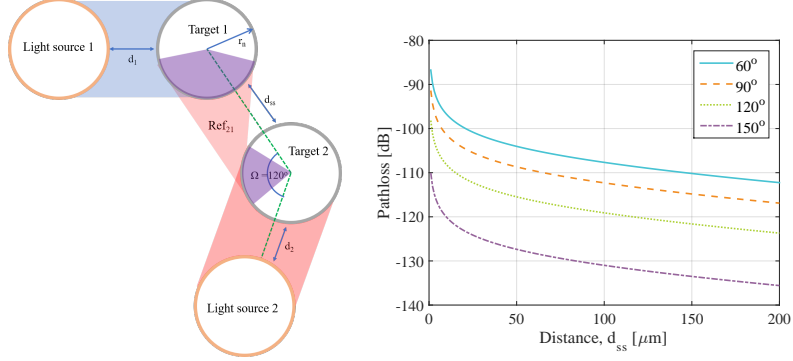
(a) Reflection interference caused by undesired light source from neighboring neuron.

(b) The path loss of the reflection caused by interference of undesired light source from neighboring target neuron as the function of distance.

Figure 10: Reflection intereference model.

5. CONCLUSION

Considering the brain morphology where diverse population of neurons in the neocortex can effect the light propagation for optogenetics at the nanoscale, deeper analysis on the phenomenon is required to observe its behavior at such scale. The interaction of the light wave on the biological tissue includes a combination of scattering, absorption, reflection, and refraction, where all this depends on the optical and geometry properties of the light wave on the medium and the neurons. Taking into consideration the optical properties while assuming spherical geometry of neuron for simplification, the focusing effect occurs as the light wave propagates in the brain tissue. This phenomenon results in an intensity increase ($\approx$ 6 dB/neuron for 100 μm diameter neuron) once the light wave leaves the soma. The analysis is based on the one axis polarized light propagation on the soma that is perfectly aligned to the propagation path. The COMSOL simulation confirms the focusing effect resulting in farther light propagation when the blocking neurons exist between the light source and the target neuron. With respect to the delay, blocking neurons cause insignificant delay (at the pico second level).

At the same time, the effect of reflection is extremely small compared to the LoS component so the interference from adjacent neurons can be ignored. The reason for this is because, for each hop of reflected light rays, the reflected light power is multiplied by a very small value of reflectance coefficient. The reflection analysis has considered the angle of the neurons for various possible position in the brain. Based on the blocking and multipath propagation models, we found that highly dense neuron population can benefit from having a blocking neuron in between a light source and the target neuron, to assist in directing and increasing the light intensity required for successful stimulation.

REFERENCES

[1] Lee, J. H., Durand, R., Gradinaru, V., Zhang, F., Goshen, I., Kim, D.-S., Fenno, L. E., Ramakrishnan, C., and Deisseroth, K., "Global and local fmri signals driven by neurons defined optogenetically by type and wiring," *Nature* **465**(7299), 788 (2010).

[2] Liu, X., Ramirez, S., Pang, P. T., Puryear, C. B., Govindarajan, A., Deisseroth, K., and Tonegawa, S., "Optogenetic stimulation of a hippocampal engram activates fear memory recall," *Nature* **484**(7394), 381–385 (2012).

[3] Chaudhury, D., Walsh, J. J., Friedman, A. K., Juarez, B., Ku, S. M., Koo, J. W., Ferguson, D., Tsai, H.-C., Pomeranz, L., Christoffel, D. J., et al., "Rapid regulation of depression-related behaviors by control of midbrain dopamine neurons," *Nature* **493**(7433), 532 (2013).

[4] Wirdatmadja, S. A., Balasubramaniam, S., Koucheryavy, Y., and Jornet, J. M., "Wireless optogenetic neural dust for deep brain stimulation," in [*e-Health Networking, Applications and Services (Healthcom), 2016 IEEE 18th International Conference on*], 1–6, IEEE (2016).

[5] Johari, P. and Jornet, J. M., "Nanoscale optical wireless channel model for intra-body communications: Geometrical, time, and frequency domain analyses," *IEEE Transactions on Communications* (2018).

[6] Guo, H., Johari, P., Jornet, J. M., and Sun, Z., "Intra-body optical channel modeling for in vivo wireless nanosensor networks," *IEEE Transactions on NanoBioscience* **15**(1), 41–52 (2016).

[7] Mountcastle, V. B., [*Perceptual neuroscience: the cerebral cortex*], Harvard University Press (1998).

[8] Klose, A. D. and Larsen, E. W., "Light transport in biological tissue based on the simplified spherical harmonics equations," *Journal of Computational Physics* **220**(1), 441–470 (2006).

[9] Xia, J. and Yao, G., "Angular distribution of diffuse reflectance in biological tissue," *Applied optics* **46**(26), 6552–6560 (2007).

[10] Scholkmann, F. and Wolf, M., "General equation for the differential pathlength factor of the frontal human head depending on wavelength and age," *Journal of Biomedical Optics* **18**(10), 105004–105004 (2013).

[11] Johari, P. and Jornet, J. M., "Nanoscale optical channel modeling for in vivo wireless nanosensor networks: A geometrical approach," *Proc. of the IEEE International Conference on Communications (ICC)* , 1–6 (2017).

[12] Andrew, A. M., "Spiking neuron models: Single neurons, populations, plasticity," *Kybernetes* **32**(7/8) (2003).

[13] Quan, T., Zheng, T., Yang, Z., Ding, W., Li, S., Li, J., Zhou, H., Luo, Q., Gong, H., and Zeng, S., "Neurogps: automated localization of neurons for brain circuits using l1 minimization model," *Scientific reports* **3** (2013).

[14] Fang-Yen, C. and Feld, M. S., "Intrinsic optical signals in neural tissues: measurements, mechanisms, and applications," 219–235, ACS Publications (2007).

[15] Levinson, A. and Serby, A., "The refractometric and viscosimetric indexes of cerebrospinal fluid," *Archives of Internal Medicine* **37**(1), 144–150 (1926).

[16] Yaroslavsky, A., Schulze, P., Yaroslavsky, I., Schober, R., Ulrich, F., and Schwarzmaier, H., "Optical properties of selected native and coagulated human brain tissues in vitro in the visible and near infrared spectral range," *Physics in Medicine and Biology* **47**(12), 2059 (2002).

[17] Bosschaart, N., Edelman, G. J., Aalders, M. C., van Leeuwen, T. G., and Faber, D. J., "A literature review and novel theoretical approach on the optical properties of whole blood," *Lasers in medical science* **29**(2), 453–479 (2014).

[18] [*COMSOL Multiphysics Simulation Software*], COMSOL. [Online]. Available: http://www.comsol.com/products/multiphysics/.

[19] Lee, K., Park, H., and Barry, J. R., "Indoor channel characteristics for visible light communications," *IEEE Communications Letters* **15**(2), 217–219 (2011).

PUBLICATION

V

Analysis of Light Propagation on Physiological Properties of Neurons for Nanoscale Optogenetics

S. Wirdatmadja, P. Johari, A. Desai, Y. Bae, E. K. Stachowiak, M. K. Stachowiak, J. M. Jornet and S. Balasubramaniam

Analysis of Light Propagation on Physiological Properties of Neurons for Nanoscale Optogenetics

Stefanus Wirdatmadja, Pedram Johari, *Student Member, IEEE,* Aesha Desai, Yongho Bae, Ewa Stachowiak, Michal Stachowiak, Josep M. Jornet, *Member, IEEE,* Sasitharan Balasubramaniam, *Senior Member, IEEE*

Abstract—Miniaturization of implantable devices is an important challenge for future Brain-Computer Interface applications, and in particular for achieving precise neuron stimulation. For stimulation that utilizes light, i.e., optogenetics, the light propagation behavior and interaction at the nanoscale with elements within the neuron is an important factor that needs to be considered when designing the device. This paper analyses the effect of light behavior for a single neuron stimulation, and focuses on the impact from different cell shapes. Based on the Mie Scattering theory, the paper analyzes how the shape of the soma and the nucleus contributes to the focusing effect resulting in an intensity increase, which ensures that neurons can assist in transferring light through the tissue towards the target cells. At the same time, this intensity increase can in turn also stimulate neighboring cells leading to interference within the neural circuits. The paper also analyzes the ideal placements of the device with respect to the angle and position within the cortex that can enable axonal biophoton communications, which can contain light within the cell to avoid interference.

Index Terms—Nano Communications, Optogenetics, Geometrical Optics Analysis, Mie scattering.

I. INTRODUCTION

Increased attention in Brain-Machine Interfaces (BMI) as well as Brain-Computer Interfaces (BCI) has driven researchers to pursue new developments that will merge brain and machines into a seamless manner [1–3]. This grand vision will witness the connection of the Brain to Computing Systems in a less invasive and more pervasive manner than existing approaches. In order to realize this paradigm, the tools provided by nanotechnology need to be leveraged to produce microscale devices that can be seamlessly embedded into the brain, enabling monitoring as well as stimulation at a single-neuron level. Recent developments have started to realize this vision which has led to several new types of materials and devices as well as new paradigms such as molecular communications aimed at modeling communication between neurons [4–7]. An example of new materials and devices is the electronic

S. Wirdatmadja is with the Department of Electrical Engineering and Communications, Tampere University of Technology, Finland. Email: stefanus.wirdatmadja@tut.fi. P. Johari and J M. Jornet are with the Department of Electrical Engineering, University at Buffalo, State University of New York. Emails: {pedramjo, jmjornet}@buffalo.edu. A. Desai, Y. Bae, E. Stachowiak and M. K. Stachowiak are with the Department of Pathology and Anatomical Sciences, University at Buffalo, State University of New York. Emails: {aeshades, yonghoba, eks1, mks4}@buffalo.edu. Sasitharan Balasubramaniam is with Tampere University of Technology, Finland and TSSG, Waterford Institute of Technology, Ireland. Email: sasi.bala@tut.fi and sasib@tssg.org.

mesh that can be injected into the brain and will unfurl within the cortex, providing new forms of long-term monitoring of neurons [8]. The vision of the neural dust [9] is to also enable wireless monitoring of neurons, where devices can be charged through ultrasound signals, and the back-scattering effect can provide feedback to an external device. A preliminary step towards this vision has already been realized with experiments conducted on the neural dust that can monitor action potential along the nervous system of a mouse [10].
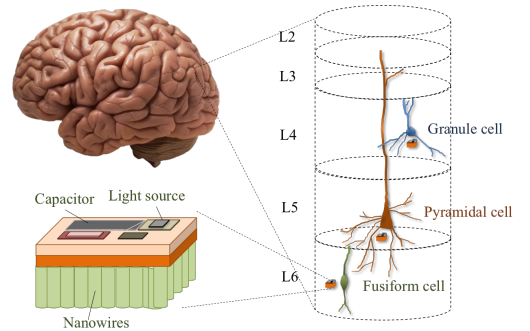
Fig. 1. Device architecture of the Wireless Optogenetic Nanonetwork Device (WiOptND), placed close to the target cell and able to convert ultrasounds to optical signals, which then stimulate the light-sensitive neurons. The figure also illustrates three neurons within the cortical column, each interfaced by a WiOptND device for stimulation, creating an embedded nanonetwork.

Our current research in Wireless Optogenetic Nanonetwork Devices (WiOptND) (Fig. 1, adapted from [11]), aims to utilize the concepts of nano communication and networks [12] (Fig. 1) to enable a new generation of BCI/BMI. The device consists of three main components, piezoelectric nanowires as an energy harvester, a capacitor as an energy reservoir, and a LED as a light source. This entails developing miniature devices that can be placed as a network into the brain, and stimulate neurons using visible light [13]. While the miniaturization brings along numerous advantages such as the ability to embed the devices into the brain for long-term deployment, as well as stimulation for small groups of cells, there are also a number of challenges. In [11], we investigated the performance of different WiOptND charging and firing strategies to ensure proper operation of the platform. In relation to this, one particular challenge is the effect of light propagation and its effectiveness in stimulating the cell, specially when compared to electrical stimulation [14]. This challenge is compounded

due to the miniature aperture of the light source and intensity, given that the components are constructed from nanoscale materials. This means that the light intensity may not reach the target cells, and this could be an issue due to cell growth and movements. The light propagation in biological tissues, including the brain, has been extensively studied in [15–18]. For example, Monte Carlo [19] and Finite Difference Time Domain (FDTD) [20] simulations can be used to simulate the light propagation in biological tissue. In [21], the light propagation based on Monte Carlo method for both regular and irregular medium propagation shape in organ level has been developed, however, not at a single-cell level. Analytically, light propagation in brain tissue can be analysed with the revised *Kubelka-Munk* model or the modified *Beer-Lambert law*. Nevertheless, none of the existing works, including our previous work [15], model the propagation of light with (sub) cellular precision.

In this paper, we investigate the propagation of light at the nano and micro scales, and the unique properties that will result with the propagation through different shapes of a neuron. A particular focus is in the nature of refraction and natural focusing effects that can occur due to refraction of light as it passes through the internal cell structure. This focusing effect is different depending on the shape of the neuron, which will have an impact on the accurate placements of the devices within the cortex. In particular, the focusing effect can result in light intensity stimulating neighboring cells that results in interference. The effect will be further investigated and validated based on the Mie Scattering theory simulation using MATLAB. The simulations will analyze the geometrical soma shape effect based on the combination of geometry optics theory and modified Beer-Lambert law.

In a separate trend, a recent study has also found that light propagation along the axon, especially within the myelin sheaths, has an internal reflection process for bio-photons that resembles an optical waveguide [22]. Therefore, integrating this phenomenon can lead to an ideal case of internal light reflection within a neuron that contains the photons and minimizes stimulation of neighboring cells. Based on these results, in this paper , we investigate how certain intensity and angle of the light source on the soma of the neuron, can result in an ideal location for stimulating the neuron that will minimize interference to the surrounding neurons. Following is a list of contributions of the current paper:

1) Combining geometrical theory and Mie scattering analysis in a single cell for three soma shapes (Pyramidal, Spherical, and Fusiform),
2) Analysing the feasibility of light containment within the axonal (biophoton communications), that is dependent on the angle and position of the light source.
3) Validation through MATLAB simulation to analyze the focusing effects in the near region of the cells.

The remaining sections of the paper are organized as follows: Sec. II elaborates about the biological properties of brain tissue and cerebral cortex. In addition to that, it also discusses about the interaction of light and neuron, particularly with the nucleus. The light interaction with respect to geometry of each soma shape is discussed profoundly in Sec. III. Sec. IV explains about the feasibility analysis for axonal biophoton communication and external light source considering the soma shapes and the neuron density. Finally, Sec. V concludes the paper based on the simulation results and analysis.

II. NEURONS AND LIGHT INTERACTION

A. Biological Structure of Cerebral Cortex

Morphologically, biological tissues can be categorized under four different types, namely, epithelium, connective tissues, muscle tissues, and nervous tissues [23]. Nervous tissues comprise the neurons and neuroglia forming the central nervous system and the peripheral nervous system. The structure of the nervous tissue is soft and possesses a certain level of elasticity which specifies the interaction with the optical wave (light). The brain, which is a part of the central nervous system, comprises gray and white matters. The gray matter is composed of various types of somata, axons, dendrites, synapses, blood vessels, and glial cells. It has an important role in the coordination of the entire body. The white matter consists of myelinated nerve fibers, blood vessels, and glial cells. On the outermost layer of the brain, the inflexible-two-layered dura mater acts as a protective coating. The outer layer is *arachnoid mater* and the inner layer is *pia mater* with *cerebrospinal fluid (CSF)* in between them. The space between the skull and the dura mater is filled with adipose tissues containing blood vessels.

B. Morphology of the Cerebral Cortex Neurons

The six-layered-cerebral cortex is populated by *cholinergic neurons* where *neurotransmitter acetylcholine (ACh)* is mainly utilized for the chemical communications. The cholinergic neurons can be categorized into four size groups: very large motor neuron (25-45 μm), large forebrain neuron (18-25 μm), medium neuron (14-20 μm), and small neuron (8-16 μm) [24]. The neurons in the cerebral cortex are categorized under the small neuron group, together with the hippocampus neurons, anterior olfactory cortex neurons, olfactory bulb (smell receptor) neurons, and dorsal horn (sensory) neurons. Based on the shape of the soma, cholinergic neurons in the cerebral cortex can be further categorized into three main groups: *pyramidal cells, granule cells,* and *fusiform/spindle-shaped cells* [25]. Brief description and location of each shape is explained in the following list:

1) Pyramidal cells: In the cerebral cortex, pyramidal cells can be found particularly in layers III and V. This multipolar cell can easily be distinguished by its pyramidal shape. This cell is further categorized into four sub-groups based on its size (height × width): *small (Schankleit)* (12 μm× 10 μm), *medium* (25 μm× 15 μm), *large* (45 μm× 15-20 μm), and *giant* (50-100 μm× 25-60 μm) [25].

2) Granule cells: Layer II and IV are mostly populated by granule cells. The granule cells in layer IV receive input from the thalamus and project the information to both the supragranular layers (layers II and III) and the infragranular layers (layers V and VI). The soma shape of a granule cell is spherical/polygonal/oval, and its size is around 15-30 μm × 10-15 μm [25].

3) Fusiform/spindle-shaped cell: These fusiform cells are located in layer VI. This layer contains efferent fibers which connect the cortex to the thalamus bringing impulses that originate from the cortex. These cells are characterized as flattened spindled-shaped somata with long apical dendrites elongated up to layer I while the basal dendrites spread into layer VI. The size of its soma is around 15-30 μm $\times$ 10-15 μm [25].

C. Light Interaction in Cerebral Cortex

When a light wave propagates in the biological tissue, both its intensity and propagation direction might change. They are caused by several light-medium interactions [26], namely:

- *Reflection and Refraction.* As light propagates from one medium to another with different refractive indices, the light can be partially reflected and partially transmitted. Furthermore, the transmitted light will experience refraction (change in the angle of propagation) due to the different refractive indices of the media [27].
- *Absorption.* The light energy decreases as it is absorbed and converted to heat due to the vibration of atoms and molecules in the biological tissues. The absorption behavior of the tissue relies heavily on the light wavelength.
- *Scattering.* The heterogeneous biological medium causes the deflection of light wave to one or more paths deviated from its straight trajectory. This situation occurs when the wave passes through two different media with different optical properties [28].

D. Light Scattering by Nucleus

The soma of a neuron contains many organelles including nucleus which is the largest amongst all the others. The size of the nucleus, along with other properties such as the refractive index of the medium and the light wavelength, determine the scattering pattern of the light when encounters the nucleus [29]. The size parameter χ defines the ratio between a particle's radius (in this case, nucleus), r, and the light wavelength, λ. It can be formulated as

$$\chi = \frac{2\pi n_o r}{\lambda} = kr \qquad (1)$$

where n_o is the refractive index of the cytoplasm, and k is the wave vector by definition.

For the 456 nm (blue light) scattered by a nucleus with diameter of 3-18 μm and refractive index of nucleus, n_{nuc}, of 1.39 [30], and cytoplasm, n_{cyto}, of 1.36-1.39 [31], the size parameter is between 28.32 - 169.89. This value lies between 0.2 and 2000 which is categorized as Mie Scattering. It also means that such particle size is comparable to the corresponding light wavelength. By employing the Mie theory, the scattering pattern of the transmitted light can be determined, which defines the intensity of the light in all directions relative to the nucleus. This calculation can be visualized using the polar plot when the dominant scattering direction is concerned (as can be seen later in Fig. 2(a)).

Mie theory gives the solution of vector wave equations for spherical object scatterer presented in spherical coordinate system (r, θ, ϕ) [32]. The matrix of scattered far field component in the scattering plane E_s^θ and its orthogonal E_s^ϕ components can be obtained from the scattering amplitudes and the incident fields, which is represented as follows [33],

$$\begin{bmatrix} E_s^\theta \\ E_s^\phi \end{bmatrix} = \frac{e^{ik(r-z)}}{-ikr} \begin{bmatrix} S_2 & 0 \\ 0 & S_1 \end{bmatrix} \begin{bmatrix} E_i^\theta \\ E_i^\phi \end{bmatrix}, \qquad (2)$$

where S_1 and S_2 are the scattering amplitudes, E_i^θ and E_i^ϕ are the incident vectors, e^{ikz} is the incident plane wave, and $\frac{e^{ikr}}{ikr}$ is the outgoing scattered wave. The scattering amplitudes S_1 and S_2 are further derived as

$$S_1(cos\theta) = \sum_{n=1}^{\infty} \frac{2n+1}{n(n+1)}(a_n \pi_n + b_n \tau_n), \qquad (3)$$

$$S_2(cos\theta) = \sum_{n=1}^{\infty} \frac{2n+1}{n(n+1)}(a_n \tau_n + b_n \pi_n). \qquad (4)$$

From those scattering amplitudes, the intensity can be obtained by

$$I = \frac{1}{2}(|S_1(\theta)|^2 + |S_2(\theta)|^2). \qquad (5)$$

The Mie coefficients a_n and b_n are obtained by

$$a_n = \frac{m^2 j_n(mx)[xj_n(x)]' - j_n(x)[mxj_n(mx)]'}{m^2 j_n(mx)[xh_n^{(1)}(x)]' - h_n^{(1)}(x)[mxj_n(mx)]'}, \qquad (6)$$

$$b_n = \frac{j_n(mx)[xj_n(x)]' - j_n(x)[mxj_n(mx)]'}{j_n(mx)[xh_n^{(1)}(x)]' - h_n^{(1)}(x)[mxj_n(mx)]'}, \qquad (7)$$

where prime sign indicates the first derivative, m is the relative refractive index of nucleus with respect to cytoplasm, $j_n(z)$ and $h_n^{(1)}(z) = j_n(z) + iy_n(z)$ are the spherical Bessel and Hankel functions of order n respectively, $y_n(z)$ is the spherical Neumann function of order n, and $n = 1$ to ∞. However, for mathematical tractability, this infinite series is truncated at n_{max} [32], where $n_{max} = x + 4x^{\frac{1}{3}} + 2$. The derivatives for the spherical functions are

$$[\alpha j_n(\alpha)]' = \alpha j_{n-1}(\alpha), \qquad (8)$$

$$[\alpha h_n^{(1)}(\alpha)]' = \alpha h_{n-1}^{(1)} - nh_n^{(1)}(\alpha), \qquad (9)$$

where α can be substituted by either mx or x. The Mie angular functions π_n and τ_n are

$$\pi_n = \frac{2n-1}{n-1} cos\theta \cdot \pi_{n-1} - \frac{n}{n-1}\pi_{n-2}, \qquad (10)$$

$$\tau_n = n cos\theta \cdot \pi_n - (n+1)\pi_{n-1}, \qquad (11)$$

where the first three orders of those functions are [34]

$$\pi_0 = 0; \;\; \pi_1 = 1 \;\; ; \pi_2 = 3 cos\theta; \qquad (12)$$

$$\tau_0 = 0; \tau_1 = cos\theta; \tau_2 = 3 cos2\theta. \qquad (13)$$

Based on the Mie theory, the scattering intensity pattern is depicted in Fig. 2 in logarithmic scale. From the polar plot (Fig. 2(a)), it can be observed that light scattering by the nucleus exhibits dominant forward scattering (on scattering angle 0° - 5°) and from Cartesian plot (Fig. 2(b)), the intensity has a decreasing tendency towards the backward direction. This scattering pattern resembles the directional antenna radiation pattern. It also exhibits the higher intensity value compared to the incident field. From optics geometry perspective, this higher forward lobe intensity phenomenon shows that the nucleus has the similar behavior as a convex lens [35].
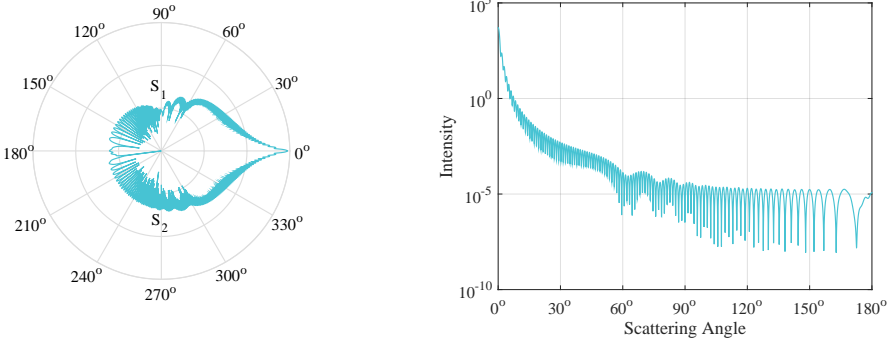
(a) The scattering amplitudes polar plot of S_1 on $0^o \leq 180^o$ and S_2 on $180^o \leq 360^o$.

(b) The logarithmic Cartesian plot of light intensity as a function of scattering angle

Fig. 2. The scattering intensity pattern when the light is scattered by the nucleus.

E. Experimental Setup to Observe the Forward Scattering Effect of Nucleus on the Incident Light

To further investigate the propagation pattern of the light inside neurons (and more specifically around the nucleus), we have set up a laboratory experiment as depicted in Fig. 3(a). Neural progenitor cells (NPCs) differentiated from human embryonic stem cells were cultured as described in [36], [37][1]. It is important to note that the cells used in the experiment have a fusiform shape (See Sec. III-B). Later in Sec. III, we thoroughly analyze the effect of different shapes of cells on the light forward scattering pattern. To monitor light propagation behavior through NPCs, an inverted microscope with a halogen lamp as the light source that shines through the specimen (NPCs) is used (Fig. 3(a))[2]. Images of the cells and the cumulated light were taken by moving the focal plane of the microscope in z-direction. Fig. 3(b) shows the microscopic image of a neuron with the nucleus highlighted in an orange circle and three distinguishable nucleoli (dark spots). Fig. 3(c) is obtained by shifting the focal plane by 5 μm in the z-direction below the cell, i.e., on the opposite side of the light source. It can be seen from this figure that the nucleus and the nucleoli can not be observed clearly since they are out of focus by 5 μm. Finally, in Fig. 3(d), the focal plane has been moved further to 10 μm away from the cell surface. The light spots in this figure show the cumulated light at a vertical distance from all three nucleoli. This happens due to the forward scattering effect of the nucleoli on the incident light. This phenomenon has been further investigated with detailed analysis in the following section.

III. GEOMETRICAL-BASED LIGHT PROPAGATION ANALYSIS

The geometrical optics analysis for homogeneous spherical soma has been conducted in details in [15]. In this paper, we

extend the analysis by including the nucleus in the soma with three different shapes, namely, pyramidal, fusiform, spherical, and its impact on the light propagation behavior. The blue-shadowed area in the figures of following subsections indicates the area in which the light propagates through the cytoplasm but not the nucleus.

A. Pyramidal shape

The neurons with pyramidal-shaped soma can be found in several areas of the brain including the cerebral cortex, the hippocampus, and the amyglada. A pyramidal neuron is a multipolar neuron, i.e., it generally possesses many dendrites and a single axon. Due to its relatively large size, this neuron type has been studied more intensively by neurophysiologists. Particularly, these neurons in layer V neocortex are considered as the semi-autonomous processing units [38].

The pyramidal cell is modeled as triangular shape on a 2D-plane. As a result, Fig. 4 illustrates the propagation of a collimated light traversing though a pyramidal soma.

Based on its geometrical analysis of the soma and nucleus, the transmitted light is focused in certain locations. In this paper, the focus point is measured from the soma surface with length h_{sm} in Fig. 4 and the center of the nucleus is located in the middle of the soma. The lower bound (f_l) and the upper bound (f_u) of the focus point outside the soma excluding light traversing through the nucleus is represented as

$$f_l = w_{sm} + \frac{r_{nc}}{tan\,\alpha^p} - \frac{r_{nc}}{arctan\left[\frac{h_{sm}}{2w_{sm}}\right]}, \quad (14)$$

$$f_u = \frac{h_{sm}}{2\,tan\,\alpha^p}, \quad (15)$$

and,

$$\theta_r^p = arcsin\left(\frac{n_{cyto}}{n_{tis}}sin\left(90^o - arctan\left[\frac{h_{sm}}{2w_{sm}}\right]\right)\right), \quad (16)$$

$$\alpha^p = \theta_r^p - 90^o + arctan\left[\frac{h_{sm}}{2w_{sm}}\right], \quad (17)$$

---

[1] For performing this experiment, 20,000 cells were plated on a glass bottom 35mm cell culture dish (MatTek, USA) for 24 hours.

[2] An inverted Zeiss AxioObserver Imager wide-field fluorescence microscope has been used for this experiment

(a) The lateral view of the experiment   (b) On the cell surface   (c) 5 μm below the cell surface   (d) 10 μm below the cell surface
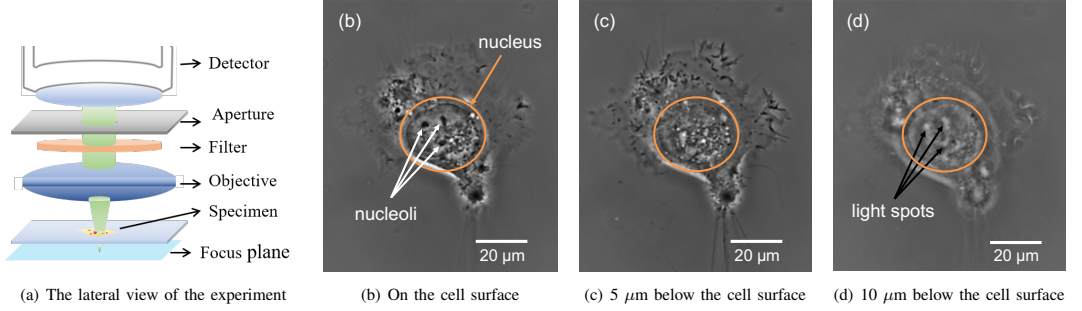
Fig. 3. Neural progenitor cells (NPCs) differentiated from human embryonic stem cells were plated on a tissue culture dish. Phase contrast images of NPCs were acquired by changing the focal plane distance using a Zeiss AxioObserver inverted wide-field fluorescence microscope. The lateral view of the experiment is illustrated in (a). The focused light were observed in three distances; (b) on the cell surface, (c) 5 μm, and (d) 10 μm below the cell surface. Orange circles in the figures are region of interest (nucleus). Arrows indicate nucleoli in (b) and light spots of cumulated light in (d).
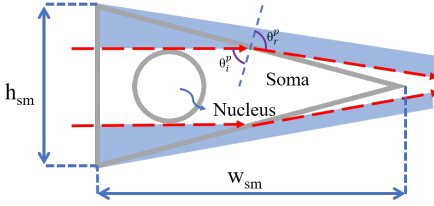

Fig. 4. The illustration of light propagation in the pyramidal shaped soma.

where r_{nc} is the radius of the nucleus, n_{cyto} is the refractive index of the cytoplasm and n_{tis} is the refractive index of the brain tissue.

For the pyramidal cell size of 30 μm $\times$ 48 μm and taking into account the refractive index of brain tissue (n_{tis} = 1.35) and neuron (n_{cyto} = 1.36), the lower and upper bounds for focus point are 200 and 254 μm, respectively.

B. Fusiform shape

Geometrically, the fusiform soma model resembles the bi-convex lens as shown in Fig. 5. Therefore, when this 2D-model is exposed to the collimated light source or plane wave, it can be analysed using a lensmaker's equation yielding the distance of the focus as

$$\frac{1}{f} = \frac{(n_{cyto} - n_{tis})}{n_{tis}} \left[\frac{1}{R_1} - \frac{1}{R_2} + \frac{w_{sm}(n_{cyto} - n_{tis})}{n_{cyto} R_1 R_2} \right], \quad (18)$$

where R_1 and R_2 denotes the curvatures of each surface of the lens, respectively, f represents the distance of the focus point measured from the center point, and d is the distance between two opposite surfaces of the neuron along the center axis.

Ideally, the soma cannot be considered as the perfect lens due to its heterogeneous content; therefore, *spherical aberration* is more likely to occur. *Spherical aberration* causes the light to be blurred, converged in the vicinity of the measured focus point. However, the distance focus approximation is still valid to determine where the light converges.
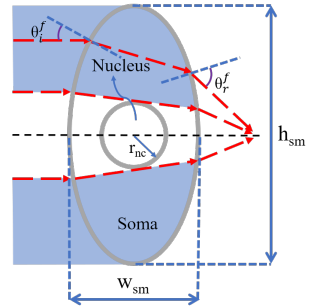
Fig. 5. Illustration of ellipse/spindle-shape neuron acting as an equiconvex lens.

According to the available data of the soma size and the equiconvex soma shape, the approximate radius of each surface can be formulated as

$$R_1 = R_2 = R_{1/2} = \frac{w_{sm}^2 + h_{sm}^2}{4 w_{sm}}, \quad (19)$$

where $R_{1/2}$ is the radius of the surface curvature, h_{sm} and w_{sm} are the height and width of the soma, respectively.

Matrix operation analysis can also explain the refraction due to each surface of the soma. The refraction model can be represented in three matrix operations [39]:

$$\underbrace{\begin{bmatrix} 1 & 0 \\ -\frac{(n_{tis} - n_{cyto})}{(R_2 n_{tis})} & \frac{n_{cyto}}{n_{tis}} \end{bmatrix}}_{\text{refration on the second surface}} \overbrace{\begin{bmatrix} 1 & w_{sm} \\ 0 & 1 \end{bmatrix}}^{\text{principal plane}} \underbrace{\begin{bmatrix} 1 & 0 \\ -\frac{(n_{cyto} - n_{tis})}{(R_1 n_{cyto})} & \frac{n_{tis}}{n_{cyto}} \end{bmatrix}}_{\text{refration on the first surface}}$$

$$\Leftrightarrow \begin{bmatrix} 1 + w_{sm} P_{12} & w_{sm} \frac{n_{tis}}{n_{cyto}} \\ P & w_{sm}(\frac{n_{tis}}{n_{cyto}}) P_{23} + 1 \end{bmatrix}, \quad (20)$$

where the refracting power for each surface is denoted by P_{12} and P_{23}, and the total power is represented by P. The power

parameters are given as

$$P_{12} = -\frac{n_{cyto} - n_{tis}}{R_1 n_{cyto}}, \tag{21}$$

$$P_{23} = -\frac{n_{tis} - n_{cyto}}{R_2 n_{tis}}, \tag{22}$$

$$P = -\frac{1}{f} = P_{23} + w_{sm}P_{12}P_{23} + \frac{n_{cyto}}{n_{tis}}P_{12}. \tag{23}$$

Based on the size of the fusiform cell in Sec. II-B, the radius can be approximated by Eq. (19) resulting in 18.75 μm curvature, for the size of $30\mu m \times 15\mu m$. Then, the focus can be obtained by applying lensmaker's equation. The focus is positioned at 0.63 mm from the center point of the soma when the curvature radius of soma is 18.75 μm. The same calculation can also be applied for the smaller soma. The $15\mu m \times 10\mu m$ soma has 8.13 μm curvature radius and 0.27 mm focus measured from the soma center point. This confirms the forward scattering and focusing effect of the nucleoli that we observed in our experiment explained in Sec. II-E. During this experiment, the size of nucleoli is 2.5 μm (Fig. 3), resulting the light to focus at approximately 10.4 μm away. This is the lower bound of focus area which is discussed with more details in Sec. III-D.

C. Spherical shape

The cross-sectional area of the spherical cell can be represented as the circular 2-D model. The 2D-model analysis is conducted by positioning the nucleus at the center of the soma. Fig. 6 depicts the cross sectional spherical soma model illuminated by collimated light.
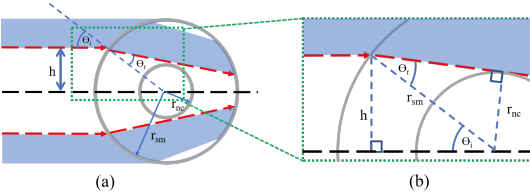

(a) (b)

Fig. 6. Light propagation through spherical soma with nucleus located at the center point.

The border between the two areas of nucleus intersection can be obtained by calculating the parameter h which is measured from the center axis (Fig. 6(b)). The equation can be derived by the following formulas of snell's law and planar geometry [15]:

$$sin\,\theta_i = \frac{h}{r_{sm}}, \tag{24}$$

$$\theta_r = arcsin\left(\frac{n_{tis}}{n_{cyto}}\frac{h}{r_{sm}}\right), \tag{25}$$

$$\theta_r = arcsin\left(\frac{r_{nc}}{r_{sm}}\right), \tag{26}$$

$$h = \frac{n_{cyto}}{n_{tis}}r_{nc}, \quad 0 \le h \le r_{sm}, \tag{27}$$

where r_{sm} and r_{nc} are the radius of soma and nucleus respectively, and θ_i and θ_r are the angle between the incoming and refracted light with respect to the center axis.

Based on the illuminated area, the light intensity which follows the geometric optics theory is

$$I_g = I_o e^{-\mu_a(\lambda)dDPF(\lambda)}cos\,\theta_i, \tag{28}$$

and the light intensity which is scattered by the nucleus is

$$I_s = I_o e^{-\mu_a(\lambda)d_i DPF(\lambda)}(1 - cos\,\theta_i), \tag{29}$$

where I_o, I_g and I_s are the light intensity at the light source, the light intensity which does not intersect the nucleus, and the light intensity which is scattered by the nucleus respectively; μ_a is the absorption coefficient; DPF is the differential path-length factor [40]; and d_i is the distance of light propagation.

D. Light Wave Superposition for different Soma Geometry

In all the aforementioned geometry scenarios, the shape of the nucleus (which plays the main role in the forward scattering and the focusing effect), is fixed and considered to be spherical. As explained earlier in Sec. II-D, and by following the Mie scattering theory, a closed form solution can be found for the light propagation around a spherical shape obstacle (in this case the nucleus). The intensity thermal plot for spherical nucleus is depicted in Fig. 7 in the close proximity of the nucleus, and in Fig. 8 for longer distances.

The nucleus placement at the center of the spherical soma model affects the lower and upper bounds of the focus points f_l and f_u. The focus points which are measured from the center for the soma can be obtained by [41]

$$f_l = r_{sm}\frac{n_{cyto}^2}{2n_{tis}\sqrt{n_{cyto}^2 - n_{tis}^2}}. \tag{30}$$

$$f_u = r_{sm}\frac{sin(\pi - \theta_i)}{sin(2(\theta_i - \theta_r))}. \tag{31}$$
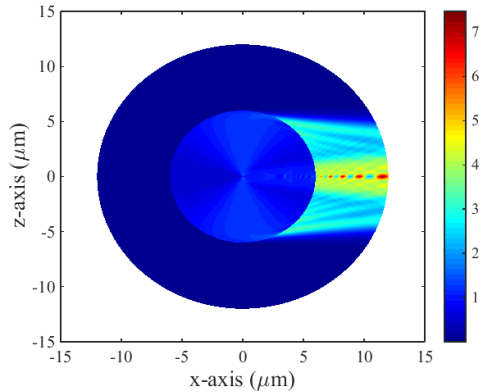

Fig. 7. The light intensity as a function of distance where coordinate (0,0) indicates the center point of the soma/nucleus.

The three previously mentioned geometries represent the shapes of the neuron soma. However, the discussion is limited to the collimated light wave and ideal shapes. In-vivo environment contributes to a more complicated situation especially in term of geometrical variation. Furthermore, the shape of the soma itself cause some changes in the direction of the collimated light as it penetrates inside the soma. This situation causes the change of light propagation behavior before and after the nucleus. In this case, the behavior can be analyzed by the superposition of multiple plane waves, $\sum_{n=1}^{N} U_n^{r(z,\rho,\phi)}|_t$, where U_n is the complex wave form at position $r(z,\rho,\phi)$ and time t.

Fig. 9 depicts different behaviors of light scattering propagation for the three soma shapes. The difference is mainly due to the size of the soma which is related to the geometry of the soma itself. The size ratio of the soma and the nucleus contributes in determining the maximum order of the Hankel function, $h_n^{(1)}$, calculation (as defined and explained earlier in Sec. II-D). As a result, the scattered field component changes according to the distance between the nucleus and the surface of the soma as formulated on Eq. (2). Furthermore, when the distance is extended to the far field region, the intensity increases to its maximum value (approximately 24 times per unit compared to the incoming intensity). This phenomenon can be seen in Fig. 8.
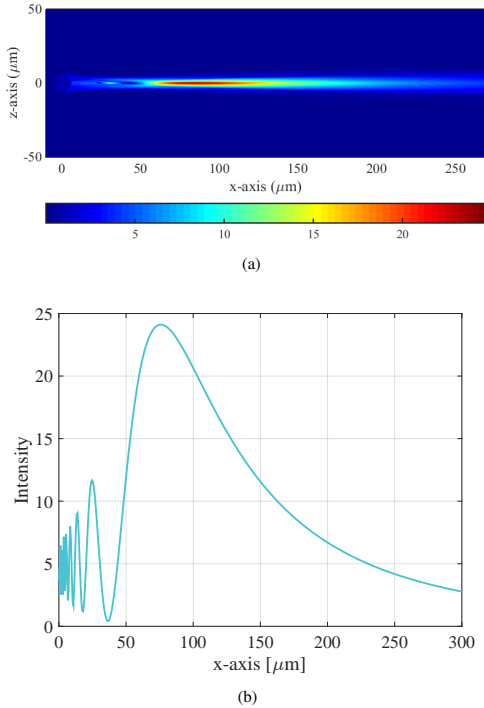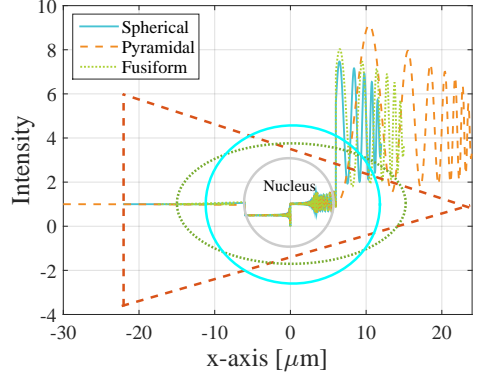

Fig. 9. The light intensity for three different shapes of soma that each has $12\mu m$ nucleus.

IV. AXONAL BIOPHOTON PROPAGATION

In [22], a new theory has been proposed on the manner of biophoton propagation along the axon, and is inspired from the properties of optical communications. In the light-based optical communication, there are three major elements required, namely, source, detector, and directed light propagation medium/waveguide. Inside the living organism, in this case human brain, a biophoton is dubbed as the natural light excited during the internal biological process of mitochondrial respiration or lipid oxidation. Meanwhile, mitochondrial centrosomes or chromophores serve as the biophoton detectors. In general, the requirements for biological waveguides include homogeneity and transmission capability. Myelin is a promising waveguide candidate due to its homogeneous structure and size [22]. Due to strong absorption by the proteins in the axons for certain wavelength (300 nm), the wavelength considered during the simulation conducted in [22] is between 400 nm and 1300 nm. This also means that keeping the wavelength within that range, for example visible light, is important in order to ensure the model is applicable.

Even though the myelin sheath has feasible properties as the waveguide, it has several imperfections which reduce the transmission effectiveness. These include the bending structure, cross-section variation, non-circularity of the shapes, cross-talk, and inhomogeneity of myelin sheath. The work in [22] addressed these imperfections along with nodal/paranodal regions and *Nodes of Ranvier* using the FDTD simulations. According to [22], the attainable biophoton transmission through 1-cm axon, depending on certain controlled parameter variation, is approximately 3-30%. While 2-mm axon gives attainable transmission of 46-96%.

Based on these results, our hypothesis in this section is to ensure that maximum light propagates down the axon based on the focusing effect. By enabling the light to propagate down the axon, this will lead to containment that will also ensure that focused light will not stimulate the neighboring neurons which can potentially avoid interference. Therefore, our aim

(a)

(b)

Fig. 8. The light intensity as a function of distance going further from the nucleus. The coordinate x=0 indicates the surface of the nucleus.

is to integrate the soma geometrical light intensity analysis with the axonal biophoton communication, and to determine the feasibility of this combined system.

A. External light propagation angle

The direction of incident relative to the axonal waveguide determines the effectiveness of the external light stimulation. Fig. 10 illustrates the feasibility to incorporate the external light source into the biophoton communication model in [22]. The Mie scattering focusing pattern elaborated in Sec. II-D determines the amount of transmitted light that will propagate into the axon if the focused point is within the cytoplasm. Therefore, the angle of incident relative to the axon line position is crucial to attain the maximum light transmission. When the size ratio of soma and nucleus is 2, the illuminated spherical cap of soma surface area has the base circle radius of 75% of the radius of the nucleus. For the soma radius of 12 μm with 6 μm-nucleus located on its center, the circle base radius of illuminated spherical surface soma cap, r_{sc} is approximately 4.5 μm. This size of cap radius can cover transitional path into the 3 μm-axon (r_{ax}), but only part of the 5 μm-myelin (r_{mye}). Whereas, for pyramidal and fusiform cells, the base circle radius of the illuminated soma surface is 55% and 68% of the radius of the nucleus, respectively. This lower percentage contributes towards a more tolerant angle (β in Fig. 10) of light projection from the light source on the neuron. It is also worthy of note that the distance between the nucleus and the axon also decreases the tolerance of the incident angle deviation.

Therefore, the percentage of the scattered external light being transmitted into the axonal waveguide depends on the illuminated axonal path area which is affected also by the distance between the nucleus and axonal waveguide entrance. In this case the effective transmission area can be obtained by

$$A_{tr} = r_{sc}^2 arccos\left(\frac{d_\beta^2 + r_{sc}^2 - r_{mye}^2}{2 d_\beta r_{sc}}\right) +$$
$$r_{mye}^2 arccos\left(\frac{d_\beta^2 + r_{mye}^2 - r_{sc}^2}{2 d_\beta r_{mye}}\right) -$$
$$\frac{1}{2}\sqrt{(-d_\beta + r_{sc} + r_{mye})(d_\beta + r_{sc} - r_{mye})} \times$$
$$\sqrt{(d_\beta - r_{sc} + r_{mye})(d_\beta + r_{sc} + r_{mye})},$$

where

$$d_\beta = Re\left\{2 r_{sm} sin\left(\frac{\beta}{2}\right)\right\} \qquad (32)$$

Fig. 11 shows the relationship between the percentage of external focused light component (which can be contained by the axonal biophoton communication) and the amount of light which is focused outside the soma.

B. Photo-thermal Effects of Light Propagation in Nervous Tissues

The tissue damage due to thermal increment is an important factor to consider whenever electromagnetic radiations inside the biological tissues is being studied [42]. However, based

(a) Spherical.

(b) Pyramidal.

(c) Fusiform.
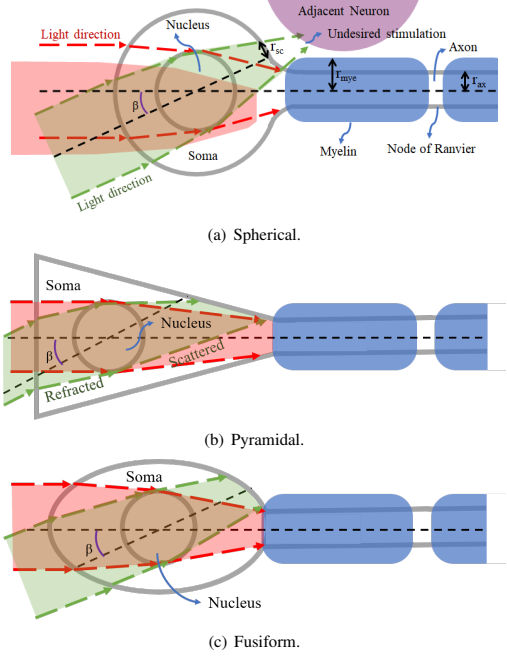
Fig. 10. An illustration of the variation of incident angles (β) to the focused light scattering due to the nucleus in the soma.
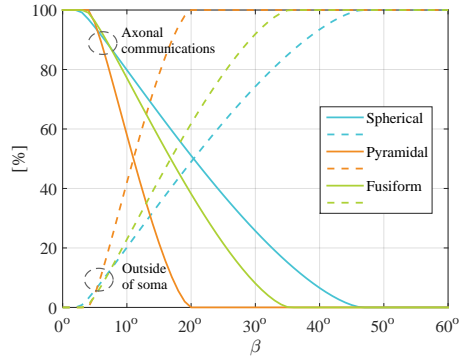
Fig. 11. The light percentage which is transmitted through axonal communications with incident light angle (β) variation.

on the experimental evaluation in [43], the light intensity safety limit is so high that the light intensity discussed in this paper is far from creating any harm on the brain tissue. The experiment observed 5-ms red and blue light pulses with intensity of 100-600 mW/mm^2 and frequency of 20, 40, and 60 Hz for the duration of 90 seconds. Furthermore, there is no phototoxic effect observed. Regarding the heat effect due to light absorption by the tissue, blue light causes higher temperature increase than red light. However, the increase is

(a) Spherical. (b) Pyramidal. (c) Fusiform.
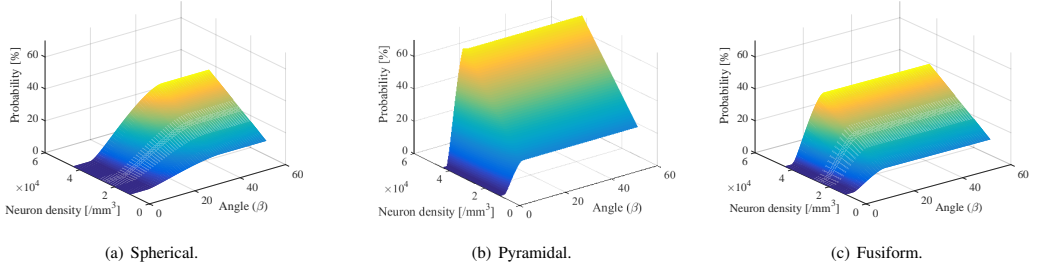
Fig. 12. The light percentage probability, which stimulates undesired neuron instead of being transmitted through axonal waveguide with respect to the incident light angle (β) and the neuron density variation.

Fig. 13. The light percentage probability, which stimulates undesired neuron instead of being transmitted through axonal waveguide with respect to the incident light angle (β) for constant neuron density of 26,000/mm^3.

still within acceptable range with a maximum increase of 1.5^oC inside the tissue. The intensity requirement of most optogenetic opsins is only around 1 to 5 mW/mm^2 which is significantly less than the intensity on the experiments in [43].

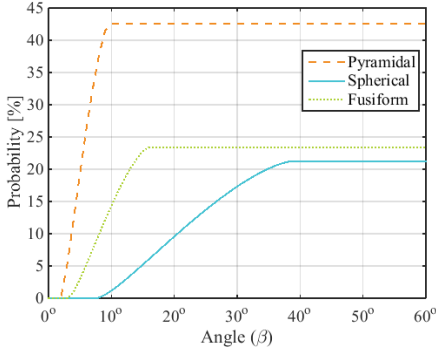### C. Interference Analysis of Undesired Light Propagation

As seen in the analysis and simulations, the focusing light traverses further beyond the target neuron which may result in undesired stimulation of surrounding optogenetic constructs (Fig. 10(a)). The probability of undesired illumination can therefore be estimated by considering the neuron density in the neocortex. The neuron density varies based on genders and individuals. On average, the density in men's neocortex is 25,924($\pm$15,110) /mm^3 and women's is 27,589($\pm$16,854) /mm^3 [44]. Based on this information, the probability of undesired neuron stimulation by a light wave that is supposed to be transmitted through axonal waveguide is obtained and it is presented in Fig. 12 and Fig. 13. These figures show the relation between the collimated light incident angle to the stimulation effectiveness and efficiency. They are derived by first calculating the portion of light that is focused by the soma, and then combining (multiplying) it with the result from Fig. 11 and the neuron density parameter in the

neocortex. In detail, by assuming that the neurons are equally distributed in the brain tissue, the undesired stimulation can be estimated. The average distance ($\overline{d}$) between neuron can also be obtained, for example, for 26,000 /mm^3, $\overline{d}$ is approximately 34 μm. The result can be analysed from Fig. 13 that the spherical soma is more tolerant to the incident angle deviation due to the short distance factor between the nucleus and the soma surface compared to other shapes. In addition to that, the probability of the external light hitting undesired neuron is lower. This finding concludes that neurons with spherical soma will ideally be selected for stimulation, and in particular for enabling the axonal biophoton communication to ensure containment.

V. CONCLUSIONS

The separate analysis based on geometrical optics or Mie scattering for the soma and nucleus is solely due to the size parameter. The spherical nucleus shape leads to focusing effect which is important for light communication in the brain. This is demonstrated using MATLAB simulation to show the light propagation behavior. Unlike the nucleus, the soma exhibits different behavior depending on its shape. The increase of the light intensity on the region after the nucleus has both advantage and disadvantage in its application. It may result in less input intensity requirement, but at the same time, it may cause undesired stimulation to other neurons. Relating this finding for axonal biophoton communication, the angle and the direction of the incoming incident light with respect to the location of the axon has to be properly considered. Furthermore, spherical shape soma is more tolerant to angle deviation due to its relatively smaller size ratio between its nucleus and soma. However, undesired stimulation is unlikely to cause phototoxic effect. Additionally, the density of the surrounding neurons defines the probability of undesired stimulation.

When the precision of single neuron stimulation for BCI is required, the understanding of the light behavior at the nanoscale is needed. This includes the shape imperfections, the optical properties gradients, the heterogeneity of the cell, and other minor deviations. This contribution will help in designing the more efficient and effective BCI system.

REFERENCES

[1] J. Wang, H. Xie, T. Chung, L. L. H. Chan, and S. W. Pang, "Neural probes with integrated temperature sensors for monitoring retina and brain implantation and stimulation," *IEEE Transactions on Neural Systems and Rehabilitation Engineering*, vol. 25, no. 9, pp. 1663–1673, 2017.

[2] J. Berg, J. Dammann III, F. Tenore, G. Tabot, J. Boback, L. Manfredi, M. Peterson, K. Katyal, M. Johannes, A. Makhlin *et al.*, "Behavioral demonstration of a somatosensory neuroprosthesis," *IEEE Transactions on Neural Systems and Rehabilitation Engineering*, vol. 21, no. 3, pp. 500–507, 2013.

[3] T. W. Berger, D. Song, R. H. Chan, V. Z. Marmarelis, J. LaCoss, J. Wills, R. E. Hampson, S. A. Deadwyler, and J. J. Granacki, "A hippocampal cognitive prosthesis: multi-input, multi-output nonlinear modeling and vlsi implementation," *IEEE Transactions on Neural Systems and Rehabilitation Engineering*, vol. 20, no. 2, pp. 198–211, 2012.

[4] N. A. Abbasi, D. Lafci, and O. B. Akan, "Controlled information transfer through an in vivo nervous system," *Scientific reports*, vol. 8, no. 1, p. 2298, 2018.

[5] H. Ramezani and O. B. Akan, "Impacts of spike shape variations on synaptic communication," *IEEE Transactions on NanoBioscience*, 2018.

[6] M. Veletić, P. A. Floor, Y. Chahibi, and I. Balasingham, "On the upper bound of the information capacity in neuronal synapses," *IEEE Transactions on Communications*, vol. 64, no. 12, pp. 5025–5036, 2016.

[7] A. Noel, D. Makrakis, and A. Eckford, "Distortion distribution of neural spike train sequence matching with optogenetics," *IEEE Transactions on Biomedical Engineering*, vol. -, no. -, pp. –, –.

[8] G. Hong, X. Yang, T. Zhou, and C. M. Lieber, "Mesh electronics: a new paradigm for tissue-like brain probes," *Current opinion in neurobiology*, vol. 50, pp. 33–41, 2018.

[9] D. Seo, J. M. Carmena, J. M. Rabaey, M. M. Maharbiz, and E. Alon, "Model validation of untethered, ultrasonic neural dust motes for cortical recording," *Journal of neuroscience methods*, vol. 244, pp. 114–122, 2015.

[10] D. Seo, R. M. Neely, K. Shen, U. Singhal, E. Alon, J. M. Rabaey, J. M. Carmena, and M. M. Maharbiz, "Wireless recording in the peripheral nervous system with ultrasonic neural dust," *Neuron*, vol. 91, no. 3, pp. 529–539, 2016.

[11] S. A. Wirdatmadja, M. T. Barros, Y. Koucheryavy, J. M. Jornet, and S. Balasubramaniam, "Wireless optogenetic nanonetworks for brain stimulation: Device model and charging protocols," *IEEE transactions on nanobioscience*, vol. 16, no. 8, pp. 859–872, 2017.

[12] I. F. Akyildiz, F. Brunetti, and C. Blázquez, "Nanonetworks: A new communication paradigm," *Computer Networks*, vol. 52, no. 12, pp. 2260–2279, 2008.

[13] S. T. Lee, P. A. Williams, C. E. Braine, D.-T. Lin, S. W. John, and P. P. Irazoqui, "A miniature, fiber-coupled, wireless, deep-brain optogenetic stimulator," *IEEE Transactions on Neural Systems and Rehabilitation Engineering*, vol. 23, no. 4, pp. 655–664, 2015.

[14] S. Ratnadurai-Giridharan, C. C. Cheung, and L. L. Rubchinsky, "Effects of electrical and optogenetic deep brain stimulation on synchronized oscillatory activity in parkinsonian basal ganglia," *IEEE Transactions on Neural Systems and Rehabilitation Engineering*, vol. 25, no. 11, pp. 2188–2195, 2017.

[15] S. Wirdatmadja, P. Johari, S. Balasubramaniam, Y. Bae, M. K. Stachowiak, and J. M. Jornet, "Light propagation analysis in nervous tissue for wireless optogenetic nanonetworks," in *Optogenetics and Optical Manipulation 2018*, vol. 10482. International Society for Optics and Photonics, 2018, p. 104820R.

[16] C.-P. Richter and X. Tan, "Photons and neurons," *Hearing research*, vol. 311, pp. 72–88, 2014.

[17] J. M. Stujenske, T. Spellman, and J. A. Gordon, "Modeling the spatiotemporal dynamics of light and heat propagation for in vivo optogenetics," *Cell reports*, vol. 12, no. 3, pp. 525–534, 2015.

[18] G. Yona, N. Meitav, I. Kahn, and S. Shoham, "Realistic numerical and analytical modeling of light scattering in brain tissue for optogenetic applications," *eneuro*, vol. 3, no. 1, pp. ENEURO–0059, 2016.

[19] Z. Wang, L. Wang, Y. Zhang, and X. Chen, "Monte carlo simulation of light propagation in human tissue models," in *Bioinformatics and Biomedical Engineering, 2009. ICBBE 2009. 3rd International Conference on*. IEEE, 2009, pp. 1–4.

[20] T. Tanifuji and M. Hijikata, "Finite difference time domain (fdtd) analysis of optical pulse responses in biological tissues for spectroscopic diffused optical tomography," *IEEE Transactions on medical imaging*, vol. 21, no. 2, pp. 181–184, 2002.

[21] V. Periyasamy and M. Pramanik, "Advances in monte carlo simulation for light propagation in tissue," *IEEE reviews in biomedical engineering*, vol. 10, pp. 122–135, 2017.

[22] S. Kumar, K. Boone, J. Tuszyński, P. Barclay, and C. Simon, "Possible existence of optical communication channels in the brain," *Scientific reports*, vol. 6, p. 36508, 2016.

[23] V. V. Tuchin, "Tissue optics and photonics: biological tissue structures," *Journal of Biomedical Photonics & Engineering*, vol. 1, no. 1, 2015.

[24] M. V. Sofroniew, P. Campbell, A. C. Cuello, and F. Eckenstein, "Central cholinergic neurons visualized by immunohistochemical detection of choline acetyltransferase," *The rat nervous system*, vol. 1, pp. 471–485, 1985.

[25] C. von Economo, *Cellular structure of the human cerebral cortex*. Karger Medical and Scientific Publishers, 2009.

[26] P. Johari and J. M. Jornet, "Nanoscale optical wireless channel model for intra-body communications: Geometrical, time, and frequency domain analyses," *IEEE Transactions on Communications*, vol. 66, no. 4, pp. 1579–1593, 2018.

[27] C. Fang-Yen and M. S. Feld, "Intrinsic optical signals in neural tissues: Measurements, mechanisms, and applications," *Acs Sym. Ser*, vol. 963, pp. 219–235, 2007.

[28] A. D. Klose and E. W. Larsen, "Light transport in biological tissue based on the simplified spherical harmonics equations," *Journal of Computational Physics*, vol. 220, no. 1, pp. 441–470, 2006.

[29] H. Guo, P. Johari, J. M. Jornet, and Z. Sun, "Intra-body optical channel modeling for in vivo wireless nanosensor networks," *IEEE transactions on nanobioscience*, vol. 15, no. 1, pp. 41–52, 2016.

[30] P. M. Groves and G. V. Rebec, *Introduction to biological psychology*. McGraw-Hill Humanities, Social Sciences & World Languages, 1988.

[31] W. Choi, C. Fang-Yen, K. Badizadegan, S. Oh, N. Lue, R. R. Dasari, and M. S. Feld, "Tomographic phase microscopy," *Nature methods*, vol. 4, no. 9, p. 717, 2007.

[32] C. F. Bohren and D. R. Huffman, *Absorption and scattering by a sphere*. Wiley Online Library, 1983.

[33] C. Mätzler, "Matlab functions for mie scattering and absorption, version 2," *IAP Res. Rep*, vol. 8, pp. 1–24, 2002.

[34] D. Dermendjian, "Light scattering by spherical polydispersions," 1969.

[35] X. Fan, W. Zheng, and D. J. Singh, "Light scattering and surface plasmons on small spherical particles," *Light: Science & Applications*, vol. 3, no. 6, p. e179, 2014.

[36] E. Stachowiak, X. Fang, J. Myers, S. Dunham, and M. Stachowiak, "camp-induced differentiation of human neuronal progenitor cells is mediated by nuclear fibroblast growth factor receptor-1 (fgfr1)," *Journal of neurochemistry*, vol. 84, no. 6, pp. 1296–1312, 2003.

[37] E. Stachowiak, C. Benson, S. Narla, A. Dimitri, L. B. Chuye, S. Dhiman, K. Harikrishnan, S. Elahi, D. Freedman, K. Brennand *et al.*, "Cerebral organoids reveal early cortical maldevelopment in schizophreniacomputational anatomy and genomics, role of fgfr1," *Translational Psychiatry*, vol. 7, no. 11, p. 6, 2017.

[38] G. H. Sydney *et al.*, *Sources of consciousness: the biophysical and computational basis of thought*. World Scientific, 1997, vol. 5.

[39] J. Watson, "Optics, learning by computing, with examples using mathcad: Kd möller; springer, berlin, 2003, xvi+ 443pp.+ cd-rom; price£ 49.00 hardback, isbn 0 387 95360 4," 2004.

[40] F. Scholkmann and M. Wolf, "General equation for the differential pathlength factor of the frontal human head depending on wavelength and age," *Journal of Biomedical Optics*, vol. 18, no. 10, pp. 105 004–105 004, 2013.

[41] P. Johari and J. M. Jornet, "Nanoscale optical channel modeling for in vivo wireless nanosensor networks: A geometrical approach," *Proc. of the IEEE International Conference on Communications (ICC)*, pp. 1–6, 2017.

[42] H. Elayan, P. Johari, R. M. Shubair, and J. M. Jornet, "Photothermal modeling and analysis of intrabody terahertz nanoscale communication," *IEEE transactions on nanobioscience*, vol. 16, no. 8, pp. 755–763, 2017.

[43] S. Senova, I. Scisniak, C.-C. Chiang, I. Doignon, S. Palfi, A. Chaillet, C. Martin, and F. Pain, "Experimental assessment of the safety and potential efficacy of high irradiance photostimulation of brain tissues," *Scientific reports*, vol. 7, p. 43997, 2017.

[44] T. Nguyen, "Total number of synapses in the adult human neocortex," *Undergraduate Journal of Mathematical Modeling: One+ Two*, vol. 3, no. 1, p. 26, 2010.

PUBLICATION

VI

Channel Impulse Analysis of Light Propagation for Point-to-point Nano Communications through Cortical Neurons

S. Wirdatmadja, J. M. Jornet, Y. Koucheryavy and S. Balasubramaniam

Channel Impulse Analysis of Light Propagation for Point-to-point Nano Communications through Cortical Neurons

Stefanus Wirdatmadja, Josep Miquel Jornet, Yevgeni Koucheryavy,

and Sasitharan Balasubramaniam

Abstract

Recent Brain-Machine Interfaces have moved towards miniature devices that can be seamlessly integrated into the cortex. In this paper, we propose communication between miniature devices using light. A number of challenges exist using nanoscale light-based communication and this includes diffraction, scattering, and absorption, where these properties result from the tissue medium as well as the cell's geometry. Under these effects, the paper analyses the propagation path loss and geometrical gain, channel impulse and frequency response through a line of neurons with different shapes. Our study found that the light attenuation depends on the propagation path loss and geometrical gain, while the channel response is highly dependent on the quantity of cells along the path. Additionally, the optical properties of the medium impact the time delay at the receiver and the width and the location of the detectors.

S. Wirdatmadja and Y. Koucheryavy are with the Department of Electronic and Communication Engineering, Tampere University, Tampere, Finland, e-mail: {stefanus.wirdatmadja, evgeny.koucheryavy}@tuni.fi.

S. Balasubramaniam is with the Telecommunication Software and Systems Group, Waterford Institute of Technology, Ireland e-mail: sasib@tssg.org

J. M. Jornet is with the Department of Electrical and Computer Engineering, Northeastern University, Boston, Massachusetts, USA, e-mail: jmjornet@northeastern.edu

Simulations were conducted for cells that are lined horizontally up to a distance of 450 μm using light wavelength of 456 nm and different neuron densities (men's neocortex (25,924($\pm$15,110) /mm^3) and women's (27,589($\pm$16,854) /mm^3)). Based on the simulations, we found that spherical cells attenuate approximately 20% of the transmitted power compared to the fusiform and pyramidal cells (35% and 65%, respectively).

Index Terms

Nano communications, Optogenetics, Light Propagation Modelling, Neural Systems.

I. INTRODUCTION

Implantable medical devices in recent years have witnessed an exponential growth due largely to numerous supporting fields, including nanotechnology, computer science, and electrical engineering. The advancements in such fields are leading to miniature devices, constructed from biocompatible materials and powered by means of energy-harvesting systems, which can be permanently implanted. In this context, the emerging field of nano-communications is aimed at enabling the exchange of information and coordination between nano-devices. Two approaches for nano-communications have been developed in parallel, namely, nano-electromagnetic (EM) communications [1] and molecular communications [2]. A number of works have looked at molecular communications for neural systems. For example, [3] conducts and analyzes invivo information transfer on the nervous system of an earthworm, [4] proposes the complete synaptic communication channel model, and [5] investigates the upper bound for neural synaptic communication. Acoustic signals have been proposed to allow devices to communicate [6], but the unit circuitry may be larger than the envisioned micron-scale size devices that needs to be placed deep in the tissue. This challenge is further exacerbated when we consider implanting the devices in the cortex of the brain. In the case of nano-EM communications, a major challenge is the selection of an appropriate frequency for signaling that is relative to the size of the antenna components. This is because the reduction in size of an antenna means that the operating

frequency also increases [1], and THz waves are unable to penetrate through biological tissues. This is due to the high energy photons interacting with living cells at the molecular scale through the process of absorption [7] [8]. This means that other modes of communication are required in order to enable devices to communicate and network in biological tissues.

In our previous work [9] a miniature device known as Wireless Optogenetic Nano Devices (WiOptND) for neural stimulation was proposed. The device utilizes ultrasound signals for energy harvesting to produce power for a light source that is used for stimulating small population of neurons, and this process is known as optogenetics. Some constraints in optogenetics stimulation are investigated in [10] in terms of distortion from the spike generation delay due to the stochastic behaviour of the surface receptors, which results in random time response delays from the time a neuron is externally stimulated. In other works, light has been used to communicate between devices through red blood cells [7]. While both THz waves and optical signals are very high frequency EM waves, one key difference is that the latter does not suffer from strong absorption compared to the former due to tissue water content. In recent years, extensive modelling has been established for behaviour of light that is used for stimulating neurons, but there have not been any proposal towards using nanoscale light communication between devices implanted into the brain. While optical signals suffers from scattering phenomenon, this does not directly translate into undesired effects since it also supports the light focusing phenomenon during the propagation process through neurons, which we found in our previous study [11]. In this paper, we propose communication between the WiOptND devices using light. As illustrated in Fig. 1, this could lead to miniature nanonetworks that are implanted into the brain cortex, and the communication and cooperation between the WiOptNDs can enable neural circuit stimulation of different micro-columns within the cortical cortex that have impaired connections.

A major challenge with light communication through neural tissue, and in particular at micron-scale, is that the propagation of the light is largely determined by the physiological shape as well as the organelles within the cell. This is due to the size of the source that produces light
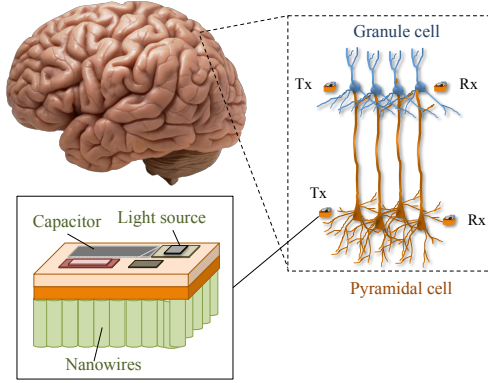
Fig. 1: Illustration of the Wireless Optogenetic Nanodevice (WiOptND) network that are placed within the cortex. The communication between the devices is established using light that penetrates through the cells.

waves that are comparable to the size of the neuron. Therefore, the propagation behaviour of the light is largely dictated by the composition of the tissue. Neural tissue is composed of cells with different physiological properties, each of which contributes differently towards the propagation pattern. In this paper, we focus on the power delay profile, femto-pulse signal analysis in both time and frequency domains, and the channel impulse response of light propagation for physical communication analysis in neural tissue. We employ a ray tracing approach to analyze the light propagation along the path of cells in the neural tissue, due to the scale of the light source being comparable to the size of the soma of the neurons, which allows us to model the propagation of individual rays spatially to understand how the shapes of the cell will influence their propagation. Additionally, when the ray tracing is combined with the modified Beer-Lambert accounting for absorption and scattering, the intensity attenuation can be computed accurately. While a Finite Difference Time Domain (FDTD) solver can increase the accuracy of the result with all available parameters, solving Maxwell's equations is much more computationally demanding that utilizing

ray tracing methods. Our aim is to determine the channel impulse response of the light signal as it propagates through different shapes as well as density of neurons. We extend the discussion in [11] and [12] in terms of fundamental propagation medium characterisation and its effect on a single line array of cells, which can affect the communication performance between two WiOptNDs devices that are communicating with each other using light. Moreover, we derived the impulse responses based on the cell's morphology, which is an analysis that is beneficial for determining the light propagation behaviour that can impact on the communication performance. The contributions of this paper are as follows:

- **Geometric Analysis of Light Propagation and Path Loss Analysis:** We derive the total path loss formula for three different neuron geometries, namely fusiform, spherical, and pyramidal based on optical properties of the brain tissue and neurons. We analyze the focusing gain for multiple-(radial-based)-cell light propagation that results from the converging and diverging light phenomena through the array of cells.

- **Numerical Analysis of Channel Impulse Response for Light Propagation:** We define a channel impulse response model based on the physiological shapes of the aforementioned neurons. This includes numerical analysis to determine the impact of light propagation through a line of neurons to determine how this impacts on the impulse response. The approach taken is through multiple ray tracings that simulates individual rays as they propagate through the array of cells.

This paper is organized as follows: In Sec. I, we present the background and motivation of this paper. In Sec. II, we elaborate the light absorption and scattering phenomena in biological tissue. In Sec. III, we derive the total path loss for three geometric neuron models. In both Sec. IV and V, we analyze the simulated system in both time and frequency domains. In Sec. VI, we elaborate the results based on the simulated light propagation system and relate them with the geometrical and optical properties of the system. Finally, we present the conclusion in Sec. VII.

II. ABSORPTION AND SCATTERING IN BIOLOGICAL TISSUE

In general, for all cell geometries, the path loss is determined by the medium in which the light traverses. In our case, the medium consists of biological tissues that contains neural cells. Each propagation medium has three significant parameters that play a role in the behaviour of light transmission, namely absorption coefficient (μ_a), reduced scattering coefficient (μ'_s) which indicates random photon path exists due to scattering, and distance (d) between the transmitter and the receiver [13] [14]. The last parameter is heavily dependent on the refraction of light as it propagates through the medium, which is governed by the cell's geometry and the refractive index of different internal components (n) of the organelles.

The propagation medium investigated in this paper consists of two biological mediums with different optical parameters. The two mediums are the brain tissue and each individual neuron. The brain tissue comprises many components including neuroglia and astrocytes, while neuron consists of cytoplasm, mitochondria, nucleus, and many other organelles. In this work, we consider that the absorption coefficients remain constant for each medium throughout the propagation path. Additionally, these mediums are modeled as homogeneous materials for computational tractability. Moreover, since the distance is very short between the homogeneous cells, the effect of other components is negligible on the scattering. However, the scattering between the cells is still considered by representing the tissue scattering coefficient as the average value of those scatterers. Therefore, the path loss analysis is based on the propagation distance, where the distance determines how the medium changes impact on the light path. The light intensity along the propagation path for each medium is analyzed using the modified *Beer-Lambert law* and is represented as [15] [16] [17] ,

$$I(\lambda, d) = I_0(\lambda)e^{-\mu_a(\lambda)dDPF(\lambda,d)}, \tag{1}$$

where $I(\lambda)$ is light intensity at λ wavelength on distance d, $I_o(\lambda)$ is the light intensity at the source, and $DPF(\lambda, d)$ is the Differential Path Length Factor, which is a scaling factor

indicating the distance traveled by the light wave that is impacted by the shifted direction due to the interaction with the neuron (please note that our light source is at nanoscale and will, therefore, be highly impacted by the cell shape).

The DPF is the element which is included in the modified *Beer-Lambert* law and is affected by the optical medium properties, namely the absorption (μ_a) and the reduced scattering (μ'_s) coefficients [18], and is represented as follows

$$DPF^{(k)}(\lambda, d) = \frac{1}{2}\left(\frac{3\mu'_s(\lambda)}{\mu_a(\lambda)}\right)^{1/2}\left[1 - \frac{1}{1 + d(3\mu_a(\lambda)\mu'_s(\lambda))^{1/2}}\right]. \tag{2}$$

The propagation channel elaborated in this paper consists of two mediums (cell and brain tissue) which are categorized as intra and inter-cell propagation mediums. Therefore, the DPF equation (2) should be applied to all paths with respect to its medium.

Based on (1) and (2), the medium light transmittance $T(\lambda, d)$ can be represented as

$$T(\lambda, d) = \frac{I(\lambda, d)}{I_0(\lambda)} = e^{-\mu_a(\lambda)dDPF(\lambda,d)}. \tag{3}$$

III. Geometric Model of Multiple Cell Path Loss

Along with other aspects such as cell organelles and the size ratio between a cell and a light wavelength, the geometry of the cell has a significant effect on the light propagation behaviour as discussed in Sec. I, and this is largely due to the size and aperture of the light source, and attenuation of the intensity. The geometrical analysis for the physiological shapes of the neurons is based on the models in [11], and the three different neurons that is analyzed in this paper are *Fusiform*, *Spherical*, and *Pyramidal* cells. In addition to the shape and size of each individual neuron, the light wave traverses a dense neural population. In this section, we elaborate the effect by the cell's geometry on the light propagation as it traverses a line of neurons that are of the same type.

Neurons that are densely packed can be structured in a straight line and examples of this is illustrated in Fig. 2. The figure shows an induced Pluripotent Stem Cell (iPSC) brain organoid
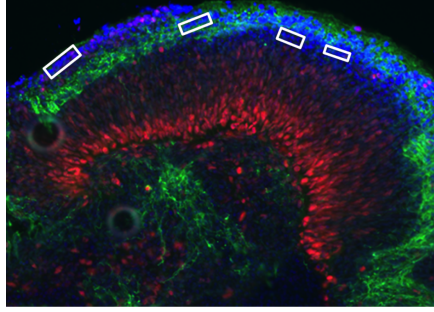
Fig. 2: Image of a 5-week old induced Pluripotent Stem Cells (iPSC) cerebral organoid with differentiated neurons [19]. The white box illustrates examples of dense cells that are arranged in a straight line.

with differentiated neurons, where the white boxes illustrates examples of spherical neurons that are in a straight line (this is based on experiments we have conducted in our past work [19]). Each cortical layer of the neocortex is populated by various types and ratio of neurons. For example, pyramidal cells are usually found in layers III and V, while fusiform cells are located in layer VI [20]. Additionally, the average neuron density in men's neocortex is 25,924($\pm$15,110) /mm^3 and women's is 27,589($\pm$16,854) /mm^3 [21]. Therefore, by considering that our device will only communicate through a line of homogeneous cells within the layers of the neocortex, the general formula for the total path loss in dB for N number of any given shape of neurons is represented as

$$
\begin{aligned}
PL_{total} = 4.343 \Big[& N\mu_a^{(c)}(\lambda)\overline{d_a}DPF(\lambda,\overline{d_a}) \\
& + (N-1)\mu_a^{(u)}(\lambda)\overline{d_e}DPF(\lambda,\overline{d_e}) \\
& + \mu_a^{(u)}(\lambda)(d_E+d_R)DPF(\lambda,(d_E+d_R)) \Big],
\end{aligned}
\tag{4}
$$

where $\overline{d_a}$ and $\overline{d_e}$ are the average propagation distances in a cell and between two cells based on its shape, respectively, d_E and d_R are the distances of the light source from the first cell and
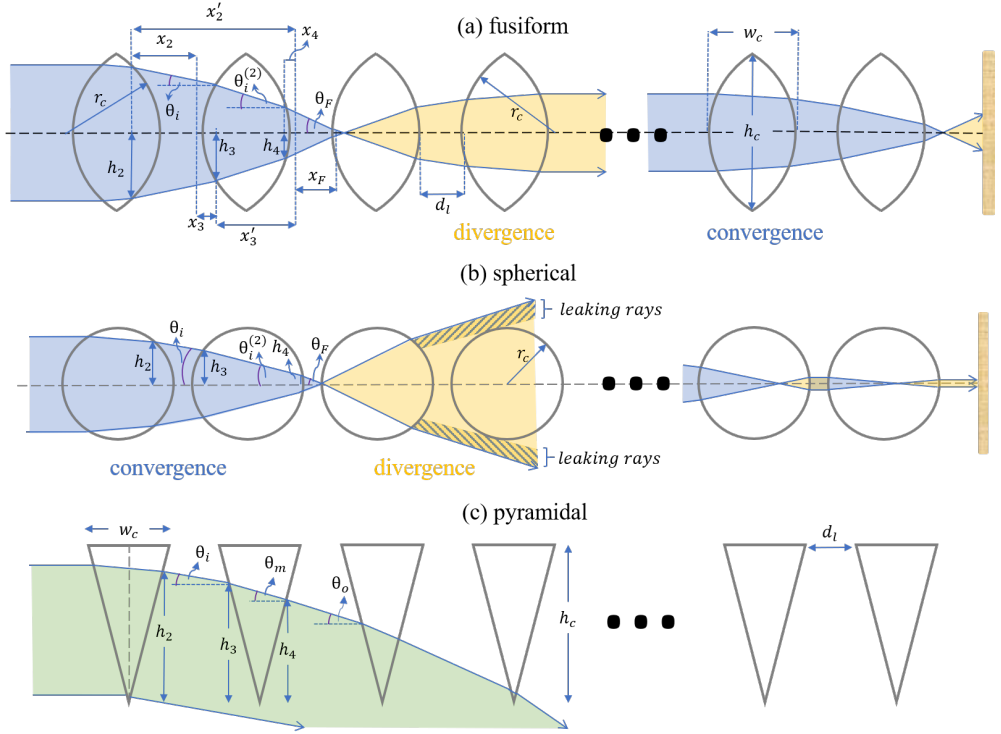
Fig. 3: Geometrical analysis of light propagation using ray tracing as it propagates through a one-dimensional array of neurons, and this includes (a) fusiform, (b) spherical, (c) pyramidal cells.

the location of the receiver from the last cell, respectively. The superscript (c) or (u) indicates whether the parameter belongs to the cell or brain tissue.

In the following subsections, we present the derivation for both $\overline{d_a}$ and $\overline{d_e}$ for the three different types of neurons, where they are cholinergic neurons that are found in the cerebral cortex [20]. The shapes for each of the cells, as well as the geometric analysis of light propagation through the tissue is illustrated in Fig. 3.

A. Fusiform cell

A fusiform cell can be projected onto a 2D-plane as an oval or convex lens, as illustrated in Fig. 3(a). The dimensions of the cell are represented with a height h_c, width w_c, a surface curvature radius of r_c, and their relationship is represented as

$$r_c = \frac{h_c{}^2 + w_c{}^2}{4w_c}. \tag{5}$$

A single neuron of this shape has a focusing behaviour when collimated light propagates through the cell. To investigate the light propagation behavior for multiple neurons organized in a one-dimensional array, several fusiform cells are positioned in a sequence so that the collimated light propagates in a non-line-of-sight manner from the second cell. Applying this model to observe the focusing phenomena leads to another light behaviour which is the divergence effect. The divergence effect occurs when the focus point becomes shorter as the light propagates through consecutive fusiform cells. Due to the cell geometry, the focusing/converging and diverging phenomena occurs alternately, and this phenomena is illustrated in Fig. 3(a). Using geometrical analysis, the average propagation distances inside the fusiform cell d_a and between the cells d_e are formulated as

$$
\begin{aligned}
\overline{d_a} = \frac{4}{h_c} \int_{\frac{r_c-h_c}{2}}^{\frac{r_c}{2}} \sqrt{r_c{}^2 - x^2} - (r_c - \frac{w_c}{2})dx \;=\; \frac{1}{6h_c}\Bigg[& 6h_c w_c - 12 r_c{}^2 \arcsin\left(\frac{r_c - h}{2r_c}\right) \\
& + 3(h_c - r_c)\sqrt{3r_c{}^2 + 2h_c r_c - h_c{}^2} \\
& + \left(2\pi + \sqrt{27}\right) r_c{}^2 - 12 h_c r_c \Bigg], \quad (6)
\end{aligned}
$$

$$
\begin{aligned}
\overline{d_e} = d_l + \frac{2}{h_c} \int_{\frac{r_c-h_c}{2}}^{\frac{r_c}{2}} \frac{w_c}{2} - \sqrt{r_c{}^2 - x^2}dx \;=\; d_l + \frac{1}{12h_c}\Bigg[& -6h_c w_c + 12 r_c{}^2 \arcsin\left(\frac{r_c - h_c}{2r_c}\right) \\
& + (3r_c - 3h_c)\sqrt{3r_c{}^2 + 2h_c r_c - h_c{}^2} \\
& + \left(-2\pi - \sqrt{27}\right) r_c{}^2 + 24 h_c r_c \Bigg]. \quad (7)
\end{aligned}
$$

B. Spherical cell

Fig. 3(b) illustrates a spherical shaped neuron with radius r_c projected onto a 2D space. The behaviour of the spherical shaped cell is similar to the fusiform cell, and this is from the focusing effects. However, depending on the density of the neurons, the distance between the cells d_l has a significant role in *leaking* light rays which does not occur in multiple fusiform neural tissue. Leaking rays are the rays that do not propagate to the next adjacent cell. Therefore, they are not further transmitted along the propagation path. However, the alternating converging and diverging phenomena are similar for both spherical and fusiform cells. The light propagation for multiple spherical neurons in a 1-dimensional array is illustrated in Fig. 3(b). For the spherical cell the average propagation distance d_a inside a cell and between cells d_e is given by

$$\overline{d_a} = \frac{2}{r_c} \int_0^{r_c} \sqrt{r_c^2 - x^2} dx = \frac{1}{2} \pi r_c, \tag{8}$$

$$\overline{d_e} = d_l + \frac{1}{r_c} \int_0^{r_c} r_c - \sqrt{r_c{}^2 - x^2} dx = d_l - \frac{1}{4}(\pi - 4) r_c{}^2. \tag{9}$$

Similar to the fusiform cell analysis, $\overline{d_a}$ and $\overline{d_e}$ of the spherical cells considers all the light rays along the propagation axis. However, the difference lies in the distance between the incoming and outgoing surfaces for the rays.

C. Pyramidal cell

The propagation behaviour for pyramidal cells is significantly different when compared to the two aforementioned neurons in terms of light ray traces, and this is illustrated in Fig. 3(c). A pyramidal cell tends to deviate the light path due to the refraction of two different medium, and takes on a behaviour that is very similar to a prism. In this case, the light traversing through multiple pyramidal cells deviates from its initial axis before it completely propagates from the line path of the arrays of cells. The light deviation behaviour with respect to the cell's geometry is illustrated in Fig. 3(c). The average propagation distance d_a inside a cell and between cells

d_e is represented as

$$\overline{d_a} = \frac{2}{h_c} \int_0^{h_c} \left[\frac{w_c}{h_c}(x - h_c) + \frac{w_c}{2} \right] dx = \frac{1}{2} w_c, \tag{10}$$

$$\overline{d_e} = d_l + \frac{1}{h_c} \int_0^{h_c} \left[\frac{w_c}{h_c}(x - h_c) + \frac{w_c}{2} \right] dx = d_l + \frac{1}{4} w_c. \tag{11}$$

The 2-D projection of the pyramidal cell can be perceived as an isosceles triangle, which is similar to a prism. Therefore, the light ray deviation angle is governed by the medium refraction indices. Both (10) and (11) include ray traces from inside a cell and between two neighbouring cells.

IV. MULTI-NEURON LIGHT PROPAGATION CHANNEL IMPULSE RESPONSE

The cell geometry and the tissue optical properties have a significant effect on the impulse response of the propagation channel. In this section, we derive how the geometrical analysis of the previous section plays a role on the channel impulse response, and how this differs between the three different types of neurons. The combination of both the cell's geometry and the optical properties results in attenuation as well as delay of the light propagation to the detector. This is largely due to the collimation as well as divergence due to the geometric shape and results in multiple propagation paths of the light rays.

The general expression of multipath impulse response considering N number of neurons that are placed in a 1-dimensional array can be formulated as [22]

$$h(t; d_{total}, \lambda) = \overset{N}{\underset{n=1}{\circledast}} h_a^{(n)}(t; d, \lambda) \circledast \overset{N+1}{\underset{n=1}{\circledast}} h_e^{(n)}(t; d, \lambda), \tag{12}$$

where $h^{(n)}(t; d, \lambda)$ represents the impulse response of the light ray corresponding to the nth cell, λ is the wavelength, t is the time, and the corresponding subscript a or e indicates if it is an intra-cell or inter-cell propagation. Furthermore, the intercell impulse response, $h_e^{(n)}$ in (12), consists of three elements, $h_c^{(n)}$, h_E, and h_R, and is represented as follows

$$\overset{N+1}{\underset{n=1}{\circledast}} h_e^{(n)}(t; d, \lambda) = \overset{N-1}{\underset{n=1}{\circledast}} h_c^{(n)}(t; d^{(n)}, \lambda) \circledast h_E(t; d_E, \lambda) \circledast h_R(t; d_R, \lambda) \tag{13}$$

where subscripts c, E, and R indicates the propagation paths between the cells, light source, and the receiver (detector), respectively, d_E is the distance between the light source and the first cell, and d_R is the distance between the last cell and the receiver. As shown in (12), the impulse response is based on the convolution as the light propagates through each individual cell along the path, and the brain tissue between the cells.

The light source applied in this system is considered as a collimated light where the generated rays has equal intensity following the uniform distribution $\mathcal{U}(0, 1)$. In order to use the ray tracing model, the infinite rays should be discretized to K rays. Since the intensity parameter is used, the discretization process has no impact on the intensity value. To further elaborate on this, each intra and inter-cell propagation impulse response can be divided into two parts, namely, the attenuation component and the delay component. The attenuation follows the modified Beer-Lambert equation, while the delay can be expressed as a delta dirac function. Thus, the impulse response for k^{th}-path is represented as

$$h_a^{(k)}(t; d^{(k)}, \lambda) = I_E T_a^{(k)}(\lambda) \delta(t - t_a^{(k)}) \circledast I_E T_e^{(k)}(\lambda) \delta(t - t_e^{(k)}), \tag{14}$$

where I_E is the intensity emitted by the light source, $T^{(k)} = e^{-\mu_a^{(k)}(\lambda) d^{(k)} DPF^{(k)}(\lambda, d^{(k)})} = e^{\underline{\eta}^{(k)}}$ is the transmittance of the kth-path, $t^{(k)} = \frac{||\underline{d}^{(k)}||_1}{v}$ represents the time delay introduced by the propagation medium and the corresponding subscript a or e indicates if it is intracell or intercell propagation.

Furthermore, when the rays from the light source are discretized into K individual paths, they will traverse through N cells which are aligned between the transmitter and the receiver. Intuitively, all the corresponding impulse responses contributing to the received signal can be obtained by (14). Furthermore, (14) can be expressed in detailed by substituting the transmittance

by the exponential equation as follows

$$
\begin{bmatrix}
h_a^{(1)} \\
h_e^{(1)} \\
h_a^{(2)} \\
h_e^{(2)} \\
\vdots \\
h_a^{(K)} \\
h_e^{(K)}
\end{bmatrix}
= I_E \cdot e^{\underline{\eta}^T}
\begin{bmatrix}
\delta(t - \frac{||d_a^{(1)}||_1}{v_a}) \\
\delta(t - \frac{||d_e^{(1)}||_1}{v_e}) \\
\delta(t - \frac{||d_a^{(2)}||_1}{v_a}) \\
\delta(t - \frac{||d_e^{(2)}||_1}{v_e}) \\
\vdots \\
\delta(t - \frac{||d_a^{(K)}||_1}{v_a}) \\
\delta(t - \frac{||d_e^{(K)}||_1}{v_e})
\end{bmatrix},
$$

where η represents the matrix product of the absorption coefficient, the distance and the DPF, v is the light velocity in the medium, and subscript a or e indicates if the path is intra or intercell propagation, respectively. The velocity value can be obtained by $v = \frac{c}{n}$, where c is the light speed in vacuum and n is the refractive index of the medium. Therefore, the matrix product η is further substituted by the multiplication of the absorption coefficient, distance, and DPF and represented as

$$
\underline{\eta} =
\begin{bmatrix}
\eta_a^{(1)} \\
\eta_e^{(1)} \\
\eta_a^{(2)} \\
\eta_e^{(2)} \\
\vdots \\
\eta_a^{(K)} \\
\eta_e^{(K)}
\end{bmatrix}
=
\begin{bmatrix}
-\mu_a^{(c)} \sum_{n=1}^{N} d_a^{(1,n)} \\
-\mu_a^{(u)} \sum_{n=1}^{N+1} d_e^{(1,n)} \\
-\mu_a^{(c)} \sum_{n=1}^{N} d_a^{(2,n)} \\
-\mu_a^{(u)} \sum_{n=1}^{N+1} d_e^{(2,n)} \\
\cdots \\
-\mu_a^{(c)} \sum_{n=1}^{N} d_a^{(K,n)} \\
-\mu_a^{(u)} \sum_{n=1}^{N+1} d_e^{(K,n)}
\end{bmatrix}^T
\begin{bmatrix}
DPF_a^{(1)} \\
DPF_e^{(1)} \\
DPF_a^{(2)} \\
DPF_e^{(2)} \\
\vdots \\
DPF_a^{(K)} \\
DPF_e^{(K)}
\end{bmatrix}.
$$

where μ_a is the absorption coefficient and the superscript (c) or (u) indicates either the neuron or the brain tissue, respectively.

V. FREQUENCY DOMAIN ANALYSIS

In optogenetics, the wavelength that is used for the neuron stimulation is based on the visible 450-480 nm blue light, and this is the same wavelength that is used for the light communication

between the WiOptND devices in our proposed model. The communication is established through light propagation that is represented as a short Gaussian shaped pulse. The Gaussian shaped pulse is the product of a cosine function and a Gaussian envelope function. For a light wave, the Gaussian pulse can be expressed as [23]

$$E_t = Re\{E_0 e^{-4ln(2)\left(\frac{t}{\tau}\right)^2 + i\omega_0 t}\} \tag{15}$$

where E_t and E_0 are the electric field with respect to time $t = 0$, respectively, ω_0 is the angular frequency of the light wave, and τ is the Full-Width at Half-Maximum (FWHM) pulse duration. On the receiver side, the time delay is added to the pulse waveform and it is formulated as

$$E_r = Re\{\gamma E_0 e^{-4ln(2)\left(\frac{t-t_d}{\tau}\right)^2 + i\omega_0(t-t_d)}\}, \tag{16}$$

where t_d denotes the time delay caused by the propagation path and $\gamma = \left(\frac{r_E}{r_D}\right)^2$ is the area (proportional to the square of radius) ratio due to the focusing effect, r_E is the radius of the light source and r_D is at the detector [12]. The result from the convolution series of the channel impulse response presented in (12) can also be obtained by analysing the Fourier transforms of the transmitted signal, $\mathcal{F}(E_t)$, and the received signal $\mathcal{F}(E_r)$. The channel impulse response can be obtained by applying the inverse Fourier transform of the division, and is represented as

$$h(t; d, \lambda) = \mathcal{F}^{-1}(H(f; d, \lambda) = \mathcal{F}^{-1}\left(\frac{\mathcal{F}(E_r(t; d, \lambda))}{\mathcal{F}(E_t(t; d, \lambda))}\right). \tag{17}$$

Based on (15) and (16), we can observe that the input and output relationship is heavily dependent on the delay caused by the propagation medium characteristics. To obtain this impulse channel characterisation, which correlates with the delay and focusing factors, we further process the transmitted and received time domain signals in the frequency domain.

VI. NUMERICAL ANALYSIS

In this paper, the light propagation is simulated using MATLAB, where the simulator generates geometrical rays that propagate through both the brain tissue as well as the three different

shapes of neurons. Our approach used for the light propagation modeling is based on a ray tracing algorithm. Algorithm 1 presents an example for the fusiform cell ray tracing process, and similar algorithms are also developed for the spherical and pyramidal cells based on their geometrical properties. This function is iteratively executed and combined with the ray tracing by applying the focusing parameter γ from (16), which is determined by the illuminated detection area. Table I lists all the parameters that was used in the MATLAB simulation.

TABLE I: Simulation Parameters

Parameter	Value [Unit]	Description
λ	456 [nm]	Visible blue light wavelength
n_c	1.36	Refractive index of the cell [24]
n_t	1.35	Refractive index of the tissue
$\mu_a^{(c)}$	0.9 [$/mm$]	Cell absorption coefficient [25]
$\mu_s'^{(c)}$	3.43 [$/mm$]	Cell reduced scattering coefficient
$\mu_a^{(u)}$	20 [$/mm$]	Tissue absorption coefficient [26]
$\mu_s'^{(u)}$	1.43 [$/mm$]	Tissue reduced scattering coefficient
τ	1 [fs]	FWHM pulse duration

A. Path Loss and Geometrical Gain

The light wave traversing in the biological tissue experiences attenuation as discussed in Sec. II. The attenuation is mainly due to the optical properties of all the biological components in the cell medium. However, the fusiform and the spherical cells focuses the light rays as it enters into the cytoplasm, and this is due to the changes in the refractive index. This focusing effect is further increased when the light propagates into the nucleus, and once again this is due to the differences in the refractive indexes of the medium [11]. Fig. 4 shows the effect of the focusing ratio and illumination radius which contribute to the overall gain of the light intensity.
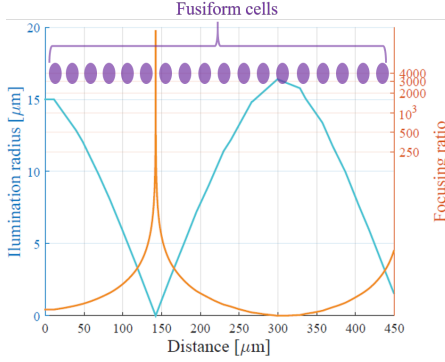
Fig. 4: Illumination radius ($h_2/h_3/h_4$) and focusing ratio γ for eighteen fusiform neurons.
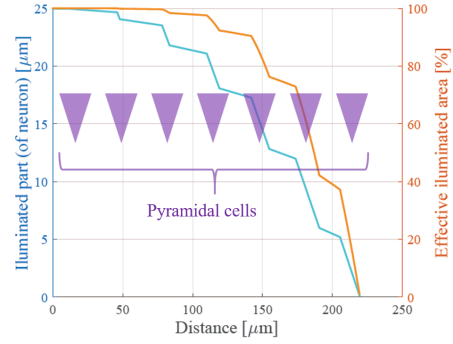

Fig. 5: Illumination height ($h_2/h_3/h_4$) and effective illumination area for seven pyramidal neurons.

This can be observed in the rise of the illumination as the light propagates through certain cells and then divergence occurs leading to reduction in the illumination.

The focusing behaviour is not found in the pyramidal shaped cell. Fig. 5 presents the illumination and shows that it gradually reduces due to the divergence of the light path away from the line of cells. This is solely due to the geometrical structure of the cell, as illustrated in Fig. 6.

Fig. 7 shows the path loss within the brain tissue for the three different neurons, where the transmitter and receiver is separated by 450 μm. In case of the pyramidal cells, the ray deviation due to the geometrical refraction causes the gradient change (marked by yellow shade). The deviation indicates that the light does not penetrate through the remaining neurons along its path, and this is because for the fusiform cells there are eighteen neurons along the propagation path, while the pyramidal cells has seven neurons due to the light path divergence.
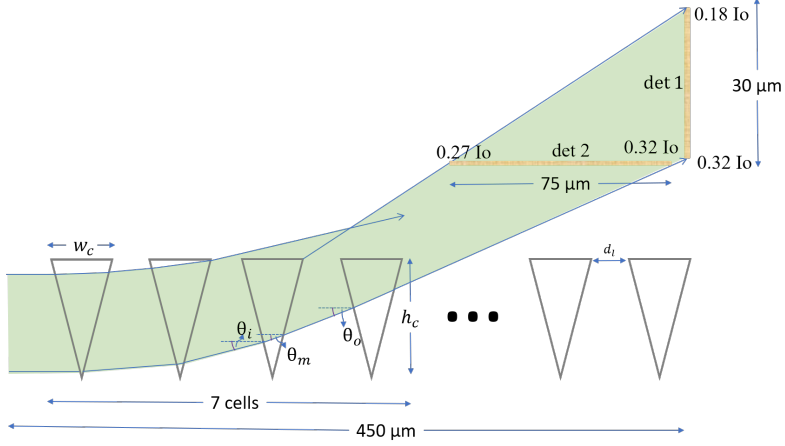
Fig. 6: Light path deviation along an array of pyramidal cells due to the geometric shape.
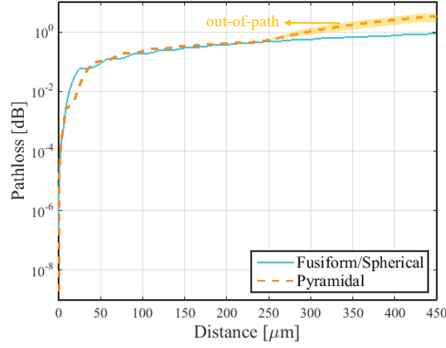

Fig. 7: Light propagation path loss for the distance of 450 μm between the transmitter and receiver with 18 cells in between.

B. Time and frequency analysis

We compare the delay and channel impulse response for the light propagation and determine how it gets impacted from the geometrics of the three neuron cells. The simulation of the light
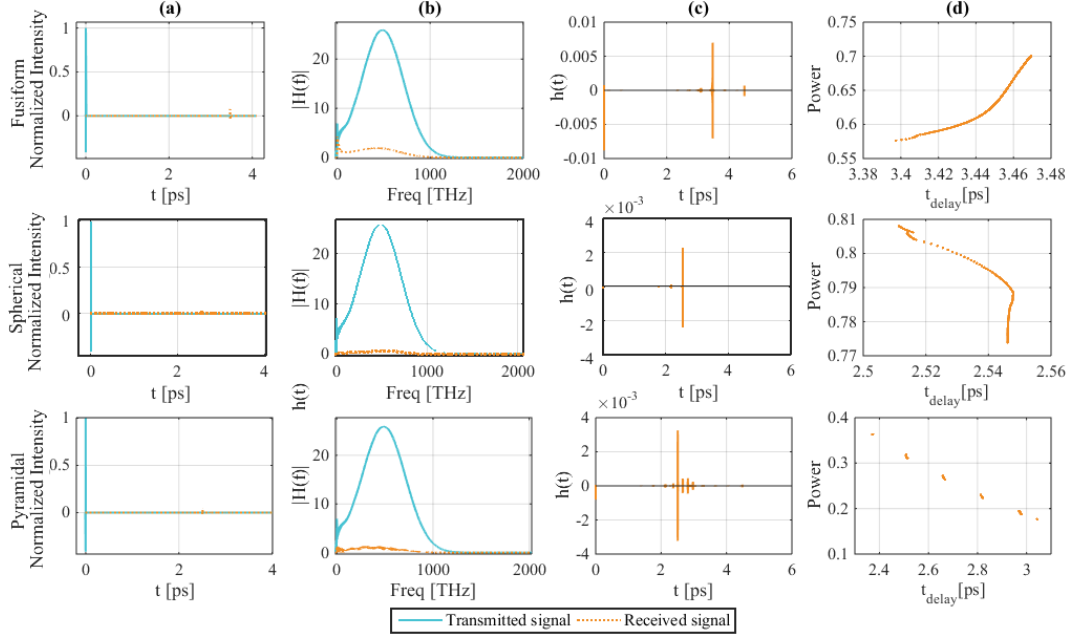
Fig. 8: Time and frequency analysis of light propagation along fusiform, spherical, and pyramidal cells. (a) The normalized intensity of the transmitted and the received signals in the time domain, (b) Absolute value of the transmitted and the received signal in the frequency domain, (c) Channel impulse response, and (d) Power delay profile.

path was for one dimension of 18 neurons that are linearly positioned along the wave propagation direction. In all cases, the receiver is located at a distance of 450 μm from the transmitter.

Fig. 8 shows both the time and frequency domain analysis. In our simulation, one femtosecond Gaussian light pulse is transmitted from a source which is located at 5 μm from the first cell on the path. The signal is analyzed at the receiver, and the peak frequency of the transmitted signal is approximately 500 THz. From the ray tracing analysis, the delay can be characterized by integrating all the incident rays at 450 μm distance from the transmitter.

Fig. 8 shows the channel impulse response of the one-dimensional neuron cells and is obtained by FFT and IFFT as explained in Sec. V. As shown in Fig. 8, the channel impulse response exhibits correlation with the power delay profile in terms of its peak magnitude of the received signal in the time domain. The light propagating through the fusiform cells experiences higher delay compared to the other two cell types since the light propagates mostly though the one dimensional array of neural tissue. In general, the speed of light in the brain tissue is faster than in the neuron because of the smaller refractive index. On the other hand, the light is absorbed less by the neurons due to its lower absorption coefficient, resulting in lower signal attenuation magnitude. The segmented time delays found in the pyramidal cells is caused by the ray leakages that occurs intermittently along the tissue. This phenomenon does not occur in two other type of cells since most of the ray propagation in two other cells are maintained along the straight path, even though there will be minor divergences and leakages along the path.

Fig. 9 depicts the channel impulse response for the three cell shapes with respect to the number of cells along the propagation path. It is obvious that the number of cells has a significant effect on the time of arrival of the signals since the refractive index of the cell is higher, resulting in slower light propagation velocity. The magnitude of the signal is dictated by the attenuation medium properties for all cell types and focusing parameters for both fusiform and spherical cells, which is determined in (16). The difference between the three cells is solely due to the geometry which affects the distance of the focus point $foc(\theta_F, x_F)$, focusing parameter γ, and the ratio of the total light propagation distance in the cell $\overline{d_a}$ and the brain tissue $\overline{d_e}$. The impulse response for the pyramidal cells increases gradually as the number of cell goes higher due to less traveled distance, before the light is diverged leading to no focusing effect.
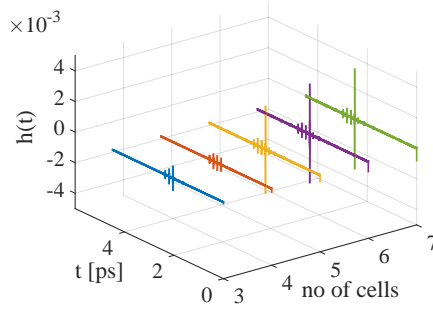
C. Power characteristics on the receiver

On the receiver, the total received signal is the result of the superposition of the light rays that arrive at the receiver surface. Fig. 10 shows the peak transmitted and received pulse shapes
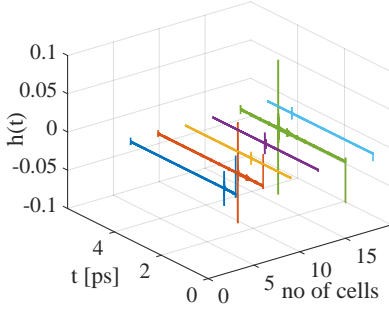
(a) Fusiform.
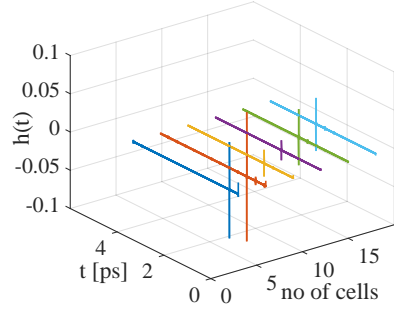
(b) Spherical.

(c) Pyramidal.

Fig. 9: Channel impulse response $h(t)$ for three shapes of cells with variable number of cells along the propagation path.

of different cell types as a result of superposition which is based on the time domain analysis elaborated in Sec. IV. Furthermore, the received signal power difference for those cells is mainly caused by the propagation distance ratio of the brain tissue for each path and the neurons, as well as the geometrical gain for each cell shape.

The previous results have shown that there are different propagation paths depending on the cell types, and this has an impact on how the detector on the receiver is designed. All the cells
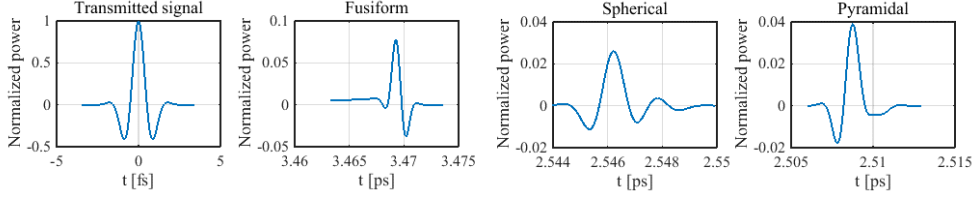
Fig. 10: The highest magnitude pulse shapes of the transmitted signal (gaussian short pulse) and the received signals after 450 μm propagation through one dimensional array of cells.

along the one-dimensional neural tissue contributes to the delay and attenuation of the light signal. Consequently, the geometry and the amount of the traversed cells also has an impact on the received power characteristics. Fig. 11 shows the received power characteristics on the detector of the receiver for both the fusiform and pyramidal cells. In the case of the fusiform cell's receiver detector, the width is 40 μm, while in the case of the pyramidal it is 30 μm. In the case
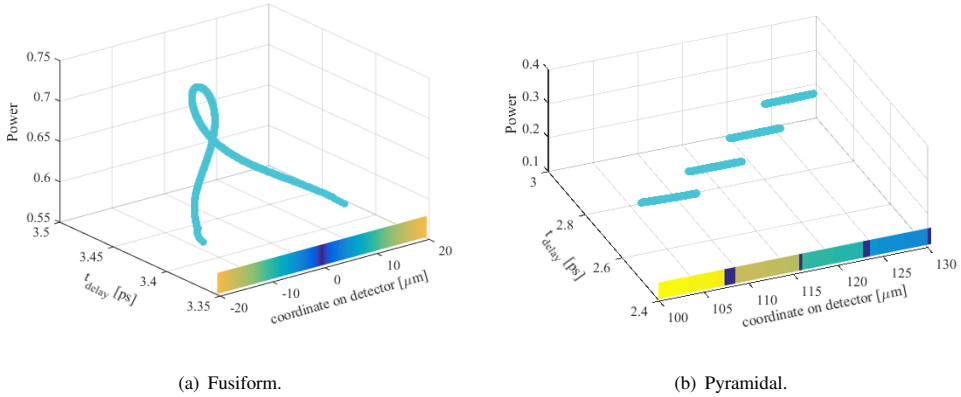

(a) Fusiform.

(b) Pyramidal.

Fig. 11: Normalized power of light ray with respect to the transmission delay when it arrives at a certain coordinate of a detector for (a) Fusiform cells, and (b) Pyramidal cells.

of the fusiform cells (Fig. 11 (a)), the power concentration is located in the middle of the detector and this is in-line to the propagation direction where the cells are aligned. This is directly linked to the focusing phenomenon that occurs in both fusiform and spherical cells. In order to detect all the transmitted rays, the detector height should be equal to the height of the cell, h_c, which is 30 μm used in our simulation. On the other hand, different characteristics is observed for the pyramidal cells where gradual power change occurs in stages and it is also segmented (Fig. 11 (b)). While the height configuration of the detector used is 30 μm, this parameter is dependent on the cell configuration (the number of traversed cells). The segmented phenomenon occurs due to leaking rays effect discussed in the earlier section. Unlike the fusiform and spherical cells, which causes power concentration at the centre of the detector, in the case of the pyramidal cells, the light rays that traverses through more cells experiences less attenuation as well as deviations from the original propagation line. Therefore, for both fusiform as well as spherical cells, the detector should be positioned at the center of the propagation line. In the case of the pyramidal cells, there are two ways for positioning the detector. As illustrated in Fig. 6, there are both horizontal and vertical orientations. The horizontal orientation provides better benefit since the propagation distance can be minimized, but the detected intensity is higher than in the vertical orientation.

VII. Conclusion

While light has been investigated for neural stimulation based on the concept of optogenetics, this paper addresses the light propagation from a nano-scale light source that can be used for communication between the WiOptND devices. The analysis presented in this paper discussed the important factors that affect the light propagation through neurons and brain tissue, namely the medium optical properties (μ_a and μ_s) and the geometric structures of the cells. The cells investigated in this paper are fusiform, spherical, and pyramidal neurons. An interesting effect is the distance and the number of the cells along the propagation axis, which affects the path

loss as well as the geometrical gain.

The channel impulse response of the light propagating along the neurons have an interesting behaviour. In the time domain, the delay of the simulated system can be observed when the light pulse is sufficiently short (femto second) since the delay is in the pico second level. This means that for longer pulses, the delay is insignificant. The time delays for the fusiform, spherical, and pyramidal are approximately 3.4, 2.5 and 2.7 ps, respectively. Additionally, radial-based geometries (fusiform and spherical) exhibit alternating high and low amplitude, while pyramidal tends to exhibit increasing amplitude signal level as the distance increases due to the path traversing through neurons more than the brain tissue. However, all shapes experience increasing delay as the distance increases. In terms of the frequency domain, the propagated signal does not experience any change in its frequency range. Both the time and frequency analysis exhibit 35%, 20%, and 65% attenuation in the signal power for the fusiform, spherical, and pyramidal cells, respectively. Moreover, the shape of the received signal is governed mainly by the geometrical shape of the cell where the diffraction causes the change in light directions for the pyramidal cell. The radial-based-geometry cell exhibited radial pattern in the power gradient at the receiver. In the case of the pyramidal cells, the position of the receiver is very important to obtain maximum light intensity for accurate detection. Our analysis found that the light intensity at the detector greatly varies across the area of the detector.

Analysis in this paper has shown that light propagation as a mode for communication between WiOptND implantable devices in the brain is a viable solution. The impulse response shows how the light propagation behaviour varies with the number of cells and how this can impact on the area design of the detector. This can lead to WiOptND devices that can be placed in various layers of the cortical column of the cortex, and coordinate their stimulation sequences of the neurons. The result of this research is a new form of Brain-Machine Interface that allows control and stimulation at single-neuron level, leading to new forms of treatments for neurodegenerative diseases.

APPENDIX A

RAY TRACING ALGORITHM FOR FUSIFORM CELL

This algorithm processes the optical properties of the medium (n_c, n_t), physical properties of the cell (r_c, d_c), and coordinates/direction of the incoming ray (x_2, h_2, θ_i). It generates the focus angle/coordinates $(foc(\theta_F, x_F))$ and propagation direction/coordinates inside the cell $(l_i(x_3', h_3), l_o(x_4, h_4), \theta_i^{(2)})$. For a series of cells, the iterative execution of this algorithm is required.

Algorithm 1 Ray tracing for fusiform cell

Require:

    n_c, n_t (refractive indices of cell and tissue)

    r_c (the radius of the cell)

    x_2 (the ray x-coordinate of the previous cell)

    h_2 (the radius of incoming illumination)

    d_c (the distance between cells)

    θ_i (the angle of the incoming ray)

Ensure:

    $foc(\theta_F, x_F)$ (the distance and angle of focus point)

    $l_i(x_3', h_3)$ (the coordinate of the incoming ray),

    $l_o(x_4, h_4)$ (the coordinate of the outgoing ray)

    $\theta_i^{(2)}$ (the ray propagation angle in the cell)

1: CALCULATE(x_2') $\triangleright$ $x_2' = x_2$ measured from the 1st surface,

$$x_2' = (d_c + 2r_c) - x_2$$

2: CALCULATE(x_3, h_3) ▷ x_3, h_3 = the coordinate where the ray hits the 1st surface,

$$m_2 = tan(180^o - \theta_i)$$

$$h_3 = \begin{bmatrix} m_2^2 + 1 \\ 2m_2(h_2 + m_2 x_2') \\ (h_2 + m_2 x_2')^2 - r_c^2 \end{bmatrix}^T \begin{bmatrix} x_3^2 \\ x_3 \\ 1 \end{bmatrix}$$

3: CALCULATE($\theta_i^{(1)}$) ▷ the incoming angle with respect to normal line of the 1nd surface

$$\theta_i'^{(1)} = arctan\left(\frac{h_3}{|x_3|}\right) - \theta_i^{(1)}$$

4: CALCULATE($\theta_o^{(1)}$) ▷ the refracted angle due to 1st surface

$$\theta_o^{(1)} = arcsin\left(\frac{n_t sin(\theta_i'^{(1)})}{n_c}\right)$$

5: CALCULATE($x_3, \theta_o^{(1)}$) ▷ with respect to 2nd surface

$$x_3' = 2r_c - (d_c + |x_3|)$$

$$\theta_i^{(2)} = \theta_i^{(1)} + (\theta_i'(1) + \theta_o^{(1)})$$

6: CALCULATE(x_4, h_4) ▷ the coordinate where the ray hits the 2nd surface

$$m_3 = tan(-\theta_i^{(2)})$$

$$h_4 = \begin{bmatrix} m_3^2 + 1 \\ 2m_3(h_3 + m_3 x_3') \\ (h_3 + m_3 x_3')^2 - r_c^2 \end{bmatrix}^T \begin{bmatrix} x_4^2 \\ x_4 \\ 1 \end{bmatrix}$$

7: CALCULATE($\theta_o^{(2)}$) ▷ the refracted angle due to 2nd surface

$$\theta_o^{(2)} = arcsin\left(\frac{n_c}{n_t}sin\left(arctan\left(\frac{h_4}{x_4}\right) + \theta_i^{(2)}\right)\right)$$

8: CALCULATE(x_F) ▷ the focus distance

$$\theta_F = \theta_o^{(2)} - arctan\left(\frac{h_4}{x_4}\right)$$

$$m_4 = tan(\theta_F)$$

$$x_F = \frac{m_4 x_4 - h_4}{m_4}$$

REFERENCES

[1] I. F. Akyildiz and J. M. Jornet, "Electromagnetic wireless nanosensor networks," *Nano Communication Networks*, vol. 1, no. 1, pp. 3–19, 2010.

[2] I. F. Akyildiz, F. Brunetti, and C. Blázquez, "Nanonetworks: A new communication paradigm," *Computer Networks*, vol. 52, no. 12, pp. 2260–2279, 2008.

[3] N. A. Abbasi, D. Lafci, and O. B. Akan, "Controlled information transfer through an in vivo nervous system," *Scientific reports*, vol. 8, no. 1, p. 2298, 2018.

[4] H. Ramezani and O. B. Akan, "Impacts of spike shape variations on synaptic communication," *IEEE transactions on nanobioscience*, vol. 17, no. 3, pp. 260–271, 2018.

[5] M. Veletić, P. A. Floor, Y. Chahibi, and I. Balasingham, "On the upper bound of the information capacity in neuronal synapses," *IEEE Transactions on Communications*, vol. 64, no. 12, pp. 5025–5036, 2016.

[6] G. E. Santagati and T. Melodia, "A software-defined ultrasonic networking framework for wearable devices," *IEEE/ACM Transactions on Networking (TON)*, vol. 25, no. 2, pp. 960–973, 2017.

[7] P. Johari and J. M. Jornet, "Nanoscale optical wireless channel model for intra-body communications: Geometrical, time, and frequency domain analyses," *IEEE Transactions on Communications*, vol. 66, no. 4, pp. 1579–1593, 2017.

[8] H. Elayan, P. Johari, R. M. Shubair, and J. M. Jornet, "Photothermal modeling and analysis of intrabody terahertz nanoscale communication," *IEEE transactions on nanobioscience*, vol. 16, no. 8, pp. 755–763, 2017.

[9] S. A. Wirdatmadja, M. T. Barros, Y. Koucheryavy, J. M. Jornet, and S. Balasubramaniam, "Wireless optogenetic nanonetworks for brain stimulation: Device model and charging protocols," *IEEE transactions on nanobioscience*, vol. 16, no. 8, pp. 859–872, 2017.

[10] A. Noel, D. Makrakis, and A. W. Eckford, "Distortion distribution of neural spike train sequence matching with optogenetics," *IEEE Transactions on Biomedical Engineering*, vol. 65, no. 12, pp. 2814–2826, 2018.

[11] S. Wirdatmadja, P. Johari, A. Desai, Y. Bae, E. K. Stachowiak, M. K. Stachowiak, J. M. Jornet, and S. Balasubramaniam, "Analysis of light propagation on physiological properties of neurons for nanoscale optogenetics," *IEEE Transactions on Neural Systems and Rehabilitation Engineering*, vol. 27, no. 2, pp. 108–117, 2019.

[12] S. Wirdatmadja, P. Johari, S. Balasubramaniam, Y. Bae, M. K. Stachowiak, and J. M. Jornet, "Light propagation analysis in nervous tissue for wireless optogenetic nanonetworks," in *Optogenetics and Optical Manipulation 2018*, vol. 10482. International Society for Optics and Photonics, 2018, p. 104820R.

[13] V. V. Tuchin, "Tissue optics and photonics: biological tissue structures," *Journal of Biomedical Photonics & Engineering*, vol. 1, no. 1, 2015.

[14] C. Fang-Yen and M. S. Feld, "Intrinsic optical signals in neural tissues: Measurements, mechanisms, and applications," *Acs Sym. Ser.*, vol. 963, pp. 219–235, 2007.

[15] J. D. Johansson, "Spectroscopic method for determination of the absorption coefficient in brain tissue," *Journal of biomedical optics*, vol. 15, no. 5, p. 057005, 2010.

[16] S. I. Al-Juboori, A. Dondzillo, E. A. Stubblefield, G. Felsen, T. C. Lei, and A. Klug, "Light scattering properties vary across different regions of the adult mouse brain," *PloS one*, vol. 8, no. 7, 2013.

[17] R. N. Renaud, C. Martin, H. Gurden, and F. Pain, "Multispectral reflectance imaging of brain activation in rodents: methodological study of the differential path length estimations and first in vivo recordings in the rat olfactory bulb," *Journal of biomedical optics*, vol. 17, no. 1, p. 016012, 2012.

[18] F. Scholkmann and M. Wolf, "General equation for the differential pathlength factor of the frontal human head depending on wavelength and age," *Journal of biomedical optics*, vol. 18, no. 10, p. 105004, 2013.

[19] L. Chuye, A. Dimitri, A. Desai, C. Handelmann, Y. Bae, P. Johari, J. Jornet, I. Klejbor, M. Stachowiak, and E. Stachowiak, "Brain organoids: expanding our understanding of human development and disease," in *Human Neural Stem Cells*. Springer, 2018, pp. 183–206.

[20] C. Von Economo, *Cellular structure of the human cerebral cortex*. Karger Medical and Scientific Publishers, 2009.

[21] T. Nguyen, "Total number of synapses in the adult human neocortex," *Undergraduate Journal of Mathematical Modeling: One+ Two*, vol. 3, no. 1, p. 26, 2010.

[22] S. P. Rodríguez, R. P. Jiménez, B. R. Mendoza, F. J. L. Hernández, and A. J. A. Alfonso, "Simulation of impulse response for indoor visible light communications using 3d cad models," *EURASIP Journal on Wireless Communications and Networking*, vol. 2013, no. 1, p. 7, 2013.

[23] C. Rulliere *et al.*, *Femtosecond laser pulses*. Springer, 2005.

[24] A. Levinson and A. Serby, "The refractometric and viscosimetric indexes of cerebrospinal fluid," *Archives of Internal Medicine*, vol. 37, no. 1, pp. 144–150, 1926.

[25] A. Yaroslavsky, P. Schulze, I. Yaroslavsky, R. Schober, F. Ulrich, and H. Schwarzmaier, "Optical properties of selected native and coagulated human brain tissues in vitro in the visible and near infrared spectral range," *Physics in Medicine & Biology*, vol. 47, no. 12, p. 2059, 2002.

[26] N. Bosschaart, G. J. Edelman, M. C. Aalders, T. G. van Leeuwen, and D. J. Faber, "A literature review and novel theoretical approach on the optical properties of whole blood," *Lasers in medical science*, vol. 29, no. 2, pp. 453–479, 2014.